On the Actuation and Kinematics for Humanoid Robots with Human-Like Motion

Zur Erlangung des akademischen Grades eines

Doktors der Ingenieurwissenschaften

von der KIT-Fakultät für Informatik
des Karlsruher Instituts für Technologie (KIT)

genehmigte
Dissertation

von

Cornelius Klas

aus Karlsruhe

Tag der mündlichen Prüfung: 09.05.2025

1. Referent: Prof. Dr.-Ing. Tamim Asfour
2. Referent: Prof. Dr. Karsten Berns

Abstract

The development of humanoid robots is a complex, challenging, and time-consuming task. Despite advances in actuation and sensor technology, designing humanoid robots with human-like strength and agility remains a significant challenge.

The goal of this work is to develop tools and mechanical as well as kinematic solutions for the design of humanoid robots. To achieve this, the research is structured into three interrelated areas.

The first key contribution focuses on gaining precise knowledge of the actuation requirements in terms of speed, acceleration, and torque for humanoid robots that aim to replicate human motion dynamics. The second part of this work presents the development of a linear actuator with two reduction stages, designed to achieve force-speed characteristics similar to those of human muscles. The third contribution introduces various mechanical implementations of quaternion joints and proposes a novel kinematic arrangement for a humanoid arm system incorporating these joints. These contributions are described in detail below.

System for the Design of Humanoid Robots

The first major contribution of this work is the development of a system for designing humanoid robot arms with human-like performance, with a particular focus on kinematics and actuation.

In the first phase, different kinematic arrangements are evaluated based on a predefined set of motions that the robot should be able to perform. Robot kinematics are defined by the selection of various joint mechanisms, their arrangement, positioning, and orientation. The results, presented as *Normalized Actuation Requirements*, serve as input for the subsequent kinematics and actuator selection.

The requirements are computed using normalized robot models executing normalized human motions from the KIT whole-body motion database. A model-law-driven normalization enables the computation of dynamic parameters for

a unified comparison of different kinematic designs and facilitates their adaptation to robots of any size and weight without the need for recalculations. The crucial step of transferring normalized human motion to normalized robot kinematics is achieved using a virtual spring-damper system. The optimal kinematic selection minimizes the performance requirements for the actuators.

In the subsequent *Actuation* phase, the normalized requirements are scaled to actual requirements based on the size, weight, and payload of the intended robot. This includes selecting the actuator types, their properties, and their positions, which in turn influence the overall weight of the robot.

The developed system evaluates the requirements against the performance characteristics of the selected components. Since certain properties follow known relationships within a design, a local optimum can be computed. The properties of the final design can be checked in the simulation.

Reaching Torque-Velocity Profiles of Human Muscles: The Adaptive Cycloidal Linear Drive

Insights from previous humanoid robot designs, along with findings from the first part of this work, highlight a significant challenge: the limitations of existing actuators regarding internal inertia and the trade-off between size, weight, force, and speed.

Therefore, the second part of this work introduces a novel linear drive designed to achieve force-speed characteristics similar to those of human muscles. This *Adaptive Cycloidal Linear Drive* is also integrated as an actuator option within the overall system.

Initially, the capabilities of human muscles are compared to those of existing mechanical systems. A key finding is that the peak power of muscle-like torque velocity profiles is considerably lower than that of drives with a fixed transmission ratio within the same operating range.

The proposed solution features an innovative gearbox composed of two separate motors, each driving different transmission ratios and coupled via an automatically switchable gearbox. This configuration generates a two-segment velocity-force profile. Motors and gearboxes operate at significantly reduced maximum mechanical power, allowing the use of much smaller components.

By combining both actuators, a variable transmission ratio is achieved, covering an operating range from fast, low-force to slow, high-force movements. This significantly outperforms conventional electric motors with a fixed transmission ratio.

Quaternion Joint based Kinematic Design for Humanoid Arms

The third key contribution of this work explores novel joint mechanisms and kinematic configurations for humanoid robots.

Most humanoid robot arms consist of a series of rotary joints. When these joints are directly actuated, the resulting system exhibits high inertia. Conversely, placing actuators remotely introduces challenges in force transmission and cable routing. Additionally, serial kinematic chains with consecutive rotary joints are prone to singularities, resulting in increased actuation demands and reduced controllability.

To address these challenges, this work investigates the use of rolling contact joint mechanism with two degrees of freedom, commonly referred to as *Quaternion Joints*. These joints offer several advantages, including a large singularity-free range of motion and a free joint center. The third part of this research presents different mechanical implementations of these quaternion joints and introduces a novel kinematic arrangement for a humanoid arm system.

The proposed design incorporates quaternion joints in the shoulder, elbow, and wrist, offering improved characteristics in terms of actuation requirements. The mechanical implementation is compact and lightweight, facilitating efficient cable routing and tendon-driven actuation through the arm. This joint mechanism is integrated into the previously developed design system. A full concept, including mechanical details for a humanoid robot arm featuring the proposed kinematic and actuation system, has been developed, demonstrating the feasibility of this approach.

Deutsche Zusammenfassung

Die Entwicklung humanoider Roboter stellt eine komplexe, herausfordernde und zeitaufwändige Aufgabe dar und trotz Fortschritten in der Antriebs- und Sensortechnologie bleibt die Entwicklung humanoider Roboter, die in Bezug auf Kraft und Beweglichkeit menschenähnliche Eigenschaften aufweisen, eine große Herausforderung.

Ziel dieser Arbeit ist daher die Entwicklung von Hilfsmitteln und mechanischen sowie kinematischen Lösungen für die Konstruktion humanoider Roboter. Dafür ist diese Arbeit in drei aufeinander aufbauende Arbeitsbereiche unterteilt.

Der erste Kernbeitrag dieser Arbeit befasst sich mit der Gewinnung von genauen Kenntnissen über die Antriebsanforderungen in Bezug auf Geschwindigkeiten, Beschleunigungen und Drehmomente für humanoide Roboter, die die menschliche Bewegungsdynamik nachahmen sollen. Im zweiten Teil der Arbeit wird ein Linearantrieb mit zwei Untersetzungsstufen für Kraft-Geschwindigkeits-Kennlinien entwickelt, die denen der menschlichen Muskeln ähneln. Der dritte Kernbeitrag beschreibt verschiedene mechanische Implementierungen von Quaternion-Gelenken und stellt eine neuartige kinematische Anordnung für ein humanoides Armsystem mit diesen Gelenken vor. Diese Kernbeiträge werden im Folgenden genauer beschrieben.

System für die Konstruktion humanoider Roboter

Der erste Beitrag und Schwerpunkt dieser Arbeit liegt auf der Entwicklung eines Systems für den Entwurf von humanoiden Roboterarmen mit menschenähnlicher Leistung, wobei der Fokus auf den Anforderungen der Kinematik und der Aktuation liegt.

Zuerst werden verschiedene kinematische Anordnungen auf der Grundlage einer Reihe von Bewegungen, die der Roboter ausführen können soll, bewertet. Die Roboterkinematik wird durch die Auswahl der verschiedenen Gelenkmechanismen sowie deren Anordnung, Position und Orientierung definiert. Die Ergebnisse, die als *Normalized Actuation Requirements* dargestellt werden,

dienen als Input für die nachfolgende Auswahl der Kinematik und der Aktoren. Die Berechnung der Anforderungen erfolgt an normalisierten Robotermodellen während der Ausführung normalisierter menschlicher Bewegungen aus der KIT-Ganzkörperbewegungsdatenbank. Die durch Modellgesetze geleitete Normalisierung ermöglicht die Berechnung der Dynamik für einen einheitlichen Vergleich kinematischer Entwürfe und deren Übertragung auf Roboter beliebiger Größe und Gewicht ohne Neuberechnung. Die entscheidende Übertragung von normalisierter menschlicher Bewegung auf normalisierte Roboterkinematiken wird durch die Anwendung eines virtuellen Feder-Dämpfer-Systems realisiert. Die optimale Wahl der Kinematik führt zu minimalen Leistungsanforderungen an die Aktoren.

In der anschließenden Phase werden die normierten Anforderungen auf die tatsächlichen Anforderungen skaliert, die auf der Größe, dem Gewicht und der Nutzlast des gewünschten Roboters basieren. Dabei werden die Aktortypen, deren Eigenschaften und Positionen ausgewählt, die wiederum das Gesamtgewicht des Roboters beeinflussen. Das entwickelte System bewertet die Anforderungen anhand der Leistungsmerkmale der ausgewählten Komponenten. Da einige Eigenschaften innerhalb einer Konstruktion bekannten Beziehungen folgen, kann das lokale Optimum berechnet werden. Nach Anpassung des Entwurfs an die verfügbaren Komponenten und deren Platzbedarf können die Eigenschaften des endgültigen Entwurfs in der Simulation überprüft werden.

Erreichen von Drehmoment-Geschwindigkeits-Profilen menschlicher Muskeln: Der adaptive zykloidische Linearantrieb

Die Erkenntnisse aus den bisherigen Erfahrungen bei der Entwicklung humanoider Roboter und die ersten Ergebnisse aus dem ersten Teil dieser Arbeit unterstreichen eine große Herausforderung: die Beschränkungen bestehender Aktoren in Bezug auf ihre interne Trägheit und das Zusammenspiel von Größe, Gewicht, Kraft und Geschwindigkeit. Daher wird im zweiten Teil der Arbeit ein lineares Getriebe für Kraft-Geschwindigkeits-Kennlinien entwickelt, die denen der menschlichen Muskeln ähneln. Dieser adaptive Zykloid-Linearantrieb wird auch als Aktoroption in das Gesamtsystem integriert. Zunächst werden die Fähigkeiten der menschlichen Muskulatur mit den Eigenschaften der bestehenden mechanischen Systeme verglichen. Besonders wichtig ist, dass die maximale Leistung muskeltypischer Drehmoment-Geschwindigkeits-Profile bei gleichem Arbeitsbereich deutlich geringer ist als die von Antrieben mit festem Übersetzungsverhältnis.

Die vorgeschlagene Lösung sieht ein neuartiges Getriebe vor, das aus zwei verschiedenen Motoren besteht, die jeweils unterschiedliche Übersetzungsverhältnisse antreiben und mit einem automatisch schaltbaren Getriebemechanismus gekoppelt sind. Diese Anordnung erzeugt ein aus zwei Segmenten bestehendes Drehzahl-Kraft-Profil. Sowohl die Motoren als auch die Getriebe arbeiten in diesem Aufbau mit deutlich reduzierten mechanischen Spitzenleistungen. Dies ermöglicht den Einsatz wesentlich kleinerer Komponenten.

Durch die kombinierte Betätigung beider Antriebe ergibt sich ein variables Übersetzungsverhältnis, das einen Betriebsbereich abdeckt, der von schnellen Bewegungen mit geringer Kraft bis zu langsamen Bewegungen mit hoher Kraft reicht. Damit wird der Arbeitsbereich eines Elektromotors mit fester Übersetzung deutlich übertroffen.

Neuartige Gelenkmechanismen und Kinematiken für humanoide Roboter

Der dritte Beitrag befasst sich mit neuartigen Gelenkmechanismen und Kinematiken für humanoide Roboter. Die meisten humanoiden Roboterarme bestehen aus einer Reihe von Drehgelenken. Wenn diese Drehgelenke direkt angetrieben werden, führt dies zu einem hohen Maß an Trägheit innerhalb des Armsystems. Bei einer entfernten Platzierung der Aktoren hingegen stellt sich das Problem der Kraftübertragung und Kabeldurchführung. Zudem sind Kinematiken mit seriellen Drehgelenken anfällig für Singularitäten, die höhere Antriebsanforderungen verursachen und die Steuerbarkeit einschränken.

Um diesen Herausforderungen zu begegnen, bietet der Einsatz von Rollkontaktgelenkmechanismen mit zwei Freiheitsgraden (DoF), auch Quaternionengelenke genannt, mehrere Vorteile. Dazu gehören ein großer Bereich von singularitätsfreien Bewegungen und ein freies Gelenkzentrum. Daher werden im dritten Abschnitt dieser Arbeit verschiedene mechanische Implementierungen dieser Quaternionengelenke untersucht und eine neuartige kinematische Anordnung für ein humanoides Armsystem vorgestellt. Dieses Design beinhaltet Quaternionengelenke in der Schulter, dem Ellbogen und dem Handgelenk. Die vorgeschlagene Kinematik zeigt verbesserte Eigenschaften hinsichtlich der Anforderungen an die Antriebstechnik. Die mechanische Umsetzung ist kompakt sowie leicht und vereinfacht die Durchführung von Kabeln und Seilzügen durch den Arm. Diese Art der Gelenkmechanik wird in das zuvor beschriebene Konstruktionssystem integriert. Ein Konzept einschließlich mechanischer Details für einen humanoiden Roboterarm mit der vorgeschlagenen Kinematik und Aktorik wird entwickelt und demonstriert die Machbarkeit des Ansatzes.

Acknowledgment

This thesis is the result of my work as a research scientist in the High Performance Humanoid Technologies Lab (H^2T) of the Institute for Anthropomatics and Robotics (IAR) at the Karlsruhe Institute of Technology (KIT).

First and foremost, I am deeply grateful to my supervisor, Prof. Dr.-Ing. Tamim Asfour, for his invaluable guidance, continuous support, and insightful feedback. His belief in my ability to develop the humanoid robot ARMAR-7 enabled me to fulfill a childhood dream. I would also like to thank Prof. Dr. Karsten Berns for co-supervising this thesis.

Special thanks go to my colleagues and fellow researchers at H^2T, whose discussions and collaborations made the research possible and my time at the lab both productive and enjoyable. I will always look back on this time and what we achieved together with joy and pride. In addition to my colleagues, I would like to thank the students I supervised who provided valuable contributions to my scientific work.

Finally, I would like to thank my family — especially my wife Barbara — for her patience, support, and understanding, as well as my children for their interest and emotional encouragement. I am also deeply thankful to my parents, Roswitha and Harald, for their constant support and belief in me.

I gratefully acknowledge the institutions and funding agencies that supported my research, particularly the Carl-Zeiss-Stiftung through the JuBot project, the German Federal Ministry of Education and Research (BMBF) under the Robotics Institute Germany (RIG), and the European Union H2020 Programme under the IMAGINE project.

Karlsruhe, Mai 2025 *Cornelius Klas*

Contents

1. Introduction

The field of humanoid robotics is emerging at the intersection of robotics, biomechanics, and artificial intelligence and aims to create machines that mimic human form and function. Humanoid robots, with their anthropomorphic features, occupy a unique position in the field of robotics, as they are designed to interact with the world and perform tasks similar to humans. The drive to construct robots that have a human-like appearance and behavior is deeply rooted in the desire to develop machines that can seamlessly fit into human environments, understand human interactions, and assist or collaborate with humans in different contexts.

The fascination with humanoid robots is not just aesthetic, but stems from the belief that a machine that mirrors human characteristics is better suited to tasks that are inherently designed for humans. These include navigating in human-friendly environments, operating tools and devices designed for human use, and social interaction with humans. The human form provides a versatile and adaptable platform for interacting with the world, making humanoid robots well-suited for applications in healthcare, home, education, entertainment, and beyond.

The development of humanoid robots is being driven by advances in robotics technology, including drive systems, sensors, and control algorithms. Actuators are crucial for mimicking human-like movements, while sensors enable robots to perceive and react to their environment. In addition, sophisticated control algorithms, often inspired by principles from neuroscience and cognitive science, are helping to enable more natural and intuitive interactions.

Despite significant progress, it is still difficult to develop humanoid robots with a level of dexterity, agility, and adaptability comparable to humans. To achieve fluid and human-like movement, complex problems related to actuation, kinematics, perception, and cognition must be solved. The background and context of humanoid robotics therefore encompasses a rich web of interdisciplinary research that draws on mechanical engineering, computer science, cognitive science, and beyond as researchers strive to unlock the full potential of these anthropomorphic machines.

The motivation behind this research arises from a profound challenge in the field of robotics — the quest to impart humanoid robots with human-like properties, specifically focusing on strength, agility, and versatile motion. This research is driven by a fundamental curiosity to unlock the potential of robotics, aspiring to bridge the gap between artificial systems and the remarkable capabilities inherent in human motion.

Experience in developing humanoid robots and analyzing existing robots has shown that achieving human-like performance often pushes technical systems to their limits. This challenge not only necessitates the optimization of the entire robotic system but also calls for innovative mechanical solutions. Namely, actuators that mimic torque-velocity profiles of human muscles and arm kinematics that demand minimal actuation power are required.

In this context, having precise knowledge of the actuation requirements in terms of velocities, accelerations, and torques is essential for humanoid robots designed to emulate human motion dynamics. The aim is to create a comprehensive system for deriving dynamic requirements, inspired by the complex dance of human movement. With this research, we aim to contribute to the advancement of humanoid robotics by unraveling the secrets of human-like movement and translating these insights into concrete design principles. Ultimately, this research is motivated by a deep-seated curiosity to enhance the capabilities of humanoid robots and pave the way for applications that extend beyond the realm of automation into the areas of assistive technology, healthcare, and human-robot collaboration.

1.1. Problem Statement

This thesis addresses the following research question:

> *How can we design humanoid robotic arms with characteristics that closely match human arms in terms of speed, acceleration, and torque?*

Despite advancements in actuation and sensor technologies, the creation of humanoid robots that replicate human-like properties in terms of strength, agility, and motion versatility remains a substantial challenge. Experience in designing humanoid robots and analyzing existing ones has shown that achieving human-like performance in humanoid robots often pushes technical systems to their limits. Consequently, it necessitates both optimizing the entire system to meet specific requirements and developing innovative mechanical solutions.

In this context, having precise knowledge of the actuation requirements in terms of velocities, accelerations, and torques is essential for humanoid robots designed to emulate human motion dynamics. This work primarily focuses on the design requirements of humanoid robot arms based on knowledge obtained from human motion data. The primary objective is to create a system for deriving dynamic requirements for humanoid robot arms from human motion data. This system should assess, compare, and optimize various solutions, encompassing the selection of optimal kinematics, the determination of motor and gearbox types and sizes, and the integration of novel drive and joint mechanisms. Figure 1.1 provides an overview of the key components and workflow of this research.

In accordance with the NASA Systems Engineering processes in Figure 1.2 (Kapurch, 2010), our *Humanoid Robot Design Assistant* aims to simplify the robot design process. While the system addresses a portion of these steps, experienced engineers are integral for incorporating stakeholder expectations (Step 1) and additional specifications. Specifically, the system simplifies the Technical Requirement Definition (Step 2) by translating them from human motion representations. Subsequently, the system performs the Logical Decomposition

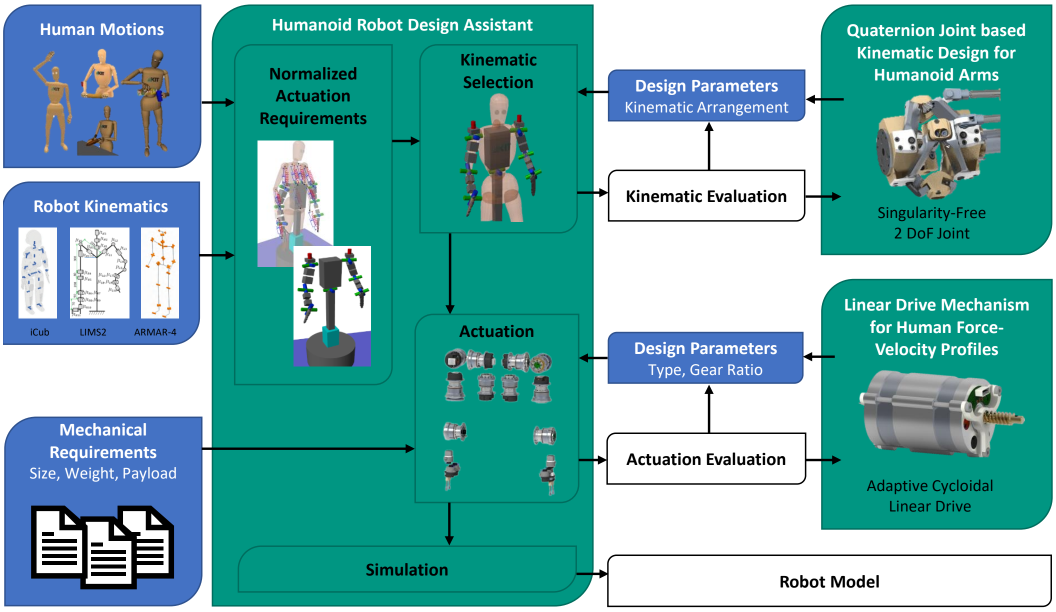

Figure 1.1.: Overview of the thesis: System for humanoid robot arm design based on human motion data, incorporating novel joint mechanisms and kinematics as well as novel adaptive cycloidal linear drives.

(Step 3) of top-level requirements into detailed specifications. Furthermore, our system supports the iterative nature of Design Solution Definition (Step 4) through our interactive Kinematics and Actuation design process, facilitating refinement and optimization.

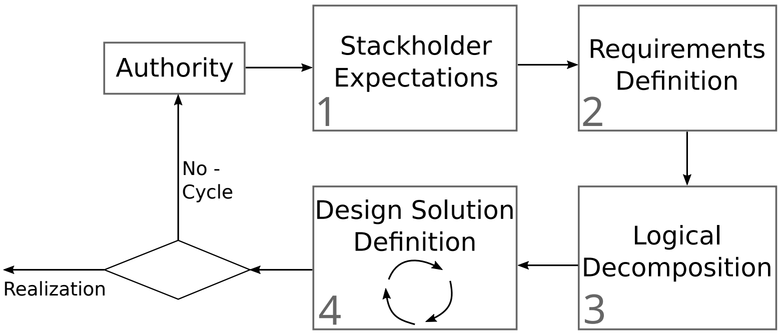

Figure 1.2.: Steps in the System Design Processes based on Kapurch (2010) and NASA.

1.2. Learning from Demonstration: A Roadmap for Robot Arm Design

Towards humanoid robotics that mimic human capabilities as faithfully as possible, the foundation of the research rests on the concept of learning from human demonstrations. This overarching theme guides the interconnected chapters that form the core of this research and provides a roadmap for the journey towards humanoid robotic arms with superior motion dynamics.

The development begins with a system for designing humanoid robotic arms, in which a framework for deriving dynamic requirements from human motion data is established. Essentially, this chapter lays the foundation for the subsequent parts by systematically translating the knowledge gained from human demonstrations into design specifications. Through the learning-from-demonstration approach, we bridge the gap between the theoretical understanding of human motion and the practical considerations that are essential for the design of humanoid robotic arms.

Building on the theoretical foundations of the first part, the second part of the dissertation deals with actuation systems, focusing on linear actuation mechanisms. Here, we investigate the possibility of emulating force-velocity profiles as observed in human arms. By pushing the boundaries of conventional drive systems, we aim to give humanoid robotic arms a level of performance that mirrors the dynamics of human demonstrations. We try to achieve this by learning from the biological example.

The third part extends our explorations into the field of kinematics and introduces a new perspective through Quaternion Joint-based design. This chapter builds on the principles outlined in the previous chapters and integrates kinematic considerations with insights gained from human demonstrations. With this approach, we seek to enhance the human-like motion capabilities of humanoid robotic arms and synthesize actuation mechanisms and kinematic structures in our pursuit of human-inspired robotics.

This triad of chapters, collectively guided by the idea of learning from human demonstration, forms the basis for exploring the design considerations underlying the development of humanoid robotic arms with human-like motion dynamics.

1.3. Contributions

The contributions of this work include a system for the design of humanoid robot arms with human performance for selected motions. Additionally, it introduces a novel linear drive and an innovative joint mechanism and kinematics, both designed as mechanical solutions to enhance motion dynamics and improve human-like movement capabilities.

Systems and Tools for Computer-Aided Design of Humanoid Robots: The first contribution of this thesis revolves around the creation of a system for the design of humanoid robot arms with human-like performance with a focus on *Kinematics* and *Actuation* requirements.

Within the *Kinematics*, different kinematic arrangements are evaluated and optimized based on a set of motions that the robot should be able to perform. The robot kinematics are defined by the selection of different joint mechanisms as well as their arrangement, position, and orientation. The results, presented as *Normalized Actuation Requirements*, serve as inputs for the subsequent phase, which is concerned with the identification of the actuation requirements. The calculation of the requirements is performed on normalized robot models during the execution of normalized human motions taken from the KIT Whole-Body Human Motion Database (Mandery et al., 2015). The normalization, guided by model laws, allows the calculation of dynamics for a uniform comparison of kinematic designs and their transfer to robots of arbitrary size and weight without recalculation. The crucial translation from normalized human motion to distinct normalized robot kinematics is realized through the application of a virtual spring-damper system. Optimal kinematic choices result in minimized total actuation power requirements.

In the subsequent *Actuation* phase, the normalized requirements are scaled to the actual requirements based on the size, weight, and payload of the desired robot. Hereby, the actuator types, their characteristics and positions are selected, which in turn influence the overall weight of the robot. The developed system evaluates the requirements against the performance characteristics of the selected components. Different actuators can be selected and compared, and an optimal gear ratio can be calculated. After the design adapts to the available components and their space requirements, the properties of the final design can be verified in simulation.

Linear Drive Mechanism for Human Force-Velocity Profiles: Insights gained from previous experiences in humanoid robot design, coupled with the initial findings from the first part of this work, underscore a significant challenge: the inherent limitations of existing actuators in terms of their internal inertia and the interplay between size, weight, force, and speed range. Therefore, in the second part of the work, a linear transmission for force-velocity characteristics that are similar to those of human muscles is developed. This adaptive cycloidal linear drive is also integrated as an actuator option into the overall system. Initially, the capabilities of human muscles are compared with the attributes of existing mechanical systems. It is particularly important that the maximum power of muscle-type torque-velocity profiles with the same working range is significantly lower than that of fixed-ratio drives.

Our proposed solution introduces a novel gearbox design featuring two distinct motors, each driving different gear ratios, coupled with an automatically switchable gearbox mechanism. This arrangement creates a speed-force profile composed of two segments, enabling adaptability to the specific requirements of various applications. Both the motors and gears in this setup operate at greatly reduced peak mechanical power levels. This allows the use of much smaller components. The combined actuation of both drives results in a variable transmission ratio, covering an operating range that spans from fast movements with low force to slow movements with high force. This substantially extends the operating range of an electric motor with a fixed gear ratio.

Quaternion Joint based Kinematic Design for Humanoid Arms: The third contribution of the thesis is a novel robot arm kinematics. The majority of hu-

Figure 1.3.: The humanoid robot ARMAR-7 (left) and relevant arm system components: SAC units for robot joints (middle) and wrist joint mechanism (right).

manoid robot arms typically consist of a series of rotary joints. When these rotary joints are directly actuated, it results in a high level of inertia within the arm system. On the other hand, when employing remote actuation, the issue of feed-through arises. Furthermore, singularities may occur in such designs, which, among other effects, increase the necessary actuation speed.

To address these challenges, the utilization of a rolling contact joint mechanism with two degrees of freedom (DOF), also called Quaternion Joints, offers several advantages. These include a large range of singularity-free motion and easy feed-through. In the third section of this thesis, we explore various mechanical implementations of these Quaternion Joints and introduce a novel kinematic arrangement for a humanoid arm system. This design incorporates Quaternion Joints in the shoulder, elbow, and wrist. The proposed kinematics shows superior properties regarding actuation requirements. The mechanical realization is compact as well as lightweight and simplifies the transmission of mechanical cables and electric wires through the arm. This type of joint mechanism is integrated into the previously described design system. A concept including mechanical details for a humanoid robotic arm with the proposed kinematics and actuation is developed and demonstrates the feasibility of the approach.

1.4. Structure of the Thesis

This thesis is divided into six chapters.

Chapter 2 presents *fundamentals* for the design of humanoid robots, namely (1) systems and tools for computer-aided design (2) drive mechanisms and (3) joint mechanisms, three research fields that are combined by the approach presented in this thesis to approach human-like performance. In particular, classical product development, systems engineering, and expert systems are introduced. In addition, *related work* on automated design of robotic and mechatronic systems as well as their applications in humanoid robotics is presented and compared.

Chapter 3 introduces the first step of the approach, the *System for the Computer-Aided Design of Humanoid Robots Based on Human Motion*. It is discussed how human motion data is normalized and applied to robotic design. Furthermore, it is described which kinematic and dynamic principles are considered in this process. Subsequently, it is explained how these principles guide the selection and arrangement of joint mechanisms. In this context, it is also motivated how human-like performance metrics are defined and used as design criteria.

Chapter 4 presents the development of a *Linear Drive Mechanism for Human Force-Velocity Profiles* that supports the design of humanoid robots. This chapter details the challenges with existing drive mechanisms and introduces the novel design and operational principles of the proposed linear drive. The chapter further demonstrates the drive's adaptability to different force-velocity requirements and evaluates its performance in replicating human muscle characteristics.

Chapter 5 presents the *Quaternion Joint based Kinematic Design for Humanoid Arms*. First, the theoretical basis for the use of Quaternion Joints in robotic arms is presented. Thereafter, the practical implementation of these joints in the humanoid robot's shoulder, elbow, and wrist is detailed, followed by a comprehensive analysis of their performance in various motions. Lastly, simulations and experimental results are discussed to evaluate the approach presented in this thesis.

Chapter 6 serves as a *conclusion* to this thesis. It summarizes the contributions, discusses its limitations, and presents possibilities for future work. This chapter reflects on the integration of the developed systems and tools in the broader context of humanoid robotics and outlines a vision for future advancements in the field.

2. Fundamentals and Related Work

This section presents fundamentals of (1) design tools and systems, (2) actuation systems, and (3) kinematics and joint mechanisms of humanoid robot arms, three research fields which are relevant for the approach presented in this work.

Starting with general tools such as guidelines for the systematic design of technical systems, classical product development, and systems engineering are described. This is followed by the presentation of more automated tools like Computer-Aided Engineering and expert systems. Thereafter, methods for the automated design of mechatronic and robotic systems are discussed. Finally, specialized systems and tools for human motion analysis and kinematic comparison are presented.

Secondly, fundamentals from drive mechanisms are explained. In particular, these include sensor-actuator units for robot joints (SAC), switchable gearboxes, and linear drives. Furthermore, related work on mechanical realizations for switchable linear actuators is presented.

Thereafter, related work in the field of joint mechanisms and kinematic designs of humanoid robots is described and categorized. Here, the focus is on novel mechanisms for humanoid robot arms.

2.1. Systems and Tools for Humanoid Robot Design

The development of humanoid robots is an enormous technical challenge due to the numerous design variables and constraints. The complexity is compounded by the non-linear relationships between these variables and the final functionality of the robot, making the search for analytical solutions particularly difficult (Sathuluri et al., 2023). To overcome these challenges, engineers employ a range of computer-aided design tools, including simulation software and advanced equation solvers.

In this chapter, we address the specific systems and tools used for the development of humanoid robots, covering general topics such as product development and systems engineering, computer-aided design, expert systems, automated design as well as specific tools for human motion analysis, motion retargeting, and kinematics comparison.

2.1.1. Computer-Aided Engineering

During the 1980s, Computer–Aided Engineering (CAE) systems emerged in parallel with the development of Computer–Aided Design and Manufacturing (CAD/CAM) and Product Data Management (PDM) tools (Ameri and Dutta, 2013). CAE tools enable engineers to simulate and analyze product behavior, improving design accuracy, and reducing testing costs.

CAE software can be broadly classified into two categories: specialized and general-purpose. Specialized CAE software is designed for a specific application or industry, such as automotive, aerospace, or civil engineering. On the other hand, general-purpose software tools provide a broad range of features and functionalities that can be applied to various engineering disciplines. General-purpose CAE software can be used for 2D and 3D modeling, simulation, and analysis, and can be applied to a wide range of engineering applications.

- CAD (Computer-Aided Design) is a type of CAE software that is used for creating, modifying, analyzing, and optimizing digital models of physical objects.
- BIM (Building Information Modeling) is a type of CAE software that is used for designing, constructing, and operating buildings and other infrastructure projects.
- DMU (Digital Mock-Up) is a type of CAE software that is used to create a digital representation of a product or system, allowing designers to visualize, analyze, and optimize their designs.
- FEM (Finite Element Method) is a type of CAE software and a numerical method that is used to simulate and analyze the behavior of complex systems, such as structural, mechanical, and thermal systems.
- CAE software can also be used to enhance creativity in robot design by providing a virtual environment to create and test different designs (Zhao et al., 2020). Similarly, the aim of this thesis is to create a framework to facilitate the design on humanoid robot arm systems.

2.1.2. Expert Systems

Expert systems aim to equal or surpass human expertise in problem-solving by integrating vast domain-specific knowledge and utilizing heuristics to streamline the solution process. "An expert system is a computer program that embodies expertise about a particular domain, and can use symbolic reasoning techniques to solve problems in this domain; problems that would need the assistance of a human expert in the real world. An expert system should also be able to explain its conclusions" (Rijckaert et al., 1988)

Originating in the late 1960s within the artificial intelligence (AI) field, expert systems addressed the limitations of early AI's general search mechanisms in complex domains. A notable advancement was the development of DENDRAL by Buchanan et al. (1968), a program for deducing molecular structures from mass spectrometry data, representing a significant step in encoding expert knowledge into rules.

Alongside MYCIN, a system for diagnosing blood infections, these early expert systems from Stanford University's Heuristic Programming Project (Russell and Norvig, 2010) exemplified the potential of AI in specialized decision-making, laying the groundwork for future AI advancements in rule-based knowledge systems.

Components of Expert Systems

Expert systems comprise several **core components** essential to their functionality (Tripathi, 2011). The **Knowledge Base** is central, containing domain-specific knowledge, structured with facts, rules, and data, often using **ontologies** to represent entities and their relationships (Van Harmelen et al., 2008). This knowledge is accessed by the **Inference Engine**, which applies logical rules to deduce new information or solve problems (Russell and Norvig, 2010). Various reasoning methods, such as forward chaining (data-to-conclusion) and backward chaining (goal-to-data), allow the system to reach specific conclusions or solutions.

To build the knowledge base, expert systems utilize a **Knowledge Acquisition Facility**, which transfers problem-solving expertise from domain experts, often with support from knowledge engineers (Wagner, 2017). Additionally, the **Explanation Facility** provides transparency by explaining the logic behind conclusions, increasing user trust and understanding. Finally, the **User Interface** allows users to input data and interact with the system in a comprehensible format, facilitating effective communication between the user and the system's internal representations (Jakus et al., 2013).

Applications in Humanoid Robotics

According to Wagner (2017), expert systems are used to tackle a wide range of challenges in different industries. They are particularly effective in medicine, manufacturing, accounting, banking, financial services, and even industries such as automotive and aerospace. According to the classification of Clancey (1985), the problems can be divided into three main categories, which are illustrated below with examples from humanoid robotics.

For **Analysis Problems** in the context of humanoid robotics, expert systems can be used for interpreting complex sensor data to recognize human emotions or intentions. It can analyze input from facial recognition and body language sensors to determine how a robot should interact with humans in social settings (Alonso-Martin et al., 2013).

In the context of **Synthesis Problems**, expert systems can be used for generating intelligent, synchronized, and coordinated gestures in humanoid robots to enhance humanoid robot interactions (Rai et al., 2009).

To solve **Combined Problems**, a humanoid robot could use an expert system to assess damage based on sensor data and then formulate a strategy to navigate through debris.

In the context of applications in humanoid robotics, Karrenbauer et al. (2018) present an ontology-based expert system for the systematic design of humanoid robots, which exemplifies how expert systems can advance the design process of humanoid robots. This system uses an ontological knowledge base to systematically support the design of humanoid robot components, in particular sensor-actuator units. By integrating existing catalog components into potential concept solutions and evaluating them against logical, physical constraints, and calculated properties, the system facilitates the generation of valid solutions. These solutions are then visualized through a user interface, showcasing the expert system's ability to not only analyze but also synthesize complex design requirements efficiently.

Advantages and Limitations

Ontology-based expert systems for the development of humanoid robots offer significant advantages, especially in the systematization of complex design knowledge. These systems improve the efficiency of the design process by utilizing structured knowledge bases as decision support.

However, the limitations of these systems have a significant impact on their application in the field of humanoid robotics. First and foremost, expert systems are limited by the amount of knowledge explicitly encoded within them. This limitation means that they are often unable to develop entirely new solutions or adapt to innovative design paradigms without significant human intervention. The inherent rigidity of expert systems makes them less flexible in accommodating new ideas and operating principles that do not fall within their predefined knowledge base. Thus, despite their usefulness in organizing and applying existing knowledge, expert systems require constant human intervention to incorporate new concepts and advances in robot design.

Given these limitations, the future role of ontology-based expert systems in the development of humanoid robots is uncertain. Exciting future developments include more dynamic and adaptive design methods that can autonomously generate innovative solutions with minimal human guidance. Technologies that utilize artificial intelligence and machine learning could reduce reliance on manually curated knowledge bases and enable more spontaneous and creative design processes. Such new approaches, like reinforcement learning, could outperform traditional expert systems and provide more flexibility and efficiency in the development of humanoid robots by learning from different data sources and real-world interactions.

2.1.3. Automated Design of Robotic Systems

In robotic design, knowledge-based systems such as expert systems and other automated design systems, with fluid boundaries between them, provide valuable support throughout the process. While some automated design tools rely on formalized human knowledge, others use physical principles or human demonstrations to create or support designs.

In the following, the state of the art in various systems for supporting mechatronic and robot design is presented and structured. These systems are categorized according to the *Optimization - Selection* dimension and the *System - Components* dimension.

The design process is supported by systems with different focuses; some help primarily in the concept phase, while others focus their support on the detailed design phase and use existing components for more detailed solutions.

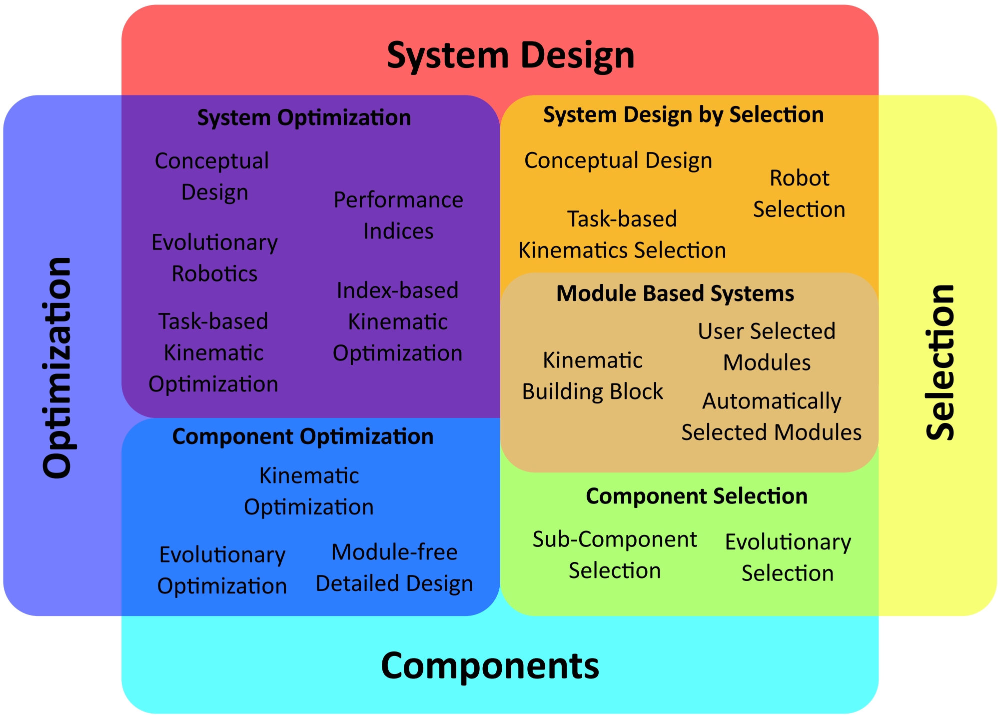

Figure 2.1.: Related work in the field of automated design of robotic and mechatronic systems. The diagram illustrates the approaches by categorizing them into five main categories according to the *Optimization - Selection* dimension and the *System - Components* dimension.

Some approaches focus on the optimization of robotic systems or components while others are used for the selection of complete robots, kinematics, or components.

This section therefore presents expert systems and analog automated systems to facilitate the selection, conceptual design, detailed design, or evolutionary design of robots and complex mechatronic systems. The classification of related work into the resulting four main categories (System Design - Optimization, System Design - Selection, Components - Optimization, Components - Selection) is illustrated in Figure 2.1.

System Optimization

At the juncture between system design and optimization, various methods are presented that focus on the design of the overall system. The systems can be used as components of larger structures, but are treated as closed units during optimization.

Conceptual Design in automated systems can support early-stage robotic design. For instance, Wu et al. (2008) uses Fuzzy Case-Based Reasoning to generate product ideas from a database, while Shaukat et al. (2016) combines fuzzy logic with ontological decision-making to enable self-reconfiguring capabilities in robotic frameworks, allowing autonomous adaptation to abnormal conditions.

Performance Indices are essential for evaluating and optimizing kinematic configurations in robotic systems. An early metric, Manipulability, proposed by Yoshikawa (1985), defines the volume of the manipulability ellipsoid to indicate preferred force or velocity directions. Building on this, Vahrenkamp et al. (2012) extends the manipulability measure by incorporating additional constraints, while reachability analyses such as those in Vahrenkamp et al. (2013) assess a robot's capacity to find suitable base positions. Other indices, like the velocity minimum metric from Zhang et al. (2013) and the condition number of the Jacobian matrix (Kim and Khosla, 1991), measure kinematic transmission and proximity to singularities, respectively. Additional performance measures, such as isotropy-based indices from Mayorga et al. (2005) and Gosselin and Angeles (1991), focus on achieving smooth, uniform motion and minimizing sensitivity to small joint angle errors. Comparisons of dexterity measures, including a new isotropy measure, are also presented by Kim and Khosla (1991).

Index-Based Kinematic Optimization techniques leverage performance indices to optimize the design of robotic systems. Jamwal et al. (2009) apply a modified genetic algorithm to optimize a soft parallel ankle rehabilitation robot, focusing on the condition number and geometric constraints. Similarly, You et al. (2019) use a kinematic optimization approach for an anthropomorphic robot hand, aiming to enhance finger interactivity. In another study, Maaroof et al. (2021) optimize a robotic arm by adjusting link lengths and angles, using redundancy resolution techniques with virtual joints; a pareto chart illustrates the balance between competing performance indices. For hand-specific design challenges, Wang et al. (2012) introduce a numerical approach based on Monte Carlo methods to optimize thumb opposition, evaluating dexterity for object manipulation tasks.

Task-Based Kinematic Optimization focuses on optimizing robot design to meet specific task requirements. Shiakolas et al. (2002) use evolutionary optimization to design SCARA robots with minimized torque, considering deflection and physical constraints, where design variables include link length and cross-sectional area. Similarly, Jun et al. (2004) propose using the proximity between desired and actual manipulation ellipsoids as a task-specific quality metric for redundant manipulators. A toolbox by Vila-Rosado and Domınguez-López (2006) applies genetic algorithms to select optimal robot mechanism types, dimensions, and configurations for trajectory-following tasks, optimizing for constraints and joint torques. For specific manipulator designs, Kim (2006) determines kinematic parameters of a two-DoF manipulator based on task requirements. In industrial settings, Gadaleta et al. (2017) optimize robot layout to minimize energy consumption for tasks within manufacturing cells. Canaday et al. (2017) introduce an interactive, iterative robot design approach using multi-rigid body simulations, which integrates user feedback on non-quantifiable factors like aesthetics. This process assesses a robot's performance through virtual testing, adjusting morphological parameters based on task needs. Similarly, Whitman and Choset (2019) present a method to co-optimize robot design and trajectory, balancing functionality and joint count, which is demonstrated in practical prototypes for applications such as a Mars mission arm and wearable robots. Finally, Jaquier et al. (2021) propose a manipulability transfer framework to align robot kinematics with manipulability ellipsoids from human demonstrations, enhancing task suitability.

Evolutionary Robotics (ER) uses environment-driven performance indices rather than manually chosen metrics, as shown by Bredeche and Montanier (2010), enabling the automatic evolution of complete robots in simulated environments. Although evolutionary algorithms are effective for optimization, accurately simulating morphology and control for real-world tasks remains challenging and often results in simplified environments. Lipson and Pollack (2000) applied fitness criteria to evolve robots with components like bars, actuators, and artificial neurons, while Frutiger et al. (2002) used an iterative evolutionary tool to optimize locomotion in legged robots. Generative representations in Hornby et al. (2003) lead to modular robot designs with improved efficiency, and Tanev et al. (2005) demonstrated the autonomous evolution of efficient sidewinding gaits for a snake-like robot. Co-optimizing robot morphology and control, Bongard (2010) showed how subjecting more morphological aspects to evolutionary pressure enhances task-specific performance. Evaluations of soft robots in diverse environments were conducted by Cheney et al. (2014), highlighting the flexibility of voxel-based designs. However, Samuelsen and Glette (2015) noted a significant ″reality gap,″ as results in real-world implementations often diverged from simulations. More recent studies by Meixner et al. (2019) and Buchanan et al. (2020) focus on specific applications, such as evolving manipulators for precise object manipulation and autonomous fabrication-ready designs, respectively. In summary, while genetic algorithms and evolutionary methods provide effective solutions for complex design optimization, they can be computationally intensive, especially as population size increases,

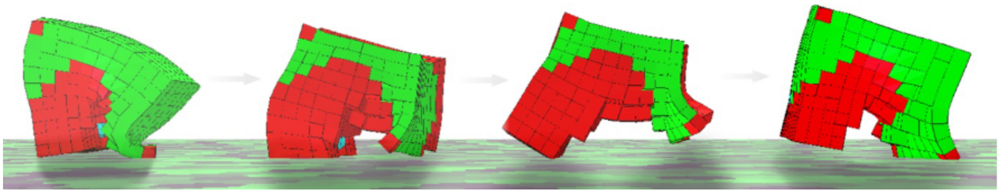

Figure 2.2.: Natural looking morphology and behavior of evolved soft robot. *Source:* (Cheney et al., 2014) © 2014 ACM.

making it challenging to ensure consistent results across simulations and real-world tests (Renner and Ekárt, 2003; Whitman and Choset, 2019).

Component Optimization

Combining component design and optimization, techniques for improving individual parts within a larger system are explored below.

Kinematic Optimization in the category **Component Optimization** focuses on refining individual components within robotic systems for optimal performance. Gosselin and Lavoie (1993) address the geometric design of three DoF parallel spherical manipulators, optimizing configurations for accuracy and isotropy to achieve decoupled motion in orthogonal directions. In a similar vein, Hassan and Abomoharam (2017) optimize the kinematic parameters of a robot gripper mechanism to enhance functionality. Further developments in compliant mechanisms are highlighted by Bilancia and Berselli (2020), who optimize a monolithic compliant design module for constant force output. Additionally, Bilancia and Berselli (2021) provide a comprehensive overview of design tools for nonstandard beam-based compliant mechanisms, which serve as adaptable building blocks for achieving specific behaviors in robotic applications.

Evolutionary Optimization methods enable multi-objective optimization in robotic design. For example, Datta and Deb (2011) address robot gripper optimization by minimizing both force variation and actuator force amplification. Saravanan et al. (2009) explore intelligent optimization algorithms, including Multi-objective Genetic Algorithm (MOGA), Elitist Non-dominated Sorting Genetic Algorithm (NSGA-II), and Multi-objective Differential Evolution (MODE), to tackle complex multi-objective problems in gripper design, aiming to achieve Pareto-optimal solutions across multiple objectives and constraints.

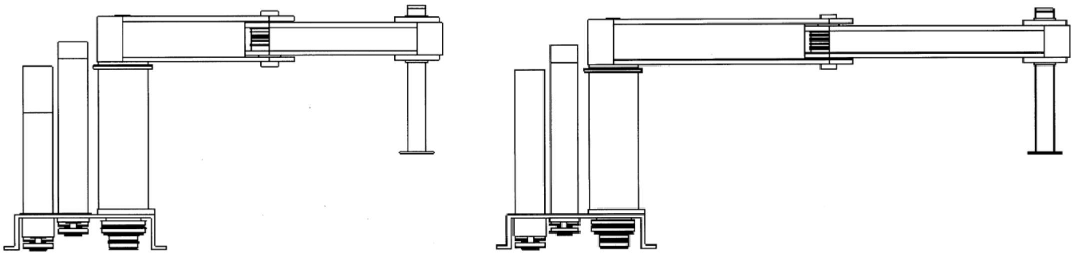

Figure 2.3.: Left: Parametric model of a SCARA, Right: Adapted for a larger reach. *Source:* (Bhatia et al., 1998) © 1998 Elsevier Science Ltd.

Module-Free Detailed Design approaches support detailed component optimization without predefined modules. Bhatia et al. (1998) present an expert system integrated with CAD for SCARA (Selective Compliance Assembly Robot Arm) design, where users input parameters like workspace and payload, which then guide calculations for link lengths, motors, and transmissions, producing an adjustable parametric SCARA model in CAD (Figure 2.3). Similarly, Myung and Han (2001) describe an expert system that automates the arrangement of catalog components within a parametric machine tool design, allowing users to select components through a GUI that then updates the CAD model dimensions. Additionally, Wang et al. (2014) introduce an automated design optimization for a headstock system, where spindle geometry impacts system stiffness and natural frequencies, managed through ontologies to coordinate dependencies among subcomponents, such as hydrostatic bearings. Specific component design, such as actuator optimization, also plays a critical role in detailed design. Pasch and Seering (1984) introduce an early heuristic for optimizing motor-gearbox combinations to achieve maximum acceleration, deriving the optimal gear ratio as $i^* = \sqrt{J_M/J_L}$—known as the principle of inertia matching, where the gear ratio balances input and output inertia.

System Design by Selection

At the interface between system design and selection, various methods are presented that focus on the design of the entire system. The systems can be used as components of larger structures, but during selection of whole robots or modules, they are treated as closed entities.

Conceptual Design approaches in system design often rely on expert systems to facilitate knowledge transfer for specific applications. For instance, Olier (1985) enhance the conceptual design of space robots by selecting optimal solutions for different elements, while Li et al. (2010) present an expert system to support innovation in general conceptual design.

Similarly, Komoto and Tomiyama (2012) propose a framework for computer-aided design of mechatronic products based on abstract geometric model evaluation. In the field of electronics within mechatronic systems, El-Nakla (2012) develops a case-based expert system to aid design.

Addressing complex robotic systems, Ziglar et al. (2017) introduce an approach for optimizing component selection and configuration to meet user requirements. Zheng et al. (2019) further support conceptual design with a requirement-driven architecture, enabling designers to choose components aligned with early-stage requirements.

In **Conceptual Design by Selection**, rather than directly optimizing an objective function, the capabilities of the robot are iteratively explored, guiding designers in adjusting parameters. This human-in-the-loop process enables engineers to incorporate domain knowledge on morphology and dynamics, leveraging computational assistance while retaining control over the final design.

Erdman et al. (1986) introduce techniques for type synthesis—generating and selecting configurations—using graph theory and expert systems to optimize kinematic topologies for robots and grippers. Similarly, Chew et al. (1991) develop an expert system for designing robotic hands that represents mechanical systems through graphs of basic joint types (gear pairs, sliding pairs, rotating pairs) to connect various components like cranks, pistons, and racks. In parallel mechanism design, Huang and Li (2003) present a systematic approach for synthesizing robot base mechanisms, selecting joint numbers and types to achieve the desired kinematic properties.

Task-Based Kinematics Selection involves selecting and optimizing kinematic configurations tailored to specific tasks. For example, Kim and Khosla (1993) propose a method for task-based kinematic design that includes distinct selection and optimization phases, demonstrated through the design of a space shuttle tile servicing robot. **Klas** et al. (2023) introduce a performance index focused on actuator requirements for selecting kinematic configurations based on retargeted human motion, aiming to enhance alignment with human movement dynamics.

Robot Selection involves using expert systems and decision-support tools to guide the selection of robots based on specific requirements. Agrawal et al. (1991) introduce software for computer-aided robot selection, where an expert system helps users set priorities and manage the selection process. Similarly,

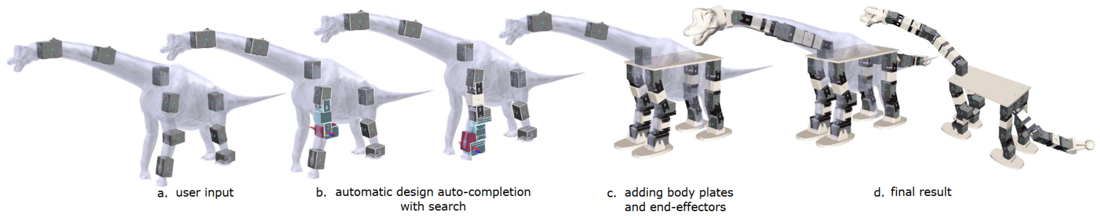

Figure 2.4.: Automatic design search with guiding mesh. *Source:* (Desai et al., 2017) © 2017 IEEE.

Pham and Tacgin (1991) present "DBGRIP," an expert system designed to assist in selecting robot grippers, featuring learning capabilities that improve through positive reinforcement. Boubekri et al. (1991) develop an expert system tailored for industrial robot selection, incorporating functional, organizational, and economic considerations. Karsak (2007) further enhances selection methods by integrating an expert system with a decision-support system, using multiple criteria decision-making (MCDM) techniques to simplify the process. For collaborative robot installations, Keller et al. (2016) provide a MATLAB-based planning assistant to aid in engineering system design. Lastly, Amici et al. (2020) adopt a task-driven approach, identifying selection criteria by comparing mini-manipulators and equivalent linear actuators for integration into complex systems.

Module Based Systems

Kinematic Building Blocks can be used for modular and automated design of robotic mechanisms. Chiou and Sridhar (1999) develop an automated conceptual design system that uses a matrix representation for kinematic building blocks, allowing for the generation of alternative conceptual designs. Expanding on this, Wahl et al. (2003) present a framework for designing single DoF mechanisms, synthesizing possible solutions and creating simplified 3D models automatically. An improved morphological matrix is employed by Chen et al. (2006) in an automated design approach, using a knowledge base to systematically guide mechanism design. Zu et al. (2009) introduce function codes to represent design requirements and kinematic building blocks, enabling the systematic enumeration of feasible functional connections. For more interactive design, Megaro et al. (2015) present a system allowing users to create customizable, 3D-printable robotic creatures by adjusting morphology, gait, and motion style; the system also optimizes stable motions and generates fabrication blueprints for legged robots. Lastly, Simionescu (2019) provides closed-form equations for analyzing linkage-mechanism building blocks, offering a rapid selection process for practical applications.

User Selected Modules provide an accessible approach for users to design and customize robotic devices using modular components. Mehta et al. (2015) introduce a system in which users can create printable robots inspired by origami by selecting from a library of mechanical, electrical, and software components. This system translates high-level design specifications into mechanical drawings, wiring instructions, and control software, enabling rapid and cost-effective fabrication for non-experts. Similarly, Desai et al. (2017) present a computational design system that allows both novices and experts to build custom robots with modular parts, including actuators, brackets, and 3D-printable components. The system provides a visual design environment for exploring configurations, auto-completes designs for ease of use, and supports physical simulation testing, demonstrated by the creation of various legged and wheeled robots. In *Skaterbots*, Geilinger et al. (2018) offer an intuitive platform to design robotic creatures with legs or wheels, allowing users to combine different mechanical elements in a graphical interface. The system automatically optimizes dimensions to ensure functional movement and provides a simulation environment to test walking, rolling, and skating behaviors customized to each unique design.

Automatically Selected Modules enable users to create custom robotic devices with minimal expertise by automating the selection and integration of modular components. Desai et al. (2018a) present a system that allows casual users to design 3D printed electromechanical devices by integrating standard components into user-defined shapes. The system optimizes the enclosure design, considering component placement, support structures, and assembly paths, significantly reducing barriers for non-experts, as demonstrated in user studies through the creation of diverse functional devices. Ha et al. (2018) introduce a computational method that designs robots to execute specific motion trajectories based on high-level requirements. Using a library of modular components, the system employs discrete optimization and heuristics to create the simplest robotic configuration for the given task. The effectiveness of the method is confirmed by the fabrication of robots that meet these motion specifications. Ramos et al. (2018) offer an ontology-based approach that aligns user-selected abilities with suitable robot types, automatically assembling robots from 3D-printable modules. It generates controllers using a visual programming language, making the platform accessible for educational use and supporting various robot types, including wheeled, snake, humanoid, and hexapod robots.

Component Selection

At the interface of component design and selection, various methods support the choice of specific components within a larger structure. These approaches focus on selecting parts that meet the overall requirements of the system, distinguishing component-focused selection from full-system design.

Sub-Component Selection methods prioritize the selection of specific parts within a system. Laugis and Vodovozov (2008) present an expert system for electric drive design that automates component selection from a database, handling the complex, multi-criteria nature of the task. Similarly, Karrenbauer et al. (2018) introduce an expert system based on ontology to design sensor actuator units in humanoid robots, using a knowledge base to efficiently create and optimize component arrangements, reducing design time for both experienced engineers and beginners. Desai et al. (2018b) offer an interactive system that automates the design of robotic arms by translating task requirements into end-effector paths, assembling modular components accordingly. The adaptability of the system is validated in simulations for various tasks, illustrating its ability to generate task-specific robotic arms.

Evolutionary Selection involves agent-based methods to optimize component configurations. For example, Campbell et al. (1999) employ an agent-based approach to generate electro-mechanical designs from catalog components, optimizing configurations to meet specific design goals.

Summary

The automated design of robotic systems spans a wide spectrum, from optimizing system designs and components to selecting and assembling modular systems. These methodologies apply varying degrees of simplification, such as modularization and parameterization, to facilitate the creation of automated design systems. However, limitations in the diversity of solutions underscore the complexity of designing advanced mechatronic components for high-performance humanoid robots. Although detailed approaches are primarily applied in laboratory and educational settings, there is a growing interest in their application to the design of advanced robotic systems, indicating significant potential for future advancements.

2.1.4. Human Motion Analysis and Motion Retargeting

Human motion analysis and motion retargeting are critical components in the development of humanoid robots with human-like motion. These processes involve the capture, analysis, and application of human motion patterns to robotic systems, enabling them to perform tasks in a manner that closely mimics human actions. This subsection explores the tools and systems that facilitate the design and implementation of such capabilities in humanoid robotics.

Information on joint actuation during the walking cycle is documented in the literature (Zelik and Kuo, 2010). However, such information is infrequently available for arm movements, particularly across various humanoid robot designs. To determine the actuator requirements for humanoid robots performing human-like actions, it is necessary to first adapt the recorded human motions to the distinct kinematic configurations of these robots. A fundamental challenge in transferring human poses to robots is the absence of a universal method to resolve the inverse kinematics for movements involving multiple joints due to the high redundancy in the human body (Bernstein, 2014).

Furthermore, there are two fundamental problems when the segment lengths of humans and robots differ: It is not possible to replicate all positions of the end effectors for full-body poses and the exact matching of robot segment positions to their human equivalents is not achievable. Various strategies, including optimizations and constraints, are described in the literature to solve the problem of motion retargeting.

In case of small kinematic differences, the kinematic model of the human can be directly used to compute the robot's joint angles or analytical methods can be employed for motion imitation (Xu et al., 2018). This is also true in scenarios where precise end-effector positions are not crucial, permitting the straightforward transfer of joint angles.

In most cases, however, especially when restrictions such as singularities have to be taken into account, the focus is on end-effector poses. Techniques employing inverse (Jaquier et al., 2020) or forward kinematics (Di Fava et al., 2016; Rakita et al., 2017; Darvish et al., 2019), enable alignment of end-effector poses while considering additional constraints. These approaches are coupled with non-linear optimization and consider additional constraints including manipulability, temporal smoothness, and joint limits. In (Di Fava et al., 2016) the focus is on multi-contact motion retargeting and quadratic programming is used to optimize for segment positions, different joint parameters (e. g. position, velocity, torque) and high level parameters (contacts, collisions). When the focus is on manipulability analysis and transfer of human movement (Jaquier et al., 2020) Riemannian manifolds can be used in addition to inverse kinematics to reach the end-effector pose. A challenge with these methods is the necessity for a detailed mathematical formulation of forward or inverse kinematics.

Alternative strategies use convolutional neural networks (Aberman et al., 2020), reinforcement learning (Kim and Lee, 2020), or unsupervised learning (Lim et al., 2019). Lastly, a real-time motion retargeting method via neural latent prediction is introduced (Wang et al., 2023). This method predicts future robot joint motion, allowing for advanced trajectory tracking and fault-tolerant capabilities in scenarios with loss of human input. However, it is uncertain whether these learning-based approaches can adapt to completely new robot kinematics as expected.

The researchers Arimoto and Sekimoto (2006) and Shin and Kim (2014) propose an alternative approach for the control of multi-joint grasping motions using a virtual spring-damper system. These methods leads the endpoint to the goal without requiring explicit solutions for inverse kinematics, inverse dynamics or pre-planned trajectories. However, these methods are based on a suitable initial configuration of the arm.

Building on the virtual spring-damper system introduced by Arimoto and Sekimoto (2006), **Klas** et al. (2023) propose an approach for handling diverse joint configurations. Traditional inverse kinematics solvers are limited to specific joint types. In contrast, the framework by **Klas** et al. (2023), built with Simulink elements, allows the creation of complex joints, such as parallel and cable-driven mechanisms. This approach simplifies the integration of new joint types, like Quaternion Joints, by avoiding complex mathematical descriptions of forward kinematics. This enables rapid evaluation and comparison of novel joint designs. To achieve motions closely resembling human demonstrations and ensure a human-like quality, the framework employs multiple virtual spring-damper systems with adjustable stiffness. This framework is also used in this thesis.

2.1.5. Kinematics Comparison

In the pursuit of creating humanoid robots with human-like motion, the study of kinematics plays a pivotal role. Kinematics, the branch of mechanics that describes the motion of points, bodies, and systems of bodies without considering the forces that cause them to move, is fundamental to the design and control of

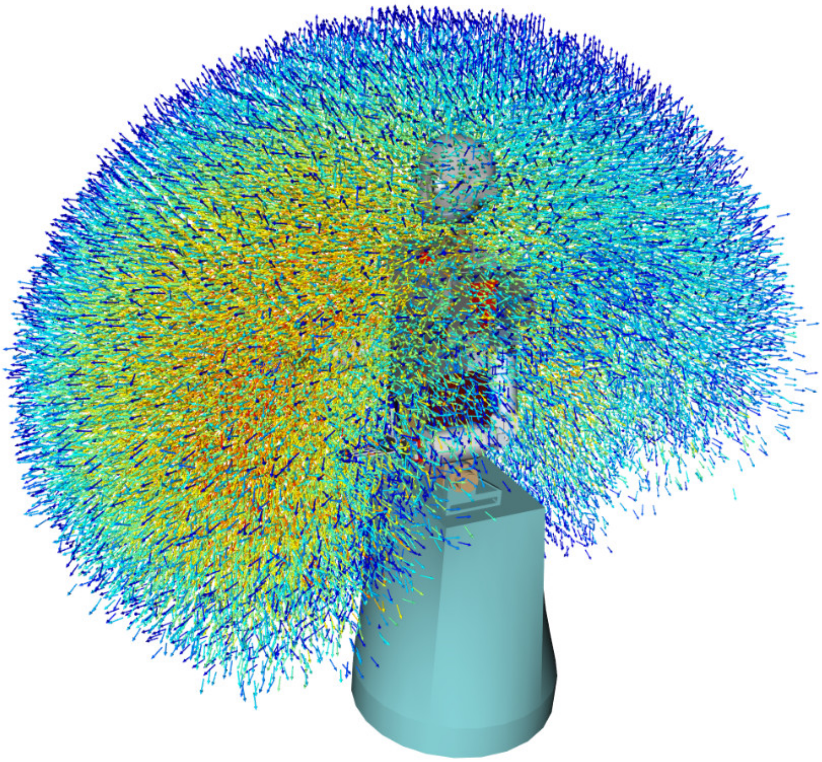

Figure 2.5.: Reachability distribution of ARMAR-III 's right TCP. The kinematic chain is covering hip and right arm with 10 DoF. *Source:* (Vahrenkamp et al., 2013) © 2013 IEEE.

humanoid robots. In the process of reviewing and comparing robot kinematics, a performance index (Zhang et al., 2013) is crucial for rapidly assessing different kinematic designs. These indices can be chosen based on general criteria relevant to a broad range of robots or tailored specifically to the application or task of interest.

Common metrics for comparing robot kinematics include reachability and manipulability analyses. Reachability analysis assesses the robot's workspace, the volume it can access with its end-effector (see Figure 2.5). Originally researched by Vahrenkamp et al. (2013) for the evaluation of different robot base placements, it also enables a comparison of kinematics. Manipulability ellipsoids are representation of the manipulability distribution (favored directions of force or velocity) in the workspace. The Yoshikawa manipulability index (Yoshikawa, 1985) provides a 6D voxelized data structure holding manipulability reference values in each voxel. It is based on the volume of the manipulability ellipsoid. The extended manipulability measure (Vahrenkamp et al., 2012) or the measure of isotropy (Kim and Khosla, 1991) include additional constraints. The velocity minimum (Zhang et al., 2013) represents the kinematic transmission ability in the direction of the robot's worst velocity performance. The global conditioning index (GCI) (Gosselin and Angeles, 1991) evaluates the condition number at all points of the manipulator workspace. The condition number of the Jacobian matrix, as explored by Kim and Khosla (1991), serves as a tool for assessing both kinematic accuracy and proximity to singular configurations. A high condition number indicates potential issues with accuracy and the robot approaching a state where its movement becomes difficult or impossible to control.

Unlike general performance metrics, application-based indices take a more specialized approach. For instance, Wang et al. (2012) evaluate humanoid hands by analyzing the intersection volume reachable by their fingertips. Jun et al. (2004) propose a task-specific quality function for redundant manipulators based on the closeness between desired and actual manipulability ellipsoids. Furthermore, Jaquier et al. (2021) introduce a framework that learns from human demonstrations to match desired manipulability ellipsoids, enabling robots to replicate specific manipulation capabilities.

Evolutionary robotics (ER) (Bongard, 2013) employs a competition-based approach to evaluate robot performance in a specific task during each evolutionary cycle. This process allows for the simultaneous evolution of a robot's sensory apparatus, morphology, and control system. For example, in a study by Cheney et al. (2014), the fitness of simulated soft robots, composed of various voxel types, is determined based on the distance they traveled across four environments. This fitness criterion of locomotive ability is also used for robots evolved through simulations from bars, actuators, and artificial neurons (Lipson and Pollack, 2000).

ER can even leverage the environment itself to define the fitness function, rather than requiring manual selection (Bredeche and Montanier, 2010). Similar approaches can be applied to the kinematic design of manipulators. For instance, Meixner et al. (2019) explores the possibility of evolving the kinematic design together with the control strategy during a simulated task, where the fitness function is based on the distance between the manipulator's object and a desired reference trajectory. However, simulating both the robot's morphology and control system to accomplish complex tasks remains a significant challenge (Doncieux et al., 2015). As a result, most ER applications focus on a limited set of tasks within simplified environments.

For robots working in a human environment and interacting with human-made tools, the inclusion of human likeness in the evaluation process is preferable. Motion retargeting techniques offer relevant metrics that can be adapted for kinematic comparison, such as the quantification of human likeness. These metrics for functional anthropomorphism include measures used by Liarokapis et al. (2013) such as Cartesian joint distance, convex hull similarity and the area of triangles between individual joints. Additional metrics encompass factors like elbow elevation (Kim et al., 2006), spatial and temporal correspondences between human and robot motion (Gielniak et al., 2013), and even considerations of human comfort and effort during interaction (Zacharias et al., 2011). Scaling laws in robotics for comparison of different sized robots can be found in Dermitzakis et al. (2011).

In previous work, we proposed a novel *performance index* based on actuator requirements for retargeted human motion (**Klas** et al., 2023). The underlying premise is that human movement has evolved over a long period of time into large capabilities, and that the development of robots that can mimic these movements is beneficial. To our best knowledge, no other existing approaches provide a kinematics *performance index* based on retargeted human motion.

2.2. Actuation Systems in Humanoid Robots

Actuators and gearboxes are crucial for meeting the challenge of integrating complex mechatronic systems into limited space in humanoid robot development. A useful method for evaluating actuator capabilities is the force-speed profile, which shows the maximum force an actuator can provide at a given speed. For rotary actuators, this corresponds to the angular velocity-torque curve. Electric motors typically deliver higher speeds and lower torques than required, necessitating gearboxes to increase torque while reducing speed. However, gearboxes with fixed ratios cannot alter the overall motor speed-torque profile or maximum mechanical power.

Human muscles, as shown in Figure 2.8, exhibit a force-speed profile with low maximum power, featuring high torque at low speeds and high speed at low torque (Alcazar et al., 2019). This characteristic is highly efficient and desirable for actuators.

While alternative actuation methods, such as artificial muscles and hydraulics, exist, they face challenges in power, durability, and control. Thus, electric actuation remains the focus of this work.

There are three primary reasons why achieving human-like performance with electric motors is challenging, even though these motors can attain higher power densities ($1\,\mathrm{kW/kg}$ (Tanaka et al., 2013) to $7\,\mathrm{kW/kg}$ (Seok et al., 2012)) compared to human muscles ($0.2\,\mathrm{kW/kg}$ (Hunter and Lafontaine, 1992)).

The first challenge lies in the strict space and weight constraints, coupled with the high demands for peak force and speed. Due to these limitations, most robot gearboxes employ a fixed gear ratio (Matsuki et al., 2019; Rader et al., 2017). To match the maximum speed and torque of a biological muscle using an actuator with fixed speed and torque limits, the motor and gearbox must provide much higher peak mechanical power (see Figure 2.8), which results in motors and gearboxes being significantly larger and heavier than human equivalent (Winter, 2009). Previous work on ARMAR-6 (Asfour et al., 2019), ARMAR-4 (Asfour et al., 2013), and KIT-Gripper (**Klas** et al., 2021) also demonstrated that electric motors with fixed ratios struggle to achieve human-like performance in speed, torque, and acceleration. In this dilemma, humanoid robots often focus on torque using high gear ratios (CENTAURO (Baccelliere et al., 2017) or HRP-5P (Kaneko et al., 2019)) at the expense of speed and agility.

The second reason involves external inertia. Heavy gears located in the joint axis require even larger gears for the upstream joints in the kinematic chain, which is a substantial drawback given the many degrees of freedom required in humanoid arms.

The third challenge relates to internal inertia. Electric motors deliver their best power densities at high speeds, making gearboxes with high transmission ratios in the range of $R = 10$ to $R = 300$ necessary (Matsuki et al., 2019). Since the motor diameter is a limiting factor in the design of humanoid robot arms, and small motors cannot directly provide the required torque, gearboxes are needed to amplify torque. These gearboxes typically have transmission ratios around $R = 100$ for sufficient torque. However, since reflected inertia increases with the square of the transmission ratio R, a very high reflected inertia, comparable to the weight of the entire arm, arises from motor inertia.

In the following, different humanoid robots are mentioned. In Table 5 in Appendix B, references to humanoid robot arms and joint mechanism are summarized.

2.2.1. Sensor-Actuator Units for Robot Joints

Sensor-actuator units (SA) are compact modules that integrate motors, sensors, gears, and bearings. When equipped with motor control electronics, they are called sensor-actuator-controller units (SAC). These preintegrated components

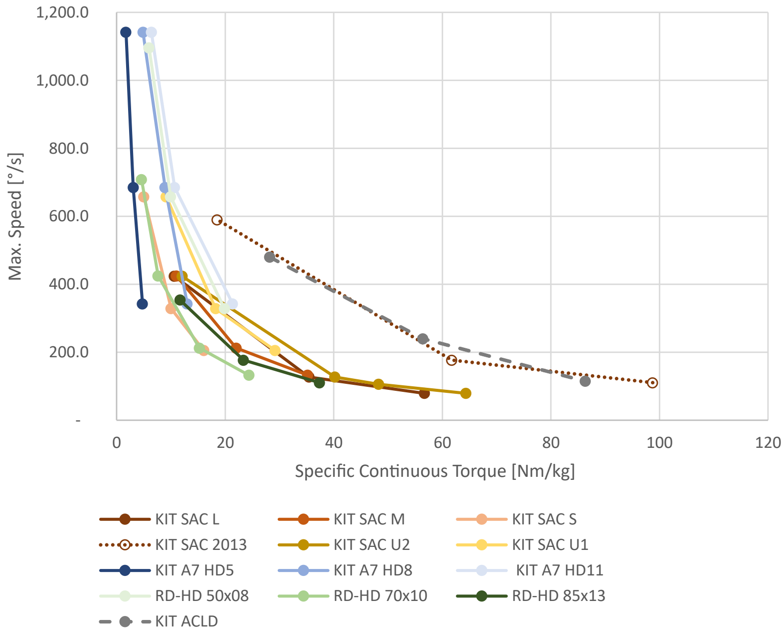

Figure 2.6.: Plot of maximum speed versus specific torque in different actuators with different transmission ratios.

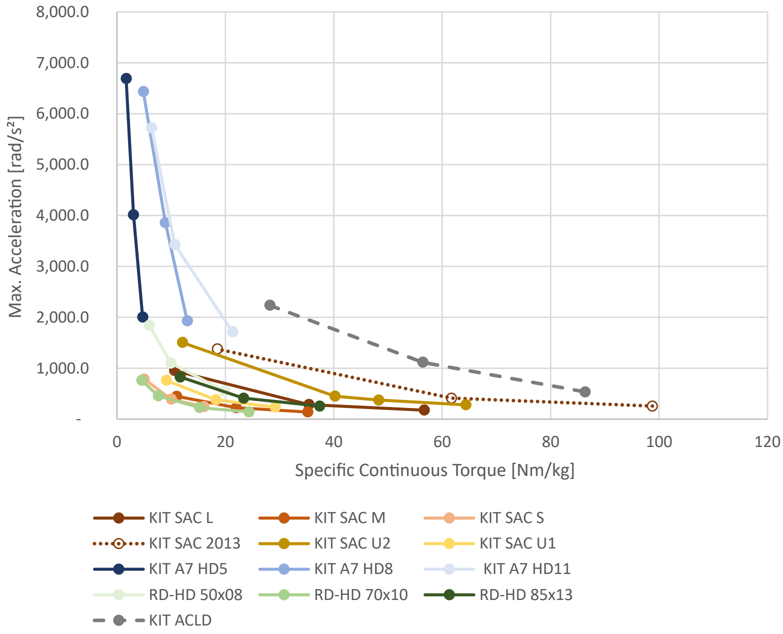

Figure 2.7.: Plot of maximum acceleration versus specific torque in different actuators with different transmission ratios.

simplify robot design, ideally enabling each joint to consist of a single SA unit with minimal mechanical structures. Key features include modularity for easy assembly, scalability for diverse connectivity, high integration for compactness, and robustness for real-world applications. Most robotic actuators use fixed transmission gearboxes (Matsuki et al., 2019; Rader et al., 2017), which simplifies design but limits performance. The two main types are rotary SA units, preferred for robot arms due to direct axis integration, and linear SA units, used in robot legs for compatibility with spring compliance, such as Series Elastic Actuators (SEAs) in the compliant robot leg CARL (Schütz et al., 2016, 2017). This section reviews related work with focus on rotary units with electric motors and fixed transmission, particularly for human-centered robots. This is exemplified in the designs of ARMAR-4, ARMAR-6, and ARMAR-7 which use these integrated components for modular robotic systems (Asfour et al., 2013; Rader et al., 2017).

In Figure 2.6 and 2.7, various actuators with different transmission ratio variants are compared by plotting maximum speed against specific torque and maximum acceleration against specific torque. The principal characteristics of these actuators are similar, and the data points are predominantly aligned along a common curve. For comparison, the ADCL with a multi-speed gearbox is also included. Table 2.1 compares these sensor-actuator units in terms of specifications and performance metrics. The first entries refer to the KIT SAC units, which differ from the related work by a comparatively high degree of integration. Following the general comparison based on key metrics, selected actuators are described in detail.

Albu-Schäffer et al. (2007) introduce the lightweight arm (LWR III) with sensor-actuator (SA) units, featuring brushless DC motors, brakes, Harmonic Drives, and control electronics. This design, consisting of seven interconnected SA units, laid the groundwork for commercially available robots like KUKA LBR arms and collaborative robots from Franka Emika (Panda), Universal Robots (UR series), and Kinova (JACO series).

Asfour et al. (2013) introduce integrated rotary sensor-actuator (SA) units for humanoid robots. The SA units in the ARMAR-4 feature a brushless DC motor, a Harmonic Drive, and various encoders, with strain gauges applied to a spoke wheel for torque sensing. Notably, the compact design of the hip and leg units features a relatively large motor. Although this may initially appear overly large, it significantly improves the maximum speed compared to the specific continuous torque shown in Figure 2.6.

The DARPA Robotics Challenge (DARPA, 2015) showcased working humanoids to a wider audience. Several teams utilized self-developed sensor-actuator units (Negrello et al., 2015; Stentz et al., 2015; Radford et al., 2015), while at least seven relied on commercially available Dynamixel units (Robotis, 2015). The Dynamixel Pro series integrates motors, gearboxes, sensors (both

Table 2.1.: Comparison of the state-of-the-art in actuators. The comparison is limited to SA/SAC units for human-centered robotics.

Name	Ratio	L	D	m	T_{cont}	T_{peak}	n_{max}	a_{max}	T_{sp}
Motor / Gear / Usage	-	mm	mm	kg	Nm	Nm	°/s	rad/s^2	Nm/kg
KIT SAC 2013	TQ ILM 85x13 / HD CPL-2A-25 Source: CAD, TQ-Group (2024); Harmonic Drive (2024)								
	160	84	112	1.4	138.2	176.0	111	259	98.7
ARMAR-4 Leg	100	84	112	1.4	86.4	157.0	177	414	61.7
	30	84	112	1.4	25.9	50.0	590	1,380	18.5
KIT SAC L	TQ ILM 70x18 / HD CPL-2A-25 Source: CAD, TQ-Group (2024); Harmonic Drive (2024)								
ARMAR-6 Cla1,Sho1,Sho2	160	157	112	2.1	119.0	176.0	80	179	56.7
	100	157	112	2.1	74.4	157.0	127	286	35.4
	30	157	112	2.1	22.3	50.0	424	954	10.6
KIT SAC M	TQ ILM 70x10 / HD CSD-2A-25 Source: CAD, TQ-Group (2024); Harmonic Drive (2024)								
ARMAR-6 Sho3, Elb1, Elb2	160	112	112	1.8	63.4	123.0	133	140	35.2
	100	112	112	1.8	39.6	110.0	212	225	22.0
	50	112	112	1.8	19.8	63.9	425	449	11.0
KIT SAC S	TQ ILM 50x08 / HD CSD-2A-20 Source: CAD, TQ-Group (2024); Harmonic Drive (2024)								
ARMAR-6 Wri1,Wri2	160	117	85	1.1	17.6	56.8	206	246	16.0
	100	117	85	1.1	11.0	35.5	329	393	10.0
	50	117	85	1.1	5.5	17.8	658	787	5.0
KIT SAC U2	TQ ILM 70x18 / HD CPL-2A-25 Source: CAD, TQ-Group (2024); Harmonic Drive (2024)								
	160	140	104	1.85	119.0	176.0	80	283	64.3
ARMAR-DE Cla1,Sho1,Sho2	120	140	104	1.85	89.3	167.0	106	377	48.3
ARMAR-DE Sho3, Elb1, Elb2	100	140	104	1.85	74.4	157.0	127	452	40.2
	30	140	104	1.85	22.3	50.0	424	1,507	12.1
KIT SAC U1	TQ ILM 50x08 / HD CSD-2A-20 Source: CAD, TQ-Group (2024); Harmonic Drive (2024)								
A.-DE: Wri1/2, A.-7: Cla1,Sho1/2	160	120	83	0.98	28.6	64.0	206	238	29.2
ARMAR-7: Sho3, Elb1	100	120	83	0.98	17.9	57.0	329	381	18.2
	50	120	83	0.98	8.9	28.8	658	762	9.1
KIT A7 HD5	FH 4221BXTH / HD CSF-5-1U-CC-F Source: CAD, Faulhaber (2024); Harmonic Drive (2024)								
	30	53	42	0.295	0.5	0.5	1142	6,691	1.7
	50	53	42	0.295	0.9	0.9	685	4,014	3.1
	100	53	42	0.295	1.4	1.4	343	2,007	4.7
KIT A7 HD8	FH 4221BXTH / HD CSF-8-1U-CC-F Source: CAD, Faulhaber (2024); Harmonic Drive (2024)								
	30	62	42	0.37	1.8	1.8	1142	6,435	4.9
ARMAR-7: Neck, Elb2	50	62	42	0.37	3.3	3.3	685	3,861	8.9
	100	62	42	0.37	4.8	4.8	343	1,931	13.0
KIT A7 HD11	FH 4221BXTH / HD CSF-11-1U-CC-F Source: CAD, Faulhaber (2024); Harmonic Drive (2024)								
	30	67	54	0.42	2.7	4.5	1142	5,720	6.4
	50	67	54	0.42	4.5	8.3	685	3,432	10.7
	100	67	54	0.42	9.0	11.0	342	1,716	21.3
KIT ACLD	Maxon RE 25 / ACDL Source: Maxon Motor (2024a); **Klas** (2023)								
	50	58	45	0.278	7.8	24.0	480	2,237	28.2
	100	58	45	0.278	15.7	24.0	240	1,119	56.4
	209	58	45	0.278	24.0	24.0	114	535	86.3
RE25 CSF8	Maxon RE 25 / HD CSF-8-1U-CC-F Source: CAD, Maxon Motor (2024a); Harmonic Drive (2024)								
	30	31	43	0.23	0.5	1.8	800	3,259	2.2
	50	31	43	0.23	0.8	3.3	480	1,956	3.7
	100	31	43	0.23	1.7	4.8	240	978	7.3
RE35 CSF14	Maxon RE 35 / HD CSF-14-1U-CC-F Source: CAD, Maxon Motor (2024a); Harmonic Drive (2024)								
	30	45	73	0.635	1.9	17.7	1300	3,181	2.9
	50	45	73	0.635	3.1	23.0	780	1,909	4.9
	100	45	73	0.635	6.2	28.0	390	954	9.8
RD-HD 50x08	TQ ILM 50x08 / HD CPL-2A-14 Source: TQ-Group (2024); Harmonic Drive (2024)								
	100	78	97	0.9	17.9	28.0	329	552	19.9
	50	78	97	0.9	8.9	18.0	658	1,103	9.9
	30	78	97	0.9	5.4	9.0	1096	1,839	6.0
RD-HD 70x10	TQ ILM 70x10 / HD CPL-2A-20 Source: TQ-Group (2024); Harmonic Drive (2024)								
	160	105	128	2.6	63.4	92.0	132	143	24.4
	100	105	128	2.6	39.6	82.0	212	229	15.2
	50	105	128	2.6	19.8	56.0	424	458	7.6
	30	105	128	2.6	11.9	27.0	708	763	4.6
RD-HD 85x13	TQ ILM 85x13 / HD CPL-2A-2 Source: TQ-Group (2024); Harmonic Drive (2024)								
	160	111	141	3.7	138.2	176.0	110	259	37.4
	100	111	141	3.7	86.4	157.0	177	414	23.4
	50	111	141	3.7	43.2	50.0	354	828	11.7

incremental and absolute), controllers, and networking, facilitating easy electrical and mechanical integration into various robot designs. This high degree of integration is superior to many other SA units (Schunk, 2011; TQ-Group, 2020; Harmonic Drive, 2016; SENSODRIVE, 2020).

In recent years, more user-friendly SA units were introduced. Examples are the ANYdrive joint (ANYbotics, 2017) and HEBI Robotics R-Series actuators (HEBI Robotics, 2019), which provide enhanced functionalities, including precise torque control without reliance on complex friction models. They also utilize EtherCAT for high-speed, real-time control and communication. To address the previous torque limitation of 38 Nm, they developed the H-Series (HEBI Robotics, 2023) actuator, which offers up to 140 Nm of continuous torque.

While compliance is not the primary focus of this related work, it is important for safe human-robot interaction (Vanderborght et al., 2013) and thus, a brief overview is provided. Series Elastic Actuators (SEAs), developed for robots like WALK-MAN (Negrello et al., 2015) and Valkyrie (Radford et al., 2015), incorporate springs for passive compliance, ensuring reliability. Nevertheless, fixed compliance parameters may limit adaptability and complicate control. Active compliance allows real-time adjustment of compliance parameters, using torque control to simulate natural behavior. This relies on techniques like current sensing (Robotis, 2015) and strain gauges (Albu-Schäffer et al., 2007; Asfour et al., 2013), requiring high bandwidth communication, such as EtherCAT, for effective implementation. Both passive SEAs, advantageous for shock tolerance and energy storage in legs, and active stiff actuators, suited for precision in arms and necks, have their respective benefits.

2.2.2. Torque-Velocity Profiles of Biological Muscles

Since humanoid robots are designed to replicate human motions, it is essential to use biological muscles as a reference to develop actuators that mimic their behavior. Actuators with mechanical properties similar to those of humans or even chimpanzees (O’Neill et al., 2017) in terms of strength and agility remain a major and unsolved challenge. The force-speed profile of human muscles provides valuable information on how actuators can be optimized for both speed and torque, similar to the natural dynamics of human movement.

Taking inspiration from nature, the force-speed profile of biological muscles, such as the biceps brachii (Figure 2.8), demonstrates an optimal balance

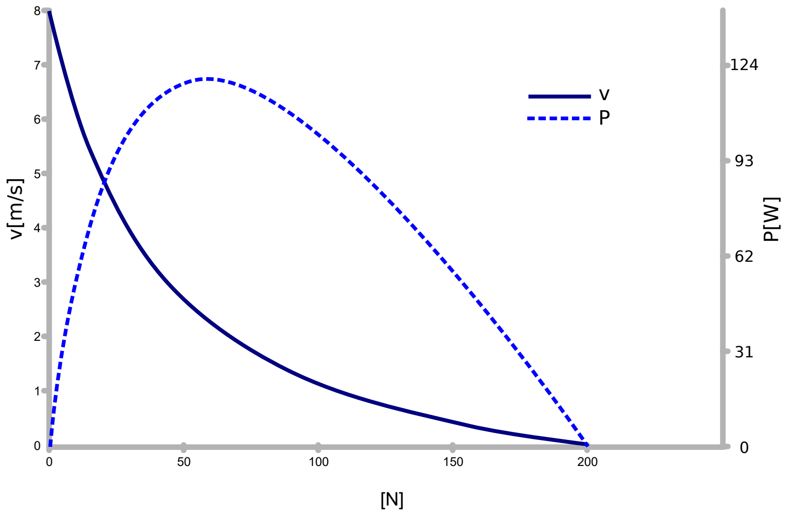

Figure 2.8.: Properties of the muscle biceps brachii. Speed and force data from Wilkie (1949), power calculated.

throughout the range of motion with relatively low maximum power. This profile shows that muscles can generate high torque at low speeds and high speed at low torque, with peak power occurring in the middle of the curve. Although the exact shape of this profile may vary between different muscles, its general form is well understood and has been studied extensively (Alcazar et al., 2019). Since maximum power dictates the overall size of a system, this low peak power is highly desirable.

By mimicking the natural force-velocity profile of muscles, actuators for humanoid robots can be designed to perform more human-like movements, combining strength and agility efficiently.

To mimic the behavior and softness of biological muscles, artificial muscles are created that utilize various physical effects, such as the HASEL actuator (Rothemund et al., 2021). Although some variants, such as pneumatic muscles, are already in industrial use, most are still not suitable for robotic systems due to limitations in power density, durability, and control. Another alternative is hydraulic actuators, which can be space-efficient for driving robots (Hyon et al., 2016; Guizzo, 2019), but have notable drawbacks, such as sensitivity to temperature changes, complex manufacturing, high costs, and the risk of leakage. For example, even in systems like the Boston Dynamic Atlas (Guizzo, 2019), hydraulic actuators can face issues of overheating during prolonged high-torque operations, especially in robotic arms.

Therefore, this work focuses on electric actuation, which offers a more practical solution to achieve the necessary balance between power, efficiency, and control in humanoid robots.

2.2.3. Switchable and Continuously Variable Transmissions

Switchable gearboxes can achieve a speed-force profile similar to human muscles, offering high maximum speed and force with low mechanical power (Figure 2.8). Linear mechanism can actuate joints from a position near the body center, reducing inertia. While manually or automatically switchable gears provide the benefit of adjustable transmission ratios, they are typically large, heavy, costly, and complex.

Continuously variable transmissions (CVTs) offer a more flexible approach by allowing continuous adjustment of the force-speed profile. One example is the rolling ring drive by Uhing (1966), a linear, friction-based CVT that converts the rotary motion of a plain shaft into linear movement. The transmission ratio is adjusted continuously by changing the angle between the ring body and the shaft. However, this adjustment is relatively slow due to the need for a separate actuator, and the mechanism is quite heavy, as it is primarily designed for fixed installations. Other approaches, such as belt-driven or pulley-based CVTs, are typically used in vehicles with a single drive train, where weight and complexity are a minor constraint (Sun, 1988).

2.2.4. Hybrid Drives

Hybrid drives combine two actuators based on the Engineering Hybridization Principle described by Zhang et al. (2010). This approach leads to innovative designs for combined mechanisms inspired by biological systems. Additionally, this concept is analogous to hybrid vehicles, which utilize two motors: one for constant mechanical power and another one for short bursts of high power. Human muscles exemplify this principle through a combination of three fiber types: slow oxidative (SO), fast oxidative (FO), and fast glycolytic (FG) fibers, enabling a range of motions from powerful bursts to low-fatigue activities (Betts et al., 2017).

The approach by Zinn et al. (2004) follows this idea by combining a high-frequency actuator with a base low-frequency actuator. This addresses challenges such as reflected inertia, limited acceleration, and crucial safety concerns for human-centered robotics. This design combines strong actuation for low frequencies and high torques in the base, acting as a series elastic actuator, with lightweight joint actuation for high frequencies and low torques. However, this solution still requires a large gearbox for the high-torque actuator.

In the DLR Hand Arm System, multiple combinations of two motors are utilized for variable stiffness actuators, including Bidirectional Antagonistic Variable Stiffness (BAVS), Floating Spring Joints (FSJ), and antagonistic actuators (Grebenstein et al., 2011; Friedl et al., 2011).

In summary, hybrid drives showcase an innovative approach to actuator design, combining the strengths of different mechanisms while addressing the inherent challenges of humanoid robotics.

2.2.5. Mechanical Realisations for Linear Actuators

In the following section, various mechanical realizations for linear actuators based on the Hybridization Principle are introduced and described. A notable linear mechanism that uses common electric motors as a power source involves two motors: one drives a nut and the other controls a threaded spindle, as described by Fickler (1984). By adjusting the speeds of these motors, the feed rate can be varied across a wide range. Another approach is presented by Kober and Rampp (1998), which details a multistage spindle drive to convert rotary motion to linear motion at different load-dependent speeds. This mechanism consists of telescopically engaged threaded elements with varying pitches, and the retraction and extension speeds can be modified based on frictional forces.

Furthermore, a rotary transmission gear unit with a selectable transmission ratio operates on the principle of a differential spindle, allowing for high transmission ratios through switching modes (Brand, 2015). Meanwhile, a load-sensitive power transmission device alters gear stages by switching between sliding and rolling motion of a nut on the spindle, activated by a brake-spring combination (Minbuta and Sotome, 2008).

However, these solutions present limitations: hollow spindles can be challenging and costly to manufacture (Kober and Rampp, 1998); significant pretension forces can lead to a solid and heavy design (Uhing, 1966); and high ratio stages can suffer from complexity and limited travel (Brand, 2015). The setup of Fickler (1985) allows for variable feed rates but restricts maximum spindle force and results in a relatively long structure. In Minbuta and Sotome (2008), the nut position on the spindle and the gearbox switching state are not directly controllable or measurable, requiring complex tuning due to a fixed switching point influenced by friction.

2.3. Kinematics and Joint Mechanisms of Humanoid Robot Arms

For achieving human-like motion in humanoid robot arms, the selected kinematics and joint mechanisms are of great interest. This section explores different solutions, including Quaternion Joints for extended singularity-free motion. In the following, different humanoid robots and joint mechanisms are mentioned. In Table 5 in Appendix B, references to humanoid robot arms and joint mechanism are summarized.

2.3.1. Master Motor Map

A unified framework is essential for comparing kinematics and joint mechanisms of humans and humanoid robot arms. The Master Motor Map (MMM) provides this framework, enabling representation, editing, and analysis of human motion for transfer to humanoid robots (Mandery et al., 2016). It includes three main components: the MMM reference model, the RobotEditor, and MMM converters.

The MMM reference model is a rigid body system with a predefined kinematic configuration and dynamic properties, normalized for size and weight. Based on biomechanical research, it includes 104 DoF: 6 DoF for pose, 23 DoF for each hand, and 52 DoF for the remaining body (arms, legs, eyes, head, and torso), as shown in Figure 2.9. Dynamic properties such as CoM, segment masses, and inertia tensors are derived from statistical data.

The RobotEditor is a tool for creating rigid body models of humanoid robots, objects, or entities, and defining marker sets on the MMM model. MMM converters enable the conversion of human motion data to and from the MMM model, allowing motion transfer to humanoid robots. Joint angles are reconstructed by positioning virtual markers on the MMM model to match real-world motion capture markers.

The KIT Whole-Body Human Motion Database offers a large collection of high-quality human motion recordings[1]. Integrated with the MMM model, it fa-

---

[1] https://git.h2t.iar.kit.edu/sw/mmm

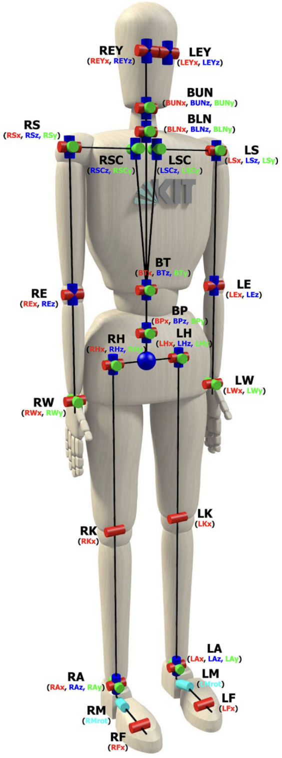

Figure 2.9.: MMM model whole body DoFs. *Source:* (Mandery et al., 2016) © 2016 IEEE

cilitates motion capture, representation, and reproduction, including human-object interactions (e.g., grasping), essential for replicating complex behaviors in robotics. The database organizes its motions using a Motion Description Tree, a hierarchical system that classifies movements based on tags and additional properties (e.g. direction, type, speed). This system supports the classification of both simple and compound movements, ensuring flexibility in motion analysis. Selected motions from this database are used to compute actuator requirements for robot kinematics (see section 3.1). Details of the selected motions can be found in Appendix A.

2.3.2. Joint Mechanisms for Humanoid Robot Arms

Previous work in the development and maintenance of our humanoid robots has shown that building robots has highlighted that achieving human-like mechanical properties, particularly in terms of strength and agility, remains a significant and unresolved challenge. One reason is the use of geared transmissions placed directly in the joint axis, leading to high inertia. Therefore, we focus on remote actuation of 2-DoF joints that allow a more favorable actuator weight distribution.

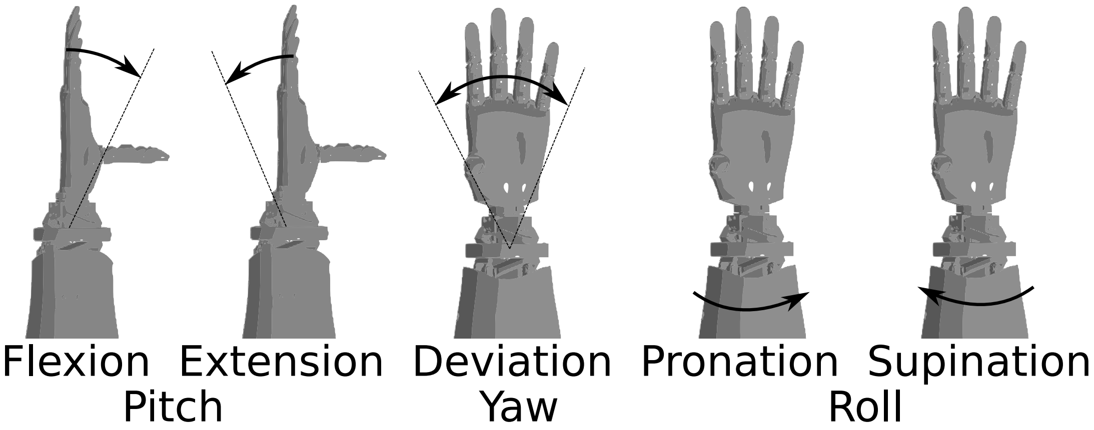

Figure 2.10.: Wrist motion directions. *Source:* (**Klas** and Asfour, 2022) © 2022 IEEE

An area of focus is the wrist, which is among the most complex joints due to its high demands for motion range and load bearing capacity within a compact design, closely resembling that of the human wrist. Mechanisms suited for the wrist joint can often be adapted for other joints in the humanoid arm.

After examining various wrist joint designs, we focus on Quaternion Joints, a promising approach to novel joint mechanisms that have not yet been widely implemented in humanoid robots. A comparison of the joint designs of two-DoF robots is presented in Table 2.2.

Table 2.2.: Specifications of realized 2-DoF robot joint designs.

Robot	Joint	Kinematic	Actuators	Range (°) fl./ext. dev.	Feed-through
ARMAR-III	Wrist	univ. joint	2 (belt, cable)	±60 ±30	no
ARMAR-4	Wrist	serial	2 (belt, cable)	±90 ±40	no
iCub	Wrist	differential	2 (tendons)	±56 ±38	yes
R1	Wrist	tripod	3 (rods)	±30 ±30	yes
Aila	Wrist	tripod	2 (rods)	±45 ±15	yes
RoboRay	Wrist	parallel	2 (rods)	±90 ±45	yes
LIMS2	Wrist	4 seg. quat.	2 (4 cables)	±90 ±90	yes
Omni-Wrist III	Sho.	4 seg. quat.	2 (pistons)	±95 ±95	yes
Omni-Wrist V	-	4 seg. quat.	3 (rotational)	±95 ±95	yes
Omni-Wrist VI	-	4 seg. quat.	2 (rotational)	±95 ±95	yes
High Angle Link	-	3 seg. quat.	2 (rotational)	±90 ±90	yes
i-wrist	-	3 seg. quat.	3 (rotational)	±90 ±90	yes
ARMAR-7	Wrist	4 seg. quat.	2 (rods)	±90 ±90	yes

References for robot joint data in Table 5.

Wrist Joint Mechanisms

The human wrist exhibits a motion range of approximately 76° for flexion, -75° for extension, and a deviation from -19° to 33° (Boone and Azen, 1979). Some robotic systems, such as ARMAR-4, RoboRay, and LIMS2, are capable of achieving similar ranges. However, it is important to recognize that the extreme flexibility of the human hand, which remains unmatched by robotic systems, necessitates a broader range of motion in robotic wrists. Additionally, direct comparisons of payload capabilities are complex, as they depend significantly on the scale of the joint and the distance between the joint and the hand.

Often modularity, scalability, and payload capacity are prioritized in humanoid robot designs. These systems typically use serial kinematics with direct actuator placement at most joints, leveraging sensor-actuator-controller (SAC) units for simplified assembly while limiting human-like acceleration due to inertia. This approach is applied in Centauro (Kashiri et al., 2019), HRP-5P (Kaneko et al., 2019), and ARMAR-6 (Asfour et al., 2019). The ARMAR-6 wrist (Rader et al., 2017), for example utilizes two SAC units with gear-driven actuation. It offers a flexion/extension range of $\pm 90^\circ$ and a deviation range of $\pm 40^\circ$. The Blue robot (Gealy et al., 2019) employs a roll joint and three equal 2 DoF units, providing an interesting modular approach. However, the wrist's rotation axes introduce singularities, necessitating a 90° rotation of the forearm for yaw motion of the end-effector. These configurations poses challenges for achieving an anthropomorphic appearance, motivating a focus on remote actuation.

Various approaches have been explored to position actuators closer to the body center, including cables (Choi et al., 2020; Kim et al., 2018a), belts (Asfour et al., 2013), differential gears (Gealy et al., 2019; Tsagarakis et al., 2007), levers, and hydraulic systems (Feng et al., 2014). However, designing joints for effective transmission of mechanical or electrical energy poses challenges.

A comprehensive review of the state of the art in artificial wrist designs can be found in Bajaj et al. (2019). The development of a new dexterous wrist for the iCub humanoid is explored by Shah et al. (2019b). They compare various mechanisms (Gimbal, iCub mk.2, Five-Bar, Six-Bar, Omniwrist, Quaternion) without focusing on mechatronic realization and include plots of Cartesian workspace alongside combinations of orientation angles, joint coordinates, and Cartesian coordinates.

A proposed 2 DoF parallel kinematic wrist shows maximum joint torques across orientations (Toedtheide et al., 2021), but is not included in our comparison with the Shadow Hand (Shadow Robot, 2022), as neither has been integrated into complete humanoid designs.

The DLR Hand Arm System (Friedl et al., 2011) features a complex double parallelogram structure for cable routing, actuated by four variable stiffness actuators (VSAs), though the range of motion is not specified. In the ARMAR-III (Asfour et al., 2006) and ARMAR-4 (Asfour et al., 2013) designs, remote actuator placement is realized through a serial kinematic structure. ARMAR-III employs cables for the first joint and a belt-driven universal joint for the second joint, which limits the range of motion to $\pm 40^\circ$. Conversely, ARMAR-4 utilizes a unique arched and belt-driven rail in the first joint to enable a broader motion range while maintaining a compact design. The second joint is actuated via Bowden cables, introducing potential backlash.

The iCub wrist (Tsagarakis et al., 2007) employs a differential drive with bevel gears, using cables for the first joint and belts for the second.

Parallel mechanisms in wrist designs offer advantages such as a higher payload-to-mass ratio, which can exceed 7 for parallel structures (Newport, 2022), compared to less than 0.15 for serial 6R robots (Merlet et al., 2016). Additionally, errors and backlash in parallel joints tend to cancel out rather than accumulate. The R1 robot wrist (Sureshbabu et al., 2017) utilizes a tripod kinematics driven by three rods, enabling elongation of $130\,\mathrm{mm}$ alongside pitch and roll motions of 30°. The mobile dual-arm robot AILA (Lemburg et al., 2011) employs a triangular arrangement with one fixed point actuated by a universal joint, while two points are driven by spindle rods.

In the RoboRay hand, a sophisticated 2 DoF wrist joint integrates wire-driven finger motions (Kim et al., 2014). Two spindles actuate a parallel mechanism that allows rolling contact joint motions in flexion/extension and normal rotation in deviation direction. The tendon-driven parallel kinematic wrist mechanism in the LIMS2-Ambidex robot provides a wide range of motion with rolling contact kinematics (Kim et al., 2018a). Actuation is achieved through two pairs of cable pulleys, enabling the transmission of mechanical energy for a subsequent roll joint. The disadvantage is that the mechanism has an elongated design.

While the Omniwrist-III (Sofka et al., 2006) has not yet been incorporated into a humanoid wrist design, its kinematics are similar to those proposed here, making it relevant for comparison. The wrist joint mechanism for the ARMAR-7 robot is partly based on this design (**Klas** and Asfour, 2022) and described in detail in chapter 5.

2.3.3. Quaternion Joints

The term Quaternion Joint was adopted from the works of Kim et al. (2018b) and Song et al. (2018). In the scientific literature, this type of joint is also referred to byp various other names, such as spherical rolling contact joint (Ghaedrahmati and Gosselin, 2022), or by joint-specific names.

Quaternion Joints mimic the motion of two spheres rolling on each other. As they can transmit angular velocities and torques evenly between two inclined shafts, they are also known as constant velocity joints. This is mostly implemented through parallel mechanisms, which provides several benefits, including a higher payload-to-mass ratio compared to serial robots. Additional advantages of Quaternion Joints include a large, singularity-free range of motion (RoM) and superior manipulability across that RoM, especially when compared to roll-pitch serial arrangements. Details of their kinematics are discussed in section 5.1. This section provides a comparative analysis of various realizations of this joint type. As can be seen in Table 2.2, the RoM of physical prototypes is typically around $90\,\mathrm{deg}$. Although a larger RoM is mathematically possible, the segments would have to be very thin, which would lead to a loss of stiffness in the joint.

Quaternion Joints can be categorized by the number of segment pairs. Although designs with pairs of 2 or ≥ 4 segments are possible, those with two pairs of segments often suffer from inadequate stiffness. On the other hand, designs with ≥ 4 segment pairs can limit the range of motion (RoM) due to the potential for self-collisions between the segments. The two main differences in the design of actuators are rotary and linear actuation.

Quaternion Joints have been utilized in various applications, such as pointing devices. Examples are the High Angle Active Link (SONE et al., 2023) for industrial visual inspection and the i-Wrist (N.T.N. Corporation, 2021). A well-known example is the Omni Wrist series. The Omni Wrist III is adapted for dexterous motion (Chang-Siu et al., 2022), ankle-foot prostheses (Xiu et al., 2022), and a fountain installation (Ross-Hime Designs, 2023).

For humanoid robotic applications, in addition to the wrist mechanisms found in the LIMS2-Ambidex robot and ARMAR-7, as discussed in section 2.3.2, the Omniwrist III has been integrated into a humanoid shoulder.

Table 2.3.: Relevant humanoid robot arms.

Robot	**DoF**	**Load** kg	**Height** cm	**Arm*** cm %	**Act.**	**Clav.**	**Elb./Wri.**
AILA	7	4	170	58 34%	SA	-	R PS(2)
Amigo	7	1.5	100-135	60 44%	SA	-	R R R R
ARMAR-III	7	3	175	59 34%	SA	-	R U(2)
ARMAR-4	8	3.6	170	55 32%	SA	CT	R R R CT
ARMAR-6	8	10	152-192	78 41%	SAC	R	R R R R
ARMAR-7	8	4.5	185	65 35%	SAC	R	R R Q(2)
Blue	7	2	-	54	SAC	-	R R R R
Centauro	7	7	170	55 32%	SAC	-	R R R R
Ballbot	7	10	150	61 41%	SAC	-	R R R R
David	7	4	180	76 42%	SA	-	R PS(2)
DRC-HUBO+	7	10	170	-	-	-	R R R R
HRP-5P	9	2.9	183	60 33%	-	R	R R R R R
HRP-4	7	0.5	151	44 29%	-	-	R R R R
iCub	7	1	104	29 28%	-	-	R R R R
Justin	7	7-14	190	79 42%	SA	-	R R R R
Jaxon	8	20	188	63 34%	SA	R	R R R R
LIMS2	7	3	-	61	SA	-	RC Q(2) R
Phoenix	7	12.5	170	-	-	-	R R R R
R1	8	1.4	115-135	55 41%	SA	-	R PS(3)
Talos	7	6	175	-	SA	-	R R R R
Tocabi	8	3	179	60 34%	SA	R	R R R R
Tw. One	7	17	147	55 37%	SA	-	R R R R
Valkyrie	7	10	190	62 33%	SAC	-	R R R R
Wabian-2	7	1.5	153	-	SA	-	R R R R
MMM	9	-	100	33 33%	-	R R	R R R R

* Arm length from shoulder joint to wrist joint.
In all robots, the shoulder joint is realized with 3 revolute joints (R R R).
References for humanoid robot arm data in Table 5.

2.3.4. Humanoid Robot Arms

Several universities, research labs, and commercial companies have developed humanoid robots over the past decades. To narrow down the relevant humanoid robot arms for this thesis, inclusion criteria were established. First, the arm must consist of at least 7-DoFs, enabling redundancy for 6D poses. Additionally, the arm should have a payload of at least 1.4 kg to effectively manipulate objects in human environments. Only robot arms actuated by electric motors were considered. A selection of these robots was also used to derive specifications of robot kinematic examples in Table 3.1. For anthropomorphic proportions, the arm length can be compared to human body heights, using the MMM model. Sizes can be compared to the 5th-95th percentile male and female (DIN 33402, 2020) which are in the range of 154 cm to 186 cm.

Several notable humanoid robots were excluded from this analysis: The original Atlas uses hydraulic actuation, for the electric one not enough information was available and Reem-C had insufficient payload. Robots with fewer than 7-DoFs, such as Toro and Hubo, were also excluded.

Table 2.3 summarizes the selected robots covered in this related work. These robots are compared based on the number of DoFs per arm, the joint type, and how many DoFs are located in the clavicular, elbow, and wrist joints. The shoulder joint in all compared robots is realized with 3 revolute joints (R). The table also includes the payload per arm, the robot's body height, and the corresponding body height based on the arm length. Lastly, robots are differentiated by their actuation type: SAC-Units or SA-Units with a separate control stack.

A notable observation is the difference between body height and arm length. In most robots, the relative arm length of the included robots is larger than in the reference model of the human body. This discrepancy is particularly evident in smaller robots like AMIGO or R1, where the arm length is notably large compared to the body height. While this increases the robot's reach, it detracts from the anthropomorphic appearance. Exceptions include ARMAR-4 and HRP-5P, where body and arm height are more balanced.

The payload per arm for the included robots is between 0.5 kg and 20 kg per arm. However, definitions of payload vary. For example, Twendy One can carry 34 kg with arms flexed, while its extended arm payload is likely lower. In contrast, robots like R1 and ARMAR-7 specify payloads with the arm extended, indicating higher potential loads when the arm is flexed. For the justin robot, the payload is given for low- and high-speed motion. Rescue robots, such as DRC-Hubo+ and Jaxon, tend to have higher payloads compared to those intended for domestic use, like ARMAR-III or R1.

Regarding DoF implementation, most 7-DoF arms use 1 rotary joint for elbow flexion/extension and 3 in the wrist joint. Different approaches are applied for wrist DoFs: ARMAR-III uses a universal joint, while ARMAR-4 employs a curved track joint. Parallel structures are used in Aila, David, and R1 (Stewart Platform). ARMAR-7 and LIMS2 implement Quaternion Joints in their wrists, with ARMAR-7 using forearm rotation for the third DoF and LIMS2 incorporating a feed-through option for end-effector rotation.

In general, Quaternion Joints are rarely used outside of wrist joints, despite their advantages for human-like motion and singularity-free range of motion

(RoM). Across all the included humanoid robots, no arm utilizes Quaternion Joints for all major joints.

2.4. Conclusion

This chapter presented the *fundamentals and related work* relevant to humanoid robot design, specifically examining systems, tools, and methodologies aimed at achieving efficient and human-like functionality in robotic arms. Key concepts were introduced, including *product development methodologies* and *systems engineering principles*, to establish procedural knowledge crucial for systematic robotic design. However, effectively applying these methods demands domain-specific knowledge, as highlighted by advancements in *knowledge representation and expert systems*.

Related work reviewed various approaches to the automation of robotic design, including comparisons of methods that address both the selection and arrangement of subcomponents. While some approaches use modularization and parameterization to achieve partial automation, these methods often restrict solution diversity, which can limit their effectiveness in designing fully integrated humanoid robots. Case studies in robot design, as well as evolutionary design approaches, primarily focus on laboratory and educational applications, with limited scalability for complex, real-world use.

In summary, no current methodology fully enables the automated design of complex kinematics and actuation for full-sized humanoid robots, nor does a systematic process exist for leveraging knowledge of human motion in computational design systems. Additionally, the review of actuation systems in humanoid robots highlights the continuous need for advanced systems, emphasizing their relevance within the context of this work.

3. Humanoid Robot Design Assistant

Humanoid kinematics, along with human-like motion trajectories and velocities, are critical for achieving intuitive human-robot interaction and collaboration in environments designed for humans. Previous research on the design and development of our ARMAR robots (Asfour et al., 2006, 2013, 2019) as well as investigations of other robots (Grebenstein et al., 2011; Ott et al., 2017; Kaneko et al., 2011; Radford et al., 2015) has demonstrated that, despite significant advancements in actuator and sensor technologies, replicating human-like force and agility in humanoids remains a substantial challenge.

This chapter introduces a comprehensive framework for humanoid robot design, focusing on the upper body due to its pivotal role in performing complex manipulation tasks. The framework covers the entire design process — from human motion data and robot kinematics inputs, to the generation of *Normalized Actuation Requirements*, data processing, kinematic configuration selection,

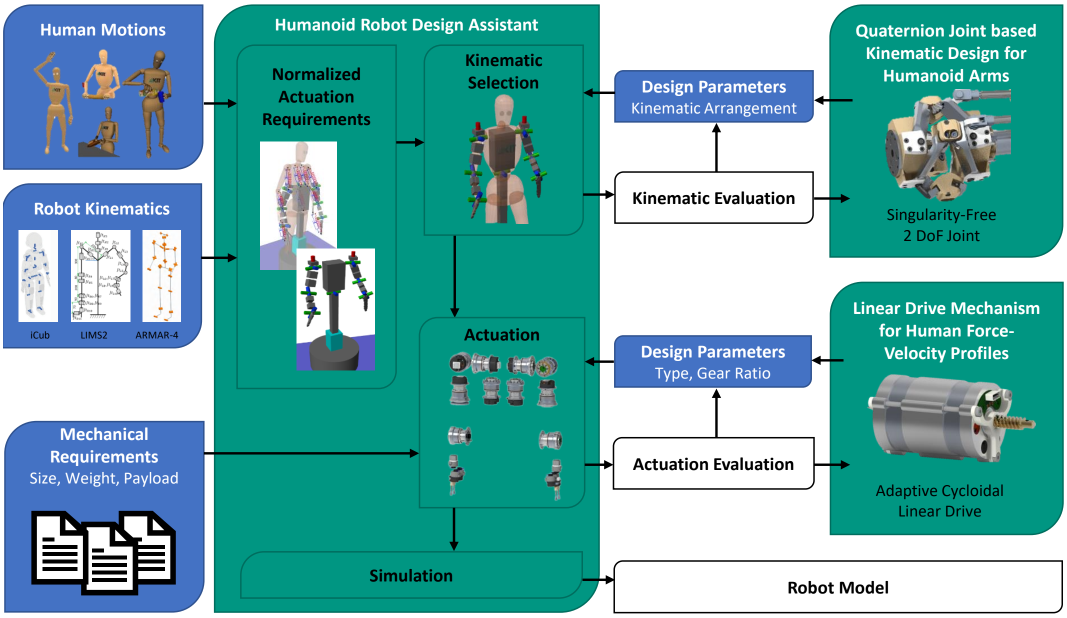

Figure 3.1.: Robot design system overview.

and actuator optimization. Parameters such as size, weight, and payload can be adjusted while comparing various kinematic setups. The framework also includes an automated gear ratio optimization and concludes with the simulation and validation of the robot model. The presented framework builds upon previous work on actuation requirements (**Klas** et al., 2023) and on the humanoid robot design assistant (Kossev, **Klas**, and Asfour, 2024). The key efforts presented in this chapter include:

- Design of a method to analyze torque, velocity, acceleration, and power requirements for humanoid robot joints across different kinematic configurations executing human-like movements.
- Development of a framework for humanoid robot arm design, integrating human motion data, kinematic configuration analysis, and actuator selection.
- Implementation of an optimization pipeline for gear ratio selection.
- Creation of an automated simulation system to assess the effectiveness of the designed robot configuration and to support further applications.

As illustrated in Figure 3.1, the system consists of several key components. **Normalized Actuation Requirements** serve as the foundation, where human motion data and robot kinematics are the inputs. In the process of **Kinematic Selection**, various robot kinematic configurations are compared and evaluated to identify the most suitable arrangement. In **Actuation**, the robot model is scaled to the specified size, weight, and payload, followed by the selection, comparison, and optimization of actuators based on type and gear ratio. The entire system is then tested through **Simulation**, where the generated robot model is evaluated to ensure that design requirements are met.

The evaluation of both kinematics and actuation within this framework highlights potential improvements through the integration of novel joint kinematics, mechanisms, and drive systems. These possibilities are explored further in the following chapters, where new developments, such as the linear drive mechanism and quaternion-based joint design for humanoid arms, are introduced to enhance the capabilities of the humanoid robot design presented here.

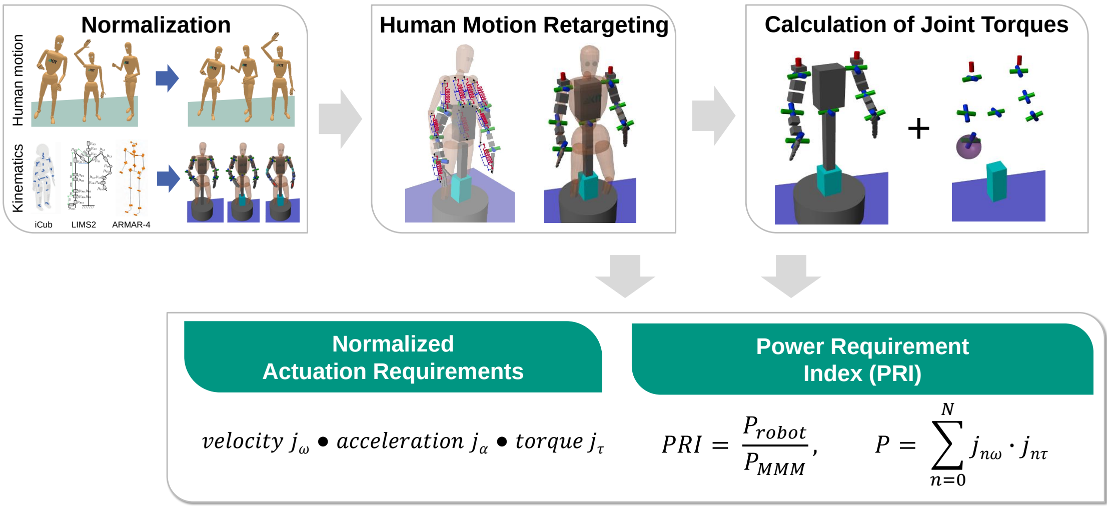

Figure 3.2.: *Normalized Actuation Requirements* calculation: 1. Normalization, 2. Virtual spring-damper systems for motion retargeting, 3. calculation of the robot joint torques with robot segment weights and with object weights.

3.1. Normalized Actuation Requirements

Humanoid robots have been developed to perform tasks in a variety of environments. Human motion data has primarily been used for motion generation (Kim et al., 2006). The actuation and kinematic requirements necessary to achieve natural, human-like motions have received comparatively less attention. To address this, it is essential to consider the execution of human-like motions as early as possible in the robot design phase. It is assumed that the *Normalized Actuation Requirements* for human-like execution of retargeted human motion on humanoid robots provide a solid foundation for comparing different robot kinematics and aligning subsequent design steps accordingly. The foundation for this section was established in **Klas** et al. (2023). Although considerable progress has previously been made in identifying actuator requirements for specific human-like tasks, such as walking, based on the analysis of the gait cycle (Zelik and Kuo, 2010), equivalent studies for a wide range of upper body motions was still lacking.

Even when human joint torques and velocities are known, they must first be mapped to the corresponding kinematics of the robot arm to be effective. In the first part of this chapter (section 3.1), a system that automatically computes actuator requirements — including velocity, acceleration, and torque — for a variety of robot kinematic configurations, based on human motion data is presented.

The system is designed to automatically calculate the necessary actuator requirements for a given robot kinematic configuration to execute selected human motions. To generate meaningful results, the robot must have a general anthropomorphic kinematic structure, with appropriate segment lengths and weight distribution.

To calculate *Normalized Actuation Requirements* for human-like execution of retargetted human motion on humanoid robots, the concept of a unified representation of the human body and motion is extended to a unified representation of humanoid robot kinematics. Specifically, diverse humanoid kinematic configurations are normalized and scaling laws are provided to adapt human motion relative to a normalized reference model, the Master Motor Map (MMM) (section 3.1.1).

To develop and validate this approach for identifying actuator requirements for human-like motions, we retarget both uni- and bimanual human demonstrations to the normalized robot kinematics, allowing us to compute joint positions, velocities, and accelerations (section 3.1.2). Additionally, joint torques are computed using the normalized dynamic properties of the MMM reference model (section 3.1.3). From this, we derive the normalized or actual minimum actuator requirements necessary for performing human-like motions on a given humanoid kinematic configuration (section 3.1.4).

The contribution of this section is two-fold. *(i)* A method for calculating the actuation requirements for humanoid robot kinematics based on a set of human motions is presented. *(ii)* A novel *performance index*, derived from the normalized required actuator power for retargeted human motions, is introduced. This facilitates the comparison of different humanoid kinematic configurations. It is demonstrated that the system enables the evaluation of actuator requirements for various upper-body humanoid kinematic models — as illustrated in Figure 3.7 — in order to execute human-like motion trajectories based on human motion data from the KIT Whole-Body Human Motion Database[1] (Mandery et al., 2015). Furthermore, it is shown how *Normalized Actuation Requirements* can be applied to evaluate a novel humanoid robot arm design that utilizes only Quaternion Joints (section 2.3.3).

---

[1] https://motion-database.humanoids.kit.edu

3.1.1. Normalization

The normalization of both human motion and different robot embodiment is crucial to ensure compatibility and comparability.

Normalization of Human Motion

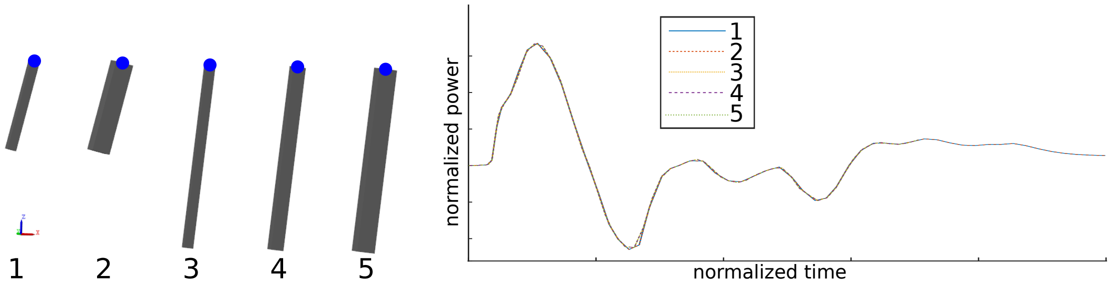

(a) Actuated bars

(b) Joint power

Figure 3.3.: Validation of scaling with model laws. Different bars with constant density are actuated at a joint (●) with a normalized trajectory. Length and weight difference is compensated by normalization leading to nearly identical curves. Different thickness lead to a small systematic error of maximum 4%. *Source:* (**Klas** et al., 2023) © 2023 IEEE

In the Master Motor Map (MMM) framework, human demonstrations are mapped to a reference model of the human body, which is scaled according to the height and weight of the individual subject(section 2.3.1). To adapt this subject-specific motion to a different scale or to the normalized MMM model, the execution speed of the motion must be adjusted to reflect the changes in dynamic properties. By normalizing the execution speed alongside the motion, we ensure that the resulting dynamic calculations are physically plausible, effectively mapping, for instance, a motion originally executed by a subject measuring $1.8\,\mathrm{m}$ and weighing $100\,\mathrm{kg}$ to a smaller subject measuring $1.5\,\mathrm{m}$ and weighing $50\,\mathrm{kg}$. Thus, we expand the conversion process in the MMM framework to facilitate motion adaptation for not only the MMM human body reference model but also for various robot kinematics. This extension enables the calculation of dynamics on normalized models, allowing for uniform comparison of kinematic designs and their application to robots of any size and weight without the need for recalculation.

To achieve this, it is essential to implement a physically accurate scaling method. The subjects who performed the human demonstrations vary in size and weight, necessitating a correct scaling of the combined calculations and results for different sized robots. Generally, for a physically accurate scaling, time changes with size, indicating that smaller entities tend to move faster.

A similar challenge is addressed in fluid mechanics with the Cordier diagram (Epple et al., 2011), which allows comparison of data from different types and sizes of fluid turbines within a single framework. When properly scaled, the most efficient machines align along a common line, regardless of their size or type. For this scaling, characteristic figures such as Reynolds or Froude numbers are kept constant while time, scale, and density are adjusted. The required scaling equations, known as model or similarity laws, can be derived from dimensional analysis (Buckingham, 1914).

For the scaling of human and robot dynamics, the Froude number $Fr = \frac{v^2}{g \cdot l} = \frac{l}{g \cdot t^2}$ is utilized, representing the ratio of the inertial force to the gravitational force. Using the scaling factors $\lambda = l_{source}/l_{target}$ and $\mu = m_{source}/m_{target}$ (with g constant), the scaling laws for time t (Equation 3.2), force F (Equation 3.3), torque τ (Equation 3.4), and power P (Equation 3.5) can be derived as follows:

$$Fr_{source} = Fr_{target} \Rightarrow \frac{l_{source}}{t^2_{source}} = \frac{l_{target}}{t^2_{target}} \quad [\frac{L}{T^2}] \tag{3.1}$$

$$\Rightarrow \lambda = \frac{t^2_{source}}{t^2_{target}} \Rightarrow t_{target} = \frac{1}{\sqrt{\lambda}} \cdot t_{source} \quad [T] \tag{3.2}$$

$$F_{target} = \frac{1}{\mu} \cdot F_{source} \quad [\frac{M \cdot L^2}{T^2}] \tag{3.3}$$

$$\tau_{target} = \frac{1}{\mu \cdot \lambda} \cdot \tau_{source} \quad [\frac{M \cdot L^2}{T^2}] \tag{3.4}$$

$$P_{target} = \frac{1}{\mu \cdot \sqrt{\lambda}} \cdot P_{source} \quad [\frac{M \cdot L^2}{T^3}] \tag{3.5}$$

The developed scaling laws were tested with a simplified simulation. The normalized human joint motion was executed on various one-DoF arms of different sizes. Normalized joint parameters (e.g., joint torque and joint power) should remain consistent, as demonstrated in Figure 3.3. Variations in arm thickness at the same length, which occur in both humans and robots, are not taken into account by the scaling laws, however, their influence on the results is negligible.

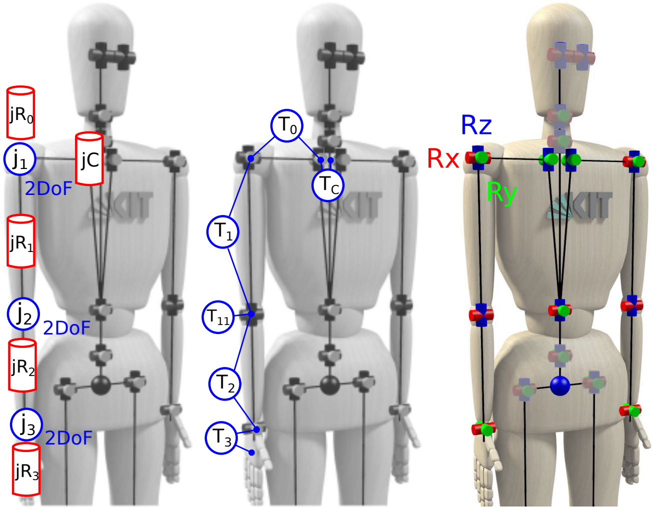

Figure 3.4.: Description of humanoid kinematics used in this work. Different joints (left) and transformations (middle) can be specified. Axis directions (right) are based on the MMM model (Mandery et al., 2016). *Source:* (**Klas** et al., 2023) © 2023 IEEE

The described formulas are first utilized for mapping human motions from subject-specific to the normalized MMM reference model. Through the process of motion retargeting described in section 3.1.2, these motions are subsequently mapped onto the normalized robot kinematics model. The same formulas can then be applied to transfer the motions from the normalized robot model to real robots of arbitrary size and weight, allowing the derivation of the actual joint requirements (section 3.2.3).

Normalization of Robot Kinematics

Our proposed representation models robot kinematics based on segment lengths, transformations between joints, and joint types. The size is scaled to match the arm lengths of the $1\,\mathrm{m}$ MMM model (measured from the center of the torso to the hand with arms extended at a 45-degree angle). Joint limits are taken into account only if they affect the desired kinematic behavior (e.g., changing the direction of elbow motion).

To standardize the segment weights of the robot arms for comparability, we set the individual segment weights of the robot to align with the MMM reference model (Mandery et al., 2016) scaled to $1\,\mathrm{kg}$. This results in a total weight of $0.08\,\mathrm{kg}$ per arm.

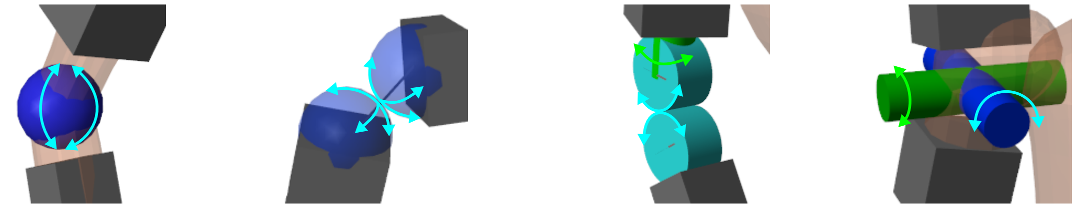

(a) cv (2 DoF) (b) $quat$ (2 DoF) (c) $roll$ (2 DoF) (d) xy (2 DoF)

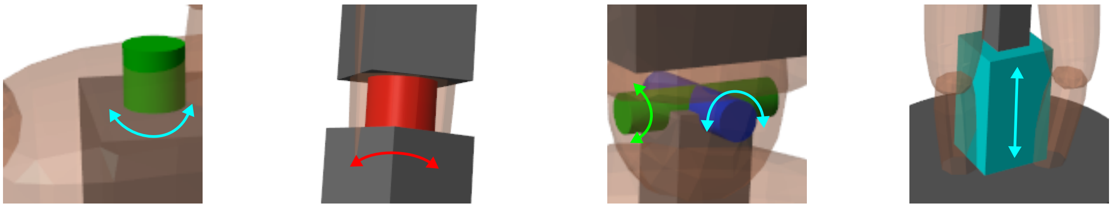

(e) j_C (f) j_{R0} to j_{R3} (g) Torso R_x,R_y (h) Torso P_z

Figure 3.5.: Implemented joint types: Const. velocity joint (cv), quaternion joint ($quat$), R_z and rolling contact ($roll$), universal joint (xy, xz), clavicula joint (j_C), arm rotation (j_{R0} to j_{R3}), rotary torso joints (R_x, R_y) and prismatic torso joint (P_z). Used for kinematics in Table 3.1. *Source:* (**Klas** et al., 2023) © 2023 IEEE

For a unified representation of the various robot kinematics, we utilize the kinematic description illustrated in Figure 3.4. The positions of the joint centers j_C, j_R, j_1, j_2, j_3, and torso can be found there.

A new robot kinematics model can be incorporated into the system by specifying the following parameters: joint types (Figure 3.5) at the joint centers j_1 to j_3, the activation of the rotational joints j_C and j_{R0} through j_{R3}, and the transformations T_C and T_0 to T_3. These transformations specify both the segment lengths and the corresponding rotations and offsets of the joints. Given that this work primarily focuses on upper-body motion, the torso movement is modeled as a holonomic platform. Thus, additional degrees of freedom can be activated in the hip (Figure 3.5g, 3.5h).

The coordinate directions (x, y, z) are based on the MMM model. The 2D joint types include universal joints with varying axes (xy, xz), a 1D rolling contact joint with orthogonal rotation ($roll$), a 2D rolling contact joint known as a Quaternion Joint ($quat$), and a constant velocity joint (cv) that determines azimuth and elevation. The arm joints with 1 DoF, such as the clavicula joint (j_R) and arm torsion joints (j_{R0} to j_{R3}), are always configured as revolute joints around the z-axis. With this system and the corresponding joint transformations, it is possible to construct humanoid robot arms with 6-8 degrees of freedom in the Simulink program using a single line of parameters. The base connects to the world through a planar joint, enabling motion on a holonomic platform, with additional joints including a prismatic joint in the z-direction (P_z) and revolute joints (R_x, R_y).

3.1.2. Human Motion Retargeting

The input to the human motion retargeting is sets of normalized MMM motions representing the desired robot tasks. Motion retargeting is performed using a virtual spring-damper system to closely mimic human motions. This approach extends the hand positioning method (Arimoto and Sekimoto, 2006) to approximate the positions of the torso, shoulder, and elbow using Cartesian spring-damper systems, as illustrated in the re-targetting step of Figure 3.2. The hand orientation is directly derived from the MMM hand orientation.

The stiffness of the springs on the hand is significantly increased to prioritize the position of the hand, which is crucial for most tasks. Optimal stiffness and damping values are necessary to strike a balance between smoothness, accuracy, and oscillations, yielding acceptable results under a variety of conditions. The inertia of the robot arm segments helps mitigate effects near singularities by limiting acceleration. Gravity is ignored during retargeting to eliminate systematic errors in the direction of gravity.

Retargeting calculations utilize ode45, a MATLAB Simulink implementation of a variable-step continuous explicit solver. This pipeline processes motion transfer, resulting in the positions, velocities, and accelerations of all joints.

3.1.3. Calculation of Joint Torques

The retargeted joint motions are executed on normalized robot models, where the joint torques are computed using multi-body dynamic simulations in MATLAB Simulink. To standardize the dynamic behavior across different kinematic models, inertia values corresponding to the MMM model are assigned to the relevant robot segments. The torque calculation is performed in two stages: one accounting for the segment weights of the robot, and the other incorporating the weights of external objects (Figure 3.2). This dual approach facilitates the independent scaling of both the robot's mass and any additional payloads. For the validation of the calculated joint torques, see section 3.3.

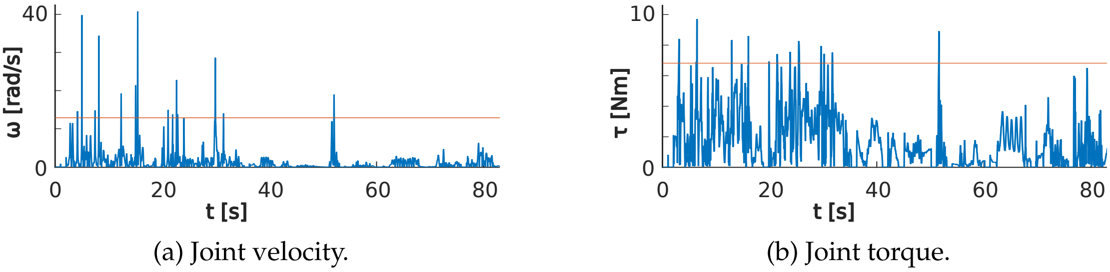

(a) Joint velocity.

(b) Joint torque.

Figure 3.6.: Temporal trajectory of velocity and torque (blue line) in the LIMS2 kinematics j1a joint together with the 99th percentile value (orange line) used in robot comparison. *Source:* (**Klas** et al., 2023) © 2023 IEEE

3.1.4. Actuator Requirements and Performance Index

The actuator requirements regarding velocity and acceleration are obtained through motion retargeting, while the torque requirements are derived from their execution on a normalized dynamic robot model. Possible joints for these calculations range from standard rotary joints and constant-velocity joints to different realizations of Quaternion Joints. To limit the influence of short peaks on the motion data, which are considered outliers, each value is capped at the 99th percentile (see Figure 3.6). The power requirements for each actuator are then calculated by multiplying torque and velocity. The specified motions result in asymmetric loads between the left and right arms. For symmetry considerations, the maximum of both arms is taken as the requirement for each actuator in the analysis.

To simplify comparisons between different robot kinematics, a performance index is introduced based on normalized actuator power. Joint power is the product of joint speed $j_{n\omega}$ and torque $j_{n\tau}$. The total actuator power for one arm is calculated as:

$$P = \sum_{n=0}^{N} j_{n\omega} \cdot j_{n\tau} \tag{3.6}$$

where N is the number of joints in the arm. The Power Requirement Index (PRI) is then defined as:

$$PRI = \frac{P_{robot}}{P_{MMM}} \tag{3.7}$$

This ratio compares the actuation power of the robot kinematics to the MMM reference model. Since actuator size and weight are roughly proportional to power output, lower PRI values indicate better efficiency, as less power is needed for the same movement.

Figure 3.7.: Rendering of a unified representation of 9 humanoid robots with different kinematics performing a retargeted Conversation motion. *Source:* (**Klas** et al., 2023) © 2023 IEEE

By applying scaling based on model laws, the actuator requirements can be scaled to robots of varying sizes and weights.

3.1.5. Requirements Analysis

In this section, the requirements for various dynamic, human-like unimanual and bimanual manipulation movements across different robotic kinematic configurations are identified. For comparison, the proposed performance index is used.

Robot Kinematics

For comparison, we selected 11 different humanoid robot kinematics, including: *LIMS2* (Song et al., 2018), *CENTAURO* (Kashiri et al., 2019), *iCub* (Tsagarakis et al., 2007), *David* (Grebenstein et al., 2011), *Justin* (Ott et al., 2017), *HRP-4* (Kaneko et al., 2011), *Valkyrie* (Radford et al., 2015), *ARMAR-III* (Asfour et al., 2006), *ARMAR-4* (Asfour et al., 2013), *ARMAR-6* (Asfour et al., 2019), and *ARMAR-7*. For details, see Table 3.1, Figure 3.5, and Figure 3.7.

We chose a diverse set of humanoid robot kinematics, each with 7 or more DoF per arm. These kinematics are defined by the types, positions, and acti-

Table 3.1.: Specifications of robot kinematic examples.

	j_R	j_1	j_2	j_3	Torso *	λ	δ **
LIMS2 (Song et al., 2018)	j_{R3}	xy	$roll$	$quat$	P_z	0.48	7%
CENTAURO (Kashiri et al., 2019)	j_{R1}	xy	xz	xz	R_x,R_y,P_z	0.40	22%
iCub (Shah et al., 2019b)	j_{R1}	xy	xz	xy	R_x,R_y,P_z	0.95	4%
David (Grebenstein et al., 2011)	j_{R1}	xy	xz	$quat$	R_x,R_y	0.39	15%
Justin (Ott et al., 2017)	j_{R2}	xy	zx	xy	R_x,P_z	0.33	20%
HRP-4 (Kaneko et al., 2011)	j_{R2}	xy	zx	xy	R_x,R_y,P_z	0.58	6%
Valkyrie (Radford et al., 2015)	j_{R2}	xy	zx	yx	R_x,R_y,P_z	0.44	2%
ARMAR-III (Asfour et al., 2006)	j_{R1}	xy	xz	xy	-	0.43	5%
ARMAR-4 (Asfour et al., 2013)	j_C, j_{R1}	xy	xz	xy	R_x,R_y,P_z	0.50	5%
ARMAR-6 (Asfour et al., 2019)	j_C, j_{R1}	xy	xz	xy	P_z	0.31	11%
New Design (Ruffler, 2023)	j_{R3}	$quat$	$quat$	$quat$	R_x,R_y,P_z	0.47	9%
MMM (Mandery et al., 2016)	j_{R0}	xy	xy	xy	R_x,R_y,P_z	1.00	0%

* A holonomic platform is added to all kinematics

** δ: Sum of segment length deviation from MMM related to arm length

Further robot details in Table 2.3

vation of the arm joints j_C, j_{R0} to j_{R3}, and j_1 to j_3 and the torso joints (Figure 3.4). The selection includes kinematics with all joints aligned in a straight line (Kaneko et al., 2011; Radford et al., 2015), alongside designs featuring a long wrist (Kashiri et al., 2019), different shoulder rotations (Kashiri et al., 2019; Tsagarakis et al., 2007; Asfour et al., 2019; Grebenstein et al., 2011; Ott et al., 2017), and varied elbow displacements (Asfour et al., 2006, 2013, 2019). In addition, some kinematics with special joint types were included (Song et al., 2018; Grebenstein et al., 2011).

In addition to these existing designs, we introduced a *New Design* based on Quaternion Joints (**Klas** and Asfour, 2022), applied in all three joint centers. Quaternion Joints offer advantages such as a large singularity-free range of motion and high manipulability, potentially leading to more human-like movement in robotic arms. Although human joints are typically modeled by rotary joints, this does not fully capture the complexity of human joint motion. This new design has not yet been optimized against the *PRI*.

Lastly, we included the MMM kinematic for comparison, which has not yet been mechanically realized. The joint positions and orientations are taken directly from the MMM model.

Human Motion Retargeting

A total of 40 motions from the KIT Whole-Body Human Motion Database (Mandery et al., 2015) were selected and grouped into four categories:

Table 3.2.: Specifications of selected motions.

	Household	Entertainment	Factory	Conversation
#	586 01	207 05	529 01	323 03
Object	0.3 kg	0 kg	0.3 kg	0 kg
Descr.	Big sponge	Drum	Pick & place	Point at left
#	589 01	316 01	663 02	323 03
Object	1 kg	0 kg	biman. 4 kg	0 kg
Descr.	Pour	Air guitar	Cast box	Point at right
#	589 03	636 15	1071 70 09	597 01
Object	0.5 kg	0 kg	5 kg	0 kg
Descr.	Pour & mix	Guitar right	Suitcase	Lean over
#	944	638 16	1758 1p25 01	597 07
Object	0.5 kg	0 kg	biman. 1.25 kg	0 kg
Descr.	Put in bowl	Violin right	Manipulate	Lean over
#	1235 04	651 01	1758 2p5 01	660 01
Object	0.5 kg	0 kg	biman. 2.5 kg	0 kg
Descr.	Book f. shelf	Head and sh.	Manipulate	Gestures
#	1235 05	995 131 01	1758 5 01	660 02
Object	0.5 kg	0 kg	biman. 5 kg	0 kg
Descr.	Book f. shelf	M. J. dance	Manipulate	Gestures
#	1259 46	1109 94 06	1759 1p25 01	1268 01
Object	0.5 kg	0 kg	biman. 1.25 kg	0 kg
Descr.	Hand over	Indian dance	Manipulate	Control table
#	1269 02	1109 94 07	1759 2p5 01	1268 05
Object	0.1 kg	0 kg	bim. 2.5 kg	0 kg
Descr.	Throw left	Indian dance	Manipulate	Control table
#	1283 01	1258 36	1759 5 01	1327 01
Object	0.1 kg	0 kg	biman. 5 kg	0 kg
Descr.	Throw right	Circular	Manipulate	Wave both
#	1071 70 09	1288 05	1759	634 01
Object	0.1 kg	0 kg	biman. 4 kg	0 kg
Descr.	Carry & lift	Left punch	Manipulate	Left wave

Household (H), Entertainment (E), Factory (F), and Conversation (C). The categories E and C involve no additional weight at the hand, whereas H and F include tasks that require objects to be held, with weights appropriate to the activity. Detailed information on these categories can be found in Table 3.2. The selected motions are mapped onto the subject-specific MMM reference model.

The normalization and retargeting process is applied to all selected robot kinematics. To assess the effectiveness of the motion retargeting method, the mean error between the motion on the normalized MMM reference model and the retargeted motion on each robot kinematic is calculated. The results are presented in Table 3.3.

Table 3.3.: Mean retargeting errors separately for end-effector and other joints for the four motion categories.

	Δ shoulder & elbow [mm]				Δ hand [mm]			
	H	E	F	C	H	E	F	C
LIMS2	25.0	24.8	25.3	22.9	2.0	2.0	1.7	1.9
CENTAURO	30.5	34.3	28.5	31.3	1.5	3.3	1.1	1.7
iCub	9.8	10.8	9.5	10.7	0.9	1.6	0.6	1.1
David	40.6	43.0	40.5	39.1	2.8	3.6	2.4	3.3
HRP-4	10.7	12.7	10.4	11.1	0.6	1.4	0.5	0.7
Justin	33.1	35.3	30.6	32.4	2.1	2.7	1.8	2.0
Valkyrie	3.4	4.1	3.2	3.3	0.4	1.1	0.4	0.4
ARMAR-III	29.8	37.8	41.4	21.4	2.4	8.9	11.9	1.5
ARMAR-4	10.6	11.2	10.1	11.0	1.0	1.5	0.9	1.2
ARMAR-6	20.4	19.4	16.8	18.2	1.8	2.0	1.4	1.7
New Design	15.1	16.2	14.9	15.5	0.9	1.5	0.9	1.0
MMM	1.0	2.3	0.9	0.6	0.3	1.1	0.3	0.4

Analysis

The joint actuation requirements for the normalized robots ($1\,\mathrm{m}$ and $100\,\mathrm{kg}$), including velocity, torque, and acceleration, were calculated for all kinematic configurations. Additionally, the derived power values and the proposed *performance index* (PRI) were determined. The maximum values are detailed in Table 3.4. The results, normalized to these maximum values, are visualized in Figure 3.8. Joint-based power requirements are denoted by abbreviations (j_C, j_R, j_{1a}, j_{2a}, j_{3a}, j_{1b}, j_{2b}, j_{3b}), corresponding to joint names in Figure 3.5. For 2 DoF joints, the two degrees of freedom are labeled as a and b. The computed power requirements and PRI values for each configuration are presented in Table 3.5.

The analysis reveals that in all motion categories, the most efficient kinematics consume only about 40% of the drive power required by the least efficient ones, underscoring the critical role of kinematic selection. Most kinematics exhibit similar performance across motion categories, although certain designs excel or underperform in specific areas. For example, Valkyrie performs exceptionally well in the Factory category, whereas ARMAR-III demands the most drive power in the same category.

The power and velocity requirements vary across kinematics. Some designs, such as CENTAURO, display uniformly high velocity and torque demands, while others, like Justin, show consistently lower values. Notably, kinematics like New Design, LIMS2, and David present increased torque but reduced velocity requirements in certain joints, which can be attributed to the transmission characteristics of their rolling contact ($quat$) joints.

While the proposed analysis and computed PRI values (see Table 3.5) indicate that the new kinematic design performs best in three out of four categories and shows strong results in the final category, the mechanical complexity of implementing this design presents a significant challenge. Further investigation is needed to fully understand the performance characteristics of each robot kinematic and identify potential improvements. Tools for this purpose are provided in the following sections.

Table 3.4.: Maximum values of velocity, acceleration, and torque for all joints and the four motion categories.

	H	E	F	C
$j_{C\omega}[rad/s]$	1.53	3.24	1.29	2.24
$j_{C\alpha}[rad/s^2]$	54.2	127.1	92.8	417.9
$j_{C\tau}[Nm]$	7.60	11.79	12.72	8.11
$j_{R\omega}[rad/s]$	10.38	23.99	11.33	6.90
$j_{R\alpha}[rad/s^2]$	184.7	692.5	207.1	377.9
$j_{R\tau}[Nm]$	2.85	5.08	4.77	2.49
$j_{1a\omega}[rad/s]$	8.71	24.21	5.28	6.19
$j_{1a\alpha}[rad/s^2]$	158.0	673.4	181.6	540.7
$j_{1a\tau}[Nm]$	7.50	10.87	10.15	6.72
$j_{2a\omega}[rad/s]$	7.30	21.54	5.54	7.76
$j_{2a\alpha}[rad/s^2]$	258.2	850.0	456.7	904.3
$j_{2a\tau}[Nm]$	5.68	9.20	11.64	8.07
$j_{3a\omega}[rad/s]$	5.55	11.58	3.36	4.26
$j_{3a\alpha}[rad/s^2]$	148.0	394.7	179.2	379.1
$j_{3a\tau}[Nm]$	1.88	2.01	4.47	1.33
$j_{1b\omega}[rad/s]$	6.15	9.60	3.21	5.17
$j_{1b\alpha}[rad/s^2]$	70.9	231.4	85.5	221.5
$j_{1b\tau}[Nm]$	13.33	19.78	15.20	13.54
$j_{2b\omega}[rad/s]$	16.33	30.98	12.59	15.03
$j_{2b\alpha}[rad/s^2]$	310.2	952.9	227.3	588.3
$j_{2b\tau}[Nm]$	5.86	8.22	11.74	4.65
$j_{3b\omega}[rad/s]$	13.02	31.42	11.71	14.65
$j_{3b\alpha}[rad/s^2]$	307.5	962.0	265.0	685.7
$j_{3b\tau}[Nm]$	1.57	2.68	3.91	1.35

Table 3.5.: Power Requirement Index (PRI) and actuation power P[W] for different humanoid robot kinematics.

	H		E		F		C	
	P	PRI	P	PRI	P	PRI	P	PRI
LIMS2	80	0.74	276	1.01	86	1.10	68	0.90
CENTAURO	155	1.43	480	1.76	175	2.24	116	1.54
iCub	99	0.91	381	1.40	78	0.99	92	1.21
David	111	1.02	322	1.18	93	1.19	71	0.94
HRP-4	84	0.78	340	1.25	77	0.98	78	1.03
Justin	77	0.71	268	0.99	76	0.98	67	0.88
Valkyrie	81	0.74	343	1.26	**67**	**0.85**	80	1.06
ARMAR-III	111	1.02	408	1.50	184	2.35	89	1.18
ARMAR-4	88	0.81	338	1.24	71	0.91	80	1.05
ARMAR-6	111	1.02	413	1.52	108	1.38	146	1.94
New Design	**63**	**0.58**	**198**	**0.73**	74	0.95	**60**	**0.79**
MMM	109	1.00	272	1.00	78	1.00	76	1.00

Figure 3.8.: Normalized velocity (—), acceleration (—), and torque (—) of all arm joints in corresponding order (j_C, j_R, j_{1a}, j_{1b}, j_{2a}, j_{2b}, j_{3a}, j_{3b}) for 12 different kinematics across four motion categories. The complete arm actuator power requirement is shown in the background (■). *Source:* (**Klas** et al., 2023) © 2023 IEEE

3.2. Implementation of the Humanoid Robot Design Assistant

The **Humanoid Robot Design Assistant** is an integrated framework designed to facilitate the complex process of humanoid robot development, particularly for upper-body configurations essential in performing tasks with human-like arm motion. Building upon research from ARMAR and similar robotics systems, this tool addresses challenges related to replicating human-like agility and force in robots. The assistant incorporates several key phases, including data processing, kinematic selection, actuator optimization, and simulation, enabling designers to tailor robot configurations to specific requirements for size, weight, and payload capacity. Through automated gear ratio optimization and simulation-based validation, this tool allows for an interactive, user-guided approach that integrates elements of human motion analysis, joint kinematics, and advanced actuation systems.

3.2.1. Data Processing

After the most important step, the calculation of *Normalized Actuation Requirements*, these data is used in the following steps of the assistant. The three section(3.2.1, 3.2.2, and 3.2.3) of this work provide information about the most important functions of each of the three main parts of the *Humanoid Robot Design Assistant* system (Kossev et al., 2024). They are implemented in Python and accessible via a GUI (section 3.2.5). The primary function of the *Data Processing* is to enable users to adjust the level of detail in the simulation data.

Data Loading

The MATLAB simulation data from section 3.1 is structured as a 3D array, $R_{n \times m \times p}$, where n represents the number of joints (22 plus a time variable), m denotes the joint properties (position, speed, acceleration, and torque), and p indicates the number of time steps. Two preprocessing steps ensure consistency by marking **empty joint data** to maintain structure and removing **interpolation** points to focus on the original motion data.

Speed, Acceleration, and Torque Limits

To normalize data and support the *norm* mode of the *Delete Small Time-Steps* algorithm, maximum limits for speed, acceleration, and torque are set for each joint. To minimize the effect of short-duration peaks, limits are defined at the 99th percentile.

Delete Small Time-steps

The MATLAB simulation generates detailed joint data for position, speed, acceleration, and torque at high frequencies. To manage data size and optimize processing time, a *Delete Small Time-Steps* function is used, allowing users to set the desired level of detail by removing less significant data points. This function operates in two modes: timestep and norm.

In **Timestep Mode**, the function calculates the difference between consecutive time steps. If the difference exceeds a user-defined threshold, the point is retained as the new *last time step*; otherwise, it is marked for deletion, ensuring the remaining points are spaced by the specified interval.

In **Norm Mode**, the function computes and normalizes the absolute difference between the current and last saved data point relative to joint limits. This difference is compared to previous values, and if it surpasses the user-defined norm parameter, the data point is retained; otherwise, it is deleted. Norm mode is particularly useful for preserving key data variations, such as peaks and troughs.

This data reduction process effectively lowers the number of data points, speeding up analysis and visualization. Both robot and object data are processed consistently to ensure uniform data reduction.

Video Frame - Data Point Matching

In the *Data Processing* and *Kinematics* GUIs (section 3.2.5 and 3.2.5), precise matching of video frames to data points is crucial, as differences in frame and data point counts, along with uneven deletions by the 'Delete small time steps' function, complicate alignment. Due to non-uniform time step removal, matching is required.

Upon loading, a dictionary maps each data point to its corresponding video frame using a conversion ratio, $r = i \cdot \frac{n_{frames}-1}{n_{datapoints}-1}$, where i is the current time step. This enables easy matching of data points to video frames. When a video frame is selected, matching data points are displayed; if none are available, the system selects the closest preceding data point.

Data Storage

The processed data must be saved to ensure its availability for future use. An object containing the following four parameters is stored for each robot: robot post-processed data, robot kinematic joint limits, video frame to data point dictionary, object post-processed data.

3.2.2. Kinematic Selection

In the Kinematic Selection step, the primary goal is to enable the comparison of different kinematic configurations based on a selected set of movements that the robot kinematic should be able to perform. This is achieved by presenting the following information to the designer: joint position data throughout the entire movement, normalized requirement volumes (hulls) for each joint (calculated based on the required speed, acceleration, and torque to execute the movements), and a kinetic score based on the actuation power requirements (PRI), detailed in section 3.1.4.

Range of Motion

Different kinematic configurations can be compared on the basis of the range of motion required to execute a given movement. In addition, insights into the structural design of each joint can be inferred from the joint position plot. For robots with joints that can rotate continuously in one direction, the joint position data, provided in radians (multiples of π), must be normalized to the range $[-\pi, \pi]$ before plotting. This is done first by checking if the difference between the minimum and maximum values exceeds 2π. If so, the modulus of the angle with respect to 2π is computed. If the remainder is greater than π, the angle is adjusted by subtracting 2π to bring it back into the desired range. Other way round, if the remainder is smaller than $-\pi$, it is adjusted by adding 2π. If the remainder is within the range $[-\pi, \pi]$, no further adjustment is needed. Once all joint positions have been normalized, the data can be plotted accordingly. In the graphical user interface, the envelope (2d Alphashape) around this joint position plot shows the range of motion and serves as an aid for visual comparison (section 3.2.5).

Alphashape

For comparison of different robot kinematics, the requirements derived from retargeted human motion must be evaluated against the actuator capabilities. To simplify and visualize this comparison, the following approach is proposed: Both requirements and capabilities are represented as 3D shapes in the dimensions of torque, speed, and acceleration. To achieve a compact representation, a convex hull of the data points in these three dimensions could be used. However, in some regions, a convex hull overestimates the required volume. This is where the concept of concave hulls, specifically the Alphashape, becomes useful.

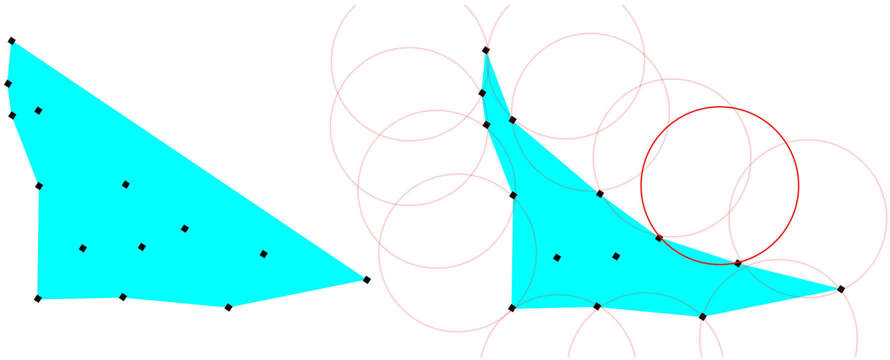

Figure 3.9.: Convex hull (left) and Alphashape (right), circle size set by α.

Alphashapes are a generalization of the convex hull, providing a more detailed geometric representation of a finite point set S in a 3D space. The parameter α (where $0 \leq \alpha \leq \infty$) allows for a smooth transition from a convex hull ($\alpha = \infty$) to increasingly concave shapes as α decreases. Visually, this means a larger radius of the circle in Figure 3.9. This flexibility enables the formation of cavities or tunnels within the shape, as spheres of radius α can fit inside without enclosing any points of S.

In the context of actuator requirements, where the data points in the torque-speed-acceleration space are often unevenly distributed, a convex hull would result in an overinflated and inaccurate boundary. In contrast, an alph ashape offers a more accurate boundary that avoids overestimation and better reflects the actual distribution. By adjusting the α parameter, the shape can be fine-tuned to capture the data structure without becoming fragmented.

To ensure consistency across different joints and motions, the torque, speed, and acceleration values are scaled relative to their maximum values. In this thesis, a Python-based implementation of Alphashapes is used to calculate these boundaries.

Data Preparation To perform the Alphashape calculation, the data must be formatted appropriately. Since the values for speed, acceleration, and torque span different ranges, they must be normalized to ensure the accuracy of the Alphashape computation. For each time step, the speed, acceleration, and torque values are divided by their respective maximum limits, determined across all available robot kinematics and motions. Mathematically, for a speed data point, this is expressed as:

$$s^* = \frac{s_i}{s_{\text{max}}},$$

where s^* is the normalized speed value, s_i is the original speed value for time step i, and s_{max} is the maximum speed across all robot kinematics and loaded motions.

Additionally, to avoid short data peaks, the values are limited to the specific robot's maximum limits from section 3.2.1. The ratio between the limit of the selected robot and the highest limit in all robots is given by:

$$r_l = \frac{s_{\text{r max}}}{s_{\text{max}}},$$

where r_l is the ratio, $s_{\text{r max}}$ is the speed limit for the chosen robot r. Any data point exceeding this ratio is scaled to match r_l.

Aphashape Calculation To compute the requirement Alphashape, we must consider both the object torque and the robot's joint speed, acceleration, and torque. Although the displayed volume is 3D in the speed-acceleration-torque space, object torque is also factored into the calculation. This is achieved by first calculating the 4D Alphashape in the speed-acceleration-robot-torque-object-torque space.

When applying the Alphashape library to a 4D data array, the output is an array of dimensions $N_{n \times m}$, where n is the number of faces of the 4D Alphashape, and $m = 4$, as each face is described by four points. The array values represent the indices of the original data points that form the Alphashape. For example, an entry like $[1, 44, 783, 11]$ indicates that one face of the 4D Alphashape is formed by the points with indices 1, 44, 783, and 11 from the original dataset.

To calculate the 3D Alphashape, all unique points from the 4D Alphashape output are extracted. This extraction is necessary because neighboring faces of the 4D Alphashape share at least one point, meaning duplicates must be removed for faster computation of the 3D Alphashape.

Kinematic Score Calculation The kinematic score, introduced in **Klas** et al. (2023) and explained in section 3.1.4, plays a key role in comparing the kinematic arrangements, along with the visual representation of the requirements volume. To calculate it, the maximum torque and speed values for each joint are required. Due to symmetry constraints, the higher limit from the corresponding left and right joints is used.

The kinematic score is divided into two components: one for the robot kinematic and one for the object torque. The robot kinematic score is calculated as per Equation 3.6 and 3.7. Taking into account the mass of the robot m_{robot}, the power requirement P and the power requirement index PRI are given by:

$$P = \sum_{n=0}^{N} j_{n\omega} \cdot (j_{n\tau,o} + j_{n\tau,r} \cdot m_{robot}) \tag{3.8}$$

$$PRI = \frac{P_{robot}}{P_{MMM}} \tag{3.9}$$

Here, $j_{n\tau,r}$ is the robot torque, calculated considering only the robot's mass. $j_{n\tau,o}$ is the object torque, calculated considering only the object's mass, without the robot's mass. P_{robot} is the Power Requirement for the selected kinematic, and P_{MMM} is the object torque score for the MMM model. The object torque score is non-zero only when at least one of the loaded motions involves an object. The index value can change depending on the expected ratio of object to robot weight. Values for the PRI and joint velocity, acceleration, and torque can be seen in Figure 3.10.

Requirement Data Storing

For the subsequent actuator selection and optimization step, the data representing the requirements according to the selected robot kinematics and motions must be stored. This is realized via the 3D requirement volume in the form of Alphashapes. The 4D Alphashape volumes are generated as previously described, with an additional final step. To obtain the actual values for speed,

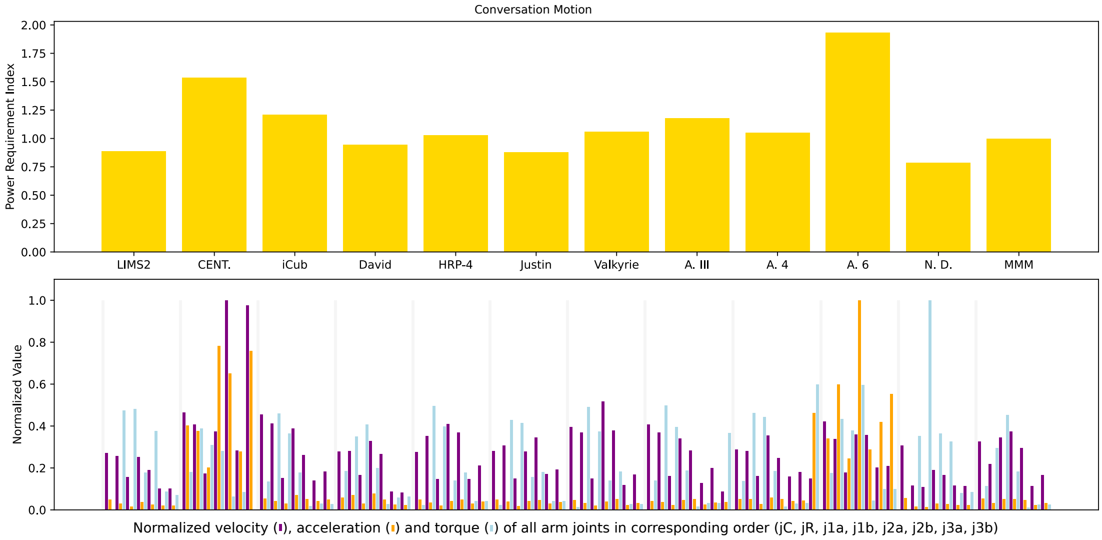

Figure 3.10.: PRI and normalized joint velocity, acceleration, and torque for conversational motions across various robot kinematics, as visualized in the Kinematics GUI.

acceleration, and torque, the points forming the 4D hull are scaled by the maximum limits across all robot kinematics for the loaded motions (s_{max}) and then saved. This process is repeated for each robot joint.

3.2.3. Actuator Selection and Optimization

The drive system is a fundamental component in the development of humanoid robots. It determines the robot's ability to generate and control movements in such a way that they resemble human movements. With the established requirements volume, the process now proceeds to the 3rd phase of the framework: the actuator optimization. This section of the robot design assistant is concerned with selecting the best actuators for the previously selected kinematics. Type, position, and transmission ratio are available as input. The output of this step is the comparison of scaled requirements with actuator capabilities, manual selection of best-fitting actuators, and optimization of actuator details. This part of the system focuses on data scaling and the introduction of a novel actuator optimization metric.

Robot Weight Adjustment and Data Scaling

The weight of the robot is a critical design parameter. In the MATLAB simulation, the torque data are initially calculated on the basis of a reference weight of 1 kg, allowing for later scaling according to the actual robot weight. To provide maximum flexibility in design, the user can define the final weight of the robot through the input parameter for the weight of the arm. Additionally, the framework allows the user to specify whether the actuators are positioned within the arm itself or housed in the robot's body. If the actuators are placed within the arm, their weight is added to the arm's weight to determine the total arm weight.

The weights of the individual arm segments in the MMM model are presented in the Table 3.6, where all arm segments collectively represent 7% (14% for both arms) of the total robot mass. This percentage is then used to compute the total robot weight based on the calculated total arm weight.

Table 3.6.: MMM model arm segment weights relative to total robot weight.

Segment	Weight (%)	Quantity	Total (%)
Shoulder	2.1	2	4.2
Elbow	2.7	2	5.4
Wrist	1.6	2	3.2
Hand	0.6	2	1.2
		Sum	14

Data scaling is applied according to the method outlined in section 3.1, using the following scaling factors:

$$\lambda = \frac{l_{mmm}}{l_{user}} \tag{3.10}$$

$$\mu = \frac{l_{mmm}}{m_{user}} \tag{3.11}$$

$$\omega_t = \frac{1}{\sqrt{\lambda}} \cdot \omega_s \tag{3.12}$$

$$\dot{\omega}_t = \frac{1}{\lambda} \cdot \dot{\omega}_s \tag{3.13}$$

$$\tau_t = \frac{1}{\mu \cdot \lambda} \cdot \tau_s \tag{3.14}$$

$$\tau_{o,t} = i_u \cdot \tau_{o,s} \tag{3.15}$$

m_{user} corresponds to the robot weight, as calculated previously, with 1 kg being the reference value. l_{user} represents the robot height as specified by the user, and 1 m is the height of the MMM robot model. ω_t is the required speed, and

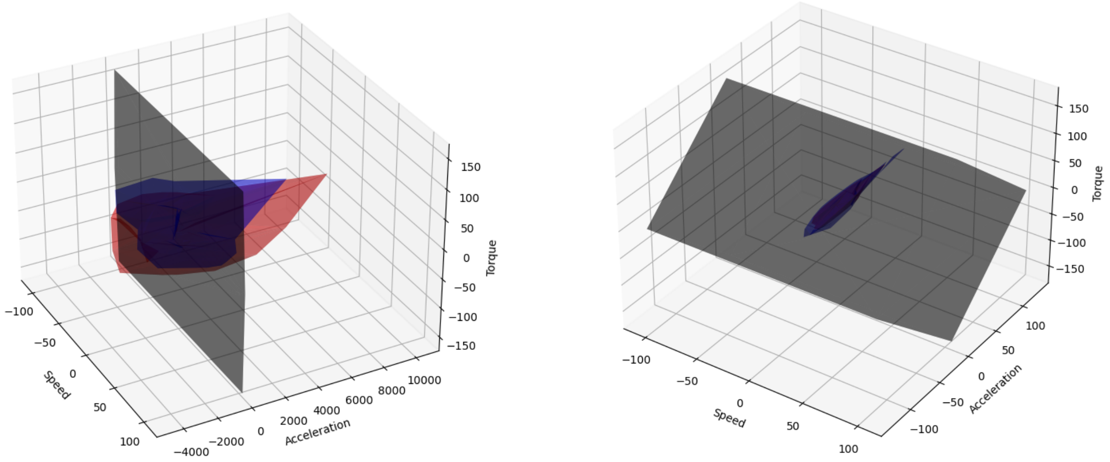

(a) Entertainment motions. Insufficient acceleration.

(b) Factory motions. Sufficient acceleration.

Figure 3.11.: Requirements volume of the ARMAR-7 robot performing different motions for the j1a joint (left: blue; right: red), compared with the capability volume of the U2 SAC unit (gear ratio: 120).

ω_s is the speed from the motion data. $\dot{\omega}_t$ is the required acceleration, and $\dot{\omega}_s$ is the acceleration from the motion data. τ_t is the required torque, and τ_s is the torque from the motion data. $\tau_{o,t}$ represents the required object torque, $\tau_{o,s}$ is the object torque from the motion data, and i_u is the user-defined scaling factor. The scaling factors for speed (ω) and acceleration ($\dot{\omega}$) are derived from the time scaling factor (defined in Equation 3.2). These scaling factors are applied across all data points to generate the real actuator requirements.

Actuation Requirement and Actuator Capability Volume

To select the optimal actuator configuration, different motor-gearbox configurations can be evaluated for each joint to assess how closely they meet the requirements in the 3D speed-acceleration-torque diagram. This can be assessed not only visually (as in Figure 3.11), but also based on the optimization index of the actuators.

The volume of actuation requirements (requirements hull) is constructed from the scaled requirements data and is utilized to calculate the AOI. The final step in acquiring the requirements data involves adding the robot and object torques for each time step. To enable separate scaling of these values, they cannot be unified until the calculation of the requirements hull. As a result, the 3D array for a time step i is structured as follows: $[S_i, A_i, T_{i,r}, T_{i,o}]$, where S_i represents the speed value, A_i is the acceleration value, $T_{i,r}$ is the robot torque, and $T_{i,o}$ is the object torque.

To calculate the AOI, the actuation capability volume (motor hull) is also required. The motor hull is constructed using the speed, acceleration, and torque values of the motor-gear combination. The motor is assumed to be ideal, capable of producing both positive and negative values equally. Thus, the calculation of the motor hull utilizes the 3D vertices presented in Table 3.7, where S represents the speed parameter, A denotes the acceleration parameter, and T stands for the torque parameter of the motor.

Table 3.7.: Actuator hull vertices.

ω	$\dot{\omega}$	τ
S	0	T
S	0	$-T$
S	A	0
S	$-A$	0
$-S$	$-A$	0
$-S$	A	0
$-S$	0	$-T$
$-S$	0	T

These parameters depend on the gear ratio for a selected motor-gear configuration. For gear ratio values not available in the manufacturer's catalog, interpolation is used on the basis of known values to identify new optimal gear ratios. Note that many gear manufacturers can produce gears with custom specifications for gear ratios.

Automated Gear Ratio Optimization

The automated gear ratio optimization process focuses on identifying the intersection between the actuation requirement (motor hull) and the actuator capacity volume (requirements hull) within the 3D space defined by speed, acceleration, and torque. Mathematically, this can be expressed as follows:

Let $V_{\mathbf{M}}$ represent the volume bounded by the convex hull (alpha-shaped hull with $\alpha = \infty$) of the actuator limits (Table 3.7) and $V_{\mathbf{R}}$ denote the Alphashape volume (with $0 < \alpha < \infty$) of the motion requirements, both situated in the $\mathbb{R}^{\omega \times \dot{\omega} \times \tau}$ space. The intersection of these two volumes results in a new volume, defined as $V_{\mathbf{I}} = V_{\mathbf{R}} \cap V_{\mathbf{M}}$. The Actuator Optimization Index (AOI) is calculated as follows:

$$AOI = \frac{V_{\mathbf{I}}}{V_{\mathbf{R}}} \tag{3.16}$$

where $V_{\mathbf{I}}$ is the volume of the intersection and $V_{\mathbf{R}}$ is the volume of the requirement hull. This ratio quantifies the extent to which the selected actuator configuration covers the requirements hull.

In the automated sequence to optimize the gear ratio, interpolation functions for speed, acceleration, and torque are derived from the actuator data table in the following forms: $f_1(i) = \omega_p$, $f_2(i) = \dot{\omega}_p$, and $f_3(i) = \tau_p$. Subsequently, an implementation of Powell's method (Powell, 1964) from the SciPy library is employed to identify a new optimal gear ratio candidate (i). Powell's method performs an iterative search along directions that are linearly independent, refining the approximation of the minimum at each step. A key advantage of Powell's method is that it does not require the computation of derivatives, making it particularly well-suited for this application, given the non-linearity inherent in the optimization index.

The new speed, acceleration, and torque parameters for a motor with the proposed candidate gear ratio are computed using the interpolation functions. Based on these parameters, a new actuator capability volume ($V_{\mathbf{M}}$) is calculated, which is then used to determine the new intersection ($V_{\mathbf{I}}$) with the requirements volume ($V_{\mathbf{R}}$). Finally, the volume ratio of this new intersection to the requirements hull is calculated.

These steps are automatically executed by the optimization algorithm until the step size is small enough (less than 0.5 in the implementation). This is followed by rounding to one decimal place and recalculating the AOI. The bounds for the optimization algorithm are set to $[i_{\text{min}} - 10; i_{\text{max}} + 20]$, where i_{min} and i_{max} denote the minimum and maximum gear ratio values for the selected actuator configuration from the actuator table, respectively. The adjustments extend the search range for the optimal gear ratio, with the assumption that the interpolation remains sufficiently accurate near the bounds of the actual values.

3.2.4. Simulation

In the simulation part of the Humanoid Robot Design Assistant, different robot instances can be simulated in MuJoCo in real time. They can either perform the predefined motion sets that are used in the previous parts (Figure 3.12) or the robot can be manually controlled (Figure 3.13). The desired joint positions from the re-targeted motion sets can be either directly set to the joints (within the possible range of the selected actuators) or controlled by a PD-Controller. As expected, the control via PD-Controller needs a larger speed and torque capability of the actuators due to oscillations around the desired position. Careful selection of the parameters can reduce these oscillations. Both insights can probably be useful for the subsequent design and control of the real robots. After the simulation, the simulation data for all joints can be plotted and compared with the simple scaling from the previous steps.

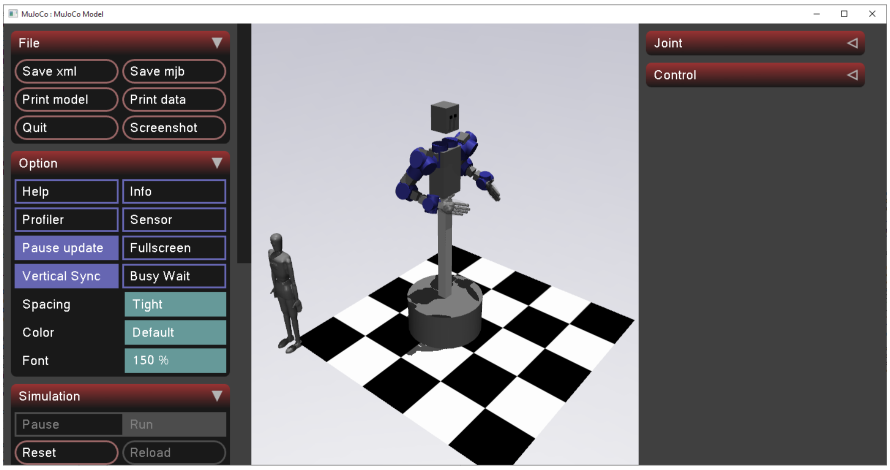

Spacing Tight
Color Default
Font 150 %

Figure 3.12.: Simulation of a robot with ARMAR-6 kinematics and the corresponding SAC Units in joint centers, scaled to 1.9 m, performing Conversation motions.

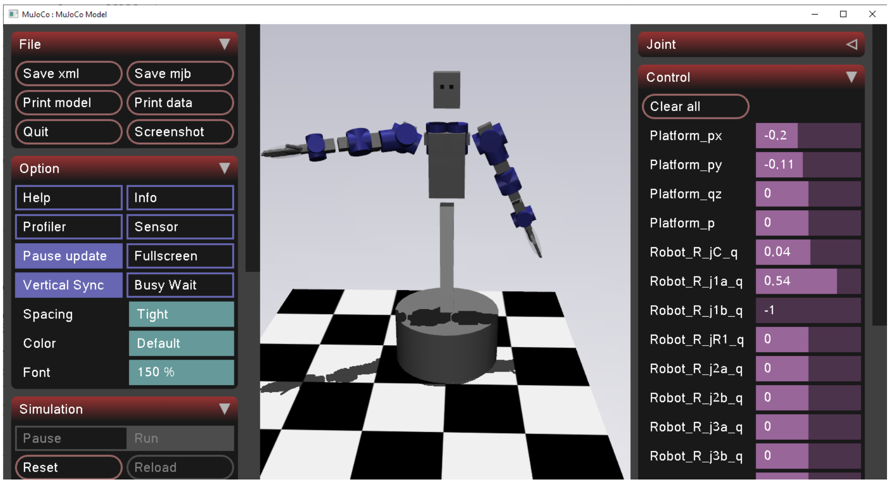

Spacing Tight
Color Default
Font 150 %

Platform_px -0.2
Platform_py -0.11
Platform_qz 0
Platform_p 0
Robot_R_jC_q 0.04
Robot_R_j1a_q 0.54
Robot_R_j1b_q -1
Robot_R_jR1_q 0
Robot_R_j2a_q 0
Robot_R_j2b_q 0
Robot_R_j3a_q 0
Robot_R_j3b_q 0

Figure 3.13.: Simulation of a robot with ARMAR-6 kinematics amd manual joint position control.

Default Robot Description File

To create special MuJoCo robot description files, a standard file serves as a template. This standard file is designed to contain essential parameters and configurations that define a generic robot model. It includes foundational elements such as kinematics, dynamics, sensor configurations, and actuator specifications with generic values.

The standard file is then adapted to the specific requirements of the various robots. This adaptation process involves modifying parameters such as joint types, link dimensions, and control strategies to reflect the unique characteristics and functionalities of the target robot. Unwanted elements are commented out. Additionally, the file may be enhanced with custom attributes to accommodate specialized sensors or actuators that are not included in the default setup.

By using the standard robot description file, designers can significantly simplify the process of creating new robot models. This approach not only reduces the time and effort required for model development but also promotes consistency and reliability across different robot configurations. In addition, the structured nature of the standard file facilitates updates and changes and allows for rapid iteration and optimization.

In summary, the standard robot description file is an important basis for the generation of MuJoCo robot models and at the same time ensures that the core functionalities and parameters remain consistent.

3.2.5. Workflow and User Interface

The principal structure of the system, shown in Figure 3.14, consists of three main components: *Data Processing*, *Kinematic Selection*, and *Actuation*. These components are interconnected through a central start-up screen, which allows the user to easily navigate between different steps based on the progress of the design process.

The user begins by providing processed human motion data, and proceeds sequentially through each step. The user is guided to select suitable robot kinematics and actuators. At the end, the system generates optimal actuator parameters and a final robot model that can be further used for testing and creating higher-level models. User interaction with the system is facilitated via the Graphical User Interface (GUI), where each component of the system is accessible.

Workflow

The workflow for utilizing the custom-designed computer system in humanoid robot design begins by selecting the desired motions from the KIT Whole Body Human Motion Database (Mandery et al., 2015). These motions must be processed through the MATLAB simulation as detailed in section 3.1. Once processed, the simulation output files are transferred to the project folder, making them accessible for use within the system.

The framework also requires a dataset of motor-gear configurations based on KIT SAC actuator units, stored in a .csv file. This dataset can be extended as new actuator configurations are developed. A corresponding .xlsx file version of the database is available, which includes automatic actuator parameter calculations based on motor and gear specifications.

The robot design process in this framework begins by opening the system and accessing the *Motion Viewer* via the start-up screen, where users can select, load, and preview motion data. Optional features include adjusting the view of specific joints and joint planes. Users then apply the *Delete Small Steps* function, selecting a mode and detail level to filter data points, before saving the refined motion data.

After closing the *Motion Viewer*, users proceed to *Kinematics Selection* to load saved motions, select a robot kinematic, and view data for each joint. Additional features enable frame-specific data visualization, kinematic scoring, and hull saving. The next stage is *Actuation*, where users upload the refined data, choose joints, and input robot parameters like height and arm weight. Automatic gear optimization is available to achieve the ideal motor gear setup, with visual analysis of speed, acceleration, and torque data.

For simulation, users open the *Simulation* panel, load robot and kinematic data, and adjust actuator settings. With Mujoco XML generation, users select motions and customize the setup (e.g., actuation, joint positions) before running the simulation, completing the robot design workflow.

The following subsections provide a detailed breakdown of the GUI composition, illustrating each element and its function.

Start-Up Screen

The start-up screen of the program, shown in Figure 3.15, serves as the central hub for accessing core functionalities and includes the following components:

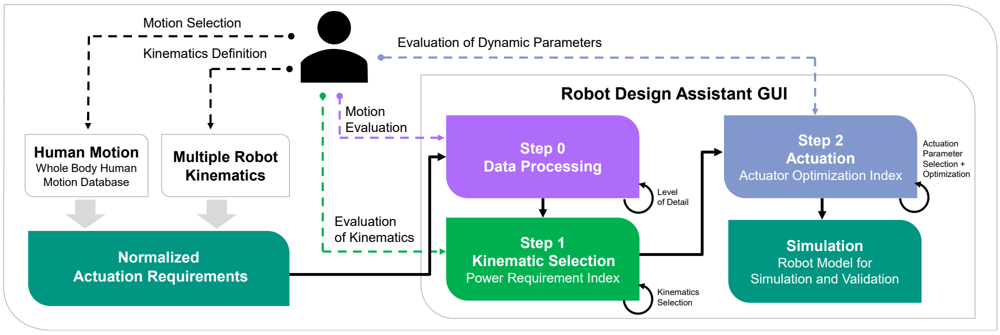

Figure 3.14.: Overview of the workflow for the *Humanoid Robot Design Assistant*.

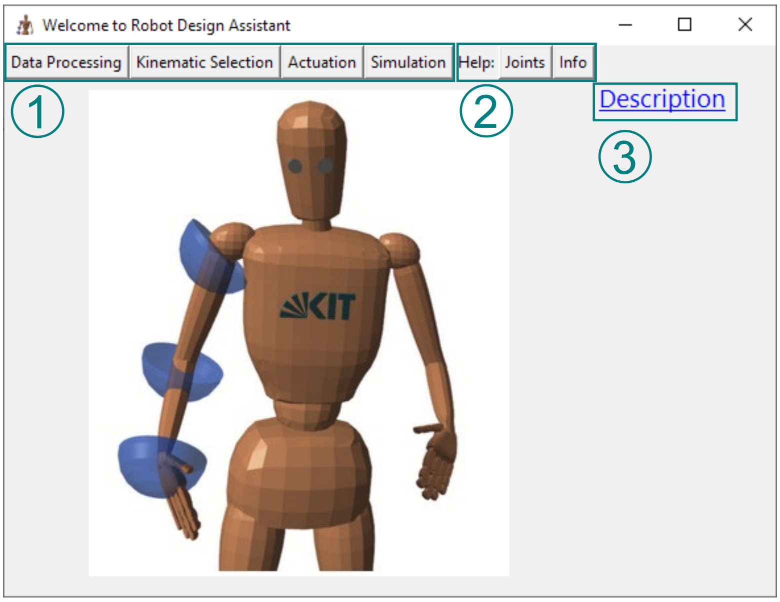

Figure 3.15.: Start-up screen.

The *Control Panel (1)* provides main action buttons for each design step. *Data Processing* opens a window for visualizing and adjusting motion data, *Kinematics Selection* allows selection and comparison of kinematic configurations, *Actuation* enables fine-tuning and optimization of actuator parameters, and *Simulation* supports virtual testing and validation of the robot's kinematics and actuation. The *Help Panel (2)* offers quick access to guidance, with *Joints* displaying a diagram of joint names in the Master Motor Map (MMM) model, and *Info* providing tips and instructions.

A link labeled *Description* (3) directs users to the GitLab repository, where additional resources and documentation are available.

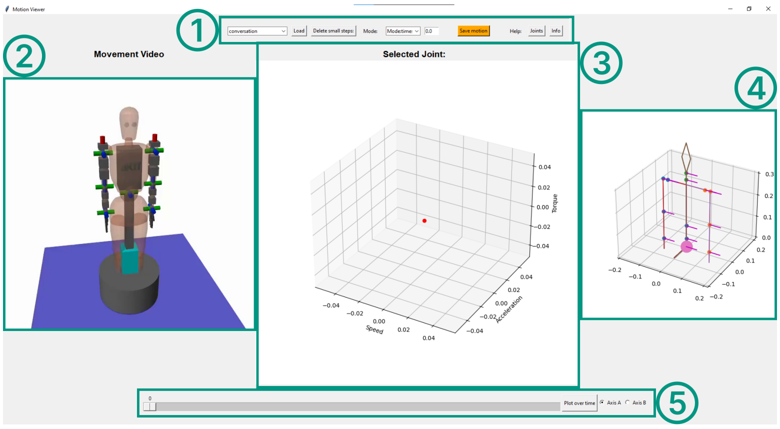
conversation

Mode: Mode:time 0.0

● Axis A ○ Axis B

Figure 3.16.: *Data Processing* window.

Data Processing

The *Top Control Panel (1)* includes widgets for selecting and loading motion files, adjusting data detail, and saving edits. Users can specify the level of detail reduction and choose the method via the *Mode* drop-down menu. A *Help* section provides guidance. The *Motion Video Display (2)* shows the motion using the MMM model for visual reference. The *Speed-Acceleration-Torque Plot (3)* displays calculated parameters for speed, acceleration, and torque. The *MMM Model Upper-Body Skeleton (4)* provides a visual representation of the MMM model's upper body, aiding in joint movement visualization. The *Bottom Control Panel (5)* contains tools for frame selection, including a slider, *Plot over time* for time-based joint analysis, and radio buttons to adjust joint plane display for 2D joints. The Motion Viewer allows users to control data detail and preview adjustments for motion parameters such as joint position, speed, acceleration, and torque. Motion data is presented in frame-by-frame view for precise editing, with data focused exclusively on the MMM model. Visualizations for other robot kinematics follow in the next design stage.

Kinematic Selection

The Kinematics window, shown in Figure 3.17, provides tools to select and compare robot kinematics, resulting in a normalized requirement volume for each joint across selected motions. The window includes the following components: The *Motion Selection (1)* section allows users to select saved motion data from a drop-down menu, add or remove motions from the loaded list, and view relevant data in the *Loaded Motions* listbox. Users can also use the *Plot All* button to display data for all motions simultaneously. The *Kinematic*

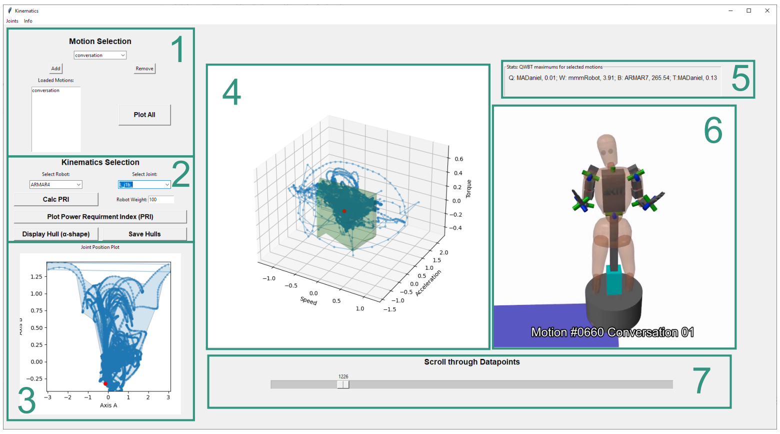

conversation

Loaded Motions: conversation

Select Robot: ARMAR4

Select Joint: L_j1b_

Robot Weight: 100

Stats: QWBT maximums for selected motions

Q: MADaniel, 0.01; W: mmmRobot, 3.91; B: ARMAR7, 265.54; T:MADaniel, 0.13

Figure 3.17.: *Kinematic Selection* window.

Selection (2) section enables users to choose specific robot kinematics and joints for visualization. It includes options for calculating the *Kinematic Score* and displaying or saving the *Alphashape Hull*, providing a visual outline of the selected or all loaded motions. The *Joint Position Plot (3)* displays joint positions for the selected motion, with only the y-axis relevant for non-2D joints. The *Speed-Acceleration-Torque Plot (4)* presents normalized values for these parameters, and the *Stats Section (5)* shows maximum values for joint position, speed, acceleration, and torque, along with the kinematic score for the chosen robot. The *Video Display (6)* provides a visual representation of the robot's movements, while the *Scroll Widget (7)* lets users select specific video frames and view corresponding data points in the plot.

In this window, users can analyze and compare robot kinematics retargeted to human motion data based on actuator requirements and kinematic performance indices (section 3.1.4). Specific motions can also be selected to focus on targeted tasks or movements.

Actuation

The layout of the Actuation window, illustrated in Figure 3.18, comprises the following components: The *Top Control Panel (1)* includes widgets for selecting robot data through the *Upload Data* menu, choosing a joint to optimize with the *Pick Joint* listbox, and viewing joint positions on the *Robot Picture*. The *Robot Parameters Panel (2)* provides fields for adjusting the robot's height, arm weight, and object weight, using both input fields and scroll widgets for fine-tuning these parameters. The *Actuator Selection (3)* section offers drop-down menus to choose motor type, gear ratio, and the actuator location (arm or robot body),

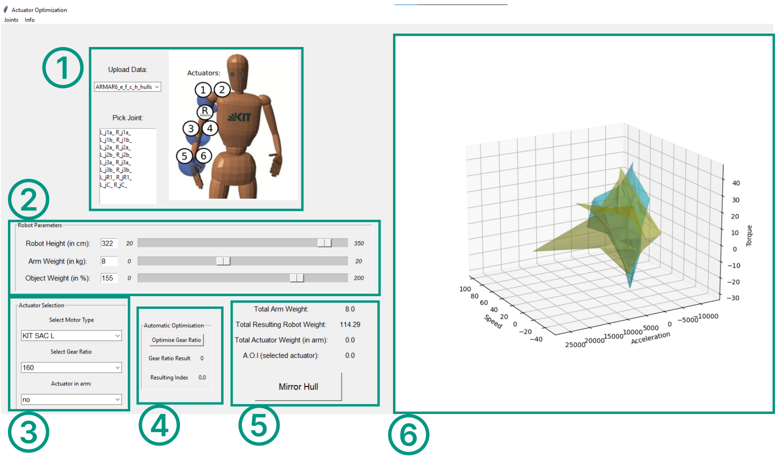

Upload Data: ARMAR6_e_f_c_h_hulls

Robot Height (in cm): 322

Arm Weight (in kg): 8

Object Weight (in %): 155

Select Motor Type: KIT SAC L

Select Gear Ratio: 160

Actuator in arm: no

Gear Ratio Result 0

Resulting Index 0.0

Total Arm Weight: 8.0

Total Resulting Robot Weight: 114.29

Total Actuator Weight (in arm): 0.0

A.O.I (selected actuator): 0.0

Figure 3.18.: Actuation GUI for actuator selection and comparison including gear ratio optimization.

which influences the total arm weight based on its placement. The *Automatic Optimisation (4)* section includes the *Optimise Gear Ratio* button, which initiates automatic optimization of the gear ratio, with results displayed in the *Gear Ratio Result* and the Actuator Optimisation Index (*AOI*). The *Middle Control Panel (5)* displays cumulative weight information, including *Total Arm Weight*, *Total Resulting Robot Weight*, *Total Actuator Weight*, and the AOI for the selected configuration. A *Mirror Hull* button allows the joint data to be mirrored in the 3D plot. The *Speed-Acceleration-Torque Plot (6)* provides a visual representation of the actuator configuration's performance across key metrics. In the Actuation window, users can experiment with various motor-gear combinations and evaluate their effectiveness through the 3D speed-acceleration-torque plot and the AOI. For additional precision, the automatic gear ratio optimization feature helps identify the optimal ratio for the selected motor-gear pair. Users can also specify the actuator placement within the arm or robot body, automatically adjusting the robot and arm weights to reflect the design accurately.

Simulation

In the simulation windows, shown in Figure 3.19, users can load robot and actuator data, configure parameters such as height and motor properties, and prepare the simulation setup. They can refine kinematic and actuation values, generate the necessary XML for Mujoco, and run the simulation with options for actuation and object interaction. At the end of the simulation, users can plot joint parameters to compare achieved positions against target positions or assess actuator torque limits. The layout of the simulation GUI window in-

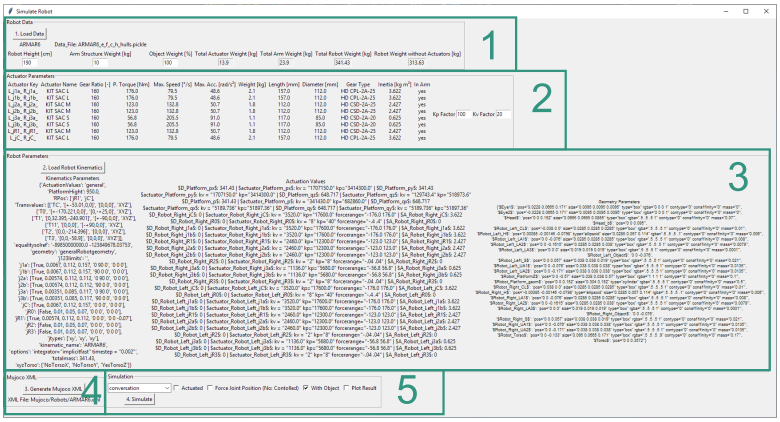

ARMAR6 Data_File: ARMAR6_e_f_c_h_hulls.pickle

Robot Height [cm]	Arm Structure Weight [kg]	Object Weight [%]	Total Actuator Weight [kg]	Total Arm Weight [kg]	Total Robot Weight [kg]	Robot Weight without Actuators [kg]
190	10	100	13.9	23.9	341.43	313.63

Actuator Key	Actuator Name	Gear Ratio [-]	P. Torque [Nm]	Max. Speed [°/s]	Max. Acc. [rad/s²]	Weight [kg]	Length [mm]	Diameter [mm]	Gear Type	Inertia [kg m²]	In Arm
L_j1a_ R_j1a_	KIT SAC L	160	176.0	79.5	48.6	2.1	157.0	112.0	HD CPL-2A-25	3.622	yes
L_j1b_ R_j1b_	KIT SAC L	160	176.0	79.5	48.6	2.1	157.0	112.0	HD CPL-2A-25	3.622	yes
L_j2a_ R_j2a_	KIT SAC M	160	123.0	132.8	50.7	1.8	112.0	112.0	HD CSD-2A-25	2.427	yes
L_j2b_ R_j2b_	KIT SAC M	160	123.0	132.8	50.7	1.8	112.0	112.0	HD CSD-2A-25	2.427	yes
L_j3a_ R_j3a_	KIT SAC S	160	56.8	205.5	91.0	1.1	117.0	85.0	HD CSD-2A-20	0.625	yes
L_j3b_ R_j3b_	KIT SAC S	160	56.8	205.5	91.0	1.1	117.0	85.0	HD CSD-2A-20	0.625	yes
L_jR1_ R_jR1_	KIT SAC M	160	123.0	132.8	50.7	1.8	112.0	112.0	HD CSD-2A-25	2.427	yes
L_jC_ R_jC_	KIT SAC L	160	176.0	79.5	48.6	2.1	157.0	112.0	HD CPL-2A-25	3.622	yes

Kp Factor 100 Kv Factor 20

Kinematics Parameters

```
{'ActuationValues': 'general',
'PlatformHight': 950.0,
'RPos': ['jR1', 'jC'],
'Transvalues': [['TC', '[+-53.01,0,0]', '[0,0,0]', 'XYZ'],
['T0', '[+-170.221,0,0]', '[0,-+25,0]', 'XYZ'],
['T1', '[0,32.395,-240.901]', '[+-90,0,0]', 'XYZ'],
['T11', '[0,0,0]', '[-+90,0,0]', 'XYZ'],
['T2', '[0,0,-214.396]', '[0,0,0]', 'XYZ'],
['T3', '[0,0,-58.9]', '[0,0,0]', 'XYZ']],
'equalitysolref': '-89850000000.0 -123849678.03753',
'geometry': 'generalRobotgeometry',
'j123limits': '',
'j1a': [True, 0.0067, 0.112, 0.157, '0 90 0', '0 0 0'],
'j1b': [True, 0.0067, 0.112, 0.157, '90 0 0', '0 0 0'],
'j2a': [True, 0.00574, 0.112, 0.112, '0 90 0', '0 0 0'],
'j2b': [True, 0.00574, 0.112, 0.112, '90 0 0', '0 0 0'],
'j3a': [True, 0.00351, 0.085, 0.117, '0 90 0', '0 0 0'],
'j3b': [True, 0.00351, 0.085, 0.117, '90 0 0', '0 0 0'],
'jC': [True, 0.0067, 0.112, 0.157, '0 0 0', '0 0 0'],
'jR0': [False, 0.01, 0.05, 0.07, '0 0 0', '0 0 0'],
'jR1': [True, 0.00574, 0.112, 0.112, '0 0 0', '0 0 -0.07'],
'jR2': [False, 0.01, 0.05, 0.07, '0 0 0', '0 0 0'],
'jR3': [False, 0.01, 0.05, 0.07, '0 0 0', '0 0 0'],
'jtypes': ['xy', 'xy', 'xy'],
'kinematic_name': 'ARMAR6',
'options': 'integrator="implicitfast" timestep = "0.002"',
'totalmass': 341.43,
'xyzTorso': ['NoTorsoX', 'NoTorsoY', 'YesTorsoZ']}
```

Actuation Values

```
$D_Platform_px$: 341.43 | $actuator_Platform_px$: kv = "1707150.0" kp="3414300.0" | $D_Platform_py$: 341.43
$actuator_Platform_py$: kv = "1707150.0" kp="3414300.0" | $D_Platform_qz$: 648.717 | $actuator_Platform_qz$: kv = "129743.4" kp="518973.6"
$D_Platform_p$: 341.43 | $actuator_Platform_p$: kv = "341430.0" kp="682860.0" | $D_Platform_qx$: 648.717
$actuator_Platform_qx$: kv = "5189.736" kp="51897.36" | $D_Platform_qy$: 648.717 | $actuator_Platform_qy$: kv = "5189.736" kp="51897.36"
$D_Robot_Right_jC$: 0 | $actuator_Robot_Right_jC$: kv = "3520.0" kp="17600.0" forcerange="-176.0 176.0" | $A_Robot_Right_jC$: 3.622
$D_Robot_Right_jR0$: 0 | $actuator_Robot_Right_jR0$: kv = "8" kp="40" forcerange="-.4 .4" | $A_Robot_Right_jR0$: 0
$D_Robot_Right_j1a$: 0 | $actuator_Robot_Right_j1a$: kv = "3520.0" kp="17600.0" forcerange="-176.0 176.0" | $A_Robot_Right_j1a$: 3.622
$D_Robot_Right_j1b$: 0 | $actuator_Robot_Right_j1b$: kv = "3520.0" kp="17600.0" forcerange="-176.0 176.0" | $A_Robot_Right_j1b$: 3.622
$D_Robot_Right_jR1$: 0 | $actuator_Robot_Right_jR1$: kv = "2460.0" kp="12300.0" forcerange="-123.0 123.0" | $A_Robot_Right_jR1$: 2.427
$D_Robot_Right_j2a$: 0 | $actuator_Robot_Right_j2a$: kv = "2460.0" kp="12300.0" forcerange="-123.0 123.0" | $A_Robot_Right_j2a$: 2.427
$D_Robot_Right_j2b$: 0 | $actuator_Robot_Right_j2b$: kv = "2460.0" kp="12300.0" forcerange="-123.0 123.0" | $A_Robot_Right_j2b$: 2.427
$D_Robot_Right_jR2$: 0 | $actuator_Robot_Right_jR2$: kv = "2" kp="8" forcerange="-.04 .04" | $A_Robot_Right_jR2$: 0
$D_Robot_Right_j3a$: 0 | $actuator_Robot_Right_j3a$: kv = "1136.0" kp="5680.0" forcerange="-56.8 56.8" | $A_Robot_Right_j3a$: 0.625
$D_Robot_Right_j3b$: 0 | $actuator_Robot_Right_j3b$: kv = "1136.0" kp="5680.0" forcerange="-56.8 56.8" | $A_Robot_Right_j3b$: 0.625
$D_Robot_Right_jR3$: 0 | $actuator_Robot_Right_jR3$: kv = "2" kp="8" forcerange="-.04 .04" | $A_Robot_Right_jR3$: 0
$D_Robot_Left_jC$: 0 | $actuator_Robot_Left_jC$: kv = "3520.0" kp="17600.0" forcerange="-176.0 176.0" | $A_Robot_Left_jC$: 3.622
$D_Robot_Left_jR0$: 0 | $actuator_Robot_Left_jR0$: kv = "8" kp="40" forcerange="-.4 .4" | $A_Robot_Left_jR0$: 0
$D_Robot_Left_j1a$: 0 | $actuator_Robot_Left_j1a$: kv = "3520.0" kp="17600.0" forcerange="-176.0 176.0" | $A_Robot_Left_j1a$: 3.622
$D_Robot_Left_j1b$: 0 | $actuator_Robot_Left_j1b$: kv = "3520.0" kp="17600.0" forcerange="-176.0 176.0" | $A_Robot_Left_j1b$: 3.622
$D_Robot_Left_jR1$: 0 | $actuator_Robot_Left_jR1$: kv = "2460.0" kp="12300.0" forcerange="-123.0 123.0" | $A_Robot_Left_jR1$: 2.427
$D_Robot_Left_j2a$: 0 | $actuator_Robot_Left_j2a$: kv = "2460.0" kp="12300.0" forcerange="-123.0 123.0" | $A_Robot_Left_j2a$: 2.427
$D_Robot_Left_j2b$: 0 | $actuator_Robot_Left_j2b$: kv = "2460.0" kp="12300.0" forcerange="-123.0 123.0" | $A_Robot_Left_j2b$: 2.427
$D_Robot_Left_jR2$: 0 | $actuator_Robot_Left_jR2$: kv = "2" kp="8" forcerange="-.04 .04" | $A_Robot_Left_jR2$: 0
$D_Robot_Left_j3a$: 0 | $actuator_Robot_Left_j3a$: kv = "1136.0" kp="5680.0" forcerange="-56.8 56.8" | $A_Robot_Left_j3a$: 0.625
$D_Robot_Left_j3b$: 0 | $actuator_Robot_Left_j3b$: kv = "1136.0" kp="5680.0" forcerange="-56.8 56.8" | $A_Robot_Left_j3b$: 0.625
$D_Robot_Left_jR3$: 0 | $actuator_Robot_Left_jR3$: kv = "2" kp="8" forcerange="-.04 .04" | $A_Robot_Left_jR3$: 0
```

Geometry Parameters

```
{'$Eye1$': 'pos="0.0228 0.0665 0.171" size="0.0095 0.0095 0.0095" type="box" rgba="0 0 0 1" contype="0" conaffinity="0" mass="0"',
'$Eye2$': 'pos="-0.0228 0.0665 0.171" size="0.0095 0.0095 0.0095" type="box" rgba="0 0 0 1" contype="0" conaffinity="0" mass="0"',
'$Head$': 'pos="0 0 0.152" size="0.0665 0.0665 0.0855" type="box" rgba=".5 .5 .5 1" contype="0" conaffinity="0" mass="0.07"',
'$Head_b$': 'pos="0 0 0.095"',
'$Robot_Left_CL$': 'pos="-0.038 0 0" size="0.0285 0.0285 0.0285" type="box" rgba=".5 .5 .5 1" contype="0" conaffinity="0" mass="0.01"',
'$Robot_Left_H$': 'pos="0.00085 -0.00146 -0.0798" type="ellipsoid" size="0.0285 0.057 0.114" rgba=".5 .5 .5 .1" contype="0" conaffinity="0" mass="0.006"',
'$Robot_Left_LA1$': 'pos="0 0 -0.076" size="0.0285 0.0285 0.0285" type="box" rgba=".5 .5 .5 1" contype="0" conaffinity="0" mass="0.008"',
'$Robot_Left_LA2$': 'pos="0 0 -0.1615" size="0.0285 0.0285 0.038" type="box" rgba=".5 .5 .5 1" contype="0" conaffinity="0" mass="0.0079"',
'$Robot_Left_LA3$': 'pos="0 0 0" size="0.019 0.019 0.019" type="box" rgba=".5 .5 .5 1" contype="0" conaffinity="0" mass="0.0001"',
'$Robot_Left_Object$': '0 0 -0.076',
'$Robot_Left_S$': 'pos="0 0 0.057" size="0.038 0.038 0.019" type="box" rgba=".5 .5 .5 1" contype="0" conaffinity="0" mass="0.021"',
'$Robot_Left_UA1$': 'pos="0 0 -0.076" size="0.038 0.038 0.038" type="box" rgba=".5 .5 .5 1" contype="0" conaffinity="0" mass="0.0135"',
'$Robot_Left_UA2$': 'pos="0 0 -0.171" size="0.038 0.038 0.038" type="box" rgba=".5 .5 .5 1" contype="0" conaffinity="0" mass="0.0135"',
'$Robot_PlatformZ$': 'pos="0 0 -0.57" size="0.038 0.038 0.57" type="box" rgba="1 1 1 1" contype="0" conaffinity="0" mass="0.1"',
'$Robot_Platform_geom$': 'pos="0 0 0.152" size="0.304 0.152" type="cylinder" rgba=".5 .5 .5 1" contype="0" conaffinity="0" mass="0.5"',
'$Robot_Right_CL$': 'pos="0.038 0 0" size="0.0285 0.0285 0.0285" type="box" rgba=".5 .5 .5 1" contype="0" conaffinity="0" mass="0.01"',
'$Robot_Right_H$': 'pos="-0.00085 -0.00146 -0.0798" type="ellipsoid" size="0.0285 0.057 0.114" rgba=".5 .5 .5 .1" contype="0" conaffinity="0" mass="0.006"',
'$Robot_Right_LA1$': 'pos="0 0 -0.076" size="0.0285 0.0285 0.0285" type="box" rgba=".5 .5 .5 1" contype="0" conaffinity="0" mass="0.008"',
'$Robot_Right_LA2$': 'pos="0 0 -0.1615" size="0.0285 0.0285 0.038" type="box" rgba=".5 .5 .5 1" contype="0" conaffinity="0" mass="0.0079"',
'$Robot_Right_LA3$': 'pos="0 0 0" size="0.019 0.019 0.019" type="box" rgba=".5 .5 .5 1" contype="0" conaffinity="0" mass="0.0001"',
'$Robot_Right_Object$': '0 0 -0.076',
'$Robot_Right_S$': 'pos="0 0 0.057" size="0.038 0.038 0.019" type="box" rgba=".5 .5 .5 1" contype="0" conaffinity="0" mass="0.021"',
'$Robot_Right_UA1$': 'pos="0 0 -0.076" size="0.038 0.038 0.038" type="box" rgba=".5 .5 .5 1" contype="0" conaffinity="0" mass="0.0135"',
'$Robot_Right_UA2$': 'pos="0 0 -0.171" size="0.038 0.038 0.038" type="box" rgba=".5 .5 .5 1" contype="0" conaffinity="0" mass="0.0135"',
'$Robot_Torso$': 'pos="0 0 -0.133" size="0.095 0.0665 0.171" type="box" rgba=".5 .5 .5 .9" contype="0" conaffinity="0" mass="0.17"',
'$Torso$': 'pos="0 0 0.3572"'}
```

XML File: Mujoco/Robots/ARMAR6.xml

conversation ☐ Actuated ☐ Force Joint Position (No: Contolled) ☑ With Object ☐ Plot Result

Figure 3.19.: *Simulation* tab in the humanoid robot arm design GUI.

cludes the following components: The *Robot Data and Actuator Parameters panels (1)* provide fields and controls for loading robot data, adjusting robot height and arm weight, specifying object weight, and viewing total weights, including the actuator and robot weights. The *Actuator Data Table (2)* displays properties for each actuator, such as torque, speed, and physical dimensions, while input fields for *Kp* and *Kv* allow adjustment of gain factors for motor control. The *Robot Parameters panel (3)* allows users to load kinematic parameters, displaying various robot properties, including platform height, joint positions, and geometry values, in dedicated sections for *Kinematics Parameters*, *Actuation Values*, and *Geometry Parameters*. The *Mujoco XML panel (4)* provides a button to create the XML file required for Mujoco simulation, with the file path displayed. This file can be altered for custom requirements. The *Simulation panel (5)* includes options for selecting the motion to be simulated via a drop-down menu and several checkboxes to control simulation parameters: *Actuated* to include actuation according to the selected motion, *Force Joint Position* to override PD control, *With Object* to include object interaction, and *Plot Result* to display simulation results. The *Simulate* button initiates the simulation.

3.3. Evaluation and Validation

Joint Torque Calculation Accuracy

The precision of the numerical torque calculation (section 3.1.3) was validated using a grasping motion performed by our humanoid robot ARMAR-6. The joint trajectory recorded during the motion was used to compute the torques, which were then compared with the measured values. Figure 3.20 illustrates the results. As the robot approaches a singularity at the end of the grasping motion, oscillations occur that cannot be fully captured by rigid-body dynamics models. This phenomenon should be taken into account when selecting actuators based on the calculated requirements. The mean error between the measured and computed torques was found to be 1.8%, demonstrating that the approach provides a sufficiently accurate estimation of the required joint torques for executing human-like movements.

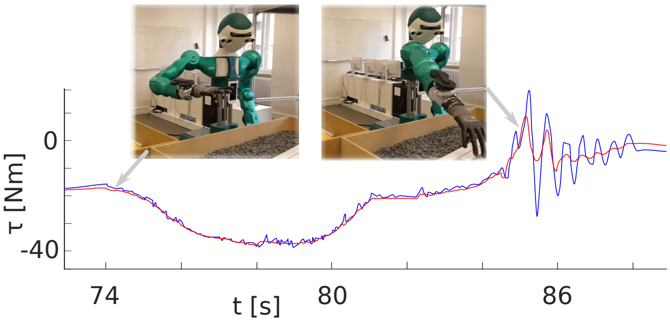

Figure 3.20.: Measured torque (—), and numerically calculated torque (—) of the first right shoulder joint (j_{1a}) of ARMAR-6 during a grasping motion. *Source:* (**Klas** et al., 2023) © 2023 IEEE

Kinematics

The Kinematics Comparison part of the Robot Design System provides insight for the best kinematics for a given task independent of the concrete realization and size of the robot. The underlying assumption is a weight distribution similar to the human one (represented by the MMM). In the example in Figure 3.21, the task would be a small and simple robot for entertainment with equal units of actuation. In this example the figure can provide help for the appropriate selection of robot kinematics. The required actuation power for the Justin kinematics is considerably lower than for other kinematics while the required speed and torque are evenly distributed over the different joints which is favorable for the repeated usage of the same actuators. The N.D. Kinematics offers a lower total actuation power, but the difficult kinematics are not suitable for a small and simple robot. In addition, the requirements are more unevenly distributed between the joints, making repeated usage of the same actuators less effective.

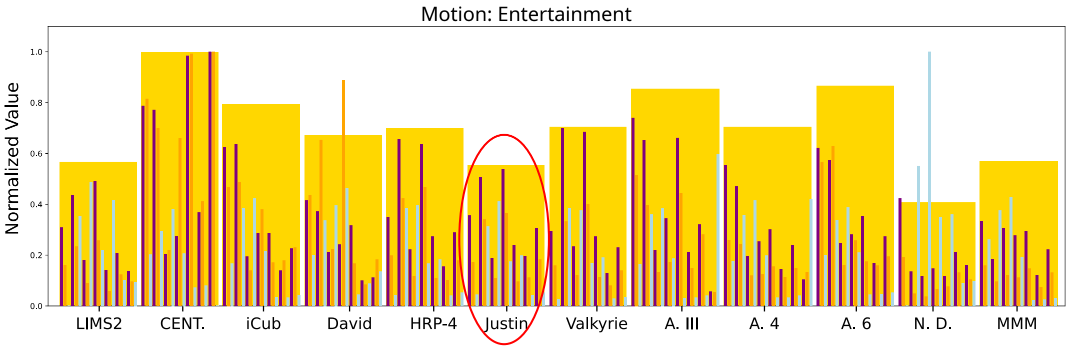

Figure 3.21.: Evaluation of robot design tool: If the goal is a simple entertainment robot with equal actuation units, the encircled kinematics would be a good fit. Normalized velocity (—), acceleration (—), torque (—), and actuator power requirement (🟨).

Actuator Optimization

Quantitative Evaluation

The framework was applied to optimize the upper-body actuators of the ARMAR-6 and ARMAR-7 robots. The data resolution was adjusted using the *Delete Small Time-steps* algorithm with a norm value of 0.25. The masses of the manipulated object were set to 100%, and the weight and height of the robot were configured according to the specifications of ARMAR-6 and ARMAR-7. The kinematic specifications of the robots are summarized in Table 3.8, where λ is the scaling factor relative to the MMM reference model, which is also included for comparison. Two sets of evaluations were performed for each robot: one for the motions Entertainment (E), Household (H), Factory (F), and Conversation (C), and another for only Entertainment and Household motions. For a detailed breakdown of the movements, see **Klas** et al. (2023). For each robot, gear ratios for the actuators of each upper-limb joint were optimized, demonstrating how the framework supports task-based design by yielding meaningfully different results based on selected motions.

Table 3.8.: Kinematic specifications of robots used for evaluation.

Name	j_R	j_1	j_2	j_3	Torso	λ
ARMAR-7	j_C, j_{R1}	xy	xy	$quat$	P_z	0.41
ARMAR-6	j_C, j_{R1}	xy	xz	xy	P_z	0.31
MMM	j_{R0}	xy	xy	xy	R_x, R_y, P_z	1.00

The results of the automatic gear ratio optimization are shown in Table 3.9, Table 3.10, Table 3.11, and Table 3.12, where SAC refers to the joint-specific KIT SAC Unit, i_C is the current gear ratio for the selected SAC Unit, AOI_C is the AOI for the current gear ratio, i_{O*} is the gear ratio obtained from the automatic optimization, AOI_{O*} is the AOI for the optimized gear ratio, and $\%*$ shows the change from the current to the optimized gear ratio.

Table 3.9.: ARMAR-6 upper-body actuator optimization. Motions: Entertainment, Factory, Conversation, Household.

Joint	SAC	i_C	AOI_C	i_{O*}	AOI_{O*}	%*
j_{1a}	L	160	0.035	44.1	0.110	214%
j_{1b}	L	160	0.048	50.2	0.124	158%
j_{2a}	M	160	0.072	50.2	0.165	129%
j_{2b}	M	160	0.050	50.0	0.146	192%
j_{3a}	S	160	0.149	50.0	0.333	123%
j_{3b}	S	160	0.103	67.0	0.147	43%
j_R	M	160	0.027	50.0	0.068	152%
j_C	L	160	0.060	54.7	0.137	128%
					Avg.	+142%

Table 3.10.: ARMAR-6 upper-body actuator optimization. Motions: Entertainment, Household.

Joint	SAC	i_C	AOI_C	i_{O*}	AOI_{O*}	%*
j_{1a}	L	160	0.104	45.1	0.108	3%
j_{1b}	L	160	0.036	49.5	0.096	167%
j_{2a}	M	160	0.029	50.5	0.065	124%
j_{2b}	M	160	0.055	50.0	0.164	198%
j_{3a}	S	160	0.120	51.4	0.232	93%
j_{3b}	S	160	0.142	62.8	0.228	61%
j_R	M	160	0.034	50.0	0.093	174%
j_C	L	160	0.071	56.7	0.155	118%
					Avg.	+117%

The results indicate that the optimized gear ratios generally reduce transmission ratios compared to the originally selected values. This is due to large acceleration spikes in the motion data, where higher transmission ratios help mitigate by providing greater acceleration. It is notable that ARMAR-6, de-

Table 3.11.: ARMAR-7 upper-body Actuator Optimization. Motions: Entertainment, Factory, Conversation, Household.

Joint	SAC	i_C	AOI_C	i_{O*}	AOI_{O*}	%*
j_{1a}	U1	160	0.077	65.6	0.140	82%
j_{1b}	U1	160	0.104	68.5	0.176	69%
j_{2a}	U1	100	0.074	62.1	0.095	28%
j_{2b}	HD8	166	0.204	58.1	0.339	66%
j_{3a}	A7W	94	0.278	92.0	1.000	260%
j_{3b}	A7W	94	0.492	81.3	0.500	2%
j_R	U1	100	0.076	56.3	0.107	41%
j_C	U1	160	0.068	72.6	0.109	60%
					Avg.	+76%

Table 3.12.: ARMAR-7 upper-body Actuator Optimization. Motions: Entertainment, Household.

Joint	SAC	i_C	AOI_C	i_{O*}	AOI_{O*}	%*
j_{1a}	U1	160	0.081	62.7	0.153	89%
j_{1b}	U1	160	0.131	69.6	0.221	69%
j_{2a}	U1	100	0.260	59.4	0.348	34%
j_{2b}	HD8	166	0.365	60	0.568	56%
j_{3a}	A7W	94	0.711	91.1	0.712	0.1%
j_{3b}	A7W	94	0.650	89.8	0.651	0.1%
j_R	U1	100	0.080	57.4	0.111	29%
j_C	U1	160	0.177	73.5	0.278	57%
					Avg.	+42%

signed for industrial applications requiring slower, high-force movements, benefits from lower transmission ratios, particularly for conversation-related motions.

This evaluation demonstrates that the framework effectively derives optimal actuator parameters based on motion requirements, facilitating task-based design. The AOI proves useful for comparing different actuator configurations, and the automatic gear ratio optimization highlights potential improvements, often identifying solutions outside of the initial parameter ranges.

Qualitative Evaluation

The selection of an optimal gear ratio is a fundamental and effective method for enhancing robot performance for specific environments. The automation of this process represents a crucial feature of the proposed framework. It provides creative freedom for robot designers as it allows flexible control over various aspects, including the granularity of motion data, motion selection, robot kinematics and actuator parameters. The provision of immediate feedback on parameter modifications accelerates the decision-making process, facilitating the identification of better solutions. While the selection of the suitable kinematics is particularly important in the initial design phase, a different transmission ratio can also be applied to existing robots.

A task-based design approach ensures that the robot's configuration is tailored to the specific movements it needs to perform, accommodating a wide range of motions. The retargeting of various human motions to different kinematic configurations and actuators is made available to the framework's gear ratio optimization. The Actuator Optimization Index (AOI) includes acceleration, velocity, and torque, effectively bridging the gap between human and robotic motion data. This index is further enhanced by a visual representation within the velocity-acceleration-torque space, which provides deeper insights than numerical outputs alone. Kinematic comparisons are enriched by these visual representations, enabling a more intuitive analysis of robot performance. The framework's interactive 3D diagrams also support informed decision making when trade-offs are required.

Although the actuator optimization does not explicitly address control strategies or structural integrity, the optimized model lays a robust foundation for the exploration of these considerations in subsequent design phases.

Simulation

In the Simulation tab of the Humanoid Robot Design Assistant, different realisations of the robots can be tested. Thereby, the error by violation of necessary assumptions as well as the effect of scaling and different simulators can be tested. Therefore, a Mujoco XML file for each simulation is automatically generated in the GUI. This file can be manually altered for further refinement. In Figure 3.22, the scaled results (joint torque and position) of the normalized Simulink simulation can be seen next to the evenly scaled robot in the MuJoCo simulation. In this figure, the weight is still distributed according to the simplified assumption from the *Kinematic Section*. It can be seen that both totally separated simulations lead to similar results. The main difference is related to torque peaks that occur in Simulink. Their absence in MuJoCo and damping in real structures make the filtering of peaks in the previous parts plausible. In contrast to the simple scaling of body parts according to the human weight distribution, the inclusion of actuator weight and inertia (internal and external) is possible in the simulation (Figure 3.23). The results show that there is a slight difference between the simplified weight distribution and the one considering actuator placement. This difference is however small and does not change the general order of magnitude of the result. Therefore, the applied simplifications can be considered permissible. Edge cases where this is not true can be identified in the simulation step before building the real robot.

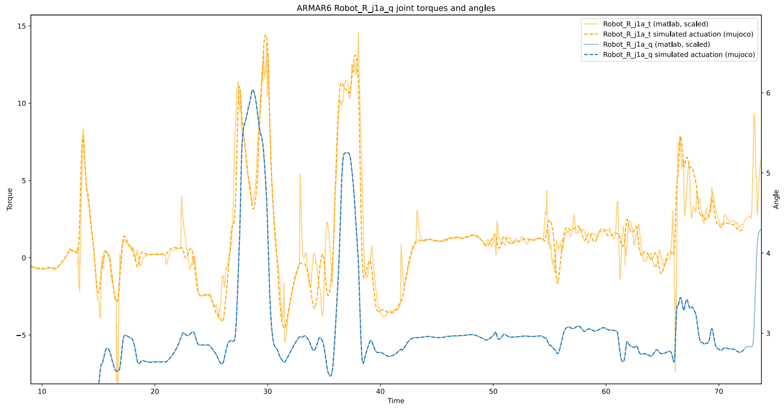

Figure 3.22.: Evaluation of scaling and simulation tools. Scaled results (joint torque and position) of the normalized Simulink simulation and the evenly scaled robot in the MuJoCo simulation.

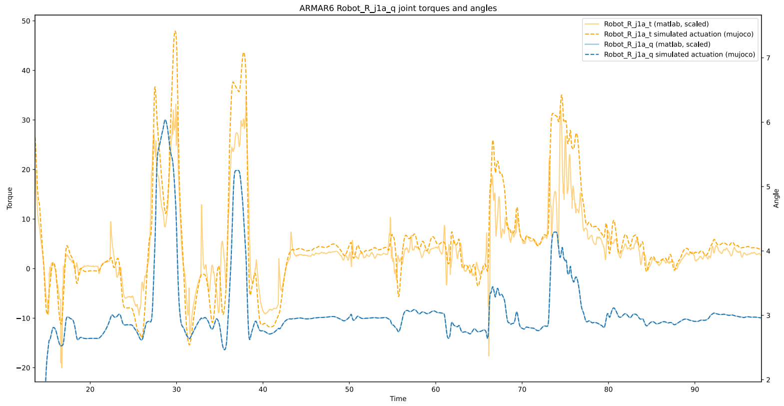

Figure 3.23.: Evaluation of weight distribution. Scaled results (joint torque and position) of the normalized Simulink simulation and the scaled robot including actuator inertia in the MuJoCo simulation.

3.4. Summary and Review

The first part of this chapter introduces a system that automatically computes the actuator requirements for humanoid robot arms based on retargeted human motion. The pipeline for transferring human-like motion trajectories proves effective across various bimanual humanoid arm kinematics. Our system calculates normalized joint torques, velocities, and accelerations (Figure 3.2) for all arm joints, demonstrating the feasibility of executing human-like motion trajectories using data from the KIT Whole-Body Human Motion Database. We showcase the utility of our novel framework to evaluate various existing and new kinematics. The speed, acceleration, and torque requirements provide a foundation for dimensioning joint actuation in future robotic systems. The introduction of the *Power Requirement Index* (PRI), a new *performance index*, enhances the evaluation of the new design based on key considerations for improving robot dynamics. Our findings indicate that, assuming a constant segment weight distribution, the robot's kinematic structure significantly influences the required joint actuation power. Looking ahead, we plan to extend the comparison of kinematic parameters and joint mechanisms toward their optimization.

The second part of this chapter presents a comprehensive review and conclusion of the proposed framework for humanoid robot arm design, focusing on kinematic selection, comparison, and actuator optimization based on human motion data. The findings from this chapter highlight the importance of a structured approach to optimize both kinematic and actuator parameters. Independently, the proposed humanoid robot arm design system can improve the design process for humanoid robots.

The framework consists of the following core components:

- Actuation requirements for human-like execution of retargeted human motion on humanoid robots (section 3.1)
- Processing and adjustment of the retargeted motion data (section 3.2.1),
- Selection of the most suitable robot kinematics (section 3.2.2), facilitated by a kinematic performance index (section 3.1.4),
- Actuator selection and optimization (section 3.2.3), including a novel actuator optimization index based on actuator requirements and motor parameters in the speed-acceleration-torque space (section 3.2.3).
- Generation and simulation of robot models (section 3.2.4).

In this framework, the gear ratios of the actuators, selected from a database, are automatically optimized using an algorithm capable of exploring solutions beyond the initial values. The optimized kinematic and actuator parameters derived from this process can then be used to create a robot model for further validation and testing. Powered by a custom software tool, this framework offers a detailed and practical approach to humanoid robot arm design, grounded in human motion data.

The application of the framework to real robot kinematics using motion data from various scenarios, such as Entertainment, Factory, Conversation, and Household, demonstrates its effectiveness.

However, the findings of this chapter also indicate the need for further research and development in two key areas, which will be explored in subsequent chapters. The first area is the challenge of replicating human force-velocity profiles in robot design, which led to the development of a linear drive mechanism, as discussed in **chapter 4**, which introduces a novel mechanism that aims to better align the performance of the robot actuator with the characteristics of human motion.

The second area of improvement lies in the kinematic design of humanoid arms. This observation led to the investigation of Quaternion Joint-based kinematic designs, which are explored in **chapter 5**, which focuses on refining the kinematic structure of humanoid arms to enhance flexibility and motion range, driven by the findings of the current framework.

Thus, the need for these two chapters emerges directly from the findings in this chapter. Together, these chapters form a coherent response to the identified challenges and further advance the design of humanoid robots by addressing both actuator performance and kinematic structure.

4. Linear Drive Mechanism for Human Force-Velocity Profiles

As seen in the related work and results from the previous chapter, conventional actuators face limitations in replicating human-like motion and a new actuator with a speed-torque profile similar to human muscles would greatly benefit humanoid robots.

As stated in section 2.2, there are three main challenges to achieving human-like performance with electric motors. Although these motors have higher power densities, ranging from $1\,\mathrm{kW/kg}$ (Tanaka et al., 2013) to $7\,\mathrm{kW/kg}$ (Seok et al., 2012)—compared to human muscles, which have a power density of approximately $0.2\,\mathrm{kW/kg}$ (Hunter and Lafontaine, 1992), significant challenges remain to utilize this potential effectively.

First, space and weight constraints make it difficult to achieve the high speed and torque required, as motors and gearboxes with higher peak power be-

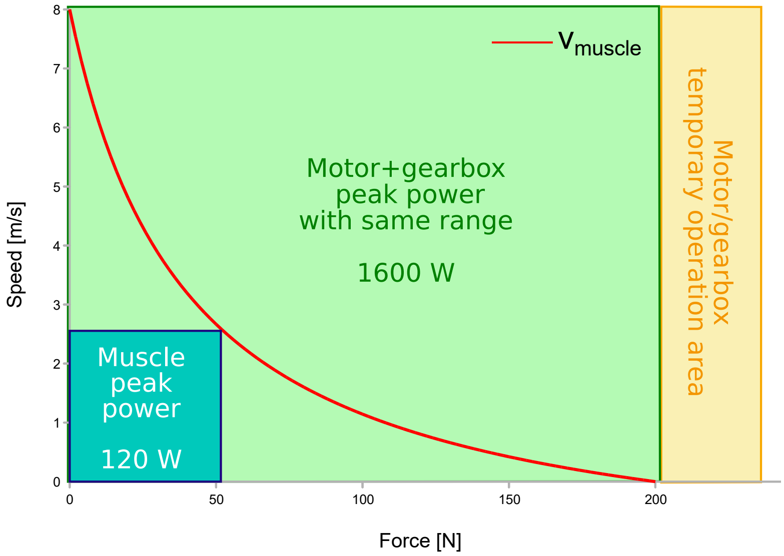

Figure 4.1.: Force and speed in the biceps brachii muscle from Wilkie (1949) and an actuator with fixed speed and torque limits and the same range of speed and force. *Source:* (**Klas** and Asfour, 2023) © 2023 IEEE

come much larger and heavier than the human model. Second, heavy gears at each joint necessitate even larger gears in upstream joints, which is problematic given the many DoF in humanoid arms. Third, electric motors perform best at high speeds, requiring high transmission ratios from $R = 10$ to $R = 300$ (Matsuki et al., 2019), but this results in high reflected inertia that can equal the weight of the entire arm.

One solution presented in related work is switchable gearboxes (section 2.2.3), which achieve a speed-force profile similar to that of human muscles. Although manually or automatically switchable gears provide the benefit of adjustable transmission ratios, they are typically large, heavy, costly, and complex.

Continuously variable transmissions (section 2.2.3) allow adjustment of the force-speed profile, although this adaptation is relatively slow due to the use of a separate actuator. Additionally, the mechanism is quite heavy, as it is typically designed for fixed installations or vehicles with a single drive system.

Hybrid Linear Drives (section 2.2.4) provide an alternative approach by combining two actuators based on the engineering principle of hybridization, taking advantage of each. Although several actuators employing this concept already exist, the mechanism introduced in the following represents a novel implementation of this approach.

To our knowledge, no existing gear mechanisms meet the criteria for a compact, cost-effective, and powerful robot with a similar design. Current solutions are generally larger and heavier, lacking specificity for muscle force-speed profiles, which are significant drawbacks.

To overcome current limitations, this chapter introduces the Adaptive Cycloidal Linear Drive (ACLD). It is a novel actuator solution inspired by the force-velocity profiles of human muscles. The ACLD is based on the patent (**Klas**, 2023) and is further elaborated on in (**Klas** and Asfour, 2023).

The evaluation of actuator capabilities often relies on the force-speed profile, which represents the maximum force an actuator provides at a given speed. For rotary actuators, this corresponds to the angular velocity-torque curve. Electric motors generally deliver higher speeds and lower torques than needed, necessitating the use of gearboxes to reduce speed and increase torque. However, fixed transmission ratios cannot alter the overall motor speed-torque profile or mechanical power.

Inspired by the force-speed profile of human muscles (Figure 4.1), which balances low maximum power across a wide range of force and speed, the ACLD seeks to mimic these characteristics. Existing robots, such as ARMAR-6 (Asfour et al., 2019), ARMAR-4 (Asfour et al., 2013), and others such as CENTAURO (Baccelliere et al., 2017) and HRP-5P (Kaneko et al., 2019), rely on fixed transmissions, which limit their performance. Quadruped robots like Spot (Guizzo, 2019) and MIT Cheetah (Seok et al., 2012) prioritize high speeds with lower transmission ratios, but such designs are less suitable for humanoid arms, which require sustained high torque.

In this chapter, the following research questions are addressed:

- How can a linear drive mechanism be designed to accurately replicate human force-velocity profiles?
- What are the optimal actuation configurations for balancing efficiency, force output, and speed in a humanoid robotic context?
- How does the linear drive mechanism compare to traditional actuation systems in terms of replicating human-like dynamic movements?

The chapter begins by introducing the concept of the ACLD. The discussion continues with subsections covering the requirements for the actuator and the concept and kinematic layout.

Next, the design and implementation of the ACLD are explored in detail. This section describes the mechanics of the gear system, which integrates a cycloidal stage with a linear spindle drive to achieve the desired adaptive transmission. It contains diagrams and technical data to illustrate the design principles.

Following the design description, the chapter presents results from experimental evaluations conducted on an ACLD prototype. This section discusses findings related to speed-torque profiles, dynamic properties, transmission ratios, efficiency, comparisons to state-of-the-art solutions, and identified limitations.

Finally, the chapter concludes with a discussion on the broader implications of the ACLD for humanoid robot design. This discussion highlights the potential of the ACLD to facilitate more natural and versatile movements in robots, especially for tasks that require both speed and strength. The chapter also outlines future research directions for the ACLD, such as scaling the design for smaller joints, enhancing its efficiency, and integrating it into complete humanoid robot systems.

4.1. The New Mechanism

Electric motors have high power densities, but the challenges of space, weight, and inertia limit their ability to fully replicate human muscle performance in humanoid robots. The ACLD offers a solution by providing a switchable gearbox with a speed-force profile similar to that of human muscles, achieving high speed and high torque while maintaining low mechanical power.

4.1.1. Requirements

The requirements for a new mechanism draw inspiration from the mechanical properties of human muscles, while utilizing existing, established mechanical components. The dual challenges of achieving strong performance in terms of weight, size, speed, and force, along with the necessity for low inertia within the kinematic chain, demand a compact design and linear actuation like in muscle-driven joints where the mass is positioned closer to the body center.

A primary influence is the force-speed profile of human muscles, which is characterized by low maximum power. For this analysis, we focus on the *biceps brachii* muscle (Wilkie, 1949) due to its well-defined curve shape. The requirements for the desired solution consist of two motors in combination with an automatically shiftable gearbox. This configuration allows for an increase in total torque while benefiting from the higher speed of the faster actuator.

Figures 2.8 and 4.2 illustrate how this approach compares to human muscles and traditional solutions. In the first figure, a $1600\,\mathrm{W}$ motor with a fixed transmission ratio is utilized, while the second figure depicts the profile achieved with two $200\,\mathrm{W}$ motors utilizing different transmission ratios. Assuming a constant power density of $1\,\mathrm{kW\,kg^{-1}}$ as provided by Tanaka et al. (2013), the weight is reduced to $2 \cdot 200\,\mathrm{g}$ instead of $1600\,\mathrm{g}$.

Similarly to human muscles, the new mechanism should enable an efficient transition between high-speed and high-torque performance. In addition, some requirements can be met by short-term operation. This flexibility allows for further improvement of the power-to-weight ratio when sustained high torque is not essential.

The motor force-speed profiles in Figure 4.1 and Figure 4.2 differ due to the fixed limits of most gearboxes in terms of speed and torque. Limiting motor power to a triangular shape is less effective since the gearbox size remains unchanged. In Figure 4.2, both potential effects are combined. However, employing rectangular areas is also a viable option.

In the specified requirements, the three challenges outlined above are addressed as follows: the segmented speed-force profile in Figure 4.2 enables adaptation to specific application needs while maintaining much lower peak mechanical power for both motors and gears, enabling the use of significantly smaller components. The linear design of the drive allows for actuation of a 2 DoF joint, as described in chapter 5, from a position closer to the body center, thus reducing inertia. Both motors contribute to torque when driving the two gear stages, and the one with a lower transmission ratio is always capable of providing the necessary torque for sudden accelerations, effectively weakening the issue of high internal inertia. Our proposed solution unites both gearboxes in a single mechanism featuring two actuators, characterized by its compact size and load-dependent automatic selection of the transmission stage.

4.1.2. Concept and Kinematic Layout

This section introduces the concept of a two-stage linear drive system with automatic and adaptive gear selection. The concept and kinematic layout of this mechanism are depicted in Figure 4.3.

The rotational movements of two actuators, Ⓘ and Ⓘⓘ, are converted into a linear movement through two operational modes that can be used individually or

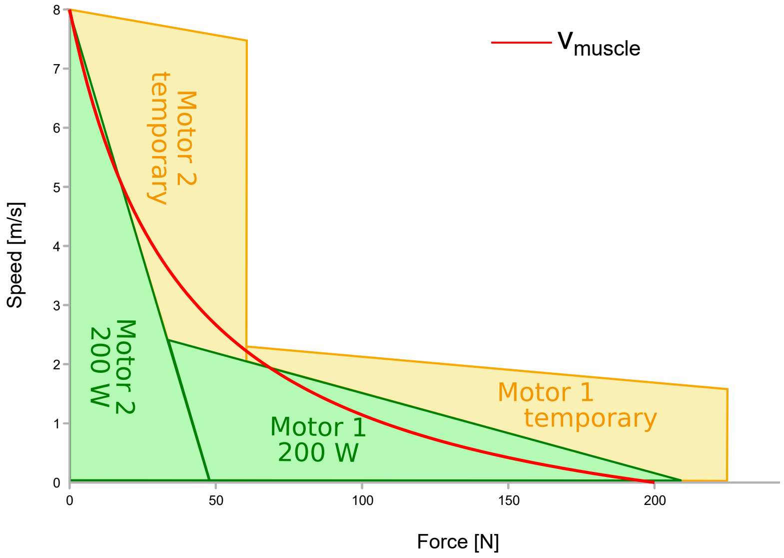

Figure 4.2.: Force and speed characteristics in the biceps brachii muscle, alongside the proposed **ACLD** concept featuring two gear ratios and triangular motor profiles. *Source:* (**Klas** and Asfour, 2023) © 2023 IEEE

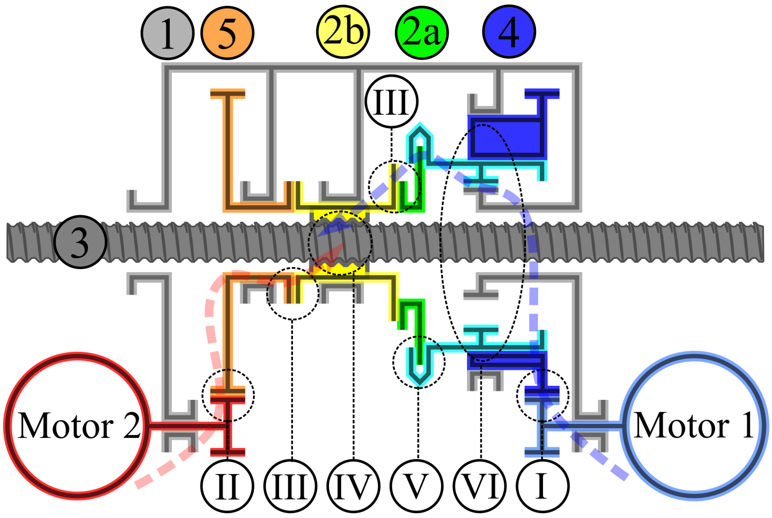

Figure 4.3.: **Concept and kinematic layout** of the ACLD featuring actuation I and II, coupling III, linear transmission IV, clutch V, and cycloidal drive VI. Power flow is depicted in blue (I) and red (II). The components correspond to Table 4.1. *Source:* (**Klas** and Asfour, 2023) © 2023 IEEE

in combination. These two modes are characterized by different transmission ratios, each driven by one of the two drive sources.

The first drive source, (I), drives a rotary-to-linear transmission (IV), which is formed by a spindle ③ and nut ④, operating through a clutch (V) and a cycloidal drive (VI). This state is referred to as the *Cycloidal Mode*. The overall transmission ratio is the product of the thread pitch and the transmission ratio of the cycloidal gear. To ensure that this mode operates independently, the clutch must be preloaded.

The second actuator, (II), directly powers the linear transmission (IV). The eccentric offset and axial forces are compensated for by a coupling (III). This configuration is referred to as the *Spindle Mode*, where the transmission ratio is determined solely by the thread pitch. This mode offers a smaller gear ratio (for high-speed output), while the *Cycloidal Mode* offers a larger gear ratio (for low-speed, high-force output).

When both drive sources are running in parallel, the *Combined Mode* is engaged. The two mechanisms are synchronized via the clutch (V), which is activated by axial load. Under low axial forces, friction in the clutch is minimal, and the spindle is primarily driven by the fast *Spindle Mode*. Depending on the clutch characteristics, the *Cycloidal Mode* can contribute to the load, thus increasing speed.

At higher axial forces, friction in the clutch increases, and both the *Cycloidal Mode* and the *Spindle Mode* work together to drive the spindle, enabling higher

Components		Functionality	
①	Housing	Ⅰ	First (cycloidal) actuation (blue)
②	Eccentric spindle nut	Ⅱ	Second (spindle) actuation (red)
(2a)	Eccentric element	Ⅲ	Coupling with force decoupling
(2b)	Spindle nut	Ⅳ	Rotary to linear transmission
③	Spindle	Ⅴ	Clutch with offset compensation
④	Cycloidal drive element	Ⅵ	Cycloidal drive
⑤	Spindle drive element		
⑥	Eccentric bearings		
⑦	Concentric bearings		
⑧	Plain bearings		

Table 4.1.: Essential components and functionality of the ACLD.

torque. Determined by the clutch characteristics, the transition between modes can be smooth.

The linear speed of the spindle ③ is proportional to the speed of the second motor Ⅱ. The current transmission ratio can be adjusted or monitored based on the speed ratios of the two motors.

4.2. Design of the ACLD Prototype

By combining two stages with different transmission ratios, a broad range of speed and torque can be achieved. A prototype was developed to validate the approach, with its specifications detailed in Table 4.2.

Components and Mechanical Realization of the ACLD

The proposed linear drive system consists of the key components illustrated in Figure 4.4. These components are: a housing ①, an eccentric spindle nut ② comprising an eccentric element (2a) and an internal thread (2b), a cycloidal drive element ④, a spindle drive element ⑤, eccentric bearings ⑥, concentric bearings ⑦, and plain bearing elements ⑧.

Various mechanical realizations for linear actuators have been discussed in related work (subsection 2.2.5). Here, we focus on detailing the mechanical implementation of the Adaptive Cycloidal Linear Drive (ACLD).

As illustrated in Figures 4.3 and 4.4, the main distinction between the conceptual design and the mechanical realization is the consolidation of the linear

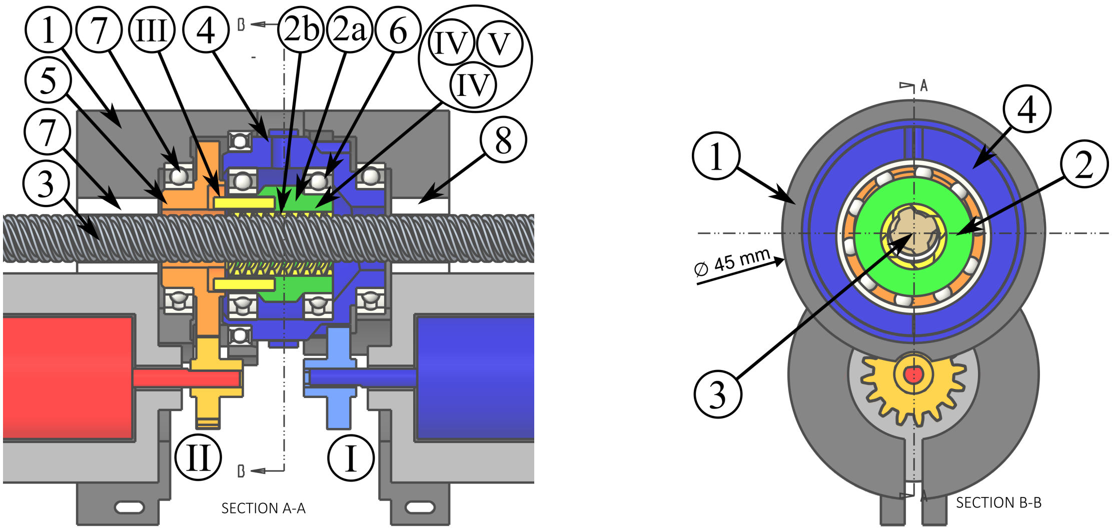

Figure 4.4.: **Mechanical realization** of the ACLD. Sectional drawing A-A (Left) and B-B (Right). *Source:* (**Klas** and Asfour, 2023) © 2023 IEEE

transmission (IV), the clutch (V), and the cycloidal drive (VI) into a single unit. This configuration enables two operational modes: the *Cycloidal Mode* and the *Spindle Mode*.

In both operational modes, the spindle ③ is guided by plain bearing elements ⑥ along a central axis within the housing ①. The position of the spindle along the axis is dictated by the rotation of the eccentric spindle nut ②. Separate measures to prevent unwanted rotational movement of the spindle are necessary.

In the *Cycloidal Mode*, the cycloidal drive element ④ is actuated by the first motor (blue) (I). This mode features geared actuation of the spindle and an indirect drive for the second motor (red). The spindle and nut engage in rolling contact without tangential sliding (see Figure 4.5a). Thereby, the rotational axis of the nut is rotating around the central axis.

As the cycloidal drive element ④ rotates, it alters the orientation of its eccentricity relative to the spindle, changing the contact point between the spindle and the eccentric spindle nut ②. This corresponds to the motion characteristic of cycloidal drives (VI).

In the *Spindle Mode*, the second motor (red) (II) directly drives the eccentric spindle nut ② through the spindle drive element ⑤. This mode allows for direct spindle actuation, yielding high-speed performance with sliding contact between spindle and nut (see Figure 4.5b). The axis of rotation of the eccentric spindle nut remains stationary. The coupling (III) is used to compensate for misalignment and to isolate axial forces.

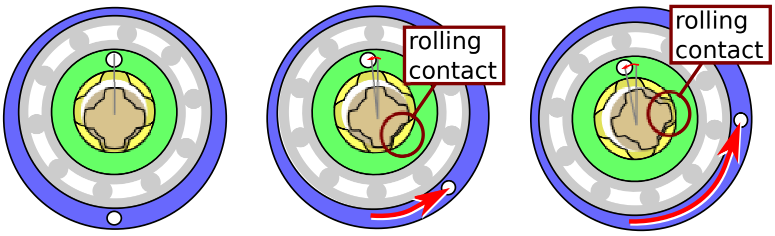

(a) *Cycloidal Mode*: Geared actuation

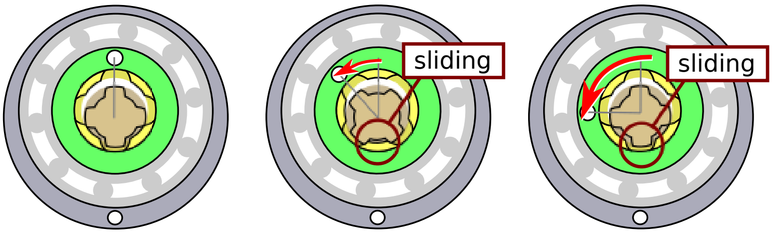

(b) *Spindle Mode*: Directly actuated

Figure 4.5.: Motion of the drive components in *Cycloidal* and *Spindle Mode*. *Source:* (**Klas and Asfour**, 2023) © 2023 IEEE

The friction generated between the spindle and nut varies with the axial load, enabling a clutch functionality Ⓥ that is responsive to axial forces. Thus, the contributions of both modes are modulated by the axial force applied.

Experimental results indicate that the transition between these modes is gradual rather than abrupt (see Figure 4.10). Notably, the cycloidal mechanism can enhance force output even at high speeds, thereby reducing the load on the spindle drive. A possible self-locking nut prevents reverse motion of the spindle motor. When the pitch and friction force are set below the self-locking threshold but below the spindle motor driving force, back-drivability is achieved.

Both the drive spindle and the drive element feature a pitch of $1.5\,\mathrm{mm}$, with the internal thread diameter of the drive element measuring $10\,\mathrm{mm}$, compared to the $8\,\mathrm{mm}$ external thread diameter of the drive spindle.

The spindle transmission ratio R_S and the cycloidal transmission ratio R_C are defined as follows: R_S at reduced friction determines the maximum speed, while R_C governs the maximum transmission ratio between both motors (see Figure 4.10). Future work may involve mathematical modeling for more detailed dynamic analysis.

The cycloidal transmission ratio R_C is derived from the effective thread diameters of the drive element D and the drive spindle d, while R_S is calculated from the spindle pitch p:

$$R_C = \frac{D}{D-d} \tag{4.1}$$

$$R_S = \frac{2 \cdot \pi}{p} \tag{4.2}$$

The spindle ③ and the nut ② engage across multiple tooth flanks, making them suitable for transmitting significant axial forces to the drive spindle.

The second drive source is equipped with overload protection via electrical power limitation or a cutoff mechanism. The two motors are connected to the hollow shaft ② and the drive element ②, respectively, through gear drives. For these experiments, the nut was fabricated from PLA using a 3D printer and lubricated with PTFE spray.

Variants

To ensure the necessary spindle rotation limitation, various design options can be considered. One approach involves incorporating an anti-rotation device directly into the gear unit using appropriate guides.

An alternative design for the linear actuator utilizes multiple coupled eccentric nuts with contact surfaces on opposite sides of the spindle. This configuration eliminates the need for separate spindle guidance in plain bearings, thereby reducing friction.

For ease of production, the spindle can be manufactured using a standard thread, such as a trapezoidal thread. By employing suitable drive elements or nuts (e.g., 3D printed), a large contact area can be achieved, preventing overlaps during movement. Alternatively, the drive element or nuts can be designed with a standard thread, while the spindle uses a complementary one.

Friction

In *Cycloidal Mode* (hollow shaft driven by first motor), friction losses are lower due to the nut's primarily rolling motion on the spindle with limited sliding. During one spindle rotation, a point on the thread moves outward and inward

Weight	$100\,\mathrm{g}$
Diameter	45 mm
Speed	$225\,\mathrm{mm\,s^{-1}}$
Payload	480 N
Power (Speed x Payload)	108 W

Table 4.2.: Specifications of the ACLD prototype.

by a single thread height. In contrast, direct drive of the drive element via the secondary drive source (*Spindle Mode*) results in significantly higher friction losses, as the nut slides along the entire spindle diameter during one rotation. However, the transmitted axial forces are lower in this mode. Figure 4.5 illustrates the motions of the parts in both modes. Frictional power losses can be estimated using the following equations:

$$P_{loss_{cycloidal}} = 2 \cdot h \cdot \nu \cdot \mu \cdot F_{ax} \tag{4.3}$$

$$P_{loss_{spindle}} = \pi d \cdot \nu \cdot \mu \cdot F_{ax} \tag{4.4}$$

where h is the tooth height, d is the spindle diameter, ν is the rotational frequency, μ is the friction coefficient, and F_{ax} is the axial force on the spindle.

Actuation

The gear mechanism utilized in the prototype experiments is powered by two DC motors RC4WD (2022), each rated at $20\,\mathrm{W}$, connected through a 2:1 spur gear. Characterization of the motors was conducted during evaluation experiments to estimate output torque, as illustrated in Figure 4.6. Various types of electrical DC or EC motors can serve as drive sources, with or without gear systems. Overload protection is incorporated in the second drive source to prevent overheating at high loads, featuring current limitations, as detailed in section 4.2.

To simplify control, the linear current-to-torque relationship in the prototype is established using DC motors and analog linear current limitations. Additionally, a prototype utilizing stepper motors was developed (see Figure 4.7) to conduct high torque tests and ensure precise speed relations between both motors. Although the stepper motors provide high torque, their considerable weight makes them less suitable for humanoid robots; however, they can effectively operate a single robot arm from a fixed base.

Both DC motors in the prototype are controlled together through voltage or current control. When employing stepper motors, the speeds of both motors are preferably adjusted according to the cycloidal transmission ratio depicted in Figure 4.10 or to achieve the desired transmission ratios.

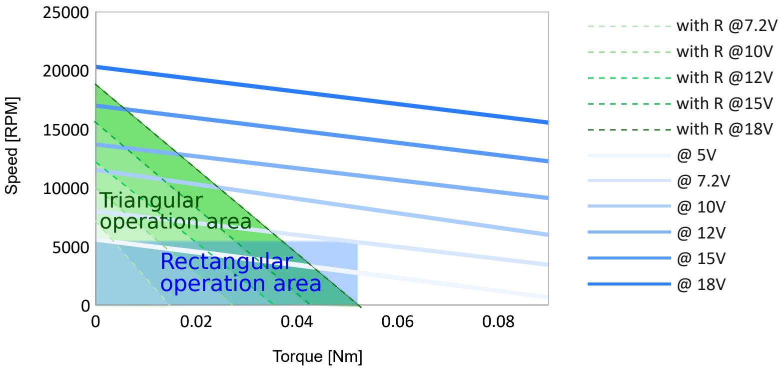

Figure 4.6.: Performance profile of motor 1 in the experimental setup. The rectangular area is constrained by motor heating, gearbox speed, and torque limits, while the triangular area is limited by series resistance. Unlimited stall currents may damage the motor and gearbox at high voltages, similar to most EC and DC motors. *Source:* (**Klas** and Asfour, 2023) © 2023 IEEE

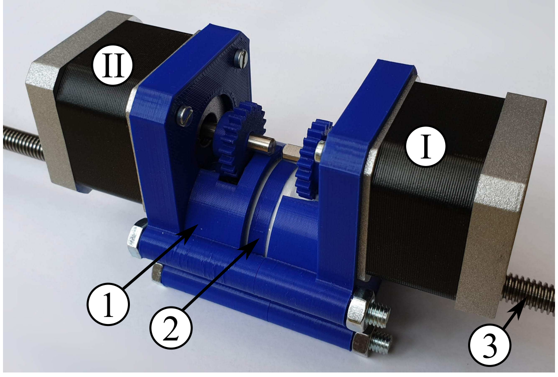

Figure 4.7.: Implementation of the **ACLD** using stepper motors. All prototypes in this study maintain a consistent gearbox size and design, differing only in motor type and spindle pitch. The components are labeled as shown in Table 4.1. *Source:* (**Klas** and Asfour, 2023) © 2023 IEEE

Electronics

When speed (which is proportional to voltage) and torque (which is proportional to current) are not constrained by fixed values but instead depend on maximum electrical power, the thermal load on both the motor and gears can be reduced, enabling higher operational speeds. This approach complements the mechanical characteristics of the ACLD, potentially allowing for a smaller motor size.

As noted by Seok et al. (2012), the recommended voltage should consider the thermal limitations to prevent failures when users operate the motor without knowledge of the coil temperature. They note that within the continuous current limit, the motor can generate significantly more power than the rated power specified by the manufacturer with a fixed voltage limit.

In addition to a continuous current limitation, an increasing current limitation further reduces the maximum power and the thermal load on the drive system, thus enabling higher maximum speeds of the spindle nut. This configuration, referred to as the triangular operating area, contrasts with the rectangular operating area. Both modes are compared for the motors in the prototype in Figure 4.6.

In the prototype, a linear relationship between maximum speed and maximum torque is generated through a series resistance designed to limit current at stall to an acceptable level. The rated voltage ($7.2\,\mathrm{V}$) can be increased up to $30\,\mathrm{V}$, resulting in significantly higher speeds without risking damage from electrical failure or frictional overheating. The current limitation in the prototype is calibrated to achieve maximum continuous torque at $18\,\mathrm{V}$. Without this limitation, the maximum torque would exceed the motor capacity at this voltage and even at nominal voltage, leading to rapid overheating.

Both the electric motor and the spindle are capable of handling short overloads due to thermal inertia, which could be leveraged in a more advanced control strategy.

Sensing

In prototype experiments, the speed was measured using commutator peaks detected in the motor current, as described by Vazquez-Sanchez et al. (2017), and verified with a digital tachometer. Force measurements were obtained through calibrated weights and a strain gauge force sensor.

In robotic applications, the gear mechanism can easily be equipped with sensors for enhanced feedback and control. Relative encoders can enable precise velocity and position control, while a simple force sensor can monitor axial load, providing direct torque feedback in the robot joint. Ideally, absolute encoders are integrated into the actuated joint for more accurate positioning.

Costs

The linear actuator offers a lean design with a high utilization of standard components (bearings, drive spindle, motors, etc.). As precision requirements are relatively low, the remaining components, such as the drive element, hollow shaft, or plain bearings, can be manufactured using friction-optimized plastics through simple production processes. Despite the use of relatively weak materials, the large force transmitting surfaces enables the generation of high forces. This advantage facilitates the production of customized, cost-effective, and lightweight linear drives with various transmission ratios.

The individual components, including the housing, hollow shaft, plain bearing elements, and drive element, can be predominantly produced without support material in FDM 3D printing. This design characteristic makes it particularly suitable for affordable and adaptable manufacturing in different sizes and gear ratios.

4.3. Experimental Evaluation

To assess the effectiveness of the proposed gear design, we measured key parameters such as speed-torque profiles using a prototype and conducted a comparative analysis against state-of-the-art solutions.

Speed-Torque Profile

To assess whether the theoretical speed-force profile was achieved by the prototype, several experiments were conducted under different load conditions (see Figure 4.8a). As expected, the resulting force was predominantly the sum of the individual torques, with only minor losses observed at higher force levels. In addition, the *Combined Mode* in the prototype was faster than the individual ones. This increase in speed can be attributed to two factors: the lower friction in the *Combined Mode* compared to the *Spindle Mode* (Table. 4.4) and the gradual transition in the transmission ratio during the shift from low to high forces (Figure 4.10), allowing the cycloidal stage to assist even at higher speeds.

Dynamic properties

The dynamic properties were assessed in an experimental setup designed to simulate a wrist drive with inertia equivalent to that of a hand holding a light tennis racquet, specifically a $0.5\,\mathrm{kg}$ bar with a length of $0.32\,\mathrm{m}$. This bar is actuated via a lever of $32\,\mathrm{mm}$, allowing for an amplitude of 40° and achieving a peak

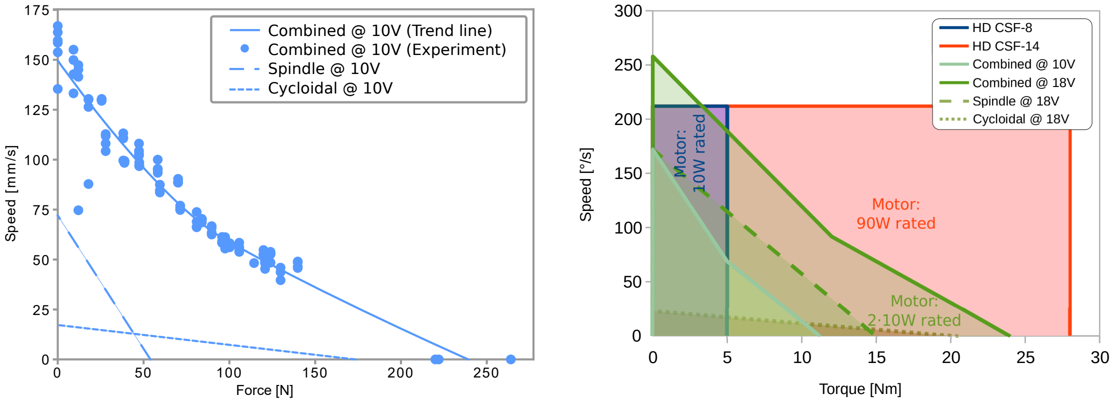

(a) Steady-state force-speed profiles at 10V.

(b) Torque and speed at various voltages.

Figure 4.8.: Experimental results for the prototype performance. Both modes separately and combined. In *Combined Mode*, forces are added and efficiency is improved. Values inTable 4.5. A comparison with Harmonic Drive CSF-8-100 and CSF-14-100, paired with Maxon RE 25 (10W) and RE 35 (90W) motors included. *Source:* (**Klas** and Asfour, 2023) © 2023 IEEE

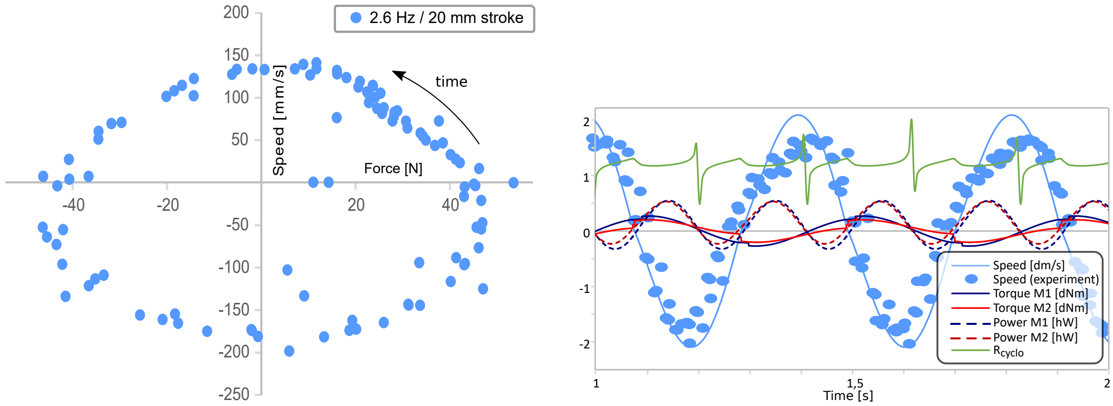

(a) Dynamic force and speed curve of the prototype in oscillating motion.

(b) Time-series data of the prototype in oscillating motion.

Figure 4.9.: The experimental setup is comparable to a drive actuating a wrist with a tennis racquet in terms of load ($0.017\,\mathrm{kg\,m^2}$), amplitude ($40°$), and obtained velocities ($300\,°\,\mathrm{s}^{-1}$). The speed is measured in the experiment, while other parameters are calculated from motor specifications, component inertia, and a constant friction force. Different inertias of the stages cause peaks in R_{cyclo} (cycloidal transmission ratio). *Source:* (**Klas** and Asfour, 2023) © 2023 IEEE

speed of $300\,°\,\mathrm{s}^{-1}$, which is comparable to the forehand wrist speeds exhibited by skilled tennis players (Loushin et al., 2022). The time-series data from this experiment is presented in Figure 4.9b. While the velocity was directly measured during the experiment, the other parameters were derived using a MATLAB Simulink model, where friction parameters were adjusted to align with findings from both static and dynamic experiments.

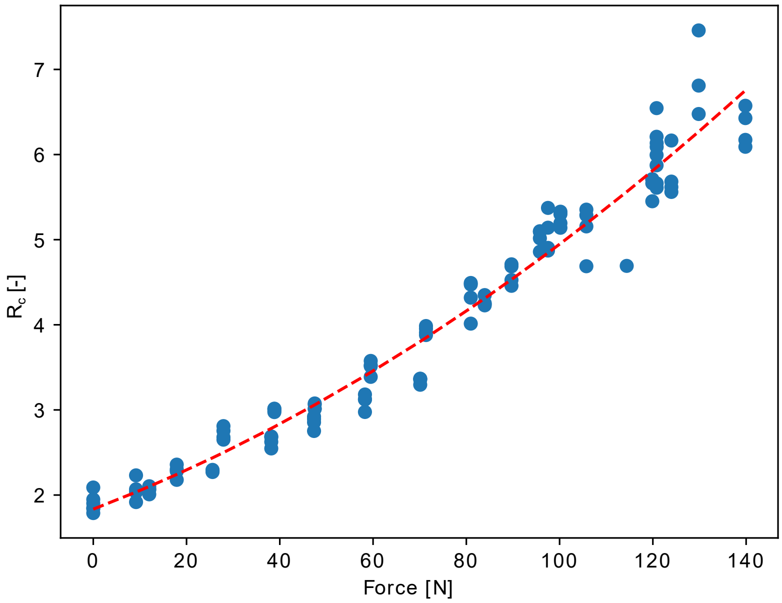

Figure 4.10.: Transmission ratio R_c of the cycloidal part of the **ACLD** corresponding to the $10\,\mathrm{V}$ force-speed profile. Fitted curve in red. *Source:* (**Klas** and Asfour, 2023) © 2023 IEEE

Transmission Ratios

The frictional characteristics of the cycloidal drive stage result in a variable transmission ratio, which depends on the effective rolling radii of the nut on the spindle and the degree of slip.

With a spindle diameter ranging from $6.2\,\mathrm{mm}$ to $8\,\mathrm{mm}$ and a nut diameter between $8.7\,\mathrm{mm}$ and $10\,\mathrm{mm}$, the possible transmission ratio is between 4.5 and 12.5 (see Equation4.1). In experiments, the measured transmission ratio of the cycloidal drive stage is between 6.3 and 7.2, indicating that the rolling contact is approximately at the midpoint of the thread, slightly closer to the outer diameter.

As shown in Figure 4.10, the transmission ratio of the cycloidal component of the ACLD gradually increases from 2 to 7 in the *Combined Mode* as the forces rise. This gradual change is advantageous as it leads to higher speeds and allows for better control compared to abrupt changes.

Efficiency

Due to their decisive influence on overall efficiency, frictional forces are the focus of this section. To calculate friction across different switching states, several experiments at varying voltages, measuring stall torque and no-load speed for

Mode	Output	Spindle Fric.	Cycloidal Fric.
Combined	Stall (220N)	72N	72N
Combined	No load speed	73N	67N
Spindle	Stall (54N)	123N	-
Spindle	No Load speed	125N	-
Cycloid	Stall (173N)	-	11N
Cycloid	No Load speed	-	92N

Table 4.3.: Absolute friction values @ 10V calculated from measured forces and maximum theoretical forces of motor current and spindle transmission.

both motors, either individually or in tandem were conducted. First the performance curves of both motors were measured, then the theoretical force without friction from the motor current was calculated and compared to the measured force. The difference is assumed to represent the frictional forces, which are detailed for different modes in Table 4.3. Table 4.4 shows the output forces at stall relative to the maximum theoretical forces derived from the motor current.

Given that friction forces can be partly constant, we expect efficiency to increase at higher loads. Notably, the force conversion efficiency of the spindle shows significant improvement when both mechanisms are engaged.

To analyze the efficiency of our ACLD prototype, the efficiency was computed from data points obtained from the $10\,\mathrm{V}$ steady-state force and speed curve. This efficiency was calculated using the mechanical motor power output, determined by current and motor speed and compared to the output power of the drive, based on measured speed and force.

For comparison, efficiency data for the Harmonic Drive CSF-14-100-2XH-F is included. Since efficiency is influenced by multiple factors, we fixed the temperature at $20\,^{\circ}\mathrm{C}$ and compared varying speeds at a given voltage with the efficiency at different speeds reported by Harmonic Drive. The efficiency of the Harmonic Drive CSF-14-100 (Harmonic Drive, 2019) at room temperature ranges from 70% to 22%, making it comparable to the ACLD's efficiency. A detailed comparison of the efficiency curves for the ACLD and Harmonic Drive is presented in Figure 4.11. As illustrated in the plot, efficiency can be approximated using a constant friction force of 25% of the maximum force, leading to the following formula:

$$\eta_{est} = \frac{F_{out} \cdot v}{F_{in} \cdot v} = \frac{F_{out}}{(F_{out} + 0.25 \cdot F_{max})} \tag{4.5}$$

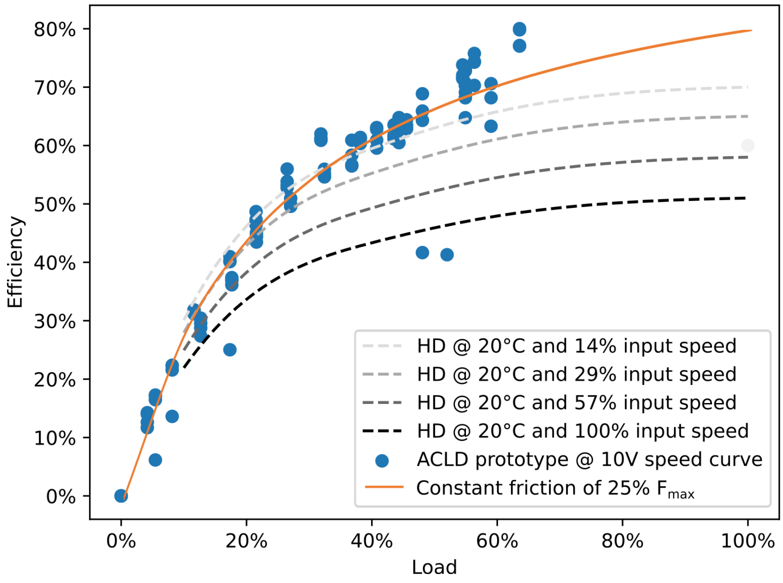

Figure 4.11.: Steady-state efficiencies of the ACLD prototype at 10V compared to the Harmonic Drive CSF-14-100-2XH-F at various speeds and 20°C. Efficiency can be estimated using a constant friction force. *Source:* (**Klas** and Asfour, 2023) © 2023 IEEE

Voltage	Mode	Force efficiency
7.2V	Combined	58.1%
7.2V	Spindle	36.4%
7.2V	Cycloid	78.1%
10V	Combined	60.4%
10V	Spindle	35.6%
10V	Cycloid	93.8%
12V	Combined	60.0%
12V	Spindle	40.0%
12V	Cycloid	97.9%

Table 4.4.: Force efficiency at stall as ratio of measured forces to maximum theoretical forces from motor current and spindle transmission.

Comparison to the state-of-the-art

Harmonic drives represent the state of the art in robotics, both in research and industry, as demonstrated by models such as the Panda (Franka Emika, 2019), UR5 and UR10 (Harmonic Drive, 2016). Therefore, we compare the Adaptive Cycloidal Linear Drive (ACLD) with the Harmonic Drive CSF (Harmonic Drive, 2019) gear units.

Given its compact size, the wrist is one of the most challenging joints in humanoid robots. Thus, we selected a 2 DoF wrist for comparison, which necessitates

Gearbox	CSF-8-100-2XH-F Harmonic Drive (2019)	CSF-14-100-2XH-F Harmonic Drive (2019)	Prototype (lever $50\,\mathrm{mm}$)
Size	$\varnothing 43\,\mathrm{mm}$	$\varnothing 73\,\mathrm{mm}$	$\varnothing 45\,\mathrm{mm}$
Length	$31\,\mathrm{mm}$	$45\,\mathrm{mm}$	$58\,\mathrm{mm}$
Power area[1]	$18\,\mathrm{W}$	$102\,\mathrm{W}$	$108\,\mathrm{W}$
Weight	$100\,\mathrm{g}$	$295\,\mathrm{g}$	$118\,\mathrm{g}$+$3\,\mathrm{g\,cm^{-1}}$
Max. speed	$212\,\mathrm{°\,s^{-1}}$	$212\,\mathrm{°\,s^{-1}}$	$258\,\mathrm{°\,s^{-1}}$
Torque	$5\,\mathrm{N\,m}$	$28\,\mathrm{N\,m}$	$24\,\mathrm{N\,m}$
Gear inertia	$3\,\mathrm{kg\,mm^2}$	$33\,\mathrm{kg\,mm^2}$	①: $4.0\,\mathrm{kg\,mm^2}$ ②: $1.3\,\mathrm{kg\,mm^2}$
Trans. ratio	100	100	①: $209 \cdot R_c$ ②: 209
Example motor	RE 25 Maxon Motor (2024a)	RE 35 Maxon Motor (2024b)	$2 \cdot$ RE 25 Maxon Motor (2024a)
Peak power	$36\,\mathrm{W}$	$204\,\mathrm{W}$	2· $32\,\mathrm{W}$
Rated power	$10\,\mathrm{W}$	$90\,\mathrm{W}$	2· $10\,\mathrm{W}$
Rotor inertia	$1\,\mathrm{kg\,mm^2}$	$7\,\mathrm{kg\,mm^2}$	$1.0\,\mathrm{kg\,mm^2}$
Refl. inertia	$40\,\mathrm{g\,m^2}$	$400\,\mathrm{g\,m^2}$	①:$240\,\mathrm{g\,m^2} \cdot R_c^2$ ②: $80\,\mathrm{g\,m^2}$
1) Limits: $\omega \cdot \tau$, $F \cdot v$	4.8 Nm · 3500 RPM	28Nm · 3500 RPM	480 N · 225 mm/s

Table 4.5.: Comparison of the ACLD with Harmonic Drives.

the tight integration of the motors. It has to perform strong holding and rapid pre-grasp motions. For this analysis, we configured the Harmonic Drives to actuate the joints directly along the joint axis, while the ACLD actuates a 2 DoF joint mechanism with an effective lever arm of $50\,\mathrm{mm}$. Examples of such joint mechanisms can be found in the works of Sofka et al. (2006); Choi et al. (2020); **Klas** and Asfour (2022).

The results of this comparison are summarized in Table 4.5. The term *power area* in the table refers to the product of speed and strength limits, representing the maximum mechanical power required by an actuator with fixed speed and force (or torque) limits to cover the same operational area.

To assess the capabilities of the prototype presented in Table 4.5 in relation to the muscles that actuate the human wrist, we consider the following metrics: maximum torque values range from $3\,\mathrm{N\,m}$ to $20\,\mathrm{N\,m}$ (Yoshii et al., 2015), influenced by individual differences and wrist position, while maximum speeds vary between $2\,\mathrm{rad\,s^{-1}}$ and $7\,\mathrm{rad\,s^{-1}}$ for a typical individual (Flores et al., 2014). The prototype demonstrates a maximum torque of $24\,\mathrm{N\,m}$ and a speed of approximately $9\,\mathrm{rad\,s^{-1}}$, placing its performance at the upper end of the human range. While a robot arm constructed with actuators akin to the prototype would require a diameter of at least $2{\cdot}45\,\mathrm{mm}$, making it thicker than human muscles, it remains suitable for humanoid robots.

Limitations

A key limitation of the proposed mechanism is its reliance on two motors. Although these motors are considerably lighter and smaller compared to a single motor that covers the entire range of speeds and forces (section 4.2), the need for additional control electronics increases cost and occupies more space.

Another constraint is that the system is designed specifically for linear actuation; there is no equivalent rotary solution available yet. Although linear actuation has several advantages, such as simpler force transmission, it also introduces limitations, and the trade-offs must be carefully considered.

Finally, if muscle-like force-speed profiles are not a priority and the goal is to maximize both speed and force, alternative drive mechanisms may offer more suitable performance.

4.4. Summary and Review

In this chapter, ACLD was introduced as a promising solution for applications where muscle-like force-velocity curves are advantageous. A prototype was developed that demonstrated that this innovative linear drive could outperform conventional motor-gearbox combinations in specific scenarios. Data from dynamic experiments suggest that using this drive in humanoid robots could enable human-like agility and power for certain motions. However, further testing is required to assess the durability and explore different sizes and versions of the mechanism.

By adjusting the spindle pitch and the cycloidal transmission, the drive can be tailored to meet the required force-speed curves. Since detailed speed-force data are available only for certain joints, more curves must be derived based on human motion, as in chapter 3. Incorporating a mathematical model into the design process could optimize system performance and provide valuable insight into the switching dynamics of the mechanism.

Various configurations can be considered for different applications, such as on-axis motors, a single motor with a clutch, or multiple displaced drive elements to eliminate the need for sliding bearings. These versions still require prototyping and testing. The next steps include developing prototypes designed for humanoid elbow and shoulder joints, considering the necessary speeds, torques, sizes, and weights.

In summary, this study investigated the potential of the ACLD to replicate the torque-velocity profiles of human muscles. The experimental data showcased its capabilities, highlighting its advantages for applications that require such profiles.

5. Quaternion Joint Based Kinematic Design for Humanoid Arms

Building humanoid robots that exhibit human-like strength, agility, and dynamic range of motion remains one of the great challenges in robotics. Achieving such high-performance characteristics requires not only sophisticated control systems but also innovative kinematic designs that can closely mimic the versatility and robustness of human joints.

In this context, manipulability and singularity are key factors in achieving fluid and efficient robot motion. Manipulability describes the ability of a robotic mechanism to generate motions efficiently in different directions, depending on its configuration. The unit circle of motor speed is mapped to an ellipse in the end-effector velocity space, reflecting the anisotropic motion capabilities of the joint. A singularity-free range of motion ensures that the robot can move smoothly without encountering positions where control becomes unstable or movement is restricted.

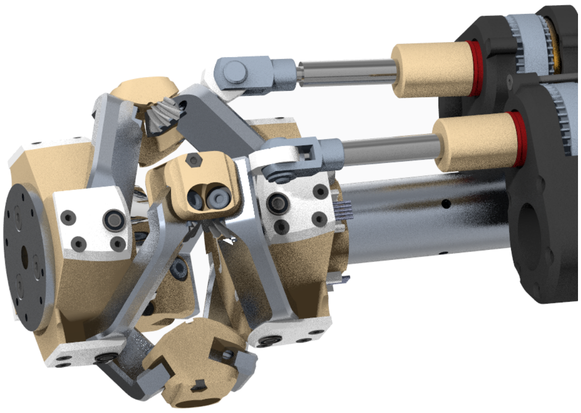

Figure 5.1.: Rendering of the novel singularity free wrist joint mechanism with large range of motion for humanoid robots.*Source:* (**Klas** and Asfour, 2022) © 2022 IEEE

Quaternion Joints (Kim et al., 2018b) are also known as N-UU joints (Shah et al., 2019a; Wu and Carricato, 2017), spherical pure rolling joints (Ghaedrahmati and Gosselin, 2022), or by specific names (Ross-Hime Designs, 2024c; N.T.N. Corporation, 2021). They offer a higher payload-to-mass ratio and improved manipulability over a large, singularity-free range of motion compared to serial robots with roll-pitch arrangements, but are generally limited to wrist joints.

This chapter introduces a novel design of Quaternion Joints (see Figure 5.1) and its application in the shoulder, elbow, and wrist of a 7 DoF humanoid robot arm. The design emphasizes compactness, lightweight construction, and singularity-free motion, providing improved manipulability compared to traditional arrangements.

The innovative mechanical configuration achieves remote actuation using Adaptive Cycloidal Linear Drives (ACLD), reducing the moving weight of the arm and enabling fast and powerful actuation (chapter 4). This leads to improved dynamic performance and low internal inertia in manipulation tasks.

The concept of a Quaternion Joint-based arm explores the kinematics, inverse kinematics, and manipulability of the joints, as well as the mechanical realization of the system. With an emphasis on achieving a human-like range of motion, the joints allow for continuous actuation and torque transmission, thus supporting high payload capacities while maintaining a lightweight arm structure.

The state of the art in Quaternion Joints, focusing on their design and application, can be found in section 2.3.3. The foundations of humanoid robot arm kinematics are presented in section 2.3.4.

This chapter builds upon prior work in the field of humanoid robot design, particularly on the development of a new wrist joint (**Klas** and Asfour, 2022), remote actuation (**Klas** and Asfour, 2023), and the integration of Quaternion Joints into the overall arm design (Ruffler, 2023).

The chapter addresses the following key research efforts:

- Design and evaluation of a novel Quaternion Joint mechanism.
- Development of a 7-DoF arm design utilizing Quaternion Joints in all major joints (shoulder, elbow, wrist). Integration of remote actuation mechanisms (ACLD) to reduce arm weight and improve performance.
- Evaluation of the manipulability and reachability of the Quaternion Joint-based arm in comparison to human-like motion capabilities.

The chapter is structured as follows: First, the fundamental principles of Quaternion Joint design are introduced, highlighting their mechanical properties and advantages over conventional kinematic chains. Next, the design considerations for a humanoid arm with Quaternion Joints are discussed, focusing on anthropometric scaling, payload capacity, and manufacturability. The subsequent section details the mechanical realization, covering kinematics, actuation mechanisms, and the integration of Quaternion Joints into a functional humanoid arm prototype. Finally, an evaluation of the proposed design is presented, assessing its performance in terms of manipulability, reachability, and singularity analysis.

By leveraging Quaternion Joints in a humanoid arm, this work contributes to advancing robotic systems with enhanced dexterity, efficiency, and anthropomorphic motion characteristics.

5.1. Quaternion Joint Mechanism

Given the limitations of existing solutions presented in section 2.3.2, a compact, powerful, and lightweight mechanism is essential for achieving human-like performance in humanoid robots. This section focuses on the wrist joint, which is particularly complex due to its demanding motion range and load requirements, while maintaining a compact design akin to that of human counterparts. The concept behind the arm kinematics discussed later is that the successful design of the wrist joint can be adapted and applied to the other joints in the arm. While the LIMS2 kinematic design is the most similar humanoid wrist, it does not fully align with our requirements due to its lack of compactness, making humanoid segment length challenging. We also aim to avoid a cable winch mechanism with long transmission cables, which introduce backlash and elasticity. The potential for high friction in wired mechanisms with extensive cable routing further motivates this alternative approach.

Two designs are proposed. One design is inspired by the Omniwrist-III (Sofka et al., 2006), featuring four pairs of levers, two of which are actuated to emulate a rolling contact motion. A key challenge is achieving a lightweight humanoid wrist design, as backlash is a significant issue in compact prototypes of the original mechanism, which relies on additional lever pairs over a long kinematic chain to maintain symmetry. The new design achieves symmetry through the use of additional gears, enabling the mechanism to function with just two lever pairs while the remaining two are optimized to improve stiffness and minimize backlash. Moreover, the new mechanism is fully symmetric about the center plane and includes a protective ring. It is realized in the ARMAR-7 wrist.

In the second design, improved stiffness is achieved by doubling the lever pairs and applying slightly different angles to each, instead of incorporating additional gears.

5.1.1. Design Requirements

The primary objectives for our joint design are to achieve an anthropomorphic appearance and human-like performance, with a particular emphasis on high accelerations to facilitate motions that closely resemble those of humans. To work towards this goal, several requirements have been established. Due to actuator weight, the joint accelerations observed in retargeted human motions (section 3.1) cannot be obtained using traditional sequential actuation with actuators aligned along the joint axis. Therefore, to enhance anthropomorphic appearance, the mechanism should be remotely actuated, preferably employing linear actuation. It must also exhibit low mass and low moments of inertia.

The mechanism should provide two rotational degrees of freedom (DoF), with the option to integrate an additional rotation (pronation/supination) to enable a 3 DoF wrist. The design should allow for straightforward cable routing through the intersection point of the axes to minimize cable motion and bending, while also enabling integration of absolute angle and force sensors without disrupting the cable routing.

A range of motion of $90°$ is suitable to compensate for the limited flexibility of robotic hands and is sufficiently large to accommodate future applications in elbow and shoulder joints. Singularity-free and low-backlash motion is crucial for effective robotic operation. Utilizing a constant velocity joint (Machekposhti et al., 2015) would be advantageous to prevent unnecessary segment accelerations, ensuring that the two parts of the mechanism remain untwisted and allow for a seamless, flexible hull. Although achieving high, human-like force and torque is not yet feasible within human dimensions, the design should be capable of performing everyday tasks effectively.

5.1.2. Concept and Kinematics

To meet the outlined requirements, we propose a rolling contact joint kinematic mechanism. This design was chosen primarily for its compatibility with linear actuation, enhanced feed-through capability, and improved manipulability.

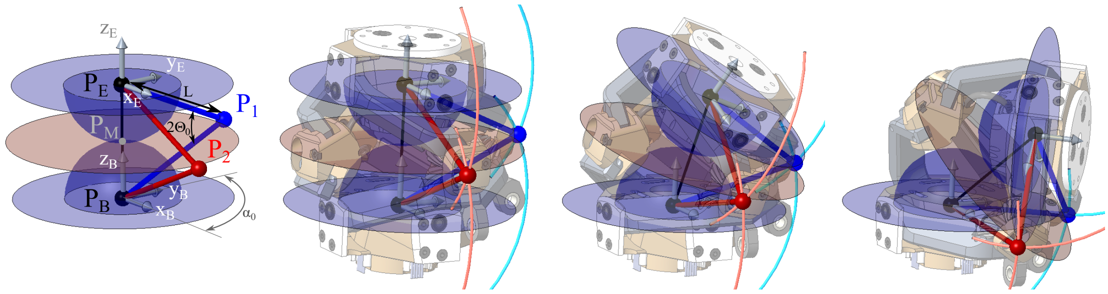

(a) Notations (b) $\Theta_z = 0°$ (c) $\Theta_z = 30°$ (d) $\Theta_z = 90°$

Figure 5.2.: Visualization of wrist kinematics. Θ_z is the zenith angle. *Source:* (**Klas** and Asfour, 2022) © 2022 IEEE

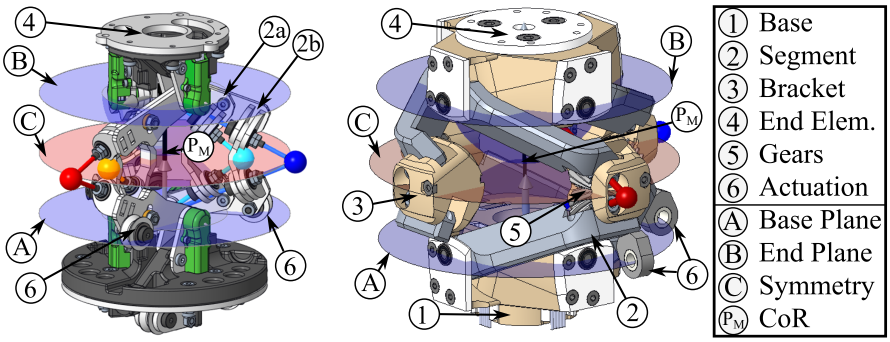

Figure 5.3.: Essential components of the joint mechanism. Variants for the 7 DoF arm (left) and ARMAR-7 wrist (right).

When using a conventional rotational joint with lever actuation, significant space is required, and singularities emerge at $\pm 90°$. In contrast, the rolling contact joint divides the total deviation of $90°$ into two $45°$ angles at P_E and P_B (Figure 5.2d), enabling efficient linear actuation with a larger range of motion. This design also minimizes cable bending and ensures smoother transmission of mechanical energy through the center of the mechanism.

For the rolling contact joint mechanism with additional pronation/supination presented by Kim et al. (2018a), the manipulability is significantly improved compared to conventional roll-pitch-roll or roll-pitch-yaw serial arrangements. This improvement is also applicable to the proposed wrist joint mechanism, as demonstrated in Figure 5.7. Within the mechanical range of motion, the design effectively avoids both serial singularities—where actuators may move while the wrist remains stationary—and parallel singularities, where wrist motion occurs without corresponding actuator movement. Additionally, parallel kinematics offer superior accuracy compared to serial robots, as errors tend to be averaged rather than accumulating across the mechanism, as highlighted by Patel et al. (2012).

The main components of the mechanism include the *Base*, which has the coordinate system x_B, y_B, and z_B at point P_B, and the *End Element*, with its coordinate system x_E, y_E, and z_E at point P_E, serving as the tool center point (TCP) unless a hand with its own TCP is integrated into the wrist. The corresponding z-planes define the *base plane* and the *end plane*.

Actuated segment pairs $\overline{P_B P_1}$ and $\overline{P_1 P_E}$, along with $\overline{P_B P_2}$ and $\overline{P_2 P_E}$, connect the *Base* and *End Element*. Two additional passive segment pairs are incorporated. The kinematic model of the proposed wrist mechanism is illustrated in Figure 5.2, while its essential components are depicted in Figure 5.3.

The mechanism has the following properties:

- The configuration (Figure 5.3) is symmetric with respect to the *middle plane* Ⓒ, where the origin is indicated as Ⓐ and the *end plane* as Ⓑ.
- Points P_1 and P_2 lie on the symmetry plane passing through P_M (Figure 5.2). Point P_1 can move along a circle around P_B with radius L in the y_B-z_B plane of the *Base*, and similarly around P_E in the y_E-z_E plane. For P_2, these planes are rotated by a fixed angle α_0 around the z-axis.
- A fixed angle of $2 \cdot \Theta_0$ exists between each pair of segments.
- The key parameters for describing an instance of this mechanism include segment length L, the angle between segment pairs of the kinematic chain $2 \cdot \Theta_0$, and the angle between the segment rotation axes α_0.

With these properties, the mechanism functions as a rolling contact joint, with the center of rotation (CoR) P_M at the contact point of virtual spheres connected to the base part ① and the end effector (TCP) ④. The rolling contact behavior is maintained by allowing points to move along fixed paths on spheres centered around P_B and P_E, ensuring that P_1 and P_2 always intersect at these paths. The fixed angle Θ_0 establishes a constant distance d between P_E and P_B. Linear actuation of P_1 and P_2 along the z-direction enables control of the position and orientation of the *End Element* in two degrees of freedom (DoF).

Symmetry in the mechanism is achieved through a symmetric structure and gears ⑤ located between the segments. This aspect is not present in the Omniwrist-III mechanism, where the intersection of the segment axes at points P_1 and P_2 relies on the addition of extra segment pairs distributed over a long kinematic chain.

The motion limits of P_E and P_B are implemented through joints connecting the segments to the *Base* and *End Element* on the *base plane* Ⓐ and *end plane* Ⓑ.

The constant angle between segments is maintained by brackets ③ with joints whose axes converge at P_1 and P_2. The point of actuation is re-positioned to ⑥.

Unlike the Omniwrist III design (Sofka et al., 2006), this mechanism operates with only two segment pairs. Additional pairs at varying angles may be incorporated to enhance stiffness and reduce backlash. For the ARMAR-7 wrist joint (kinematics depicted in Figure 5.2 and Figure 5.3), an angle α_0 of $90°$ was selected for both the actuated segments and the two supplementary segment pairs.

The orientation of the TCP ④, represented by the vectors x_E, y_E, and z_E, can be determined from its position by utilizing the symmetry of the structure relative to the middle plane. Specifically, mirroring the x_B and y_B vectors across the middle plane yields the x_E and y_E vectors, while the z_E vector is inverted to maintain a right-handed coordinate system.

The orientation can be expressed in terms of azimuth Θ_A, declination Θ_D, and zenith angle Θ_Z (Figure 5.5). The azimuth angle Θ_A is calculated as $\Theta_A = \operatorname{atan2}(P_{Ex}, P_{Ey})$, aligning the azimuth angle of z_E with the direction of $\overline{P_B P_E}$. The declination angle Θ_D is derived from z_{Ez} using $\Theta_D = \operatorname{asin}(z_{Ez})$, while the zenith angle is given by $\Theta_Z = \pi/2 - \Theta_D$. The distribution of the zenith angle is radially symmetric across the plot of P_{Ex} and P_{Ey}.

For integration into a kinematics solver that accommodates only rotational and translational joints, an equivalent kinematic representation can be utilized:

$$\mathbf{Q} = \mathbf{R}_z(-\Theta_A)\mathbf{R}_x(-\Theta_Z/2)\mathbf{T}_z(d)\mathbf{R}_x(-\Theta_Z/2)\mathbf{R}_z(\Theta_A)$$

Variants

As shown in Figure 5.3, the configuration of the Quaternion Joint design for the 7 DoF arm resembles concept 4 (Figure 5.4f). It is slightly different to the one for the ARMAR-7 wrist (Figure 5.4e): instead of four segment pairs arranged at $\alpha_0 = 90°$, three doubled segment pairs are positioned at $\alpha_0 = 120°$. Unlike the right mechanism in Figure 5.3, where gears are used for coupling, this design employs links. As a result, the segment axes do not naturally intersect at a single point (e.g., P_1), and symmetry is only achieved through the addition of extra segment pair. To enhance stiffness without affecting the motion pattern, each segment pair is doubled with a smaller angle Θ_0. This mechanism is driven by cables instead of rigid rods. The mechanism for the ARMAR-7 neck is a combination with two directly driven double segment pairs in $\alpha_0 = 90°$ arrangement (Figure 5.4d).

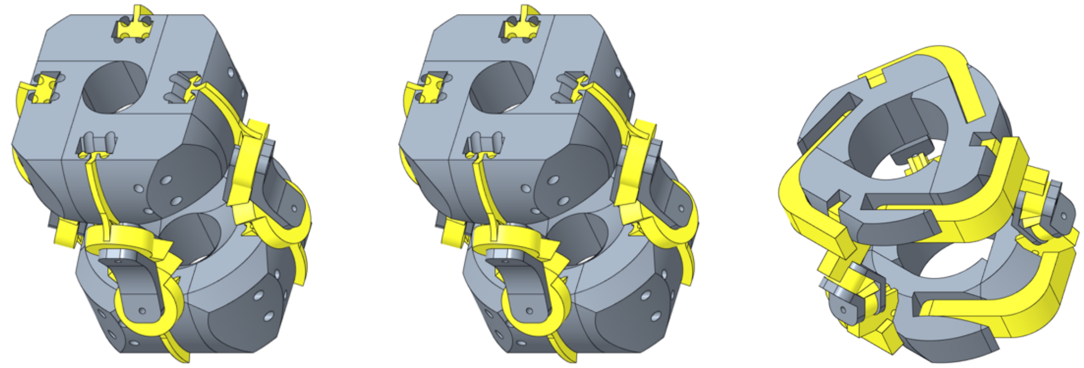

(a) Concept 1. 4 geared segment pairs.

(b) Concept 2: 4 geared segment pairs.

(c) Concept 3: 3 geared segment pairs.

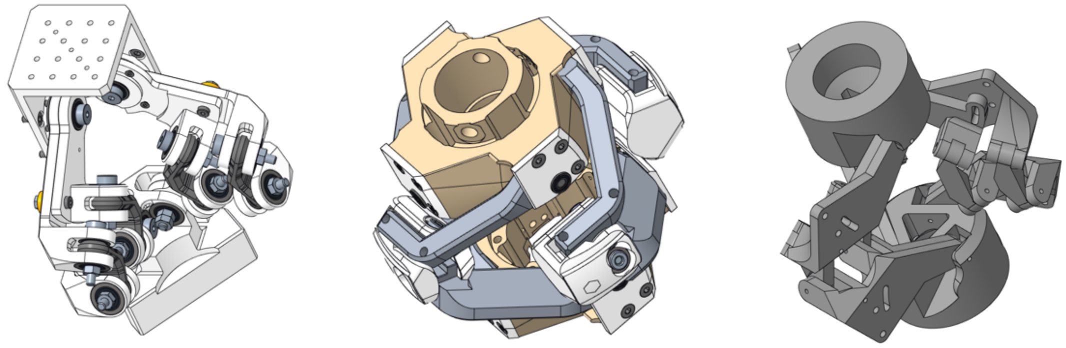

(d) ARMAR-7 neck: 2 double segment pairs.

(e) ARMAR-7 wrist: 4 geared segment pairs.

(f) Concept for 7-DoF Arm: 3 doubled segment pairs.

Figure 5.4.: Overview of developed Quaternion Joint concepts and the kinematics used in ARMAR-7 neck, ARMAR-7 wrist, and the 7-DoF arm concept.

Inverse and Forward Kinematics

In the following section, the forward and inverse kinematics of the wrist mechanism are presented, focusing on the constant angles θ_0 and α_0, which may vary across different mechanical implementations.

The goal of inverse kinematics is to derive the linear actuation **q** (P_{1z}, P_{2z}) from the TCP coordinates (P_{Ex}, P_{Ey}) or the orientation parameters (Θ_A, Θ_Z). The TCP orientation can be computed from its position. In parallel mechanisms, finding the inverse kinematics is generally more straightforward than determining the forward kinematics. The inverse kinematics can be calculated by constructing the middle plane from $P_E/2$ and intersecting it with the motion circles of points P_1 and P_2. The required actuation for a specific position of the end effector is illustrated as orange and blue arrows in Figure 5.6.

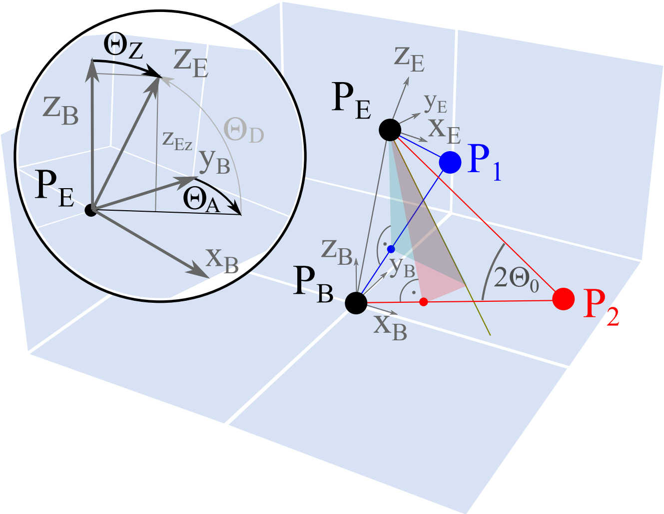

Figure 5.5.: Derivation of the forward kinematics. *End Element* orientation in zenith angle Θ_Z and azimuth angle Θ_A. *Source:* (**Klas** and Asfour, 2022) © 2022 IEEE

For the forward kinematics, which means converting linear actuation $\mathbf{q}$ to TCP coordinates, the intersection of two planes and a sphere at P_E can be utilized (see Figure 5.5).

Manipulability ellipsoids represent the mapping of a unit sphere of joint velocities through the Jacobian matrix, transforming it into an ellipse in the joint velocity space, expressed as $\dot{\mathbf{x}} = J(\mathbf{q}) \cdot \dot{\mathbf{q}}$.

The principal axes of the ellipsoid indicate the directions of highest and lowest speed, while a degenerated (flat) ellipsoid signifies proximity to a singular configuration. The length of an axis serves as the scaling factor between joint and TCP velocities in that direction.

The angular velocity for different end effector orientations of a mechanism that is linearly actuated at ⑥ in the z-direction with $\|\dot{\mathbf{q}}\| = 1$ is shown in Figure 5.7. A discrete set of linear actuation speed combinations, $\dot{\mathbf{q}}$, of the two motors is transferred to different end-effector velocities, $\dot{\mathbf{x}}$, in various directions. The colors encode a unique combination of the two motor speeds. There are multiple ellipsoids for different joint positions. In a continuous plot, this forms ellipsoids that show the transmission between a unit circle of the two motor speeds and the end-effector speed. Joint positions and velocities are represented in an azimuth-zenith plot.

The speed ratio from linear actuation to angular velocity remains relatively constant up to a zenith angle of $75°$. Furthermore, the shape and size of the ellipsoids can be adjusted by varying the angles Θ_0 and α_0, as well as the positions of the actuation points ⑥.

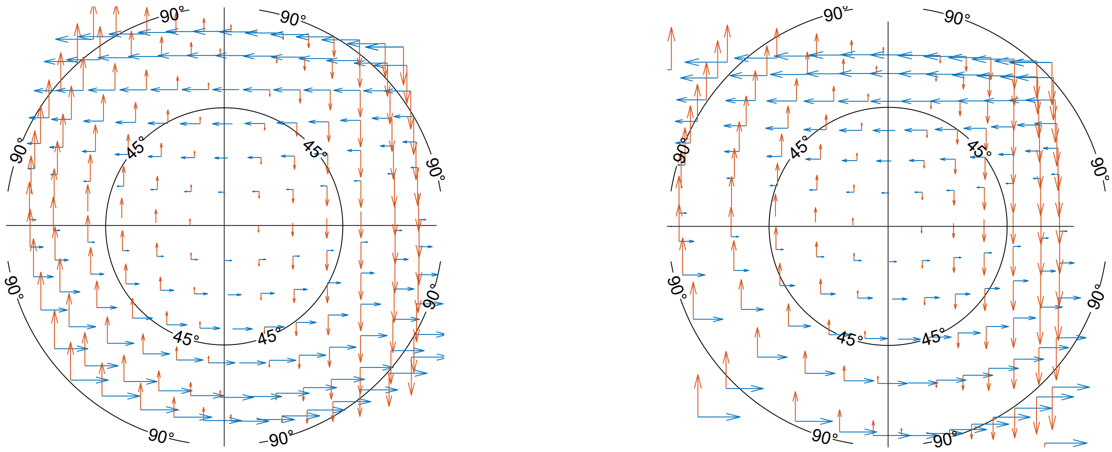

(a) Actuated at ⑥.

(b) Actuated at P_1 and P_2.

Figure 5.6.: Inverse kinematics for linear actuation at different points. The end effector orientation is displayed in an azimuth-zenith plot with circles for the zenith angles of $45°$ and $90°$. The two required actuator motions for the corresponding orientation are plotted as red and blue arrows. *Source:* (**Klas** and Asfour, 2022) © 2022 IEEE

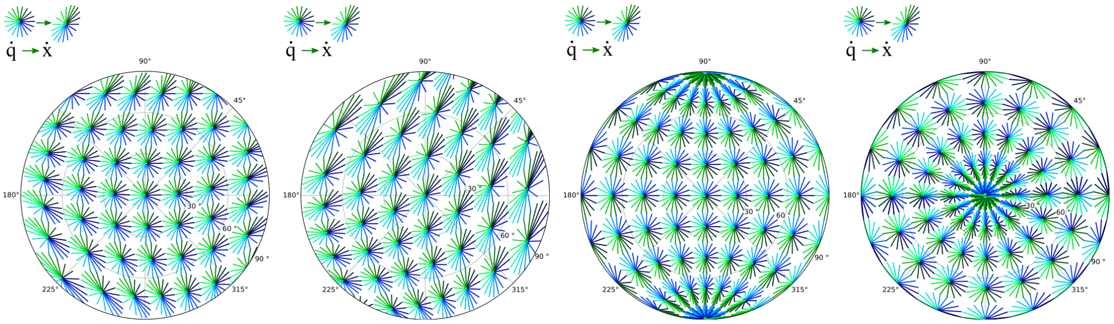

(a) $\alpha_0 = 90°$.

(b) $\alpha_0 = 120°$.

(c) Pitch-Yaw joint.

(d) Roll-Yaw joint.

Figure 5.7.: Manipulability ellipsoids for different 2-DoF joint types. These ellipsoids show the transmission between the two motor speeds and the end-effector speed in different directions. The colors encode a unique combination of the two motor speeds. There are multiple ellipsoids for different joint positions. The end-effector orientation is displayed in an azimuth-zenith plot. Figure 5.7a refers to the ARMAR-7 wrist, Figure 5.7b to a variant. Singularities occur in Pitch-Yaw and Roll-Yaw joints. There are circles for the zenith angles of $30°$, $60°$ and $90°$ as well as radial lines every $45°$ for the azimuth angles. *Source:* (**Klas** and Asfour, 2022) © 2022 IEEE

5.1.3. Realization

A prototype of the wrist mechanism for a humanoid robot arm has been tested, followed by the development of similar versions for the ARMAR-7 wrist and a variant for the neck. For both the prototype and the implementations in the robot, an angle of $\alpha_0 = 90°$ was chosen between the two actuated segment pairs,

Table 5.1.: Mechanical components of the wrist prototype.

Comp.	Description
ⓐ	NEMA17 stepper motor (prototype) 4221BXTH brushless motor (robot)
ⓑ	MXL 012 mini-pitch belt drive
ⓒ	Igus DST-JFRM spindle nut
ⓓ	DST-LS-6P35X5P08-R-ES Spindle
ⓔ	Bearing with encoder magnet
ⓕ	Clevis Joints similar to DIN 71752
ⓖ	Aluminum tube with internal cabling
ⓗ	Protective ring
ⓘ	Jointed motor mount

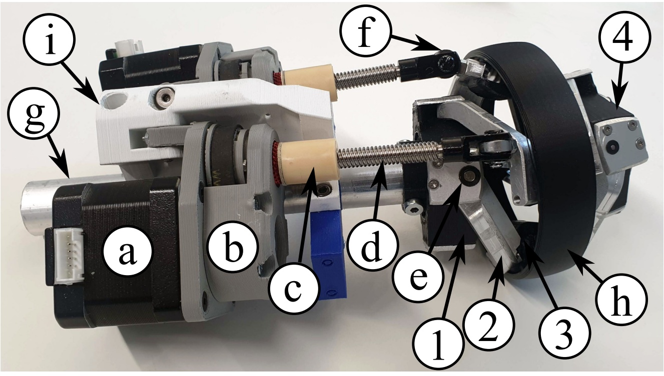

Figure 5.8.: Prototype of the new wrist mechanism. *Source:* (**Klas** and Asfour, 2022) © 2022 IEEE

with two additional segment pairs also positioned at $90°$ to enhance stiffness. In contrast, the design for the 7-DoF arm utilizes an angle of $\alpha_0 = 120°$.

A symmetric design relative to the middle plane (Ⓒ in Figure 5.3) allows for stiffer segments and accommodates bevel gears ⑤. The gears connecting all segment pairs ensure symmetry and prevent skewed axes. The conical shape of the bevel gears enforces the angle of $2 \cdot \Theta_0$.

Virtual points P_1 and P_2 are realized as the intersections of the bracket axes (Figure 5.3, ③) using miniature ball bearings. The 3D-printed brackets move in a circular motion within the middle plane during wrist operation. This design permits the installation of a protective ring (ⓗ in Figure 5.8), which serves as a protective element. The friction generated by the relative movement between the protective ring and the brackets is negligible, as the relative motion is minimal and the connection features a loose fit.

Table 5.2.: Specifications of the complete wrist prototype

Total weight	910 g
Mechanism weight	350 g
Motor weight	2 × 280 g
Wrist diameter	8 cm
Footprint	19 cm × 12 cm
Speed	500 °/s
Payload	5 kg

Figure 5.9.: Realization of the Quaternion Joint mechanism for the wrist and neck joints in the ARMAR-7 robot.

Structure and Actuation

The prototype of the wrist mechanism is shown in Figure 5.8, and the symbols refer to this figure as well as Figure 5.3. In constructing the wrist mechanism, the focus is on achieving a lightweight, cost-effective design with high stiffness. This is accomplished through a combination of 3D-printed and milled parts alongside standard components. The main structure consists of an aluminum tube ⓖ, which facilitates internal cabling connected to the *base part* ①. The segments ② are machined from aluminum and paired with 3D-printed bevel gears ⑤. It is encased by a protective 3D-printed ring ⓗ. 3D-printed brackets ③ connect the four segment pairs. In the prototype, the mechanism utilize plain bearings, while they are substituted with F-682-X2Z miniature ball bearings in the robot.

The joint is actuated by two motors ⓐ, which drive a MXL 012 mini-pitch belt ⓑ, actuating an Igus DST JFRM spindle nut ⓒ. This setup generates linear motion in the Igus DST-LS-6P35X5P08-R-ES spindle ⓓ. The entire actuation system is arranged in parallel axes, utilizing clevis joints similar to DIN 7175 at the actuated segments ⓕ and the motor mounts ⓘ. In the prototype, NEMA17 stepper motors are used, whereas the robot is equipped with 4221BXTH brushless motors (Faulhaber, 2024).

Sensing and Electronics

The mechanism can be outfitted with various sensors for feedback and control. In the prototype, the relative position is determined by counting the steps of the stepper motors. In the robot, all motors are equipped with incremental encoders for precise velocity control. For force measurement, an ATI mini 25 6-axis force-torque sensor can be recessed in the end effector ④, which is crucial for maintaining a compact design and proximity of the hand to the wrist joint center. Additionally, force sensors can be placed at the motor mount. The four base segment joints ⓔ contain magnets for rotary magnetic encoders, and compact, high-speed RLS RM08 sensors designed for harsh environments fit within the base ①.

Space for electronics is allocated beneath the tube on the opposite side of the motors. In the prototype, control of the stepper motors is managed by an Arduino board along with an appropriate CNC shield. The robot forearm features a dedicated motor controller board equipped with ELMO brushless DC controllers. The specifications for the wrist prototype are provided in Table 5.2.

5.1.4. Evaluation of Quaternion Wrist Joint

Evaluation of the Prototype

The design and assembly of the different wrist prototype demonstrated the feasibility of constructing this wrist joint mechanisms. Experiments confirmed that all the necessary cables and power supplies for a humanoid hand could be routed through the center of the joint mechanisms, where the cables experienced a minimal change in length. Further experiments indicated that flexible shafts could also be routed through the joint center. Furthermore, in the ARMAR-7 wrist, a 6-axis force-torque sensor was embedded, along with its cables.

The analytical solutions for both forward and inverse kinematics were validated with numerical results obtained from MATLAB Simulink and successfully implemented in real robot control applications. In the subsequent evaluation, key parameters will be assessed to analyze the proposed design.

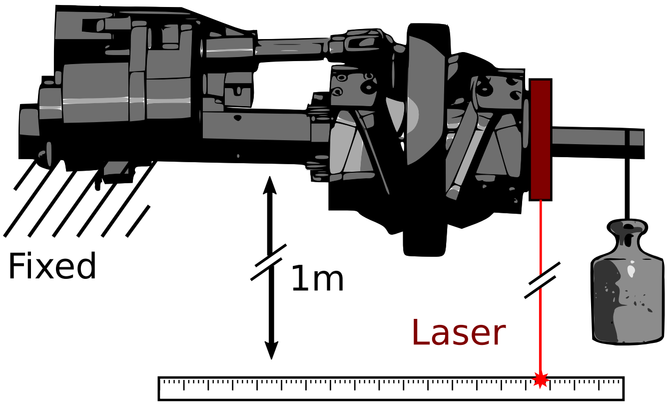

Figure 5.10.: Experimental setup for evaluation experiments. *Source:* (**Klas** and Asfour, 2022) © 2022 IEEE

Experimental Setup For the evaluation experiments, the prototype was securely attached to a table, with a laser pointer affixed to the end effector (EE) as shown in Figure 5.10. When conducting experiments with external loads, various weights were attached at a fixed distance from the joint center. The position of the laser dot was recorded on a distant scale to enhance visibility of small angular changes. Given the significant distance, changes in the EE position can be considered negligible in comparison to the minor angular deflections measured during the experiments. The relative positions of the actuated segments across the full motion range were adjusted via a Python interface connected to the stepper motor controller. For varying loads and motion directions, the entire prototype was rotated while the force and laser remained oriented towards the floor.

Mechanical Evaluation The prototype demonstrates a range of motion with a feed-through for all necessary hand supply cables of $\pm 95^\circ$ for flexion/extension and deviation motions, while motion diagonal to these directions achieves

$\pm 88^\circ$. These values can be further increased by using smaller bearings or slight adjustments to the angle θ_0.

Experimental results show significant improvements in the wrist mechanism compared to an earlier prototype of the same size utilizing the Omniwrist III kinematics, which exhibited an axial backlash of $2.5\,\mathrm{mm}$ and an angular backlash of 7°. In contrast, the new wrist mechanism is free of axial backlash, with a total angular backlash reduced to 1.7°. For the wrist alone, the angular backlash is minimized to 0.6°, with the remaining error primarily arising from the 3D-printed motor-spindle system, suggesting potential for further enhancements in future iterations. This results in an error of approximately $2.9\,\mathrm{mm}$ at the hand center position, with a distance of $100\,\mathrm{mm}$, and $1\,\mathrm{mm}$ for the wrist alone.

The observed reduction in backlash can be attributed to the symmetrical design and the intersection of the lever axes in the Omniwrist III, which relies on additional segment pairs to maintain this symmetry over a long kinematic chain. Achieving a very stiff design for all segments and joints is essential but challenging given the desired weight and size constraints.

Calculations for joint positions near the initial position indicate that in a setup without gears, similar to the Omniwrist III design, the maximum radial bearing torques can rise to 16 times the total joint torque. Conversely, in a geared setup with an assumed equal load distribution across parallel segment pairs, each gear experiences a load of only half the total joint torque, thus reducing the maximum radial bearing torques to 2.5 times the total joint torque.

The elasticity of the prototype was assessed in both orthogonal (torque around x and y) and diagonal orientations. The diagonal stiffness measures $1.3\,\mathrm{Nm/deg}$, while the orthogonal stiffness is $1.4\,\mathrm{Nm/deg}$.

Repeatability tests for achieving the same angle involved 10 consecutive rotations. The resulting angles were derived from the error of a point located $1\,\mathrm{m}$ away, where the translational error remained negligible compared to the rotational error. The average error around the x axis was 0.2°, while around the y axis it was 0.1°. For rotations along a diagonal involving simultaneous actuation of both motors, the error increased to 0.4°, translating to a hand center position error of approximately $0.2\,\mathrm{mm}$ to $0.7\,\mathrm{mm}$. By incorporating absolute encoders in the lever rotation joints, the backlash and elasticity can be effectively measured and compensated. The angular static friction within the joint measures $0.1\,\mathrm{N\,m}$, a favorable value compared to cross roller bearings of a similar size used in serial robots, which typically range from $0.3\,\mathrm{N\,m}$ to $3\,\mathrm{N\,m}$ (THK, 2023), and the LIMS system with friction less than $1\,\mathrm{N\,m}$ (Kim et al., 2018a).

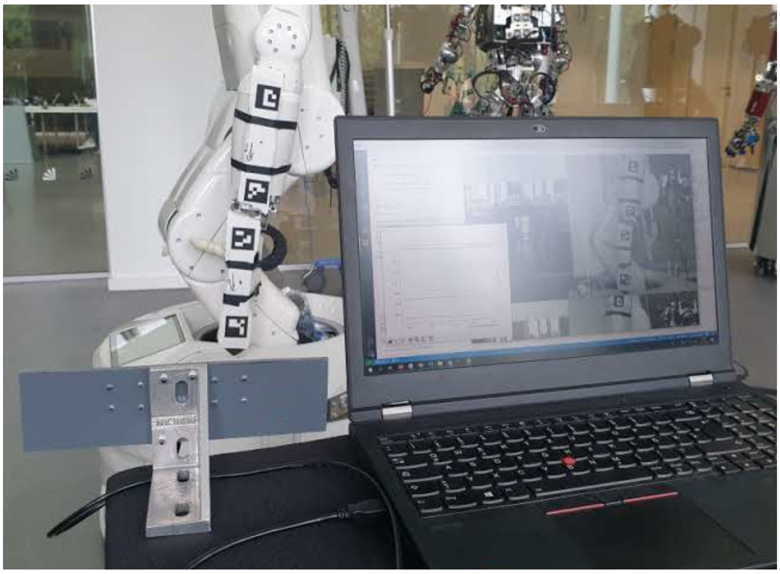

Figure 5.11.: Experimental setup for robot joint evaluation using ArUco markers.

Load experiments were conducted with a weight of 5 kg positioned at the anticipated hand location.

Mechanical Evaluation within the ARMAR-7 Robot

Experimental Setup The experimental setup for evaluating the robot joint mechanisms is illustrated in Figure 5.11. This configuration utilizes ArUco markers for precise tracking of joint positions. Specifically, two markers, designated as M2 and M3, are placed on the forearm, while markers M0 and M1 are positioned on the hand.

A stereo camera system measures the positions of these markers using a Python script, which enables accurate data collection. The stereo information allows for the correction of distances between the markers, which can be difficult to ascertain in a two-dimensional image. The global angle of the line connecting markers M0 and M1 is calculated, along with the global angle of the line between M2 and M3. From these measurements, the relative angle between the forearm and wrist is derived.

The system achieves a relative error in angle measurement of approximately 0.1 degrees; however, this error can increase slightly during camera motion. Figure 5.12 provides insights into the accuracy measurement process employed in this evaluation. Overall, this experimental setup facilitates a comprehensive assessment of the robot joint mechanisms' performance and effectiveness.

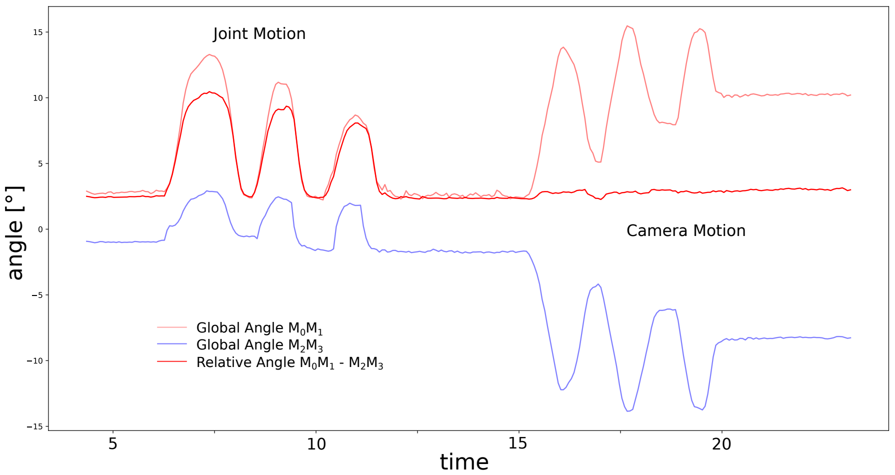

Figure 5.12.: Accuracy meassurement of robot joint evaluation using ArUco markers.

Results The comparison of wrist dimensions across various humanoid robots reveals notable differences in size, which can significantly affect their manipulation capabilities. The ARMAR-DE features a hand distance of 125 mm, with a height of 152 mm and a width of 139 mm, while the ARMAR-6 shows slightly larger dimensions at 138 mm in hand distance, 155 mm in height, and 143 mm in width. In contrast, the ARMAR-7 exhibits much smaller dimensions, with a hand distance of only 40 mm, and both height and width measuring 73 mm. Similarly, the ARMAR-III has a hand distance of 45 mm, with a height of 59 mm and a width of 65 mm. These size variations highlight the design choices made for each robot and their implications for anthropomorphic appearance and functionality in manipulation tasks.

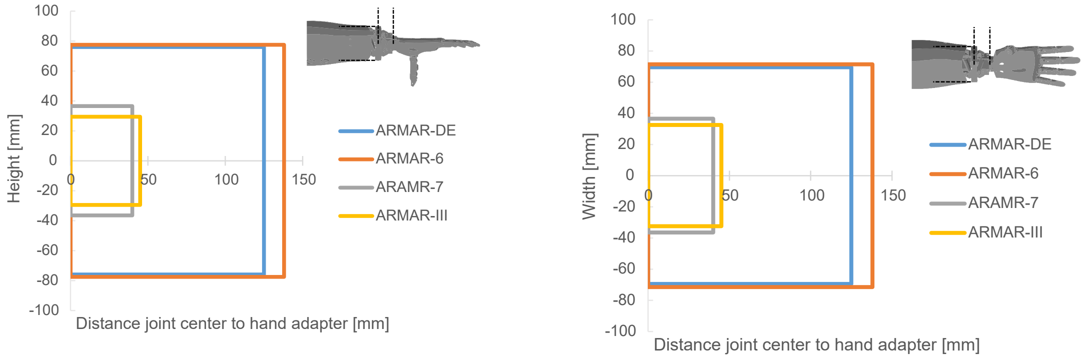

Figure 5.13.: Comparison of wrist sizes for different robots.

The range of motion for various humanoid robot wrists varies significantly. The ARMAR-DE and ARMAR-6 both exhibit a flexion/extension range of 180°, with deviations of 70° and 80°, respectively. The ARMAR-7 and LIMS2 demonstrate a superior range, achieving 180° in both flexion/extension and deviation.

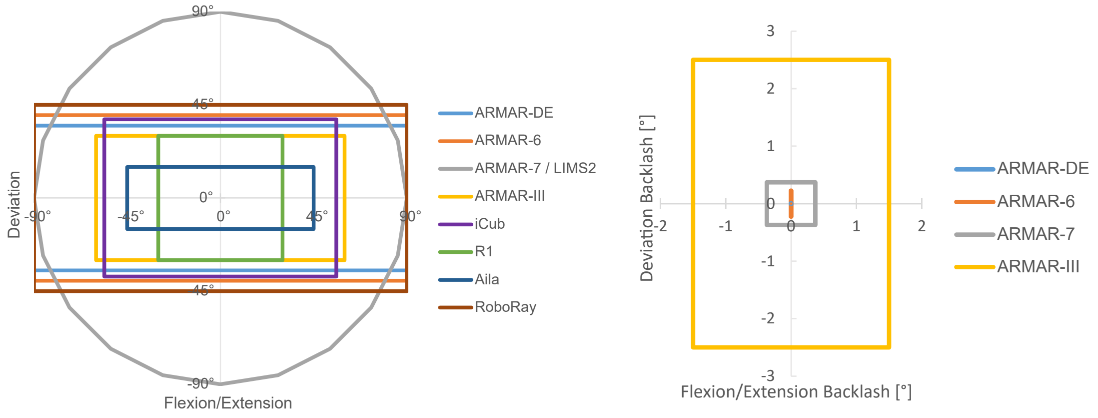

(a) Range of motion

(b) Backlash

Figure 5.14.: Comparison of wrist parameters for different robots.

In contrast, the ARMAR-III offers a more limited motion with $120°$ flexion/extension and $60°$ deviation, while the ARMAR-IIIb has a flexion/extension measurement of $98.66°$ and a deviation of $48.12°$. The iCub shows a flexion/extension of $112°$ and a deviation of $76°$, whereas R1 has equal ranges of $60°$ for both motions. The Aila robot has a flexion/extension of $90°$ and a deviation of $30°$, while RoboRay achieves a flexion/extension of $180°$ with a deviation of $90°$.

The backlash measurements of various wrist mechanisms highlight significant differences in precision. The ARMAR-DE and ARMAR-6 exhibit minimal backlash, with values of $0.01\,\mathrm{mm}$ for flexion/extension, while the ARMAR-6 shows a slightly higher deviation backlash of $0.45\,\mathrm{mm}$. In contrast, the ARMAR-7 presents a backlash of $0.74\,\mathrm{mm}$ in both axes. The ARMAR-III has the highest backlash, with measurements of $3\,\mathrm{mm}$ for flexion/extension and $5\,\mathrm{mm}$ for deviation.

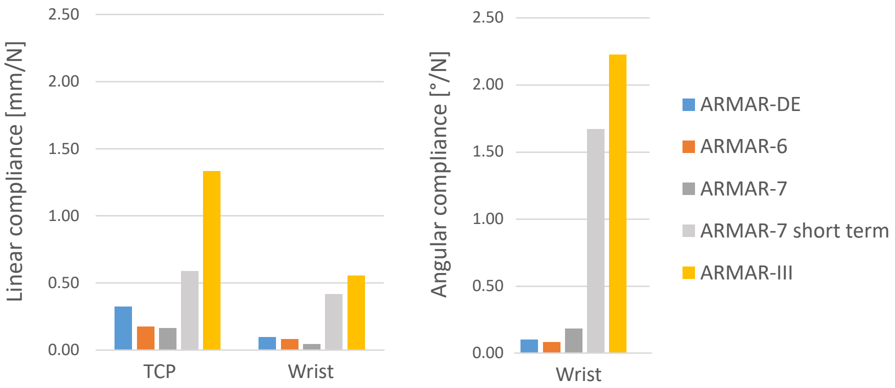

Figure 5.15.: Comparison of wrist compliance for different robots.

The elasticity characteristics of various humanoid robot wrists reveal significant differences in stiffness and compliance. For instance, the ARMAR-DE wrist demonstrates a TCP stiffness of $3.1\,\mathrm{N/mm}$ and wrist stiffness of $10.2\,\mathrm{N/mm}$, with a compliance of $0.32\,\mathrm{mm/N}$ at the TCP. In comparison, the ARMAR-6 shows improved values with a TCP stiffness of $5.7\,\mathrm{N/mm}$ and wrist stiffness of $12.1\,\mathrm{N/mm}$, yielding a TCP compliance of $0.18\,\mathrm{mm/N}$. The ARMAR-7 offers the highest wrist stiffness at $22\,\mathrm{N/mm}$ and the lowest TCP compliance at $0.16\,\mathrm{mm/N}$. Notably, the difference between the ARMAR-7 and the ARMAR-7 short-term measurement, which recorded a TCP compliance of $0.59\,\mathrm{mm/N}$, can be attributed to control adjustments; longer impact times allow for measured deviations to be compensated effectively. In contrast, the ARMAR-III has the lowest stiffness values, with a wrist stiffness of only $1.8\,\mathrm{N/mm}$ and a TCP compliance of $1.33\,\mathrm{mm/N}$.

5.2. Humanoid Arm Design with Quaternion Joints

Achieving human-level performance in humanoid robot arms remains a challenge, which is surprising given the capabilities of electric motors. Modeling the human arm with revolute joints offers advantages, such as reduced complexity and the widespread availability of rotary motors. However, the potential for singularities—such as when two joint axes coincide—adds complexity to actuator control.

The implementation of Quaternion Joints in humanoid robot arms provides benefits, including a large singularity-free range of motion (RoM) and enhanced manipulability across their spherical motion pattern. The results of chapter 3 indicate that a robotic kinematic design utilizing three Quaternion Joints could lead to lower actuation power requirements. Moreover, this approach can facilitate more human-like movement of the robot arm. While human joints are often modeled using revolute joints, this does not accurately replicate the motion dynamics of human joints. Specifically, the shoulder joint involves a composite movement of three joints with a variable center of rotation (CoR) (Amabile et al., 2016), which is typically modeled using three revolute joints with intersecting axes and a fixed CoR. Quaternion Joints, with their motion pattern that resembles two spheres that roll over one another and constantly changing CoR, may more effectively emulate the behavior of human joints. By actuating the arm with the ACLD introduced in chapter 4, it is possible to achieve a fast and powerful performance that mirrors human capabilities. The detailed design of this approach is outlined by Ruffler (2023).

This section focuses on developing a concept for a humanoid robot arm equipped with Quaternion Joints. The objective is to conceptualize the design of a 7-DoF humanoid robot arm that incorporates three 2-DoF Quaternion Joints and one rotational DoF, all actuated by ACLDs. It outlines the requirements and concepts employed in the design of a humanoid robot arm utilizing Quaternion Joints.

5.2.1. Requirements

To the best of the author's knowledge, no humanoid robot arm currently employs Quaternion Joints for the shoulder, elbow, and wrist. This chapter should introduce a novel 7-DoF humanoid arm design with a focus on cost efficiency. If the system proves promising, a prototype can be manufactured for further testing using cost-effective methods. Complex geometries should be 3D printed, while laser-cut aluminum parts should be used to provide structural integrity. Standard bearings and standard components should be used wherever possible to minimize the need for expensive custom parts.

Anthropomorphic Dimensions

For a humanoid robot designed to operate and interact in human environments, its dimensions should closely match those of a human. This ensures that the robot has a comparable workspace and facilitates human-robot interaction. To achieve this, the robot arm is scaled to the 50th percentile of male dimensions based on DIN 33402 (Deutsches Institut für Normung, 2020), corresponding to a height of $1.75\,\mathrm{m}$. The lengths of the arm segments (that is, the distances between the joint centers) are calculated using MMM, with the resulting values shown in Table 5.3.

Table 5.3.: Segment lengths for $1.75\,\mathrm{m}$ body height corresponding to MMM.

Arm Segment	**Scaling Factor**	**Segment Length (mm)**
Center - Clavicular	0.087	152.25
Clavicular - Shoulder	0.023	40.25
Shoulder - Elbow	0.188	329.00
Elbow - Wrist	0.145	253.75

Payload

To effectively manipulate its environment, the arm must be capable of lifting adequate payloads. For use in a domestic setting, a maximum continuous payload of $2\,\mathrm{kg}$ with the arm extended and $4\,\mathrm{kg}$ when flexed is sufficient for daily tasks. Additionally, it should support peak payloads of $4\,\mathrm{kg}$ and $8\,\mathrm{kg}$, respectively, for short-term use.

Quaternion Joint

To compare different joint designs, prototypes were 3D printed and tested. Different variants of the design offer different advantages and disadvantages. Comparing the different physical prototypes, double-segment pair designs proved stiffer than single-segment pairs, and gears are difficult to manufacture. For the cable-driven concept of the 7-DoF arm, we opted for a configuration with three double-segment pairs. Since cables only allow pulling, not pushing, all joint segments must be actuated to ensure the full range of motion. The three-pair design offers a good balance between stiffness and complexity, outperforming the less stiff two-pair configuration while being simpler than the four-pair option.

Actuation

As discussed earlier in this thesis, remote actuation improves the dynamic behavior of the arm. Therefore, the emphasis is on remotely actuating the Quaternion Joints. These joints should be powered by Dyneema cables, a strong and lightweight ultrahigh molecular weight polyethylene fiber (Smith and Lemstra, 1980). To balance dynamic performance with sufficient payload capacity, ACLD should be used for actuation. More details on the ACLD can be found in chapter 4.

5.2.2. Resulting Kinematics

The results of this design study confirm the feasibility of transforming the proposed kinematics into a physical prototype. It is shown in Figure 5.16 as a rendered image of the Quaternion Joint arm. The arm has Quaternion Joints in the shoulder, elbow, and wrist, along with a revolute joint for wrist rotation. The Quaternion Joints are powered by ACLD, while the revolute joint shares the same actuator to minimize costs. For rendering, the KIT Prosthetic Hand (Weiner et al., 2018) is attached to the wrist as the end effector.

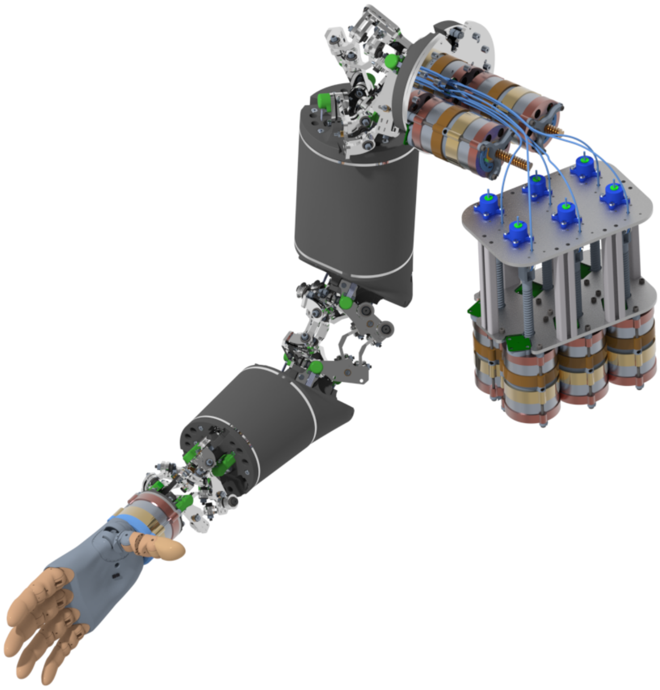

Figure 5.16.: Rendering of the concept for a humanoid robot arm with Quaternion Joints.

The serial kinematics of a robot arm encompasses the joint distances, their orientations, and the implemented joints along with their limits. This robot arm features 7 DoFs, realized through three 2-DoF Quaternion Joints located at the shoulder, elbow, and wrist, in addition to one rotational DoF in the wrist joint.

To visualize the motion patterns of the Quaternion Joints, which are inadequately represented by the conventional cylindrical elements, a new visualization method is employed. The shoulder, elbow, and wrist joints are depicted using two hemispheres, effectively illustrating the rolling contact behavior of Quaternion Joints. This representation aligns with the visualization introduced by **Klas** et al. (2021). Figure 5.17 illustrates the 7 DoFs of a humanoid dual arm system, presented in a neutral arm position, enhancing intuitive understanding.

The joint limits for each joint are summarized in Table 5.4. To represent the joint limits of the Quaternion Joints, they are categorized into roll and pitch. Although the joints do not adhere strictly to these classifications, this notation provides a clear overview of the 7 DoF.

The segment lengths and orientation of the Quaternion Arm joints, depicted in Figure 5.17, can be determined from the position of the neutral joint, as the Quaternion joints exhibit a variable center of rotation (CoR). The segment lengths will be further evaluated in section 5.2.4 and compared against the required lengths based on the anthropomorphic dimensions.

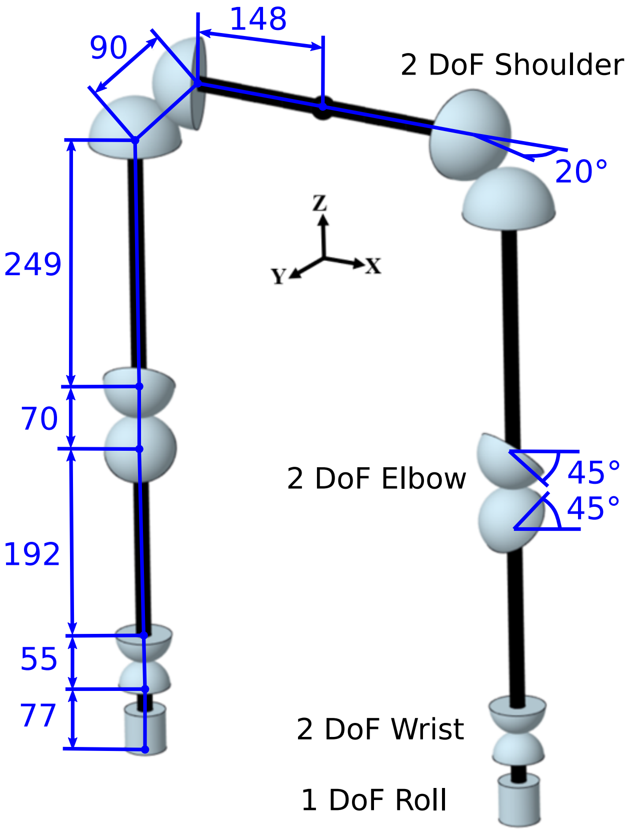

Figure 5.17.: Kinematics of the humanoid dual-arm system. Distances in mm.

Table 5.4.: Joint limits.

Limits	Roll [°]	Pitch [°]	Yaw [°]
Shoulder	±91	±91	-
Elbow	±89	±89	-
Wrist	±87	±87	±180

5.2.3. Resulting Design

The Quaternion Joint arm consists of 2D, 3D, and turned aluminum parts, 3D printed components, standard elements (bearings, screws, fork heads), actuators, and sensors. The assembly includes the actuator setup, shoulder, elbow, and wrist joints, supporting structure, and wrist rotation. The detailed design is based on the work by Ruffler (2023).

Dimensions

Table 5.5.: Quaternion Joint sizes.

Joint	Shoulder	Elbow	Wrist
r [mm]	45.00	35.00	27.50
$\Theta_0 a$ [°]	76	76	76
$\Theta_0 b$ [°]	50	50	50
Aluminum Thickness [mm]	3.5	3.0	2.5

The sizes of the Quaternion Joints are shown in Table 5.5 and Figure 5.18. The shoulder joint, with a rolling sphere radius (r) of $45\,\mathrm{mm}$ and an end-to-pivot distance of $90\,\mathrm{mm}$, is the largest, designed to handle higher loads and offer a wider range of motion. The elbow and wrist joints are progressively smaller, reflecting the smaller need for torque. The consistent angular ranges (Θ_{0a}, Θ_{0b}) ensure uniform motion, while the aluminum thickness decreases from $3.5\,\mathrm{mm}$ at the shoulder to $2.5\,\mathrm{mm}$ at the wrist, providing a balance between strength and weight.

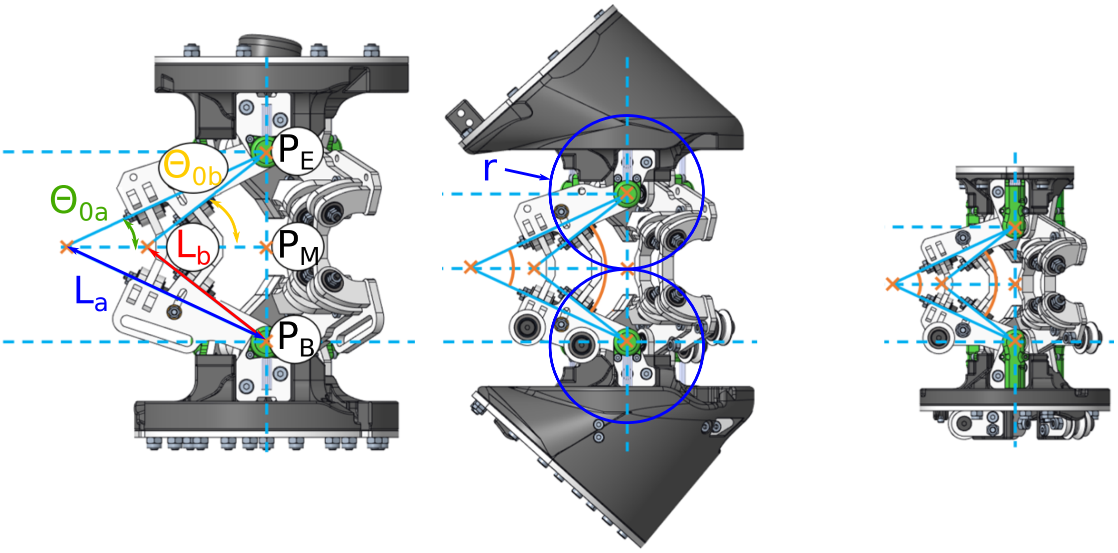

(a) Shoulder joint (b) Elbow joint (c) Wrist joint

Figure 5.18.: Comparison of the shoulder, elbow, and wrist joints of the Quaternion Joint arm.

Actuation

To reduce cable tension, a pulley system was added to the outer segments of the elbow and wrist joints, resulting in reductions of approximately 2.5 for the elbow and 1.5 for the wrist. The cables are routed through the pulley system and secured with a screw and bolt. In the elbow joint, a 3D printed base allows an alternative routing option with only the outer pulley, reducing the ratio to 1.5, which is useful when less spindle travel is needed. Actuation cables and sensor wires are always routed through the center of each joint and arm segment, using pulleys where possible. Tubes with metal links are used for free-form bends.

Elbow and wrist actuators are compactly mounted opposite the body center line to minimize the radius of cable bend, using $1.5\,\mathrm{mm}$ Dyneema cables guided through friction reduced tubes. The shoulder joint is directly actuated by ACLDs, reducing the number of actuators required. All joints share a similar design, differing mainly in the actuation and pulley configurations.

The wrist rotation is achieved using a cycloidal gear drive with a reduction ratio of 6:1, powered by a frameless DC motor, enabling a maximum wrist torque of $9.6\,\mathrm{N\,m}$. It uses the same actuator as the first half of the ACLD to minimize cost and complexity. The end-effector is mounted on the output shaft, secured by a 3D printed housing.

Structure

The supporting structure connecting the joints is made from standard $10\,\mathrm{mm}$ x $20\,\mathrm{mm}$ aluminum profiles, covered by 3D printed housings.

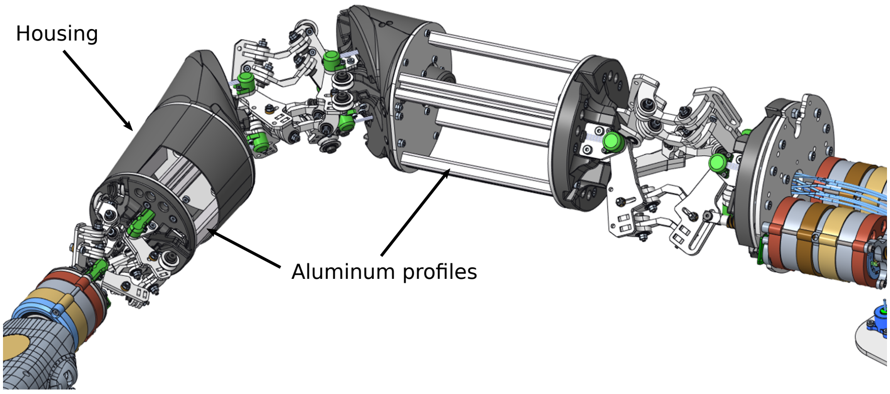

Figure 5.19.: Supporting structure of the arm with aluminum profiles and 3D printed housing.

5.2.4. Evaluation of 7 DoF Arm Kinematics

This section evaluates key aspects of the Quaternion Joint arm: physical properties such as weight and payload, singularities, segment lengths, joint range of motion compared to anthropometric data, dynamic properties, and an analysis of manipulability and reachability.

Mechanical Attributes

Table 5.6.: Summary of weight and maximum actuation force.

	Weight (kg)	**Max. Actuation Force (N)**
Actuator Module	4.6	-
Shoulder	2.9	1361
Shoulder Joint Base	1.8	-
Shoulder Joint	0.8	-
Upper Arm	0.3	-
Elbow	1.2	1255
Elbow Joint	1.0	-
Forearm	0.1	-
Wrist	1.1	604
Wrist Joint	0.4	-
Wrist Rotation	0.3	-
End Effector	0.4	-
Miscellaneous	0.3	-
Total Moving Weight	3.7	
Total Weight	10.1	

The Quaternion Joint arm, including the actuators, weighs 10.1 kg, with moving parts totaling 3.7 kg due to the remote actuation of 6 out of 7 DoFs. A detailed overview of the weight distribution and maximum actuation forces is given in Table 5.6.

Although the overall weight is comparable to the ARMAR-7 arm (10.8 kg) with direct actuator placement, the main difference lies in the weight of the moving parts. In ARMAR-7, most of the components are directly actuated, resulting in a higher moving weight of 9.8 kg. As discussed before, reducing the moving weight is crucial for achieving human-like performance in humanoid robot arms. The moving weight of the Quaternion Joint arm is 2.65 times lower than that of ARMAR-7, making it more efficient for dynamic movements.

It aligns well with other robot arms that use remote actuation. For example, the LIMS2 arm weighs $6.8\,\mathrm{kg}$ in total, with $2.6\,\mathrm{kg}$ in moving parts. The weight reduction in the Quaternion Joint arm is thus comparable to similar systems.

The minimum payload requirements, as defined in section 5.2.1, are $2\,\mathrm{kg}$ at the EE in an extended arm position and $4\,\mathrm{kg}$ in a flexed position. Based on these payloads and the weight distribution shown in Table 5.6, the forces needed to actuate these weights are calculated. The maximum actuation forces for each joint and their respective transmissions are also summarized in the table.

For the shoulder joint, the limiting factor is the maximum force of the actuator, while for the elbow and wrist joints, it is the ultimate load of the cables or the maximum force of the actuator, reduced by the pulley system. The continuous payload limits are determined by the ACLD forces, with a maximum payload of $5\,\mathrm{kg}$ in an extended arm position and $6\,\mathrm{kg}$ in a flexed position. The calculative maximum payload is $12\,\mathrm{kg}$, equally distributed between the two positions of the arm due to the greater force capacity of the shoulder joint compared to the elbow and wrist joints.

Although these values are calculated, they demonstrate the potential of the system. Stronger materials and FEM analysis could validate the actual payload capacity in future versions.

Singularities

Internal singularities, or joint space singularities, occur when two joint axes align, causing the loss of a degree of freedom in the kinematics. For instance, when two axes coincide, the rotation of one causes the same segment orientation as the motion of the other, leaving the other orientation axis unchangeable. These singularities pose control challenges for humanoid robot arms, as they may lead to infinite inverse kinematic solutions and require extremely high joint speeds for small movements. A well-known example is "gimbal lock".

While the Quaternion Joint itself is singularity-free, the arm design still allows the possibility of singularities if the wrist or wrist rotation axes align with the shoulder joint axis. However, because of the geometry of the arm, this is not physically possible. The distance between the shoulder and elbow joints is greater than that between the elbow and wrist, and the range of motion (RoM) of the wrist and elbow joints ensures that their axes cannot coincide. As a result, the Quaternion Joint arm kinematics are singularity-free.

Anthropometric Data

Table 5.7.: Comparison of segment lengths and RoMs for a 1.75 m human.

Category	**Human** (mm)	**Quaternion Joint** (mm)
Center - Shoulder	192.50	193.00
Shoulder - Elbow	329.00	329.00
Elbow - Wrist	253.75	254.00
Elbow - TCP	350.00	426.50

Evaluating segment lengths using scaling factors provides an estimate of how closely the robot arm mirrors human proportions, although it idealizes the complex structure of human joints. Table 5.7 compares the segment lengths of a human with those of the Quaternion Joint arm. The spine-shoulder, shoulder-elbow, and elbow-wrist segments show minimal deviation ($<1\%$), while the elbow-TCP axis differs by about 18%. This is mainly due to the compact human wrist and the simplified wrist design of the Quaternion Joint arm wrist, which places rotation after the Quaternion Joint to reduce complexity.

The range of motion of the shoulder, elbow, and wrist joints is compared to human values from the Thieme Atlas of Anatomy (Schuenke et al., 2020). Although the Quaternion Joint cannot perfectly replicate human shoulder movement due to its simpler 2-DoF design, it exceeds the human RoM in flexion and extension around the horizontal axis as visible in Figure 5.20.

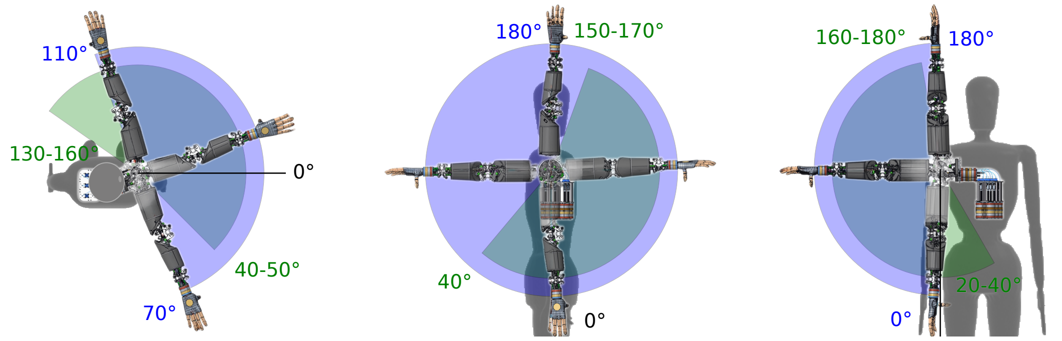

(a) Flexion and extension at 90° abduction

(b) Horizontal flexion and extension

(c) Sagittal abduction and adduction

Figure 5.20.: RoM of the shoulder joint for robot arm (blue) and human (green).

The elbow joint in Figure 5.21 shows a comparable but shifted range for internal and external rotation and a slightly higher range for flexion and extension.

This is achieved through the moving center of rotation (CoR) of the Quaternion Joint, allowing a flexion of 170°, 34° more than the revolute joint design of ARMAR-7.

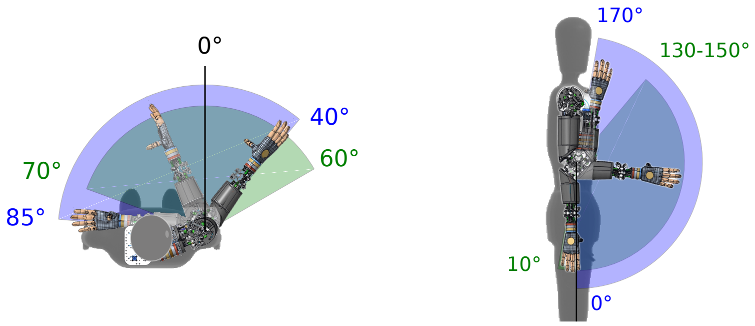

(a) Internal and external rotation (b) Flexion and extension

Figure 5.21.: RoM of the elbow joint for robot arm (blue) and human (green).

Wrist joint movements, visible in Figure 5.22, including radial/ulnar deviation and supination/pronation, generally exceed human range, benefiting from the large range of the Quaternion Joint and the simplicity of electric motor-driven rotation. However, because rigid robotic hands lack the flexibility of human hands, such an extensive range of motion is beneficial.

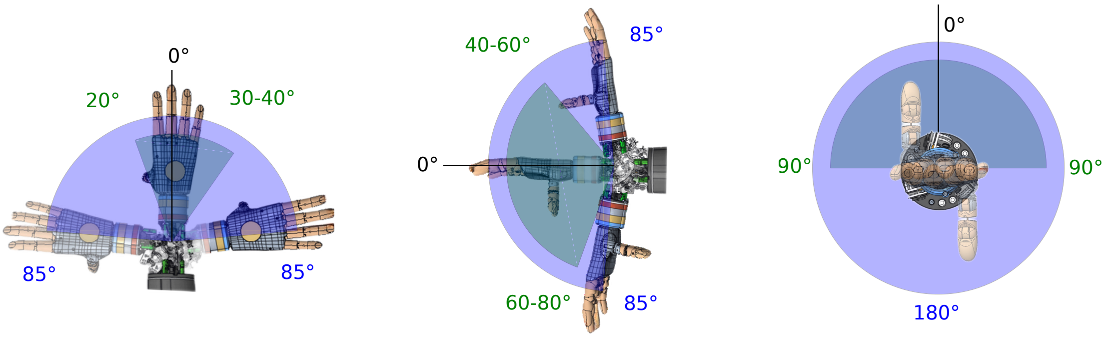

(a) Radial/ulnar deviation (b) Flexion and extension (c) Supination/pronation

Figure 5.22.: RoM of the wrist joint for robot arm (blue) and human (green).

Overall, the Quaternion Joint arm shows little restriction compared to human elbow and wrist joints, with potential shoulder limitations solvable by adding a clavicular joint. This would also benefit the overall kinematics and performance of the arm.

Dynamic Properties

In the following, the joint speeds and the effect of motor inertia at the end effector between the ARMAR-7 and the Quaternion Joint arm are compared. All relevant calculations for this section are provided by Ruffler (2023).

Table 5.8 summarizes the joint speeds for each joint, with two-dimensional Quaternion Joint motions compared to equivalent robot joints for clearer comparison with ARMAR-7 DoFs. Although the Quaternion Joints do not follow strict roll-pitch mechanics, the movement of the Quaternion Arm can mimic a rotation similar to that of the ARMAR-7 arm, as seen in Figures 5.20, 5.21 and 5.22c. For reference, ARMAR-7 achieves wrist yaw through forearm rotation, which differs from the Quaternion Arm implementation.

Table 5.8.: Joint speeds comparison.

Joint	Quaternion Arm (°/s)	ARMAR-7 (°/s)
Shoulder (Sho1/Sho2)	243	206 (Basse, 2021)
Elbow (Sho3/Elb1)	427	330 (Basse, 2021)
Wrist (Roll/Pitch)	441	500 (**Klas** and Asfour, 2022)
Wrist Yaw (Elb2)	3000	287 (Basse, 2021)

Generally, the joint speeds are similar between both arms, except for wrist yaw, where the Quaternion Arm exhibits significantly higher speed due to the lower transmission ratio of the 3D-printed cycloidal gear (i = 6). Future designs may use a higher transmission to decrease speed while increasing torque.

Table 5.9 presents the inertia and the equivalent weight at the end effector. Although joint speeds are comparable, the high inertia of ARMAR-7 SAC units in the shoulder and elbow joints restricts high-speed operations. Due to the high transmission in the ARMAR-7 SAC units, the equivalent weight at the end effector is up to 68.5 times higher than that of the ACLDs, highlighting the benefits of the ACLDs in enhancing agility and speed.

Table 5.9.: Internal inertia and equivalent weight at EE.

Joint	J_{SAC} (kg cm^2)	J_{ACLD} (kg cm^2)	m_{SAC} (kg)	m_{ACLD} (kg)
Shoulder	6400	109	1.12	0.02
Elbow	2500	32	1.37	0.02

Reachability and Manipulability

Analyzing the workspace of humanoid robot arms involves assessing reachability and manipulability using Simox, a robotics toolbox for simulation, motion, and grasp planning. This analysis provides insights into reachable areas with multiple pose redundancies and their maneuverability within those regions. The results are displayed as a heat map, where warm colors (red and orange) signify high reachability or manipulability, while cool colors (blue and turquoise) indicate lower levels. In this section, we compare the kinematics of the Quaternion Joint arm with ARMAR-7, both with 7 and 8 degrees of freedom, alongside human working zones. To facilitate a more accurate comparison, the kinematics of the ARMAR-7 arm are scaled to a body height of $175\,\mathrm{cm}$, matching that of the Quaternion Joint arm.

Humanoid robots are designed to operate in environments designed for human use. Humans exhibit areas of high reachability and manipulability, typically in front of the body, as well as zones of low reachability and manipulability, usually located on the sides, back, or when arms are extended. As a result, workplaces that involve physical labor are often organized into specific working zones (see Figure 5.23). This principle applies not only to factory workstations but also to various aspects of daily life, such as the stove or sink in a kitchen. Therefore, it is beneficial for humanoid robot arms to possess reachability and manipulability profiles similar to those of humans.

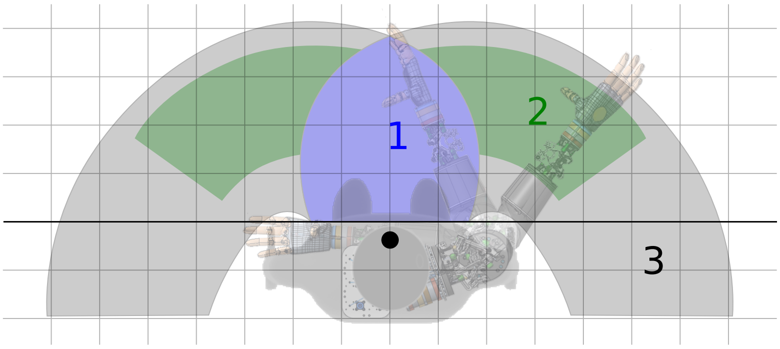

Figure 5.23.: Human working zones based on Schmauder and Spanner-Ulmer (2022) on a $10\,\mathrm{cm}$ grid.

In the reachability analysis, the joint angles are randomly assigned to various positions within their limits. The frequency with which a voxel is reached determines its color, with warmer hues indicating higher frequency, scaled to the maximum. The resulting reachability map serves as a qualitative measure, as the maxima across different analyses may vary. Although these analyses are not directly comparable, reachability maps highlight locations that the arm can access with a high degree of pose redundancy.

The kinematics of the ARMAR-7 arm, equipped with a large number of continuous rotation joints, demonstrate a greater general reachability than that of the Quaternion Joint arm. However, when analyzing the distribution of reachability, the Quaternion Joint arm exhibits a more favorable pattern. While the reachability of ARMAR-7 is predominantly concentrated on the sides of the body, the areas of high reachability of the Quaternion Joint arm are located directly in front of the body. This is particularly evident in the decline between the 8-DoF and 7-DoF versions of the ARMAR-7 arm, underscoring the significant impact of the 8th DoF on reachability.

To qualitatively compare the resulting reachability maps, the maps are superimposed on the working zone graphic. The Simox graphics are scaled to align with the measurements on the axes of the working zone graphic. Figure 5.24 shows the reachability comparisons and illustrates that the quaternion articulated arm, although it covers a smaller area, effectively includes the relevant working areas.

Manipulability, as introduced by Yoshikawa (1985), quantifies the ability of a system to position and orient its end effector. This well-established technique assesses how effectively a system can navigate its workspace, providing insights into the ease of adjustments within that space. Yoshikawa found that the most favorable manipulability postures often resemble those of human arms and fingers. Unlike reachability analysis, manipulability analysis offers a quantitative measure, allowing for direct comparisons across different analyses.

Manipulability, as indicated by the analysis, varies significantly between the kinematics of the Quaternion Joint arm and the ARMAR-7 arm. The Quater-

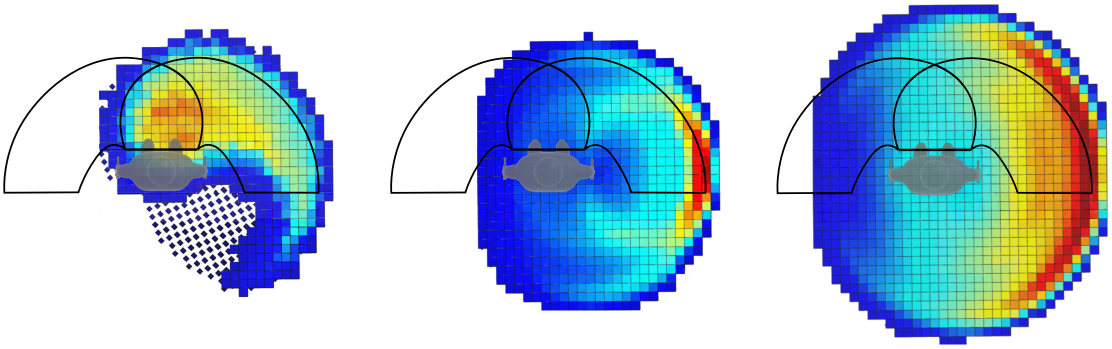
(a) Quaternion Arm (7 DoF) (b) ARMAR-7 (7 DoF) (c) ARMAR-7 (8 DoF)

Figure 5.24.: Reachability compared to human based on working zones.

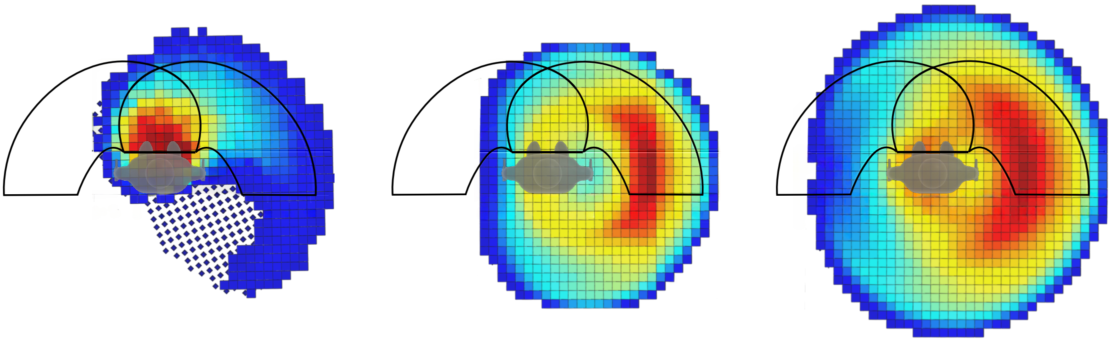

(a) Quaternion Arm (7 DoF) (b) ARMAR-7 (7 DoF) (c) ARMAR-7 (8 DoF)

Figure 5.25.: Manipulability compared to human based on working zones.

nion Joint arm, while covering a smaller area, demonstrates a higher concentration of manipulability in areas directly in front of the body. Conversely, the ARMAR-7 arm manipulability is more dispersed towards the edges of the working zones, making it less suitable for tasks performed in front of the body, particularly with the 7-DoF configuration.

Figure 5.25 illustrates the manipulability comparisons, emphasizing that although the Quaternion Joint arm coverage is smaller, it effectively matches the human working zones. This focus on areas in front of the body suggests that the design of the Quaternion Joint arm is well-suited for various tasks, with its manipulability distribution densely concentrated near the sternum. The addition of a clavicular joint, as discussed previously, could further enhance this manipulability, allowing for a more favorable distribution in the working center.

5.3. Summary and Review

This chapter has two main focuses, both based on quaterion joint mechanics. First, it details the concept, kinematics, mechanical design, and hardware implementation of a compact, lightweight, singularity-free, and cost-effective 2-DoF wrist mechanism tailored for humanoid robot arms. The chapter covers the integration of this wrist mechanism into a fully functional humanoid robot arm for ARMAR-7, the next generation of ARMAR robots. An analytical framework for both forward and inverse kinematics has been established and validated through numerical methods. The experimental evaluations demonstrated that the joint functions effectively, exhibiting satisfactory performance metrics in terms of payload capacity and accuracy. However, the mechanical elasticity of the new joint should be improved if compliance is undesirable. The future development of simpler control methods for these mechanisms would be beneficial.

Second, it presented the development of a new concept for a humanoid robot arm kinematics featuring Quaternion Joints at all three joint centers including the shoulder and elbow in addition to the wrist. The potential for applying this joint design to the humanoid arm was explored covering reachability, manipulability and dynamic properties. Future efforts could focus on optimizing the kinematic parameters of the mechanism and the entire arm to better replicate the characteristics of human motion.

6. Conclusion and Future Work

This thesis aimed to answer the following research question:

> *How can we design humanoid robotic arms with characteristics that closely match human arms in terms of speed, acceleration, and torque?*

To address this, a systematic approach was developed, which can be divided into three main stages:

The first step involved creating a framework for *translating human motion data* into robot design parameters. This system, called the Humanoid Robot Design Assistant, normalized human motion data and applied it to robotic design requirements. Kinematic and dynamic principles were incorporated, forming a basis for comparing various joint mechanisms and selecting those best suited to achieve the target human-like performance metrics.

In the second stage, a novel *linear actuation mechanism* was developed specifically to replicate human force-velocity profiles. This included designing and evaluating the Adaptive Cycloidal Linear Drive (ACLD), a custom actuator intended to balance high-speed motion and substantial force output, mimicking human muscle dynamics. Experimental results showed the ACLD's potential to enable efficient, human-like movement patterns in robotic arms.

Finally, the third stage explored *Quaternion Joint-based kinematic design*. This stage introduced a new kinematic structure for humanoid robotic arms, integrating Quaternion Joints in the shoulder, elbow, and wrist. This design provided benefits in range of motion, singularity-free operation, and allowed for more natural motion patterns, closely resembling human arm movements. Evaluations demonstrated that this kinematic structure significantly improved reachability and manipulability within human-centered workspaces, supporting practical manipulation tasks in front of the body.

In summary, the research presented here contributes a comprehensive framework for designing humanoid robotic arms with characteristics inspired by human motion. The system integrates advanced actuation and kinematics, achieving a high degree of anthropomorphism and dynamic capability in humanoid robotics.

6.1. Scientific Contributions of the Thesis

The presented approach and its evaluation result in the three main scientific contributions of this thesis, which will be summarized in the following.

6.1.1. Humanoid Robot Design Assistant

The first scientific contribution of this thesis is the development of a system for the design of humanoid robots, with a specific focus on achieving human-like performance in robotic arm design. This system integrates both *kinematic* and *actuation* requirements derived from human motion data to guide the design process and enable optimized performance across various robotic tasks.

Key components of this contribution include:

1. **Kinematic Design:** The system evaluates and optimizes different kinematic arrangements based on a predefined set of human-like movements that the robot should be able to perform. The motion is based on normalized data from the KIT Whole-Body Human Motion Database. Through a virtual spring-damper system, human motions are effectively retargeted for robotic design. The robot kinematics are defined by selecting joint mechanisms, their arrangement, position, and orientation, resulting in a set of *Normalized Actuation Requirements*. Kinematics with minimal actuation power requirements can be selected. These normalized requirements serve as inputs for the subsequent actuation phase.
2. **Actuation Requirements and Component Selection:** In the actuation phase, the normalized requirements are scaled to the specific dimensions, weight, and payload of the target robot. This phase includes the selection of actuator types, characteristics, and positions that collectively determine the robot's weight and dynamic capabilities. The system assesses these requirements against the performance specifications of selected actuators and components, calculating an optimized transmission ratio for efficient performance.
3. **Simulation and Validation:** The final design is validated in simulation to ensure that the chosen kinematics and actuation configurations meet the intended performance criteria. This simulation phase verifies that the robot's design aligns with expected motion dynamics and actuation demands, offering insights into potential optimizations or adjustments before physical prototyping.

In summary, this system contributes a comprehensive framework for humanoid robot design, integrating kinematic and actuation selection and optimization based on human motion data. This design approach should enable humanoid robots to achieve efficient, human-inspired performance across a wide range of motion tasks.

6.1.2. Linear Drive Mechanism

The second scientific contribution of this thesis focuses on the development and integration of a **Linear Drive Mechanism** designed to emulate human muscle force-velocity characteristics in humanoid robots. This patented mechanism (**Klas**, 2023), termed the **Adaptive Cycloidal Linear Drive (ACLD)**, represents a novel approach in robotic actuation aimed at addressing limitations in existing drive systems — particularly constraints related to internal inertia and the relationship between size, weight, force, and speed range.

Key aspects of this contribution include:

1. **Human Muscle-Inspired Torque-Velocity Profile:** By emulating the force-velocity characteristics of human muscles, the ACLD enables humanoid robots to achieve more dynamic and adaptable motion profiles that closely align with human muscle behavior, enhancing agility and precision.
2. **Dual Motor and Variable Gear System:** The ACLD incorporates two motors operating with distinct gear ratios, connected through a switchable gearbox mechanism. This setup facilitates a two-segment speed-force profile, enabling seamless adjustment between high-speed, low-force movements and low-speed, high-force outputs as required for various tasks. This adaptability significantly expands the operational range of the mechanism beyond the limits of traditional fixed-gear motors.
3. **Reduction in Peak Mechanical Power Requirements:** The drive configuration reduces peak power demands, allowing the use of smaller, lighter components without compromising performance. This not only optimizes energy efficiency but also contributes to the robot overall weight reduction, thus supporting faster and more efficient movements.
4. **Experimental Validation** The ACLD performance was evaluated in experimental settings, demonstrating its capacity to replicate muscle-like characteristics effectively. This development serves as a scalable solution,

applicable across various robotic platforms requiring human-like actuation performance.

In summary, this linear drive mechanism contributes to the advancement of humanoid robotics by offering a versatile, efficient, and muscle-like actuation option that enhances motion dynamics, aligns with human-inspired force-velocity requirements, and broadens the operational capabilities of humanoid robots.

6.1.3. Quaternion Joint Based Kinematics

The third contribution of this work is the development of a novel kinematic structure for humanoid robotic arms based on **Quaternion Joints**. This includes both the individual Quaternion Joint design, which offers unique advantages for multi-axis movement, and the overall assembly into a 7-DoF arm, termed the Quaternion Joint arm, that closely mimics human joint functionality.

Key elements of this contribution include:

1. **Quaternion Joint Design:** The design of different Quaternion Joint variants, two-degree-of-freedom (2-DoF) joint designs for multi-directional movement. This joint leverages rolling contact mechanics, reducing inertia and allowing a broad range of singularity-free motion. Designed for compactness and light weight, the Quaternion Joint provides a potential foundation for high-performance humanoid arms.
2. **Design and Actuation of the Quaternion Joint Arm:** The complete 7-DoF Quaternion Joint arm consists of three 2-DoF Quaternion Joints and one 1-DoF revolute joint, powered by Adaptive Cycloidal Linear Drives (ACLD). This novel kinematic configuration is designed to achieve human-like proportions, optimize payload capacity, and balance cost-efficiency. The actuation system was developed to support efficient and precise motion in the shoulder, elbow, and wrist joints.
3. **Physical Properties and Performance of the Quaternion Joint Arm:** The designed arm provides a low moving weight of $3.7\,\mathrm{kg}$, can handle continuous loads up to $5\,\mathrm{kg}$, and has a peak load capacity of $12\,\mathrm{kg}$. The arm design aligns closely with human proportions, providing an effective range of motion (RoM) in the elbow and wrist joints. Minor limitations in shoulder joint flexion and extension could be addressed by adding a clavicular joint in future designs.

4. **Reachability and Manipulability Analysis:** The workspace of the Quaternion Joint arm closely matches typical human working zones, supporting effective manipulation tasks within the front workspace. Reachability and manipulability assessments confirm its suitability for human-like reach and payload requirements. Preliminary findings suggest that the Quaternion Joint arm could achieve fluid, human-like movements in a humanoid robotic system.

In summary, this contribution provides a robust framework for human-inspired kinematics in humanoid robots. The individual Quaternion Joint design and the integrated Quaternion Joint arm collectively offer significant advancements in weight, payload capacity, and singularity avoidance.

6.2. Discussion and Future Work

The methodological approach outlined in this thesis and the resulting system represent a first contribution to advancing the development of humanoid robot technology. Given the considerable potential in this emerging field, this work can be seen as a foundation for future research efforts. In the following, we will highlight possible avenues for future research arising from the limitations of our current approach.

6.2.1. System for the Design of Humanoid Robots

In this work, the focus is on the upper body, as it is essential for complex manipulation tasks, and most of the robots are positioned on a platform, reducing the need to address lower-body dynamics. In the future, the system could be extended to the lower body if required, which is more complex due to interaction forces with the environment that are not yet available in the database. For the sake of simplicity, equivalent rotary actuators are currently used in the existing kinematics, but linear actuators could also be added to additional kinematics in the future. Having linear drives already in use in the mobile base demonstrates that simple integration into the existing system is possible.

In summary, the System for the Design of Humanoid Robots represents a valuable step towards designing human-like robotic systems with optimized performance. However, continued development and refinement in areas such as data integration, optimization, simulation accuracy, usability, and modularity will be crucial to fully realize its potential in creating versatile, high-performance humanoid robots.

Linear Drive Mechanism

The Linear Drive Mechanism, particularly the Adaptive Cycloidal Linear Drive (ACLD), was designed to replicate human muscle force-velocity characteristics, providing flexibility and adaptability in humanoid robotic applications. This approach demonstrates significant potential in achieving fluid, human-like motions; however, there are notable areas for improvement to enhance its applicability and integration.

Integration with Existing Robotic Systems of the ACLD requires attention to compatibility with standard robotic joints and structures. Further research could investigate modular interfaces and standardized mounting options to streamline the integration process, making the ACLD more accessible for various humanoid robot architectures. Ensuring compatibility with common robotic control systems is also essential for seamless functionality.

One of the major limitations of the approach is the **inherent complexity** of the dual-motor setup and the associated internal inertia. Although this configuration enables the desired adaptability, it also introduces challenges in terms of mechanical simplicity and maintenance. Reducing the system complexity, potentially by refining the gearbox design or exploring alternate mechanisms with lower inertia, could improve reliability and ease of use.

The **Maintenance Requirements** of the system to ensure optimal performance, especially due to the complexity of its moving parts and the dual-motor configuration have to be assessed. Future designs could focus on increasing durability and reducing maintenance needs, potentially through wear-resistant materials or self-lubricating components. Minimizing maintenance requirements would enhance the practicality in long-term robotic applications.

In summary, the Linear Drive Mechanism offers a flexible and innovative solution for humanoid robotic actuation. However, addressing these limitations in flexibility, integration, power efficiency, and maintenance will be essential to fully leverage its capabilities and expand its application in humanoid robotics.

6.2.2. Quaternion Joint Based Kinematics

The wrist prototype of the Quaternion Joint and its ARMAR-7 implementation serve as a solid foundation, but further developments are essential. Different variants are developed and planned for individual joints in order to improve or control elasticity. Control at the individual joint level is also an ongoing research topic. An improved joint design that focuses on minimized elasticity or incorporates controllable elasticity could greatly enhance precision, robustness, and flexibility in movement. Optimizing joint elasticity would provide greater control over force distribution, particularly for tasks that require delicate human-like adjustments.

The next steps for the Quaternion Joint-based arm include manufacturing, assembling, and thoroughly analyzing a prototype. Most parts are either commercially available or can be 3D printed, and aluminum components can be produced by various manufacturers. Therefore, the production of a first prototype should be feasible in a timely manner. As the control systems of the arm are programmed, tests can assess overall reliability and identify key areas for improvement. The plan for inverse kinematics foresees adaptation of re-targetting based on springs and dampers to real-time motion control.

Future iterations of the prototype can incorporate several improvements. For example, replacing 2D aluminum and standard components with custom, more intricate parts would reduce weight and footprint. Furthermore, employing different types of Quaternion Joints tailored to specific areas would allow for a more compact and anthropomorphic wrist design. Expanding the range of motion of the shoulder through an additional DoF, such as a revolute clavicular joint, could further enhance reachability and manipulability, although this would pose routing challenges for cable actuation.

Given the novelty of this kinematic approach, further simulation and testing are essential, especially to understand joint center-of-rotation errors and to evaluate the effectiveness of ACLD and cable actuation. This concept marks a promising step in humanoid robot arm design, with considerable potential to develop better kinematics for humanoid applications.

Appendix

A. Specifications of Selected Motions

The following Appendixprovides detailed specifications of the selected motions from the KIT Whole Body Human Motion Database (Mandery et al., 2016). These motions were chosen for retargeting onto various robotic kinematic structures, as outlined in chapter 3.

Table 1.: Household (H)

#	586 01	589 01	589 03	944	1235 04
Object	0.3 kg	1 kg	0.5 kg	0.5 kg	0.5 kg
Descr.	Big sponge	Pour	Pour & mix	Put in bowl	Book f. shelf
#	1235 05	1259 46	1269 02	1283 01	1071 70 09
Object	0.5 kg	0.5 kg	0.1 kg	0.1 kg	0.1 kg
Descr.	Book f. shelf	Hand over	Throw left	Throw right	Carry & lift

Table 2.: Entertainment (E)

#	207 05	316 01	636 15	638 16	651 01
Object	0 kg	0 kg	0 kg	0 kg	0 kg
Descr.	Drum	Air guitar	Guitar right	Violin right	Head and sh.
#	995 131 01	1109 94 06	1109 94 07	1258 36	1288 05
Object	0 kg	0 kg	0 kg	0 kg	0 kg
Descr.	M. J. dance	Indian dance	Indian dance	Circular	Left punch

B. Humanoid Robot and Mechanism References

In the sections on actuation systems (section 2.2) and kinematics (section 2.3), different humanoid robots and joint mechanisms are mentioned. In Table 5, the references for humanoid robot arms and joint mechanism data are summarized.

Table 3.: Factory (F)

#	529 01	663 02	1071 7009	1758 1p2501	1758 2p501
Object	0.3 kg	bima. 4 kg	5 kg	bima. 1.25 kg	bima. 2.5 kg
Descr.	Pick&place	Cast box	Suitcase	Manipulate	Manipulate
#	1758 501	1759 1p2501	1759 2p501	1759 501	1759
Object	bima. 5 kg	bima. 1.25 kg	bima. 2.5 kg	bima. 5 kg	bima. 4 kg
Descr.	Manipulate	Manipulate	Manipulate	Manipulate	Manipulate

Table 4.: Conversation (F)

#	323 03	323 03	597 01	597 07	660 01
Object	0.3 kg	bima. 4 kg	5 kg	bima. 1.25 kg	bima. 2.5 kg
Descr.	Point at left	Point at right	Lean over	Lean over	Gestures
#	660 02	1268 01	1268 05	1327 01	634 01
Object	bima. 5 kg	bima. 1.25 kg	bima. 2.5 kg	bima. 5 kg	bima. 4 kg
Descr.	Gestures	Control table	Control table	Wave both	Left wave

Table 5.: References for humanoid robot arm and joint mechanisms data.

Robot	Source
AILA	Lemburg et al. (2011)
Amigo	Willems (2011)
ARMAR-III	Asfour et al. (2006); Albers et al. (2006)
ARMAR-4	Asfour et al. (2013)
ARMAR-6	Asfour et al. (2019)
ARMAR-7	Basse (2021); **Klas** and Asfour (2022)
Blue	Gealy et al. (2019)
Centauro	Klamt et al. (2019)
Ballbot	Shuy and Hollis (2019)
David	Friedl et al. (2011)
DRC-HUBO+	Lim et al. (2017)
HRP-5P	Kaneko et al. (2019)
HRP-4	Kaneko et al. (2011)
High Angle Link	SONE et al. (2023)
i-wrist	N.T.N. Corporation (2021)
iCub	Shah et al. (2019b)
Justin	Ott et al. (2017)
Jaxon	Kojima et al. (2015)
LIMS2	Song et al. (2018)
MMM	Mandery et al. (2016)
Omni-Wrist III (4-UU)	Ross-Hime Designs (2024c); Shah et al. (2019a)
Omni-Wrist V	Ross-Hime Designs (2024a)
Omni-Wrist VI	Ross-Hime Designs (2024b)
Phoenix	Sanctuary AI (2023)
R1	Parmiggiani et al. (2017); Sureshbabu et al. (2017)
RoboRay	Kim et al. (2014); Toedtheide et al. (2021)
Talos	Stasse et al. (2017)
Tocabi	Schwartz et al. (2022)
Tw. One	Iwata and Sugano (2009)
Valkyrie	Radford et al. (2015)
Wabian-2	Ogura et al. (2006)

References used for data in Table 2.3 and Table 2.2.

List of Figures

List of Tables

Acronyms

ACLD Adaptive Cycloidal Linear Drive
AI Artificial Intelligence
AOI Actuator Optimization Index

CAD Computer-Aided Design
CoR Center of Rotation
CT Curved Track Joint

DARPA Defense Advanced Research Projects Agency
DoF Degree of Freedom

EE End Effector
ER Evolutionary Robotics

GUI Graphical User Interface

KIT Karlsruher Institut für Technologie (Karlsruhe Institute of Technology)

MMM Master Motor Map

NASA National Aeronautics and Space Administration

PD Proportional Derivative
PRI Power Requirement Index
PS(2) Parallel Structure with 2 DoF
PS(3) Parallel Structure with 3 DoF

Q(2) Quaternion Joint with 2 DoF

R Revolute Joint
RC Rolling Contact Joint
RoM Range of Motion

SA Sensor Actuator
SAC Sensor Actuator Controller

TCP Tool Center Point

U(2) Universal Joint with 2 DoF

Bibliography

Aberman, K., Li, P., Lischinski, D., Sorkine-Hornung, O., Cohen-Or, D., and Chen, B. (2020). Skeleton-aware networks for deep motion retargeting. *ACM Transactions on Graphics (TOG)*, 39(4):62–1. *Cited on page 24.*

Agrawal, V. P., Gupta, S., and Kohli, V. (1991). Computer aided robot selection: The 'multiple attribute decision making' approach. *International Journal of Production Research*, 29(8):1629–1644. *Cited on page 19.*

Albers, A., Brudniok, S., Ottnad, J., Sauter, C., and Sedchaicharn, K. (2006). Upper body of a new humanoid robot-the design of ARMAR III. In *IEEE/RAS International Conference on Humanoid Robots (Humanoids)*, pages 308–313. *Cited on page 155.*

Albu-Schäffer, A., Haddadin, S., Ott, C., Stemmer, A., Wimböck, T., and Hirzinger, G. (2007). The DLR lightweight robot - design and control concepts for robots in human environments. *Industrial Robot: An International Journal*, 34(5):376–385. *Cited on pages 30 and 32.*

Alcazar, J., Csapo, R., Ara, I., and Alegre, L. M. (2019). On the shape of the force-velocity relationship in skeletal muscles: The linear, the hyperbolic, and the double-hyperbolic. *Frontiers in Physiology*, 10:769. *Cited on pages 27 and 33.*

Alonso-Martin, F., Malfaz, M., Sequeira, J., Gorostiza, J. F., and Salichs, M. A. (2013). A multimodal emotion detection system during human–robot interaction. *Sensors*, 13(11):15549–15581. *Cited on page 12.*

Amabile, C., Bull, A. M. J., and Kedgley, A. E. (2016). The centre of rotation of the shoulder complex and the effect of normalisation. *Journal of Biomechanics*, 49(9):1938–1943. *Cited on page 129.*

Ameri, F. and Dutta, D. (2013). Product lifecycle management: Closing the knowledge loops. *Computer-Aided Design and Applications*, 2:577–590. *Cited on page 10.*

Amici, C., Pellegrini, N., and Tiboni, M. (2020). The robot selection problem for mini-parallel kinematic machines: A task-driven approach to the selection attributes identification. *Micromachines*, 11. *Cited on page 20.*

ANYbotics (2017). *ANYdrive robot joint: Integrated, robust, torque controllable. Cited on page 32.*

Arimoto, S. and Sekimoto, M. (2006). Human-like movements of robotic arms with redundant DOFs: virtual spring-damper hypothesis to tackle the Bernstein problem. In *IEEE International Conference on Robotics and Automation (ICRA)*, pages 1860–1866. ISSN: 1050-4729. *Cited on pages 24 and 53.*

Asfour, T., Regenstein, K., Azad, P., Schroder, J., Bierbaum, A., Vahrenkamp, N., and Dillmann, R. (2006). ARMAR-III: An integrated humanoid platform for sensory-motor control. In *IEEE/RAS International Conference on Humanoid Robots (Humanoids)*, pages 169–175. *Cited on pages 40, 45, 55, 56, and 155.*

Asfour, T., Schill, J., Peters, H., **Klas**, C., Bücker, J., Sander, C., Schulz, S., Kargov, A., Werner, T., and Bartenbach, V. (2013). ARMAR-4: A 63 DOF torque controlled humanoid robot. In *IEEE/RAS International Conference on Humanoid Robots (Humanoids)*, pages 390–396. *Cited on pages 28, 30, 32, 39, 40, 45, 55, 56, 91, and 155.*

Asfour, T., Waechter, M., Kaul, L., Rader, S., Weiner, P., Ottenhaus, S., Grimm, R., Zhou, Y., Grotz, M., and Paus, F. (2019). ARMAR-6: A high-performance humanoid for human-robot collaboration in real-world scenarios. *IEEE Robotics & Automation Magazine*, 26(4):108–121. *Cited on pages 28, 39, 45, 55, 56, 91, and 155.*

Baccelliere, L., Kashiri, N., Muratore, L., Laurenzi, A., Kamedula, M., Margan, A., Cordasco, S., Malzahn, J., and Tsagarakis, N. G. (2017). Development of a human size and strength compliant bi-manual platform for realistic heavy manipulation tasks. In *IEEE/RSJ International Conference on Intelligent Robots and Systems (IROS)*, pages 5594–5601. *Cited on pages 28 and 91.*

Bajaj, N. M., Spiers, A. J., and Dollar, A. M. (2019). State of the art in artificial wrists: a review of prosthetic and robotic wrist design. *IEEE Transactions on Robotics*, 35(1):261–277. *Cited on page 39.*

Basse, P. (2021). Entwicklung eines hochintegrierten Arms für den humanoiden Roboter ARMAR-7. Bachelor's thesis, Karlsruhe Institute of Technology. *Cited on pages 140 and 155.*

Bernstein, N. A. (2014). *Dexterity and its development*. Psychology Press. *Cited on page 23.*

Betts, J. G., Wise, J., Young, K. A., Desaix, P., Johnson, E., Johnson, J. E., Korol, O., Kruse, D., Poe, B., and Womble, M. D. (2017). *Anatomy and Physiology*. XanEdu ; OpenStax College, Rice University, Acton, MA, Houston, Texas. OCLC: 1083766492. *Cited on page 34.*

Bhatia, P., Thirunarayanan, J., and Dave, N. (1998). An expert system-based design of scara robot. *Expert Systems with Applications*, 15(1):99–109. *Cited on page 18.*

Bilancia, P. and Berselli, G. (2020). Design and testing of a monolithic compliant constant force mechanism. *Smart Materials and Structures*, 29(4):044001. *Cited on page 17.*

Bilancia, P. and Berselli, G. (2021). An overview of procedures and tools for designing nonstandard beam-based compliant mechanisms. *Computer-Aided Design*, 134:103001. *Cited on page 17.*

Bongard, J. (2010). The utility of evolving simulated robot morphology increases with task complexity for object manipulation. *Artificial Life*, 16(3):201–223. *Cited on page 16.*

Bongard, J. C. (2013). Evolutionary robotics. *Communications of the ACM*, 56(8):74–83. *Cited on page 26.*

Boone, D. C. and Azen, S. P. (1979). Normal range of motion of joints in male subjects. *JBJS*, 61(5):756–759. *Cited on page 39.*

Boubekri, N., Sahoui, M., and Lakrib, C. (1991). Development of an expert system for industrial robot selection. *Computers & Industrial Engineering*, 20(1):119–127. *Cited on page 20.*

Brand, M. (2015). Rotation-translation gearbox with shiftable transmission. Patent DE102013015257B3, Mathias Brand, March 2015. *Cited on page 35.*

Bredeche, N. and Montanier, J.-M. (2010). Environment-driven embodied evolution in a population of autonomous agents. In *International Conference on Parallel Problem Solving from Nature*, pages 290–299. Springer. *Cited on pages 16 and 26.*

Buchanan, B., Sutherland, G., and Feigenbaum, E. A. (1968). *Heuristic DENDRAL: a Program for Generating Explanatory Hypotheses in Organic Chemistry*. Stanford University Stanford. *Cited on page 11.*

Buchanan, E., Goff, L. L., Li, W., Hart, E., Eiben, A., Carlo, M. D., Winfield, A., Hale, M. F., Woolley, R., Angus, M., Timmis, J., and Tyrrell, A. (2020). Bootstrapping artificial evolution to design robots for autonomous fabrication. *Robotics*, 9:106. *Cited on page 16.*

Buckingham, E. (1914). On physically similar systems; illustrations of the use of dimensional equations. *Physical review*, 4(4):345. *Cited on page 50.*

Campbell, M. I., Cagan, J., and Kotovsky, K. (1999). A-Design: An agent-based approach to conceptual design in a dynamic environment. *Research in Engineering Design*, 11(3):172–192. *Cited on page 22.*

Canaday, B., Zapolsky, S., and Drumwright, E. (2017). Interactive, iterative robot design. In *IEEE International Conference on Robotics and Automation (ICRA)*, pages 1188–1195. *Cited on page 16.*

Chang-Siu, E., Snell, A., McInroe, B. W., Balladarez, X., and Full, R. J. (2022). How to use the Omni-Wrist III for dexterous motion: An exposition of the forward and inverse kinematic relationships. *Mechanism and Machine Theory*, 168:104601. *Cited on page 41.*

Chen, Y., Feng, P., He, B., Lin, Z., and Xie, Y. (2006). Automated conceptual design of mechanisms using improved morphological matrix. *Journal of Mechanical Design*, 128(3):516–526. *Cited on page 20.*

Cheney, N., MacCurdy, R., Clune, J., and Lipson, H. (2014). Unshackling evolution: evolving soft robots with multiple materials and a powerful generative encoding. *ACM SIGEVOlution*, 7(1):11–23. *Cited on pages 16, 17, and 26.*

Chew, M., Issa, G. F., and Shen, S. N. T. (1991). Expert system for robot hand design using graph representation. In *CAD/CAM Robotics and Factories of the Future'90*, pages 466–471. Springer. *Cited on page 19.*

Chiou, S.-J. and Sridhar, K. (1999). Automated conceptual design of mechanisms. *Mechanism and Machine Theory*, 34(3):467–495. *Cited on page 20.*

Choi, K., Kwon, J., Lee, T., Park, C., Pyo, J., Lee, C., Lee, S., Kim, I., Seok, S., Kim, Y.-J., et al. (2020). A hybrid dynamic model for the ambidex tendon-driven manipulator. *Mechatronics*, 69:102398. *Cited on pages 39 and 107.*

Clancey, W. J. (1985). Heuristic classification. *Artificial Intelligence*, 27(3):289–350. *Cited on page 12.*

DARPA (2015). DARPA robotics challenge finals 2015. `https://archive.darpa.mil/roboticschallenge/`. *Cited on page 30.*

Darvish, K., Tirupachuri, Y., Romualdi, G., Rapetti, L., Ferigo, D., Chavez, F. J. A., and Pucci, D. (2019). Whole-body geometric retargeting for humanoid robots. In *IEEE/RAS International Conference on Humanoid Robots (Humanoids)*, pages 679–686. *Cited on page 23.*

Datta, R. and Deb, K. (2011). Optimizing and deciphering design principles of robot gripper configurations using an evolutionary multi-objective optimization method. Technical report, India, Technical report. *Cited on page 17.*

Dermitzakis, K., Carbajal, J. P., and Marden, J. H. (2011). Scaling laws in robotics. *Procedia Computer Science*, 7:250–252. Proceedings of the 2nd European Future Technologies Conference and Exhibition 2011 (FET 11). *Cited on page 27.*

Desai, R., McCann, J., and Coros, S. (2018a). Assembly-aware design of printable electromechanical devices. In *The 31st Annual ACM Symposium on User Interface Software and Technology*, pages 457–472. ACM. *Cited on page 21.*

Desai, R., Safonova, M., Muelling, K., and Coros, S. (2018b). Automatic design of task-specific robotic arms. *arXiv preprint arXiv:1806.07419*. *Cited on page 22.*

Desai, R., Yuan, Y., and Coros, S. (2017). Computational abstractions for interactive design of robotic devices. In *IEEE International Conference on Robotics and Automation (ICRA)*, pages 1196–1203. *Cited on pages 20 and 21.*

Deutsches Institut für Normung (2020). DIN 33402-2: Ergonomie – Körpermaße des Menschen – Teil 2: Werte. Beuth Verlag, Berlin. *Cited on pages 43 and 130.*

Di Fava, A., Bouyarmane, K., Chappellet, K., Ruffaldi, E., and Kheddar, A. (2016). Multi-contact motion retargeting from human to humanoid robot. In *IEEE/RAS International Conference on Humanoid Robots (Humanoids)*, pages 1081–1086. *Cited on page 23.*

Doncieux, S., Bredeche, N., Mouret, J.-B., and Eiben, A. E. (2015). Evolutionary robotics: what, why, and where to. *Frontiers in Robotics and AI*, 2:4. *Cited on page 26.*

El-Nakla, S. (2012). Case-based expert system to support electronics design in mechatronic system. In *Applied Mechanics and Materials*, volume 229, pages 2793–2797. Trans Tech Publ. *Cited on page 19.*

Epple, P., Durst, F., and Delgado, A. (2011). A theoretical derivation of the cordier diagram for turbomachines. *Proceedings of the Institution of Mechanical Engineers, Part C: Journal of Mechanical Engineering Science*, 225:354 – 368. *Cited on page 50.*

Erdman, A. G., Thompson, T., and Riley, D. R. (1986). Type selection of robot and gripper kinematic topology using expert systems. *The International Journal of Robotics Research*, 5(2):183–189. *Cited on page 19.*

Faulhaber (2024). 4221 BX4TH DC-Servomotor. `https://www.faulhaber.com/de/produkte/serie/4221bxth/`. *Cited on pages 31 and 123.*

Feng, S., Whitman, E., Xinjilefu, X., and Atkeson, C. G. (2014). Optimization based full body control for the atlas robot. In *IEEE/RAS International Conference on Humanoid Robots (Humanoids)*, pages 120–127. *Cited on page 39.*

Fickler, H. (1984). Linear drive device with two engines. Patent DD211768A5, East Germany, July 1984. *Cited on page 35.*

Fickler, H. (1985). Linear drive device with two motors. Patent CH647306A5, January 1985. *Cited on page 35.*

Flores, D. C., Laurendeau, S., Teasdale, N., and Simoneau, M. (2014). Quantifying forearm and wrist joint power during unconstrained movements in healthy individuals. *Journal of NeuroEngineering and Rehabilitation*, 11(1):1–7. *Cited on page 107.*

Franka Emika (2019). *Panda Datasheet*. Franka Emika. *Cited on page 106.*

Friedl, W., Höppner, H., Petit, F., and Hirzinger, G. (2011). Wrist and forearm rotation of the DLR hand arm system: Mechanical design, shape analysis and experimental validation. In *IEEE/RSJ International Conference on Intelligent Robots and Systems (IROS)*, pages 1836–1842. *Cited on pages 35, 40, and 155.*

Frutiger, D. R., Bongard, J. C., and Iida, F. (2002). Iterative product engineering: Evolutionary robot design. In *International Conference on Climbing and Walking Robots*, pages 619–629. Professional Engineering Publishing. *Cited on page 16.*

Gadaleta, M., Berselli, G., and Pellicciari, M. (2017). Energy-optimal layout design of robotic work cells: Potential assessment on an industrial case study. *Robotics and Computer-Integrated Manufacturing*, 47:102–111. SI: FAIM 2015. *Cited on page 16.*

Gealy, D. V., McKinley, S., Yi, B., Wu, P., Downey, P. R., Balke, G., Zhao, A., Guo, M., Thomasson, R., Sinclair, A., et al. (2019). Quasi-direct drive for low-cost compliant robotic manipulation. In *IEEE International Conference on Robotics and Automation (ICRA)*, pages 437–443. *Cited on pages 39 and 155.*

Geilinger, M., Poranne, R., Desai, R., Thomaszewski, B., and Coros, S. (2018). Skaterbots: Optimization-based design and motion synthesis for robotic creatures with legs and wheels. *ACM Transactions on Graphics (TOG)*, 37(4):160. *Cited on page 21.*

Ghaedrahmati, R. and Gosselin, C. (2022). Kinematic analysis of a new 2-DOF parallel wrist with a large singularity-free rotational workspace. *Mechanism and Machine Theory*, 175:104942. *Cited on pages 41 and 112.*

Gielniak, M. J., Liu, C. K., and Thomaz, A. L. (2013). Generating human-like motion for robots. *The International Journal of Robotics Research*, 32(11):1275–1301. *Cited on page 27.*

Gosselin, C. and Angeles, J. (1991). A global performance index for the kinematic optimization of robotic manipulators. *Journal of Mechanical Design*, 113(3):220–226. *Cited on pages 15 and 26.*

Gosselin, C. M. and Lavoie, E. (1993). On the kinematic design of spherical three-degree-of- freedom parallel manipulators. *The International Journal of Robotics Research*, 12(4):394–402. *Cited on page 17.*

Grebenstein, M., Albu-Schäffer, A., Bahls, T., Chalon, M., Eiberger, O., Friedl, W., Gruber, R., Haddadin, S., Hagn, U., Haslinger, R., et al. (2011). The DLR hand arm system. In *IEEE International Conference on Robotics and Automation (ICRA)*, pages 3175–3182. *Cited on pages 35, 45, 55, and 56.*

Guizzo, E. (2019). By leaps and bounds: An exclusive look at how boston dynamics is redefining robot agility. *IEEE Spectrum*, 56(12):34–39. *Cited on pages 33 and 91.*

Ha, S., Coros, S., Alspach, A., Bern, J. M., Kim, J., and Yamane, K. (2018). Computational design of robotic devices from high-level motion specifications. *IEEE Transactions on Robotics*, 34(5):1240–1251. *Cited on page 21.*

Harmonic Drive (2016). *Robotic and Automation*. *Cited on pages 32 and 106.*

Harmonic Drive (2019). *Speed Reducers for Precision Motion Control, Reducer Catalog, Gear Units CSF Mini*. *Cited on pages 105, 106, and 107.*

Harmonic Drive (2024). *Harmonic Drive Getriebe Katalog*. *Cited on page 31.*

Hassan, A. and Abomoharam, M. (2017). Modeling and design optimization of a robot gripper mechanism. *Robotics and Computer-Integrated Manufacturing*, 46:94–103. *Cited on page 17.*

HEBI Robotics (2019). *X-Series Actuator - Technical Specifications*. *Cited on page 32.*

HEBI Robotics (2023). *H-Series Actuator - Technical Specifications*. *Cited on page 32.*

Hornby, G. S., Lipson, H., and Pollack, J. B. (2003). Generative representations for the automated design of modular physical robots. *IEEE Transactions on Robotics and Automation*, 19(4):703–719. *Cited on page 16.*

Huang, Z. and Li, Q. C. (2003). Type synthesis of symmetrical lower-mobility parallel mechanisms using the constraint-synthesis method. *The International Journal of Robotics Research*, 22(1):59–79. *Cited on page 19.*

Hunter, I. W. and Lafontaine, S. (1992). A comparison of muscle with artificial actuators. In *Technical Digest IEEE Solid-State Sensor and Actuator Workshop*, pages 178–185. *Cited on pages 28 and 89.*

Hyon, S.-H., Suewaka, D., Torii, Y., and Oku, N. (2016). Design and experimental evaluation of a fast torque-controlled hydraulic humanoid robot. *IEEE/ASME Transactions on Mechatronics*, 22(2):623–634. *Cited on page 33.*

Iwata, H. and Sugano, S. (2009). Design of human symbiotic robot TWENDY-ONE. In *IEEE International Conference on Robotics and Automation (ICRA)*, pages 580–586. *Cited on page 155.*

Jakus, G., Milutinović, V., Omerović, S., and Tomažič, S. (2013). Knowledge representation. In *Concepts, Ontologies, and Knowledge Representation*, pages 47–62. Springer. *Cited on page 12.*

Jamwal, P. K., Xie, S., and Aw, K. C. (2009). Kinematic design optimization of a parallel ankle rehabilitation robot using modified genetic algorithm. *Robotics and Autonomous Systems*, 57(10):1018–1027. *Cited on page 15.*

Jaquier, N., Rozo, L., Caldwell, D. G., and Calinon, S. (2021). Geometry-aware manipulability learning, tracking, and transfer. *The International Journal of Robotics Research*, 40(2-3):624–650. *Cited on pages 16 and 26.*

Jaquier, N., Rozo, L., and Calinon, S. (2020). Analysis and transfer of human movement manipulability in industry-like activities. In *IEEE/RSJ International Conference on Intelligent Robots and Systems (IROS)*, pages 11131–11138. *Cited on pages 23 and 24.*

Jun, B.-H., Lee, P.-M., and Lee, J. (2004). Manipulability analysis of underwater robotic arms on rov and application to task-oriented joint configuration. In *MTS/IEEE Techno-Ocean*, volume 3, pages 1548–1553. *Cited on pages 15 and 26.*

Kaneko, K., Kaminaga, H., Sakaguchi, T., Kajita, S., Morisawa, M., Kumagai, I., and Kanehiro, F. (2019). Humanoid robot HRP-5P: An electrically actuated humanoid robot with high-power and wide-range joints. *IEEE Robotics and Automation Letters*, 4(2):1431–1438. *Cited on pages 28, 39, 91, and 155.*

Kaneko, K., Kanehiro, F., Morisawa, M., Akachi, K., Miyamori, G., Hayashi, A., and Kanehira, N. (2011). Humanoid robot HRP-4 - humanoid robotics platform with lightweight and slim body. *IEEE/RSJ International Conference on Intelligent Robots and Systems (IROS)*, pages 4400–4407. *Cited on pages 45, 55, 56, and 155.*

Kapurch, S. J. (2010). *NASA Systems Engineering Handbook*. Diane Publishing. *Cited on pages 3 and 4.*

Karrenbauer, O., Rader, S., and Asfour, T. (2018). An ontology-based expert system to support the design of humanoid robot components. In *IEEE/RAS International Conference on Humanoid Robots (Humanoids)*, pages 532–539. *Cited on pages 12 and 22.*

Karsak, E. E. (2007). Expert decision system for robot selection. *Wiley Encyclopedia of Computer Science and Engineering*, pages 1–11. *Cited on page 20.*

Kashiri, N., Baccelliere, L., Muratore, L., Laurenzi, A., Ren, Z., Hoffman, E. M., Kamedula, M., Rigano, G. F., Malzahn, J., Cordasco, S., et al. (2019). CENTAURO: A hybrid locomotion and high power resilient manipulation platform. *IEEE Robotics and Automation Letters*, 4(2):1595–1602. *Cited on pages 39, 55, and 56.*

Keller, S., Hausmann, R., Kressner, L., and Koenig, A. (2016). An approach of a computerized planning assistant to the system design of collaborative robot installations. In *IEEE International Conference on Emerging Technologies and Factory Automation (ETFA)*, pages 1–4, [Piscataway, New Jersey]. *Cited on page 20.*

Kim, J. (2006). Task based kinematic design of a two DOF manipulator with a parallelogram five-bar link mechanism. *Mechatronics*, 16(6):323–329. *Cited on page 16.*

Kim, J.-O. and Khosla, K. (1991). Dexterity measures for design and control of manipulators. In *IEEE/RSJ International Conference on Intelligent Robots and Systems (IROS)*, pages 758–763 vol.2. *Cited on pages 15, 25, and 26.*

Kim, J.-O. and Khosla, P. (1993). Design of space shuttle tile servicing robot: an application of task based kinematic design. In *IEEE International Conference on Robotics and Automation (ICRA)*, pages 867–874 vol.3. *Cited on page 19.*

Kim, S., Kim, C., and Park, J. H. (2006). Human-like arm motion generation for humanoid robots using motion capture database. In *2006 IEEE/RSJ International Conference on Intelligent Robots and Systems*, pages 3486–3491. *Cited on pages 27 and 47.*

Kim, T. and Lee, J.-H. (2020). C-3po: Cyclic-three-phase optimization for human-robot motion retargeting based on reinforcement learning. In *IEEE International Conference on Robotics and Automation (ICRA)*, pages 8425–8432. *Cited on page 24.*

Kim, Y.-J., Kim, J.-I., and Jang, W. (2018a). Quaternion joint: Dexterous 3-DOF joint representing quaternion motion for high-speed safe interaction. *IEEE/RSJ International Conference on Intelligent Robots and Systems (IROS)*, pages 935–942. *Cited on pages 39, 40, 115, and 125.*

Kim, Y.-J., Kim, J.-I., and Jang, W. (2018b). Quaternion joint: Dexterous 3-DOF joint representing quaternion motion for high-speed safe interaction. In *IEEE/RSJ International Conference on Intelligent Robots and Systems (IROS)*, pages 935–942. *Cited on pages 41 and 112.*

Kim, Y.-J., Lee, Y., Kim, J., Lee, J.-W., Park, K.-M., Roh, K.-S., and Choi, J.-Y. (2014). Roboray hand: A highly backdrivable robotic hand with sensorless contact force measurements. In *IEEE International Conference on Robotics and Automation (ICRA)*, pages 6712–6718. *Cited on pages 40 and 155.*

Klamt, T., Schwarz, M., Lenz, C., Baccelliere, L., Buongiorno, D., Cichon, T., DiGuardo, A., Droeschel, D., Gabardi, M., Kamedula, M., Kashiri, N., Laurenzi, A., Leonardis, D., Muratore, L., Pavlichenko, D., Periyasamy, A. S., Rodriguez, D., Solazzi, M., Frisoli, A., Gustmann, M., Roßmann, J., Süss, U., Tsagarakis, N. G., and Behnke, S. (2019). Remote mobile manipulation with the CENTAURO robot: Full-body telepresence and autonomous operator assistance. *Journal of Field Robotics*, 37(5):889–919. *Cited on page 155.*

Klas, C. (2023). Linear drive having two reduction stages. Patent WO2023006350A1, Karlsruher Institut für Technologie, February 2023. *Cited on pages 31, 90, and 147.*

Klas, C. and Asfour, T. (2022). A compact, lightweight and singularity-free wrist joint mechanism for humanoid robots. In *IEEE/RSJ International Conference on Intelligent Robots and Systems (IROS)*, pages 457–464. *Cited on pages 38, 40, 56, 107, 111, 112, 115, 119, 120, 121, 124, 140, and 155.*

Klas, C. and Asfour, T. (2023). Reaching torque-velocity profiles of human muscles: The adaptive cycloidal linear drive. *IEEE/ASME Transactions on Mechatronics*, 28(6):3470–3479. *Cited on pages 89, 90, 93, 94, 96, 97, 100, 103, 104, 106, and 112.*

Klas, C., Hundhausen, F., Gao, J., Dreher, C. R., Reither, S., Zhou, Y., and Asfour, T. (2021). The KIT gripper: A multi-functional gripper for disassembly tasks. In *IEEE International Conference on Robotics and Automation (ICRA)*, pages 715–721. *Cited on pages 28 and 132.*

Klas, C., Meixner, A., Ruffler, D., and Asfour, T. (2023). On the actuator requirements for human-like execution of retargeted human motion on humanoid robots. In *IEEE/RAS International Conference on Humanoid Robots (Humanoids)*, pages 1–8. *Cited on pages 19, 24, 27, 46, 47, 49, 51, 52, 54, 55, 60, 66, 80, and 81.*

Kober, K. and Rampp, A. (1998). Multistage spindle drive for converting rotary motion into linear motion. Patent EP0776285B1, Al Ko Kober SE, June 1998. *Cited on page 35.*

Kojima, K., Karasawa, T., Kozuki, T., Kuroiwa, E., et al. (2015). Development of life-sized high-power humanoid robot jaxon for real-world use. In *IEEE/RAS International Conference on Humanoid Robots (Humanoids)*, pages 838–843. *Cited on page 155.*

Komoto, H. and Tomiyama, T. (2012). A framework for computer-aided conceptual design and its application to system architecting of mechatronics products. *Computer-Aided Design*, 44(10):931–946. *Cited on page 19.*

Kossev, V., **Klas**, C., and Asfour, T. (2024). Humanoid robot design assistant - requirements from human motion. In *IEEE/RAS International Conference on Humanoid Robots (Humanoids)*, pages 425–432. *Cited on pages 46 and 61.*

Laugis, J. and Vodovozov, V. (2008). Expert system for electric drive design. In *IEEE International Power Electronics and Motion Control Conference*, pages 1017–1019. *Cited on page 22.*

Lemburg, J., de Gea Fernández, J., Eich, M., Mronga, D., Kampmann, P., Vogt, A., Aggarwal, A., Shi, Y., and Kirchner, F. (2011). AILA - design of an autonomous mobile dual-arm robot. In *IEEE International Conference on Robotics and Automation (ICRA)*, pages 5147–5153. *Cited on pages 40 and 155.*

Li, W., Li, Y., Wang, J., and Liu, X. (2010). The process model to aid innovation of products conceptual design. *Expert Systems with Applications*, 37(5):3574–3587. *Cited on page 19.*

Liarokapis, M. V., Artemiadis, P., Bechlioulis, C. P., and Kyriakopoulos, K. J. (2013). Directions, methods and metrics for mapping human to robot motion with functional anthropomorphism: A review. *School of Mechanical Engineering, National Technical University of Athens, Tech. Rep*. *Cited on page 27.*

Lim, J., Chang, H. J., and Choi, J. Y. (2019). PMnet: Learning of disentangled pose and movement for unsupervised motion retargeting. In *BMVC*, volume 2, page 7. *Cited on page 24.*

Lim, J., Lee, I., Shim, I., et al. (2017). Robot system of DRC-HUBO+ and control strategy of team KAIST in DARPA robotics challenge finals. *Journal of Field Robotics*, 34(4):802–829. *Cited on page 155.*

Lipson, H. and Pollack, J. B. (2000). Automatic design and manufacture of robotic lifeforms. *Nature*, 406(6799):974–978. *Cited on pages 16 and 26.*

Loushin, S. R., Kakar, S., Tetzloff, S. U., Lubbers, P., Ellenbecker, T. S., and Kaufman, K. R. (2022). Upper extremity kinematics and electromyographic activity in uninjured tennis players. *Applied Sciences*, 12(9):4638. *Cited on page 103.*

Maaroof, O. W., Dede, M. İ. C., and Aydin, L. (2021). A robot arm design optimization method by using a kinematic redundancy resolution technique. *Robotics*, 11(1):1. *Cited on page 15.*

Machekposhti, D. F., Tolou, N., and Herder, J. (2015). A fully compliant constant velocity universal joint. In *International Design Engineering Technical Conferences and Computers and Information in Engineering Conference*, volume 57120, page V05AT08A014. American Society of Mechanical Engineers. *Cited on page 114.*

Mandery, C., Terlemez, Ö., Do, M., Vahrenkamp, N., and Asfour, T. (2015). The KIT whole-body human motion database. In *IEEE International Conference on Advanced Robotics (ICAR)*, pages 329–336. *Cited on pages 5, 48, 56, and 74.*

Mandery, C., Terlemez, O., Do, M., Vahrenkamp, N., and Asfour, T. (2016). Unifying representations and large-scale whole-body motion databases for studying human motion. *IEEE Transactions on Robotics*, 32(4):796–809. *Cited on pages 36, 37, 51, 56, 153, and 155.*

Matsuki, H., Nagano, K., and Fujimoto, Y. (2019). Bilateral drive gear—a highly backdrivable reduction gearbox for robotic actuators. *IEEE/ASME Transactions on Mechatronics*, 24(6):2661–2673. *Cited on pages 28, 29, and 90.*

Maxon Motor (2024a). RE25 DC-Motor Ø25 mm, Graphite brushes, 20 Watt. `https://www.maxongroup.de/maxon/view/product/motor/dcmotor/re/re25/118748`. *Cited on pages 31 and 107.*

Maxon Motor (2024b). RE35 DC-Motor Ø35 mm, Graphite brushes, 90 Watt. `https://www.maxongroup.de/maxon/view/product/motor/dcmotor/re/re35/273755`. *Cited on page 107.*

Mayorga, R. V., Carrera, J., and Oritz, M. M. (2005). A kinematics performance index based on the rate of change of a standard isotropy condition for robot design optimization. *Robotics and Autonomous Systems*, 53(3-4):153–163. *Cited on page 15.*

Megaro, V., Thomaszewski, B., Nitti, M., Hilliges, O., Gross, M., and Coros, S. (2015). Interactive design of 3d-printable robotic creatures. *ACM Transactions on Graphics (TOG)*, 34(6):216. *Cited on page 20.*

Mehta, A., DelPreto, J., and Rus, D. (2015). Integrated codesign of printable robots. *Journal of Mechanisms and Robotics*, 7(2):021015. *Cited on page 21.*

Meixner, A., Hazard, C., and Pollard, N. (2019). Automated design of simple and robust manipulators for dexterous in-hand manipulation tasks using evolutionary strategies. In *IEEE/RAS International Conference on Humanoid Robots (Humanoids)*, pages 281–288. *Cited on pages 16 and 26.*

Merlet, J.-P., Gosselin, C., and Huang, T. (2016). Parallel mechanisms. In *Springer handbook of robotics*, pages 443–462. Springer. *Cited on page 40.*

Minbuta, H. and Sotome, M. (2008). Load-sensitive drive power transmission device. Patent DE102007059457A1, SMC Corp, June 2008. *Cited on page 35.*

Myung, S. and Han, S. (2001). Knowledge-based parametric design of mechanical products based on configuration design method. *Expert Systems with Applications*, 21(2):99–107. *Cited on page 18.*

Negrello, F., Garabini, M., Catalano, M. G., Malzahn, J., Caldwell, D. G., Bicchi, A., and Tsagarakis, N. G. (2015). A modular compliant actuator for emerging high performance and fall-resilient humanoids. In *IEEE/RAS International Conference on Humanoid Robots (Humanoids)*, pages 414–420. *Cited on pages 30 and 32.*

Newport (2022). *HexGen HEX500-350HL Datasheet*. *Cited on page 40.*

N.T.N. Corporation (2021). Technical review no.88: Application examples and function improvements of the wrist joint module "i-wrist™". *Cited on pages 41, 112, and 155.*

Ogura, Y., Aikawa, H., Shimomura, K., Kondo, H., et al. (2006). Development of a new humanoid robot WABIAN-2. In *IEEE International Conference on Robotics and Automation (ICRA)*, pages 76–81. *Cited on page 155.*

Olier, E. (1985). Conceptual design for space robots using expert systems. *IFAC Proceedings Volumes*, 18(16):145–150. *Cited on page 18.*

Ott, C., Roa Garzon, M. A., Schmidt, F., Friedl, W., Englsberger, J., Burger, R., Werner, A., Dietrich, A., Leidner, D., Henze, B., et al. (2017). Mechanisms and design of DLR humanoid robots. *Humanoid Robotics: A Reference*, pages 1–26. *Cited on pages 45, 55, 56, and 155.*

O'Neill, M. C., Umberger, B. R., Holowka, N. B., Larson, S. G., and Reiser, P. J. (2017). Chimpanzee super strength and human skeletal muscle evolution. *Proceedings of the National Academy of Sciences*, 114(28):7343–7348. *Cited on page 32.*

Parmiggiani, A., Fiorio, L., Scalzo, A., Sureshbabu, A. V., Randazzo, M., Maggiali, M., Pattacini, U., Lehmann, H., Tikhanoff, V., Domenichelli, D., et al. (2017). The design and validation of the R1 personal humanoid. In *IEEE/RSJ International Conference on Intelligent Robots and Systems (IROS)*, pages 674–680. *Cited on page 155.*

Pasch, K. A. and Seering, W. P. (1984). On the drive systems for high-performance machines. *Journal of Mechanisms, Transmissions, and Automation in Design*, 106(1):102–108. *Cited on page 18.*

Patel, Y., George, P., et al. (2012). Parallel manipulators applications—a survey. *Modern Mechanical Engineering*, 2(03):57. *Cited on page 115.*

Pham, D. T. and Tacgin, E. (1991). DBGRIP: A learning expert system for detailed selection of robot grippers. *The International Journal of Production Research*, 29(8):1549–1563. *Cited on page 20.*

Powell, M. J. D. (1964). An efficient method for finding the minimum of a function of several variables without calculating derivatives. *The Computer Journal*, 7(2):155–162. *Cited on page 71.*

Rader, S., Kaul, L., Weiner, P., and Asfour, T. (2017). Highly integrated sensor-actuator-controller units for modular robot design. In *IEEE International Conference on Advanced Intelligent Mechatronics (AIM)*, pages 1160–1166. *Cited on pages 28, 29, 30, and 39.*

Radford, N. A., Strawser, P., Hambuchen, K., Mehling, J. S., Verdeyen, W. K., Donnan, A. S., Holley, J., Sanchez, J., Nguyen, V., Bridgwater, L., et al. (2015). Valkyrie: NASA's first bipedal humanoid robot. *Journal of Field Robotics*, 32(3):397–419. *Cited on pages 30, 32, 45, 55, 56, and 155.*

Rai, L., Lee, B.-H., Hong, J., and Hahn, H. (2009). Intelligent gesture generation in humanoid robot using multi-component synchronization and coordination. *ICROS-SICE International Joint Conference*, pages 1388–1392. *Cited on page 12.*

Rakita, D., Mutlu, B., and Gleicher, M. (2017). A motion retargeting method for effective mimicry-based teleoperation of robot arms. In *ACM/IEEE International Conference on Human-Robot Interaction (HRI)*, pages 361–370. *Cited on page 23.*

Ramos, F., Vázquez, A. S., Fernández, R., Olivares-Alarcos, A., Schlenoff, C., Balakirsky, S., and Christensen, H. (2018). Ontology based design, control and programming of modular robots. *Integrated Computer-Aided Engineering*, 25(2):173–192. *Cited on page 21.*

RC4WD (2022). RC4WD 540 crawler brushed motor 55t. `https://tamico.de/RC4WD-540-Crawler-Brushed-Motor-55T`. Accessed: 2022-12-15. *Cited on page 99.*

Renner, G. and Ekárt, A. (2003). Genetic algorithms in computer aided design. *Computer-Aided Design*, 35(8):709–726. *Cited on page 17.*

Rijckaert, M., Debroey, V., and Bogaerts, W. (1988). Expert systems: the state of the art. *Mathematical models for decision support*, pages 487–517. *Cited on page 11.*

Robotis (2015). *Dynamixel Pro*. `http://www.robotis.com`. *Cited on pages 30 and 32.*

Ross-Hime Designs (2023). Case studies: Wet design. `https://www.anthrobot.com/casestudies/casestudy_wetdesign.php`. *Cited on page 41.*

Ross-Hime Designs (2024a). Omni-Wrist V. `https://www.anthrobot.com/omni-wrist-v/`. *Cited on page 155.*

Ross-Hime Designs (2024b). Omni-Wrist VI. `https://www.anthrobot.com/omni-wrist-vi/`. *Cited on page 155.*

Ross-Hime Designs (2024c). Robotic Surrogate III. `https://www.anthrobot.com/surrog_III/`. *Cited on pages 112 and 155.*

Rothemund, P., Kellaris, N., Mitchell, S. K., Acome, E., and Keplinger, C. (2021). Hasel artificial muscles for a new generation of lifelike robots—recent progress and future opportunities. *Advanced Materials*, 33(19):2003375. *Cited on page 33.*

Ruffler, D. (2023). Concept for a humanoid robot arm with quaternion joints. Master's thesis, Karlsruhe Institute of Technology (KIT). September 01, 2023. *Cited on pages 56, 112, 130, 134, and 140.*

Russell, S. J. and Norvig, P. (2010). *Artificial Intelligence: A Modern Approach*. Prentice-Hall series in artificial intelligence. Prentice-Hall, Upper Saddle River, NJ, 3. edition. *Cited on page 11.*

Samuelsen, E. and Glette, K. (2015). Real-world reproduction of evolved robot morphologies: Automated categorization and evaluation. In *European Conference on the Applications of Evolutionary Computation*, pages 771–782. Springer. *Cited on page 16.*

Sanctuary AI (2023). Product. `https://sanctuary.ai/product/`. *Cited on page 155.*

Saravanan, R., Ramabalan, S., Ebenezer, N. G. R., and Dharmaraja, C. (2009). Evolutionary multi criteria design optimization of robot grippers. *Applied Soft Computing*, 9(1):159–172. *Cited on page 17.*

Sathuluri, A., Sureshbabu, A. V., and Zimmermann, M. (2023). Robust codesign of robots via cascaded optimisation. In *IEEE International Conference on Robotics and Automation (ICRA)*. *Cited on page 9.*

Schmauder, M. and Spanner-Ulmer, B. (2022). *Ergonomie: Grundlagen zur Interaktion von Mensch, Technik und Organisation*. Hanser, München, 2 edition. *Cited on page 141.*

Schuenke, M., Schulte, E., Schumacher, U., and Johnson, N. (2020). *General Anatomy and Musculoskeletal System (THIEME Atlas of Anatomy)*. Thieme Medical Publishers, Stuttgart, 3 edition. *Cited on page 138.*

Schunk (2011). *Montage- und Betriebsanleitung Leichtbaumodul Typ PRL*. *Cited on page 32.*

Schütz, S., Mianowski, K., Kotting, C., Nejadfard, A., Reichardt, M., and Berns, K. (2016). RRLAB SEA — a highly integrated compliant actuator with minimised reflected inertia. In *IEEE International Conference on Advanced Intelligent Mechatronics (AIM)*, pages 252–257. *Cited on page 30.*

Schütz, S., Nejadfard, A., Mianowski, K., Vonwirth, P., and Berns, K. (2017). CARL — A Compliant Robotic Leg Featuring Mono- and Biarticular Actuation. In *IEEE/RAS International Conference on Humanoid Robotics (Humanoids)*, pages 289–296. *Cited on page 30.*

Schwartz, M., Sim, J., Ahn, J., Hwang, S., et al. (2022). Design of the humanoid robot TOCABI. In *IEEE/RAS International Conference on Humanoid Robots (Humanoids)*, pages 322–329. *Cited on page 155.*

SENSODRIVE (2020). *SENSO-Joints: Torque-controlled actuator*. *Cited on page 32.*

Seok, S., Wang, A., Otten, D., and Kim, S. (2012). Actuator design for high force proprioceptive control in fast legged locomotion. In *IEEE/RSJ International Conference on Intelligent Robots and Systems (IROS)*, pages 1970–1975. *Cited on pages 28, 89, 91, and 100.*

Shadow Robot (2022). Dexterous hand series: The world's most dexterous humanoid robot hands. `https://www.shadowrobot.com/dexterous-hand-series/`. *Cited on page 40.*

Shah, D., Metta, G., and Parmiggiani, A. (2019a). Comparison of workspace analysis for different spherical parallel mechanisms. In Gasparetto, A. and Ceccarelli, M., editors, *Mechanism Design for Robotics*, volume 66 of *Mechanisms and Machine Science*, pages 193–201. Springer International Publishing, Cham. *Cited on pages 112 and 155.*

Shah, D., Wu, Y., Scalzo, A., Metta, G., and Parmiggiani, A. (2019b). A comparison of robot wrist implementations for the iCub humanoid. *Robotics*, 8(1):11. *Cited on pages 39, 56, and 155.*

Shaukat, A., Burroughes, G., and Gao, Y. (2016). Self-reconfiguring robotic framework using fuzzy and ontological decision making. pages 133–152. *Cited on page 15.*

Shiakolas, P. S., Koladiya, D., and Kebrle, J. (2002). Optimum robot design based on task specifications using evolutionary techniques and kinematic, dynamic, and structural constraints. *Inverse Problems in Engineering*, 10(4):359–375. *Cited on page 15.*

Shin, S. Y. and Kim, C. (2014). Human-like motion generation and control for humanoid's dual arm object manipulation. *IEEE Transactions on Industrial Electronics*, 62(4):2265–2276. *Cited on page 24.*

Shuy, R. and Hollis, R. (2019). Development of a humanoid dual arm system for a single spherical wheeled balancing mobile robot. In *IEEE/RAS International Conference on Humanoid Robots (Humanoids)*, pages 499–504. *Cited on page 155.*

Simionescu, P. (2019). Kinematics of the RRR, RRT (passive) and RRRR, RRRT (active) linkage-mechanism building blocks with applications and reporting of new findings. *Journal of Mechanisms and Robotics*, 11:1–24. *Cited on page 20.*

Smith, P. and Lemstra, P. J. (1980). Ultra-high-strength polyethylene filaments by solution spinning/drawing. *Journal of Materials Science*, 15:505–514. *Cited on page 131.*

Sofka, J., Skormin, V., Nikulin, V., and Nicholson, D. (2006). Omni-Wrist III - a new generation of pointing devices. Part I. laser beam steering devices-mathematical modeling. *IEEE Transactions on Aerospace and Electronic Systems*, 42(2):718–725. *Cited on pages 40, 107, 113, and 117.*

SONE, K., ISOBE, H., and YAMADA, K. (2023). High angle active link. Technical report, N. T.N. Corporation. *Cited on pages 41 and 155.*

Song, H., Kim, Y.-S., Yoon, J., Yun, S.-H., Seo, J., and Kim, Y.-J. (2018). Development of low-inertia high-stiffness manipulator LIMS2 for high-speed manipulation of foldable objects. *IEEE/RSJ International Conference on Intelligent Robots and Systems (IROS)*, pages 4145–4151. *Cited on pages 41, 55, 56, and 155.*

Stasse, O., Flayols, T., Budhiraja, R., et al. (2017). TALOS: A new humanoid research platform targeted for industrial applications. In *IEEE/RAS International Conference on Humanoid Robots (Humanoids)*, pages 689–695. *Cited on page 155.*

Stentz, A., Herman, H., Kelly, A., Meyhofer, E., Haynes, G. C., Stager, D., Zajac, B., Bagnell, J. A., Brindza, J., Dellin, C., George, M., Gonzalez-Mora, J., Hyde, S., Jones, M., Laverne, M., Likhachev, M., Lister, L., Powers, M., Ramos, O., Ray, J., Rice, D., Scheifflee, J., Sidki, R., Srinivasa, S., Strabala, K., Tardif, J.-P., Valois, J.-S., Weghe, J. M. V., Wagner, M., and Wellington, C. (2015). CHIMP: The CMU highly intelligent mobile platform. *Journal of Field Robotics*, 32(2):209–228. *Cited on page 30.*

Sun, D. (1988). Performance analysis of a variable speed-ratio metal v-belt drive. *ASME Journal of Mechanical Transmission, Automation, and Design*, 110:472–481. *Cited on page 34.*

Sureshbabu, A. V., Chang, J. H., Fiorio, L., Scalzo, A., Metta, G., and Parmiggiani, A. (2017). A parallel kinematic wrist for the R1 humanoid robot. In *IEEE International conference on advanced intelligent mechatronics (AIM)*, pages 1215–1220. *Cited on pages 40 and 155.*

Tanaka, Y., Sakama, S., Nakano, K., and Kosodo, H. (2013). Comparative study on dynamic characteristics of hydraulic, pneumatic and electric motors. In *Fluid Power Systems Technology*, volume 56086, page V001T01A037. American Society of Mechanical Engineers. *Cited on pages 28, 89, and 92.*

Tanev, I., Ray, T., and Buller, A. (2005). Automated evolutionary design, robustness, and adaptation of sidewinding locomotion of a simulated snake-like robot. *IEEE Transactions on Robotics*, 21(4):632–645. *Cited on page 16.*

THK (2023). *Cross Roller Ring General Catalog*. *Cited on page 125.*

Toedtheide, A., Kühn, J., Fortunić, E. P., and Haddadin, S. (2021). An integrated, force-sensitive, impedance controlled, tendon-driven wrist: Design, modeling, and control. In *IEEE/RAS International Conference on Humanoid Robots (Humanoids)*, pages 25–32. *Cited on pages 39 and 155.*

TQ-Group (2020). *RD50/70/85-HD Gear motors*. *Cited on page 32.*

TQ-Group (2024). *ILM-E70x18 Frameless Hollow Shaft Motor*. *Cited on page 31.*

Tripathi, K. P. (2011). A review on knowledge-based expert system: Concept and architecture. *IJCA Special Issue on Artificial Intelligence Techniques-Novel Approaches & Practical Applications*, 4:19–23. *Cited on page 11.*

Tsagarakis, N. G., Metta, G., Sandini, G., Vernon, D., Beira, R., Becchi, F., Righetti, L., Santos-Victor, J., Ijspeert, A. J., Carrozza, M. C., et al. (2007). iCub: the design and realization of an open humanoid platform for cognitive and neuroscience research. *Advanced Robotics*, 21(10):1151–1175. *Cited on pages 39, 40, 55, and 56.*

Uhing, J. (1966). Rolling ring drive for converting a rotary movement into a feed movement. Patent DE1210647B, UHING JOACHIM ING, February 1966. *Cited on pages 34 and 35.*

Vahrenkamp, N., Asfour, T., and Dillmann, R. (2013). Robot placement based on reachability inversion. In *IEEE International Conference on Robotics and Automation (ICRA)*, pages 1970–1975. *Cited on pages 15 and 25.*

Vahrenkamp, N., Asfour, T., Metta, G., Sandini, G., and Dillmann, R. (2012). Manipulability analysis. In *IEEE/RAS International Conference on Humanoid Robots (Humanoids)*, pages 568–573. *Cited on pages 15 and 25.*

Van Harmelen, F., Lifschitz, V., and Porter, B. (2008). *Handbook of knowledge representation*. Elsevier. *Cited on page 11.*

Vanderborght, B., Albu-Schäffer, A., Bicchi, A., Burdet, E., Caldwell, D. G., Carloni, R., Catalano, M., Eiberger, O., Friedl, W., Ganesh, G., Garabini, M., Grebenstein, M., Grioli, G., Haddadin, S., Hoppner, H., Jafari, A., Laffranchi, M., Lefeber, D., Petit, F., Stramigioli, S., Tsagarakis, N., Damme, M. V., Ham, R. V., Visser, L. C., and Wolf, S. (2013). Variable Impedance Actuators: A Review. *Robotics and Autonomous Systems*, 61(12):1601–1614. *Cited on page 32.*

Vazquez-Sanchez, E., Sottile, J., and Gomez-Gil, J. (2017). A novel method for sensorless speed detection of brushed dc motors. *Applied Sciences*, 7(1):14. *Cited on page 101.*

Vila-Rosado, D. N. and Domınguez-López, J. A. (2006). A MATLAB toolbox for the optimal design of robot manipulators using evolutionary techniques. *International Conference on Mechatronic Technology (ICMT)*. *Cited on page 15.*

Wagner, W. P. (2017). Trends in expert system development: A longitudinal content analysis of over thirty years of expert system case studies. *Expert Systems with Applications*, 76:85–96. *Cited on pages 11 and 12.*

Wahl, J.-C., Sartor, M., Paredes, M., et al. (2003). A general framework for automated conceptual design of one dof mechanisms. In *International Conference on Engineering Design (ICED), Stockholm*, pages 17–18. *Cited on page 20.*

Wang, H., Fan, S., and Liu, H. (2012). An anthropomorphic design guideline for the thumb of the dexterous hand. In *IEEE International Conference on Mechatronics and Automation (ICMA)*, pages 777–782. *Cited on pages 15 and 26.*

Wang, Q., Chen, X., Yin, Y., and Lu, J. (2014). Ontology-based coupled optimization design method using state-space analysis for the spindle box system of large ultra-precision optical grinding machine. In *IEEE International Conference on Enterprise Systems*, pages 273–278. *Cited on page 18.*

Wang, T., Zhang, H., Chen, L., Wang, D., Wang, Y., and Xiong, R. (2023). Robust real-time motion retargeting via neural latent prediction. *IEEE/RSJ International Conference on Intelligent Robots and Systems (IROS)*, pages 3696–3703. *Cited on page 24.*

Weiner, P., Starke, J., Hundhausen, F., Beil, J., and Asfour, T. (2018). The KIT prosthetic hand: Design and control. In *IEEE/RSJ International Conference on Intelligent Robots and Systems (IROS)*, pages 3328–3334. *Cited on page 132.*

Whitman, J. and Choset, H. (2019). Task-specific manipulator design and trajectory synthesis. *IEEE Robotics and Automation Letters*, 4(2):301–308. *Cited on pages 16 and 17.*

Wilkie, D. (1949). The relation between force and velocity in human muscle. *The Journal of Physiology*, 110(3-4):249–280. *Cited on pages 33, 89, and 92.*

Willems, B. (2011). Control and safety of a 7 DOF anthropomorphic robotic arm: AMIGO's first gesture. Master's thesis, Eindhoven University of Technology. *Cited on page 155.*

Winter, D. A. (2009). *Biomechanics and motor control of human movement*. John Wiley & Sons. *Cited on page 28.*

Wu, M.-C., Lo, Y.-F., and Hsu, S.-H. (2008). A fuzzy CBR technique for generating product ideas. *Expert Systems with Applications*, 34(1):530–540. *Cited on page 14.*

Wu, Y. and Carricato, M. (2017). Synthesis and singularity analysis of n-UU parallel wrists: A symmetric space approach. *Journal of Mechanisms and Robotics*, 9(5). *Cited on page 112.*

Xiu, H., Han, Y., Wang, X., Zhang, Y., Liang, W., Wei, G., Ren, L., and Ren, L. (2022). Design, development, and clinical validation of a two degrees of freedom compliant ankle-foot prosthesis based on a 4-4r parallel mechanism. *Mechanism and Machine Theory*, 172:104818. *Cited on page 41.*

Xu, W., Li, X., Xu, W., Gong, L., Huang, Y., Zhao, Z., Zhao, L., Chen, B., Yang, H., Cao, L., et al. (2018). Human-robot interaction oriented human-in-the-loop real-time motion imitation on a humanoid Tri-Co robot. In *IEEE International Conference on Advanced Robotics and Mechatronics (ICARM)*, pages 781–786. *Cited on page 23.*

Yoshii, Y., Yuine, H., Kazuki, O., Tung, W.-l., and Ishii, T. (2015). Measurement of wrist flexion and extension torques in different forearm positions. *BioMedical Engineering OnLine*, 14(1):1–10. *Cited on page 107.*

Yoshikawa, T. (1985). Manipulability of robotic mechanisms. *The International Journal of Robotics Research*, 4(2):3–9. *Cited on pages 15, 25, and 142.*

You, W. S., Lee, Y. H., Kang, G., Oh, H. S., Seo, J. K., and Choi, H. R. (2019). Kinematic design optimization for anthropomorphic robot hand based on interactivity of fingers. *Intelligent Service Robotics*, 12(2):197–208. *Cited on page 15.*

Zacharias, F., Schlette, C., Schmidt, F., Borst, C., Rossmann, J., and Hirzinger, G. (2011). Making planned paths look more human-like in humanoid robot manipulation planning. In *IEEE International Conference on Robotics and Automation (ICRA)*, pages 1192–1198. *Cited on page 27.*

Zelik, K. E. and Kuo, A. D. (2010). Human walking isn't all hard work: evidence of soft tissue contributions to energy dissipation and return. *Journal of Experimental Biology*, 213(24):4257–4264. *Cited on pages 23 and 47.*

Zhang, P., Yao, Z., and Du, Z. (2013). Global performance index system for kinematic optimization of robotic mechanism. *Journal of Mechanical Design*, 136(3):031001. *Cited on pages 15 and 25.*

Zhang, W. J., Ouyang, P. R., and Sun, Z. H. (2010). A novel hybridization design principle for intelligent mechatronics systems. In *The Abstracts of the international conference on advanced mechatronics: Toward evolutionary fusion of IT and mechatronics: ICAM 2010.5*, pages 67–74. The Japan Society of Mechanical Engineers. *Cited on page 34.*

Zhao, A., Xu, J., Konaković-Luković, M., Hughes, J., Spielberg, A., Rus, D., and Matusik, W. (2020). RoboGrammar: Graph grammar for terrain-optimized robot design. *ACM Transactions on Graphics (TOG)*, 39(6):1–16. *Cited on page 10.*

Zheng, C., Eynard, B., Qin, X., Li, J., Bai, J., Gomes, S., and Zhang, Y. (2019). A requirement-driven architecture definition approach for conceptual design of mechatronic systems. *Integrated Computer-Aided Engineering*, -(Preprint):1–22. *Cited on page 19.*

Ziglar, J., Williams, R., and Wicks, A. (2017). Context-aware system synthesis, task assignment, and routing. *arXiv preprint arXiv:1706.04580*. *Cited on page 19.*

Zinn, M., Roth, B., Khatib, O., and Salisbury, J. K. (2004). A new actuation approach for human friendly robot design. *The International Journal of Robotics Research*, 23(4-5):379–398. *Cited on page 34.*

Zu, Y., Xiao, R., and Zhang, X. (2009). Automated conceptual design of mechanisms using enumeration and functional reasoning. *International Journal of Materials & Product Technology*, 34(3):273. *Cited on page 20.*

Own Publications

Kossev, V., **Klas**, C., and Asfour, T. (2024). Humanoid robot design assistant - requirements from human motion. In *IEEE/RAS International Conference on Humanoid Robots (Humanoids)*, pages 425–432.

Klas, C., Meixner, A., Ruffler, D., and Asfour, T. (2023). On the actuator requirements for human-like execution of retargeted human motion on humanoid robots. In *IEEE/RAS International Conference on Humanoid Robots (Humanoids)*, pages 1–8.

Klas, C. and Asfour, T. (2023). Reaching torque-velocity profiles of human muscles: The adaptive cycloidal linear drive. *IEEE/ASME Transactions on Mechatronics*, 28(6):3470–3479.

Klas, C. (2023). Linear drive having two reduction stages. Patent WO2023006350A1, Karlsruher Institut für Technologie, February 2023.

Klas, C. and Asfour, T. (2022). A compact, lightweight and singularity-free wrist joint mechanism for humanoid robots. In *IEEE/RSJ International Conference on Intelligent Robots and Systems (IROS)*, pages 457–464.

Klas, C., Hundhausen, F., Gao, J., Dreher, C. R., Reither, S., Zhou, Y., and Asfour, T. (2021). The KIT gripper: A multi-functional gripper for disassembly tasks. In *IEEE International Conference on Robotics and Automation (ICRA)*, pages 715–721.

Asfour, T., Schill, J., Peters, H., **Klas**, C., Bücker, J., Sander, C., Schulz, S., Kargov, A., Werner, T., and Bartenbach, V. (2013). ARMAR-4: A 63 DOF torque controlled humanoid robot. In *IEEE/RAS International Conference on Humanoid Robots (Humanoids)*, pages 390–396.